2017

Nondestructive Evaluation and Health Monitoring of Adhesively Bonded Composite Structures

William Walker Roth
University of South Carolina

Nondestructive Evaluation and Health Monitoring of Adhesively Bonded Composite Structures

by

William Walker Roth

Bachelor of Science
University of South Carolina 2011

Master of Engineering
University of South Carolina 2017

Submitted in Partial Fulfillment of the Requirements

for the Degree of Doctor of Philosophy in

Mechanical Engineering

College of Engineering

University of South Carolina

2017

Accepted by:

Victor Giurgiutiu, Major Professor

Lingyu Yu, Committee Member

Michel van Tooren, Committee Member

Paul Ziehl, Committee Member

Bin Lin, Committee Member

Cheryl L. Addy, Vice Provost and Dean of the Graduate School

Acknowledgments

I would like to acknowledge my academic advisor, Dr. Victor Giurgiutiu, for his support and guidance over the past few years. His mentoring has helped me expand my horizons. I would also like to acknowledge and thank Dr. Lingyu Yu, Dr. Michel van Tooren, Dr. Paul Ziehl and Dr. Din Lin for being part of my committee and providing their guidance on this subject. Lastly, I would like to thank my wife for her unwavering support of my academic pursuits; I would not have made it to this level without her encouragements.

William W. Roth

Abstract

As the growth of fiber reinforced composite materials continues in many industries, structural designers will have to look to new methods of joining components. In order to take full advantage of composite materials, such as increased stiffness, decreased weight, tailored material properties and increased fatigue life, mechanical fasteners will need to be replaced by adhesive bonding or welding, when possible. Mechanical fasteners require the drilling of holes, which damages the laminate and becomes the source of further fatigue damage. Also, an increase in laminate thickness or inclusion of other features is required for the material to withstand the bearing stress needed to preload fasteners. Adhesives transfer the load over a large area, do not require additional machining operations, provide increased stiffness through the joint, provide corrosion protection when joining dissimilar materials, and provide vibrational damping. Additionally, the repair of composite structures, which will become a major concern in the near future, will require the use of adhesive bonding for thermoset composites. In order for adhesives to be used to join primary aerospace structures they must meet certification requirements, which includes proof that the joint can withstand the required ultimate load without structural failure. For most components, nondestructive inspection is used to find critical flaws, which is combined with fracture mechanics to ensure that the structure can meet the requirements. This process works for some of the adhesive flaws, but other critical defects are not easily detected. Weak interface bonding is particularly challenging. This type of defect results in an interphase zone that may be only a dozen microns in thickness. Traditional bulk wave ultrasonic techniques cannot easily distinguish this zone from the

interface between adherend and adhesive. This work considers two approaches to help solve this problem.

Guided elastic wave propagation along laminate structures is highly dependent on the boundary conditions at the surface and between plies, especially at high frequencies. This work investigates how interfacial defects can alter the propagation of guided waves through bonded fiber reinforced composite materials. As well as how this information can be used to determine the interface properties and correlate the results with fracture parameters. The second approach investigates how structural health monitoring can be used to detect the growth of disbonds from service loads. A mode selection technique is proposed for selecting frequency ranges for electromechanical impedance spectroscopy.

Table of Contents

List of Tables

List of Figures

Part I

Overview of Adhesively Bonded Structures

Chapter 1

Introduction

1.1 Structure

Adhesives and laminated materials have been used for thousands of years to join different materials to exploit the benefits that each material. In the early 20th century, laminated wood products and adhesives in the construction of aircraft, before metallic materials began to dominate the industry. Modern adhesives have been used on aircraft since World War II, and this long service history has proven the benefits and potential reliability of adhesives. Several DE Havilland Aircraft began using Redux 775, a toughened phenolic adhesive, in the late 40s, and Fokker used Redux 775 in the 50s and 60s on the F27 and F28 [1]. Beevers [2] analyzed parts from a DE Havilland Comet and stated that "Mechanical properties of the joints removed from old Comet bonded panels showed little or no loss of (mechanical strength) performance during their 30-year life". High temperature epoxies began to be used in the Boeing 727 and 737 in the 60s [1]. The use of adhesively bonded composite structures continues to expand, but the absence of a method of proving the strength of the bond, primarily at the interface, has limited the application or resulted in the addition of extra safety features, such as mechanical fasteners at the edges of joints.

There are several advantages that adhesives offer over mechanical fastening systems [3]:

- A decrease in stress concentrations with a more uniform distribution of stress, permitting the fabrication of thinner, lighter and stronger structures

- Joints can be formed smoothly over contours and other complex shapes
- Provides a means of joining dissimilar materials, such as composite-to-metal, and provides a barrier to electrolytic corrosion
- Creates a damping layer for vibration and sound
- Also acts as a sealant and electrical insulator, or a conductor if desired
- Has the potential to reduce fabrication cost and time

There are also several disadvantages that must be considered [3]:

- Can require long cure times and or high curing temperatures and pressures
- May degrade under environmental exposure
- Cannot be visually inspected; difficult to perform quality insurance and NDE
- Restricted service temperatures, special adhesives required for high temperature applications
- Requires very tight process control on surface preparation, handling and curing

Adhesives have been used on nearly every part of aircraft, helicopter, rocket and missile structures. A few common areas include wing structure, fuselage, rudder, doors, tail sections, floor panels, bulk heads, nose cones, nozzles and motor casings [3]. The use adhesive in these structures is typically chosen in order to reduce weight and/or form smooth joint contours. Structural adhesives are generally grouped into three categories; thermosetting, thermoplastic and elastomer; although most modern adhesives combine all of these categories in order to optimize strength and toughness. Adhesive is generally available in four forms; liquid, paste, film or powder. Film adhesives have come to dominate most structural applications because they eliminate the mixing process, provide bond line thickness control and are easy to apply to

curved or complicated surfaces. There are several types of bonded joints; metal-to-metal, metal-to-composite, metal-to-rubber, composite-to-composite, honeycomb core to face sheet, or fiber reinforced composites. Figure 1.1 shows several possible joint designs. Each of these designs provides advantages in terms of stress distribution,

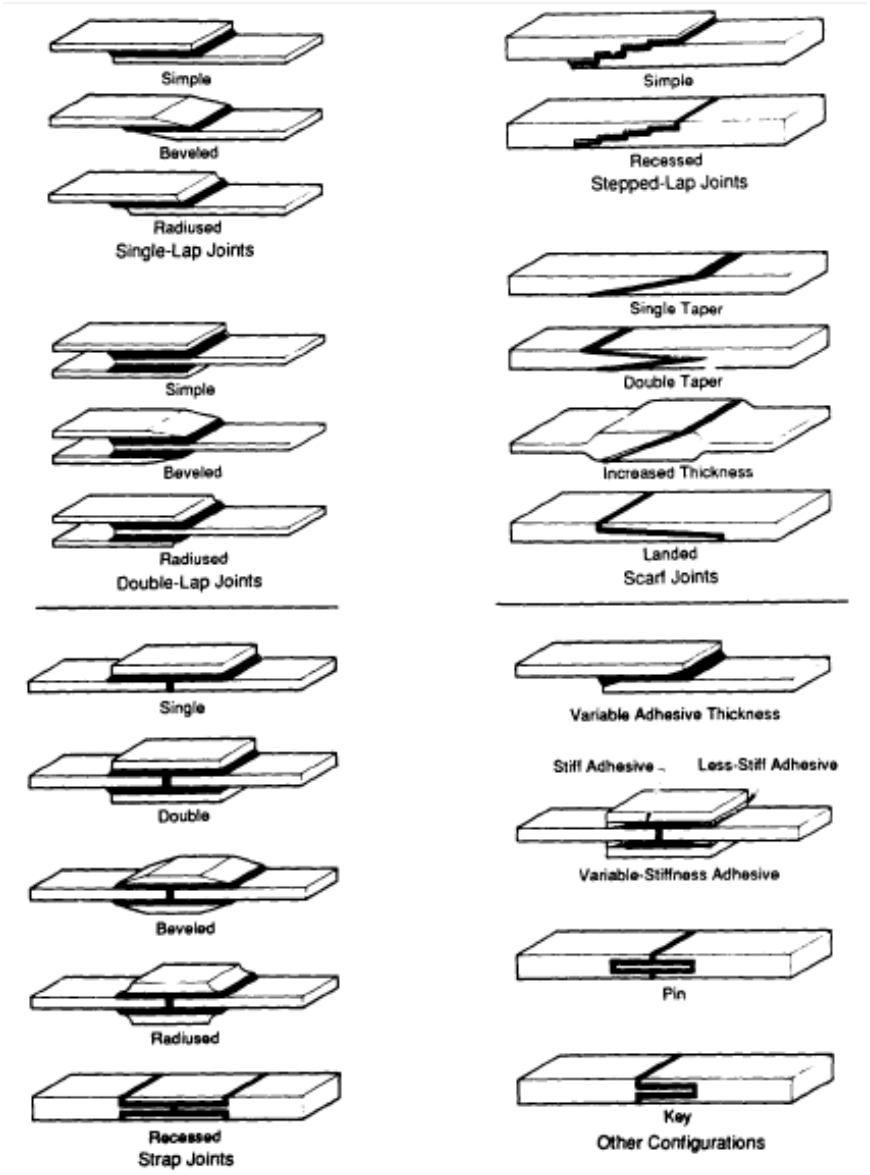

Figure 1.1: Adhesive joint designs [3]

stiffness, complexity, smooth contour, etc. A detailed discussion on stress analysis and fracture mechanics is provided in a later section. These basic designs are then combined to form a structural assembly, as shown in Figure 1.2.

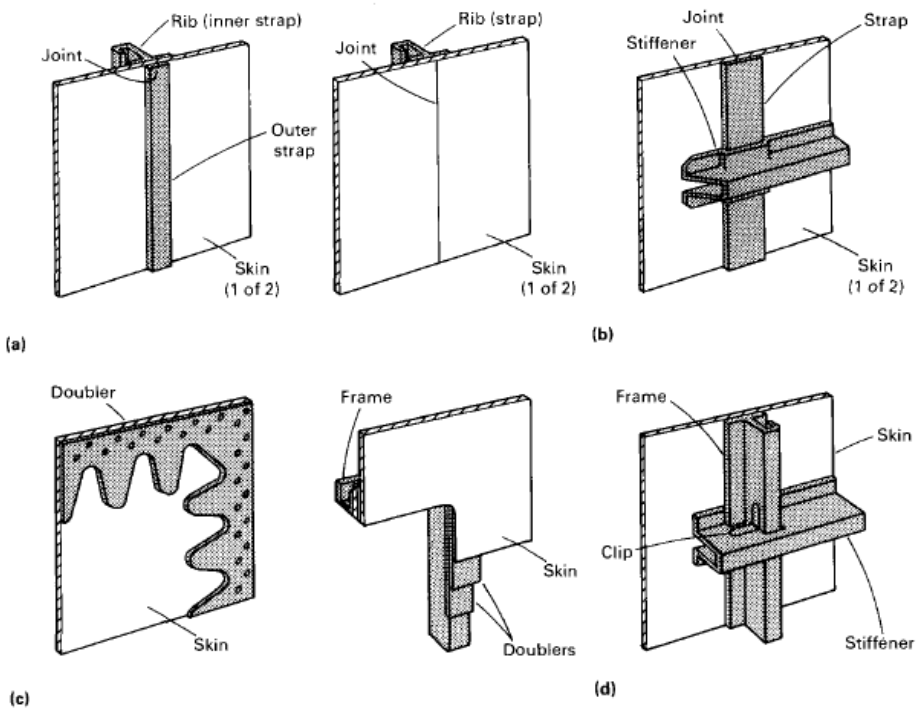

Figure 1.2: Adhesively bonded structural assemblies [4]

Honeycomb structures often use adhesive film to join the face sheet to the core material, especially if the face sheet and core are mode of different materials. Upon curing this should form an adhesive fillet, as shown in Figure 1.3. In addition to the

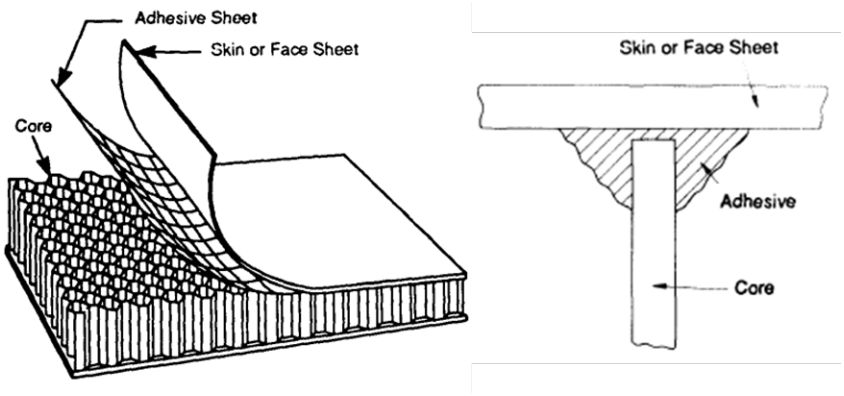

Figure 1.3: Honey comb structure [4]

adhesive film, honeycomb assembly generally requires expandable adhesive to fill the edge core in order to prevent crushing. Other types of adhesive may be used to bond enclosure parts and provide additional edge stiffness, as shown in Figure 1.4.

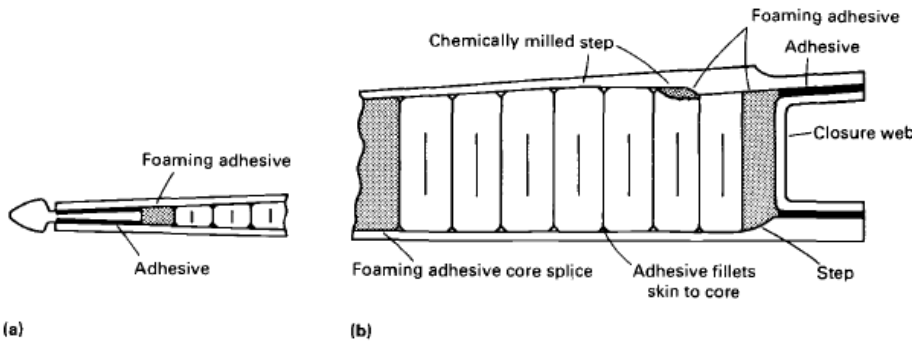

Figure 1.4: Diagram of an example of honeycomb assembly [4]

1.2 Defects

The following section discusses the types of defects found in adhesively-bonded composite structures. A literature review of the subject has resulted in an exhaustive list of possible defects that may occur in a bonded structure. These defects have been lumped into three general categories; defects found within a fiber reinforced laminate, defects found within an adhesive bond line, and lastly defects which are specific to core material, such as honeycomb. Additionally, metallic adherends have a set of unique defects which will only be casually mentioned in this paper, since these defects are best addressed by inspection techniques designed specifically for metallic structures. It is important to mention at this point in the paper that the presence of a defect does not necessarily require the rejection or even repair of the structure. Wang et al. [5] showed that the short term strength of adhesive joints, as proved through the tension testing of single lap joints, may not be significantly reduced by the presence of large disbonds. However, the long term durability of the structure may be reduced due to the presence of defects; additionally, the defects may act as nucleation sites for more extensive damage [6]. As a result, the acceptable tolerances for each type of damage must be assessed and included in the design of the structure.

Light [3], Hagemaier [4], Adams [7, 6], and Bode [8] have written excellent review papers on adhesive defects and inspection which are recommended as an initial read

for anyone interested in the NDE of adhesive bonds. These important review papers have influenced the following discussion on the key defects within adhesive joints.

According to Adams [6], adhesive bond defects can be grouped into three categories; (1) poor adhesion, i.e. weak interfacial bonding, (2) poor cohesive strength and (3) complete voids, disbonds and porosity. This categorization of the defects has progressed from earlier descriptions which grouped the defects in two groups; cohesive defects and interfacial defects. The change reflects the current challenges in the NDE of adhesive joints. The last category of defects are easily identified with current commercial techniques and constitute the majority of defects found in these structures. Hagemaier [4] found that voids and disbonds constituted 74% of rejectable flaws in adhesive assemblies. The remaining flaws mostly consisted of core material flaws. The second category, poor cohesive strength, is the result of improper mixing, incomplete cure or an improper adhesive formulation. These defects can be prevented by careful monitoring of the manufacturing process, as well as proper design of the adhesive joint. The first category, poor adhesion, is a result of contamination or improper preparation of the bonding surface. This type of defect is preventable when a proper surface preparation procedure is implemented and great care is taken to prevent contamination; however, it is still possible to create a weak interfacial bond and current NDE techniques are not sensitive to this condition.

All of the references agree on the following list of general defects found in adhesive bonds: porosity, incomplete cure, cracks, voids, disbonds and zero thickness disbonds or weak bonding. These defects are shown in Figure 1.5. Hagemaier [4] produced a more extensive list of defects for the ASM Handbook, Volume 17, see Figure 1.6. This list expands on the previous discussion with the addition of fillet and adhesive flash issues, inclusions, core defects, and the mechanisms which cause the flaw; however, Hagemaier did not consider laminated composite structures.

Bode et al. [8] created a list of five requirements that will lead to a durable

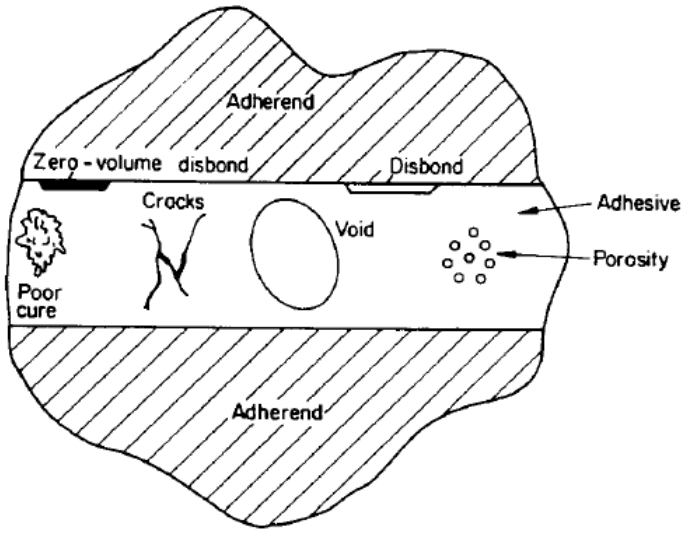

Figure 1.5: Common defects in adhesive joints [7]

Flaw-producing mechanism	Generic flaw type				
	Metal-to-metal	Metal-to-core	Core	Surface	Adhesive
Disbonds, internal	X				
Disbonds, part edge	X	X			
Disbonds, high core	X				
Porosity	X	X	X		X
Unremoved protective release film from adhesive	X	X			
Foam adhesive in film adhesive bond line	X	X			
Cut adhesive	X	X			X
Adhesive gaps	X	X			
Missing adhesive	X	X	X		
Weak bonds	X	X	X		
Extra layers of film adhesive	X	X			
Foreign objects	X	X	X		X
Double drilled or irregular holes	X			X	
Disbonds, low core		X			
Void or gap, chemical milled land		X			
Void or gap, doublers		X			
Missing fillets		X			
Void, closure-to-core		X			
High-density inclusions (chips, etc.)	X	X			X
Voids, foam joint		X	X		
Disbond, shear ties	X	X			
Lack of sealant at fasteners		X			
Thick foam adhesive		X			
Broken fasteners	X	X			
Crushed core			X		
Wrinkled core			X		
Condensed core			X		
Distorted core			X		
Blown core			X		
Node bond separation			X		
Missing core (short core)		X	X		
Cut core		X	X		
Water in core			X		
Cracks				X	
Scratches				X	
Blisters				X	
Protrusions				X	
Indentations (dents/dings)				X	
Wrinkles				X	
Pits				X	

Figure 1.6: Exhaustive list of defects for adhesive joints with metallic adherends[4]

adhesive bond.

1. Properly preparing the substrate surfaces for bonding
2. Correctly mixing and applying the adhesive materials
3. Controlling the bond line thickness
4. Applying uniform and correct clamping pressure during cure
5. Properly curing the adhesive with correct temperatures and times

The authors found that any deviations from this list of requirements will lead to a decrease in the apparent strength and durability of the adhesive joint and lead to the formation of other defects.

It is valuable to understand how these types of defects are formed in the bonding process so that they may be prevented or properly detected. As a result, the following several paragraphs will discuss how each type of defect is formed.

1.2.1 Porosity

The creation of volatiles and entrapped gases, such as air or water vapor, within the adhesive lead to porosity [7]. It may also be created when these volatiles are prevented from escaping from the joint, particularly when bonding large areas. Additionally, poor curing pressure or a very thick bond line will lead to an increase in porosity. The presence of porosity will significantly decrease the strength of the joint.

Porosity is prevented by keeping the bond line thin, applying enough pressure during the cure, properly applying and spreading the adhesive and joining the adherends to prevent the entrapment of air, and providing a way for the volatiles to escape during the cure.

1.2.2 Voids

There are a variety of reasons that a void may form in an adhesive bond line. Common causes include; applying an insufficient amount of adhesive, not spreading out the adhesive in a uniform layer and excess adhesive loss during cure, air entrapment during the layup, and entrapment of volatile gases. Sometimes, voids maybe formed from the coalescence of porous areas [7]. When film adhesives are used, voids can be formed from film wrinkles or gaps at the boundaries of layers.

Voids are prevented with very similar measures to porosity. Properly apply the adhesive, careful layup, sufficient pressure, thin bond lines, prevent excess resin loss during the cure, provide a path for the expelling of volatiles.

1.2.3 Cracks

Adhesive cracking is less common than the other defects, especially with the advent of modern high toughness adhesives. Cracks can form and grow under high service loads and fatigue, but they are less common at the time of manufacture. When cracks do form it is generally associated with thermal shrinkage and thermal coefficient mismatching from a high temperature cure. As mentioned, this is more common with brittle adhesives, especially high temperature adhesives [7].

Cracks and fractures can also form during transportation, handling and assembly. This would be from excessive loads, and accidental impacts.

The prevention of adhesive cracks is achieved through careful handling, proper adhesive and adherend selection, and careful control of curing parameters.

1.2.4 Poor Cure

Poor or improper cure is caused by an incorrect mixture or from an improper or incomplete temperature or pressure cycle. Sometimes poor cure can occur locally due to the reaction with a contaminant or the formation of condensation. Also, localized

poor cure can form in large bonding areas due to the variance in temperature and pressure during the cure cycle.

Careful and proper mixing of the adhesive components will prevent poor cure. Some manufactures choose to use film adhesives, which are premixed and are kept at very low temperatures to prevent curing. A proper cure cycle should be the easiest parameter to control, but careful considerations must be made when bonding large areas to ensure that the entire region is cured properly.

1.2.5 Disbonds and Poor Adhesion

Bode at al. [8] define a disbond as a loss of the ability to transfer loads across an interface regardless of the state of contact between the substrate and adhesive. The most common causes of disbonds, as well as poor adhesion, are surface contamination, inadequate surface preparation, or insufficient pressure. A detailed analysis of the adhesive interface is provided in a later section, where the origin of these theories are analyzed. Also, some disbonds are formed from weak bonds after thermal shrinkage or structural loading.

These defects are prevented through proper and careful surface preparation, careful handling of the surfaces after preparation, limiting the time between surface preparation and bonding, and applying sufficient pressure during the cure.

1.2.6 Core Defects

There are a number of defects that can occur in the fabrication of honeycomb structures. The primary defect involving the adhesive is the lack of a proper adhesive fillet, or a disbond and subsequent lack of bonding. This can be caused by insufficient pressure, insufficient adhesive or improper surface preparation. Core specific defects include; crushed core, blown core, condensed core, node separation, voids in the expanding adhesive, short core and foreign objects. Crushed core occurs when

there is an impact or dent in the skin or when the bonding pressure is excessive. This leads to buckling or wrinkling of the cell wall. Wrinkling may be acceptable, but buckling is usually not. Condensed cores occur when the side of the core is compressed laterally. This may occur from an impact, or other load during handling. Additionally, this may occur if the core is shifting during fabrication. Node separation may occur during the manufacturing of the honey comb core; there is also a risk of node separation if high pressure leaks into a cell during autoclave during. A blown core may occur during sudden changes in pressure, such as under vacuum. Voids can occur in the expanding adhesive or foam used to fill in the edge cells for increased stiffness and to prevent core crushing. This will occur if the fill area is greater than expected, leading to an insufficient amount of adhesive to fill the volume. May also occur if there is slumping in the adhesive or if the adhesive fails to fill into all of the crevices and tangs. A short core will occur if the core material is milled too short and a gap will form between the core and skin. Foreign objects can be left in the core during the fabrication and lead to further damage in assembly or operation. Figure 1.7 provides a graphical view of some of the core defects.

1.2.7 Laminated Composites

Laminated fiber reinforced composites have many of the same defects as found in adhesive joints, such as porosity, voids, delaminations, poor cure, cracking, weak interlaminar bonding and weak fiber-to-resin bonding. There are several specific defects that are worth mentioning here. The first is air entrapment. This will occur during layup if there is a wrinkle or overlapping laminae, see Figure 1.8. This can be avoided with careful planning and practice during layup.

Resin rich areas or dry areas can form in a lamina. This can occur when the resin does not sufficiently wet the fibers, or when the tows are not spread out evenly and bundle together. This issue is less common in hand laid sheets prepreg, but could be

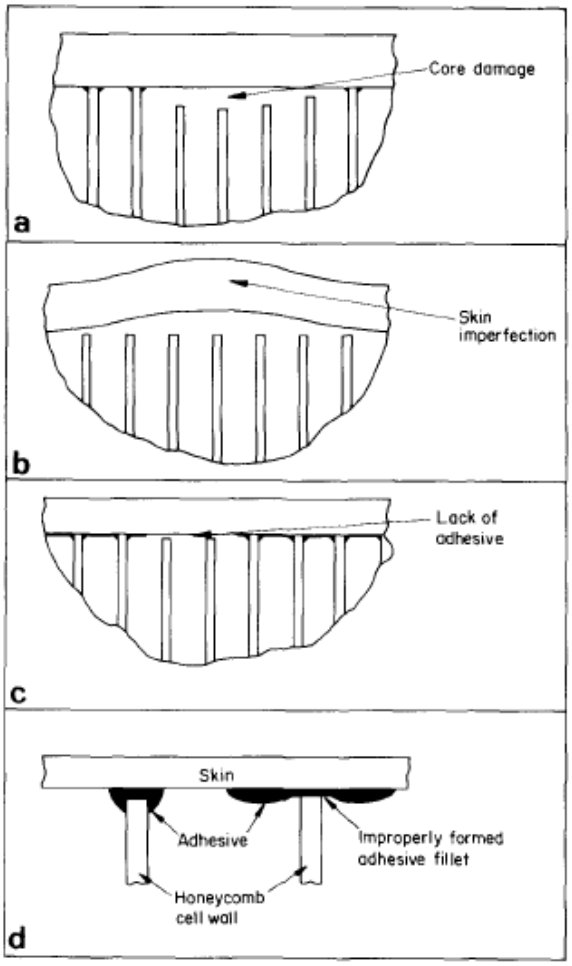

Figure 1.7: Honeycomb bonding defects[7]

a serious issue when thin layers are placed onto the part, such as filament winding or fiber placement. This is also a serious concern in resin infusion processes.

1.2.8 Fillet Defects

A proper adhesive fillet is required to reduce the stresses at the edges of adhesive joints, as will be seen in the next chapter. There are several defects that can occur within this fillet. A lack of fillet may occur form an insufficient application of adhesive and is easily identified through visual inspection with the aid of feeler gauges. A frothy or porous filter can occur when the heating rate is too high. This will drive out volatiles at a rapid rate causing bubbling in the fillet and a porous bondline. The

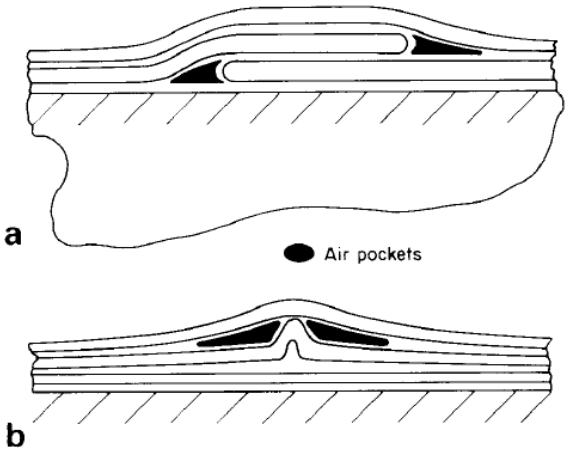

Figure 1.8: Air entrapment from a) overlapping and b) wrinkling [7]

fillet can be fractures from mishandling, such as drops, excess flexing, or tool impacts.

1.2.9 Machining Issues

Machining operations can lead to any of the defects mentioned in the previous sections, or they may increase the severity of defects that are already present. Machining operation post cure should be kept to a minimum, and when they are required the process variables should be controlled carefully. These include feed rate, feed force, rotational velocity and the use of cutting fluid. One type of defect that is specific to machining and drilling is burned or over-cured adhesive. Measures should be taken to ensure that the part does not overheat during these operations.

1.2.10 In-Service Defects

The most common causes of defects in-service include impact damage, overloads, corrosion, and fatigue issues. Of these, only impacts and overloads cause unexpected damage. Corrosion and fatigue issues should be prevented through careful design, manufacturing and operation. Many defects that are later found during operation likely originated in the manufacturing process but went undetected. Weak interfacial bonding will generally lead to disbonding when subject to loading. In general, periodic

inspection is required due to the environmental degradation that can occur, leading to a reduction in the strength of the adhesive joint.

1.3 Bond Quality

Many articles and researchers will discuss bond quality. This is a difficult measure to express quantitatively. As Light and Kwun [3] stated "Quality of a bond is related to the functional usefulness of the bonded assembly. Although no definition is universally accepted, the bond quality generally refers to absence of defects such as disbonds, delaminations, voids, or foreign substances; mechanical strengths of the bonded joint; and joint durability in the expected service environment." While there is no consensus on this term, the following factors are known to influence the bond quality: joint type and geometry, adherend material, adhesive type and composition, surface treatment, environmental conditions, curing process, bondline thickness, residual stress, defects (fabrication or in-service), workmanship, and environmental degradation.

Light and Kwun [3] divided the bond variables into intrinsic and extrinsic properties. Where the intrinsic properties affect the cohesive strength and include the degrees of cure, adhesive chemistry, bondline thickness and presence of voids, and the extrinsic properties affect the adhesive strength and include the surface cleanliness, surface contamination, primer type, application and wetting properties. The authors determined that even if all intrinsic properties were within tolerance, the bond could still fail prematurely due to extrinsic properties. As a result, a multidisciplinary approach must be taken which combines NDE and fracture mechanics.

Sometimes bond quality and strength or durability or used interchangeably. This is generally not a favorable interchange or terms because there are some means of evaluating bond quality, but the only reliable way to measure bond strength is through destructive tests. However, fracture mechanics can be used to evaluate joint strength, and the failure of the joint generally occurs from the propagation of cracks, disbonds

or delaminations; therefore, bond quality can give an indication of the remaining strength or life.

Chapter 2

Stress Analysis and Fracture Mechanics

2.1 Stress analysis

While adhesives have been used to join materials for thousands of years, detailed analysis of the stresses within adhesive joints and the mechanisms of failure did not begin until the early 20th century, when they were used in aircraft structures. Volkerson [9] and then Goland and Reissner [10] provided the earliest two dimensional analytical models for determining the stress and strain distributions within a uniform lap joint. These models only considered the distribution along the length of the bond line and neglected the through thickness distribution. Additional analytical and numerical models were developed through the 20th century in order to accommodate adhesive and adherend nonlinearity, composite adherends, dissimilar adherends and three dimensional affects; da Silva et al. [11] and Gleich [12] have provided thorough reviews on the various lap joint models. All of the models depict stress as having a peak value near the edge of the joint and decreasing towards the center. Also, as the joint thickness decreases, the maximum shear and peel stresses decrease. The shear stress and peel stress distributions are shown in Figure 2.1 and Figure 2.2 for several analytical models. All of the models provide close agreement.

Various continuum failure models were used to predict the strength of the joint, including max stress, max strain, plastic strain, von Mises, as well as strain energy density [12]. However, experimental data has shown that failure load with respect to bondline thickness first increases to a maximum value and then decreases with

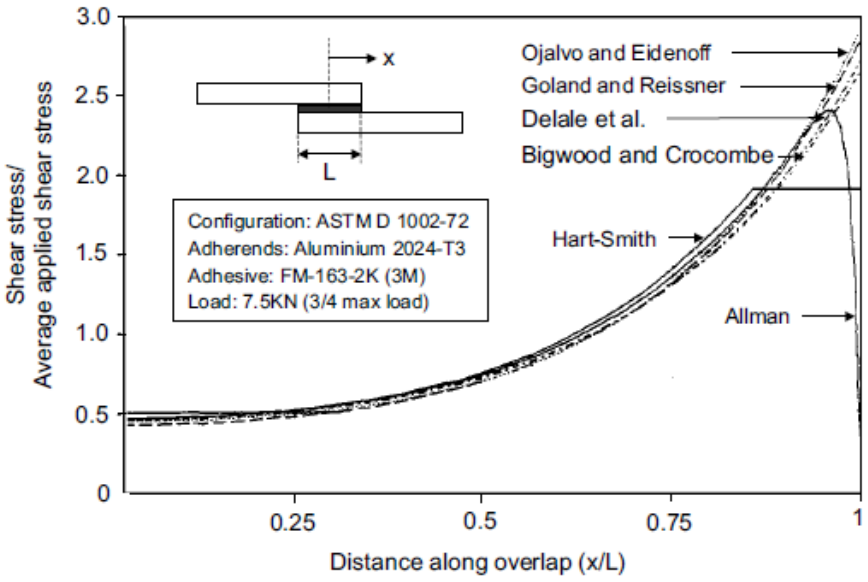

Figure 2.1: Comparison of shear stress distribution of selected classical theories [12]

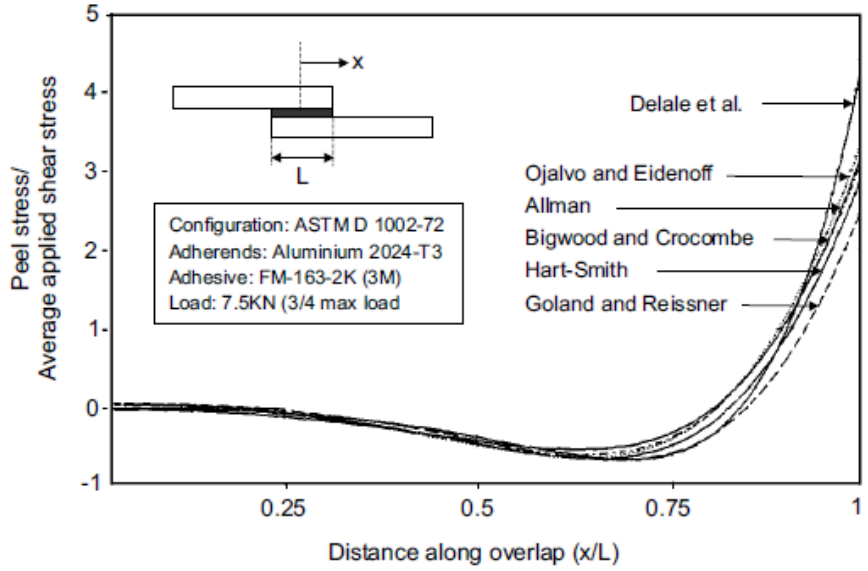

Figure 2.2: Comparison of peel stress distribution of selected classical theories [12]

increasing thickness [12]. This result does not agree with the analytical stress models, which predict an inverse correlation between bondline thickness and maximum stress. Detailed finite element analysis has shown that the stresses vary through the thickness and that the stresses at the interface increase with bondline thickness as a result of bending due to the misaligned load path in single lap joints [12]. While the FE analysis provides a better prediction of the relationship between strength and bondline thickness, it does not fully predict the observed trend. Figure 2.3 shows this relationship and how FE results have improved the prediction but do not match experimental results.

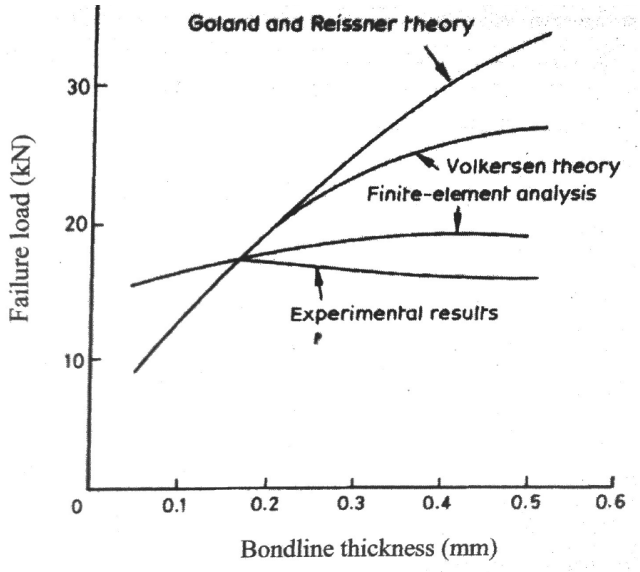

Figure 2.3: Effect of bondline thickness on failure load in a single lap joint [12]

Also, the application of FE analysis in hindered by the stress singularities at the joint tips; therefore, the stress results become mesh dependent. This often requires the exclusion of stresses near the singularities when using FE generated stress distribution. Figure 2.4 shows some of the singularity points in adhesive joints. The addition of a fillet at the edge of the bondline was used to reduce the stress at the edges, but it has been shown that the stress singularities still exist with the fillet, and the stress distribution becomes dependent on the fillet radius.

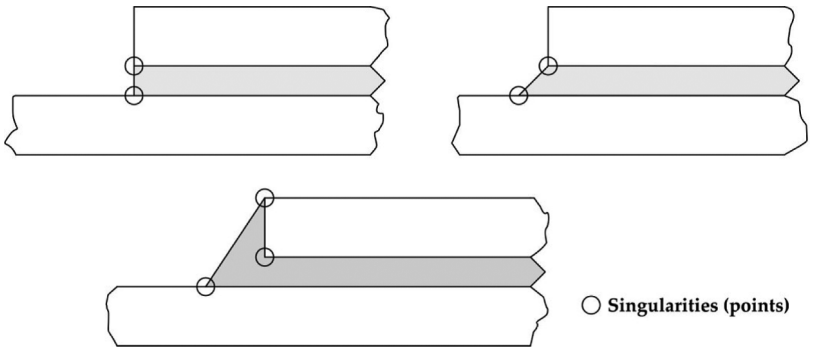

Figure 2.4: Singularities in adhesive joints [13]

2.2 Fracture mechanics

As a result of the unexplained strength dependence on the bondline thickness and the presence of stress singularities many researchers began looking at fracture mechanics as a way of prediction joint failure. Initial work considered linear elastic fracture mechanics and the application of energy release rate [13]. ASTM D3433 was developed in order to experimentally determine the mode one energy release rate through a double cantilever beam test, specimen configuration is shown in Figure 2.5. Performing this test while varying the adhesive thickness has revealed a similar trend as seen in the failure testing of single lap joints. This trend is most likely due to the size of the plastic zone [14], which increases as the thickness increases until it reaches a maximum energy release rate and then decreases until it plateaus at the energy release rate of the bulk adhesive, this trend is shown in Figure 2.6. It has been theorized that this dependence is due to the constraints placed on the plastic or process zone due to the limited adhesive thickness, and once this adhesive thickness is greater than the plastic zone the energy release rate will be similar to that observed in the bulk material, this idea is demonstrated in Figure 2.7.

This result led to the development of tough adhesives. Plasticizers were added to structural epoxies, increasing the energy release rate of the bulk material through cavitation and crack bridging of the plastic particles, as shown in Figure 2.8 [15]. The

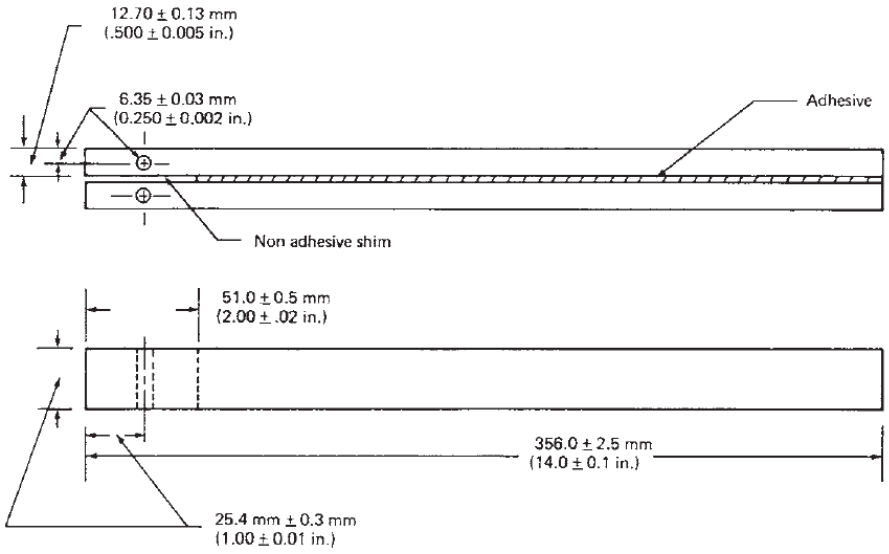

Figure 2.5: ASTM D3433 flat adherend schematic

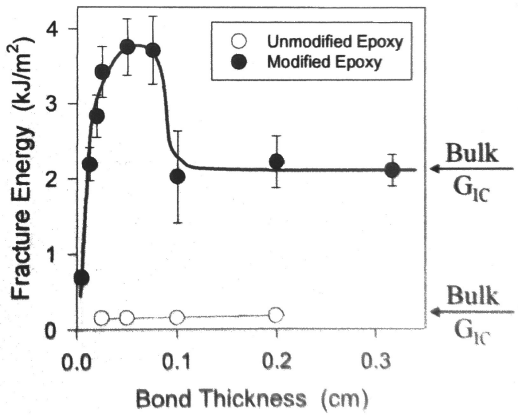

Figure 2.6: Fracture energy as a function of bond thickness [14]

DCB testing also showed that the energy absorption of the substrate also plays an important role in the observed energy release rate [15]. If a thin ductile substrate is used, then the substrate will deform and absorb a large amount of energy, increasing the measured G_{IC}; however, if a thick stiff substrate is used, then very little energy is absorbed by this layer and the adhesive fails with a low G_{IC} [15].

While the DCB testing and LEFM provide a good method for comparing adhesives and substrates in order to find a combination with the largest energy release rate, the use of tough nonlinear adhesives and ductile substrates invalidates the use

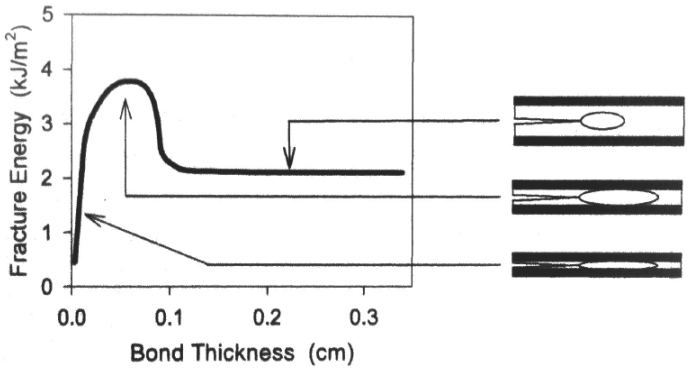

Figure 2.7: Fracture energy and plastic zone size [14]

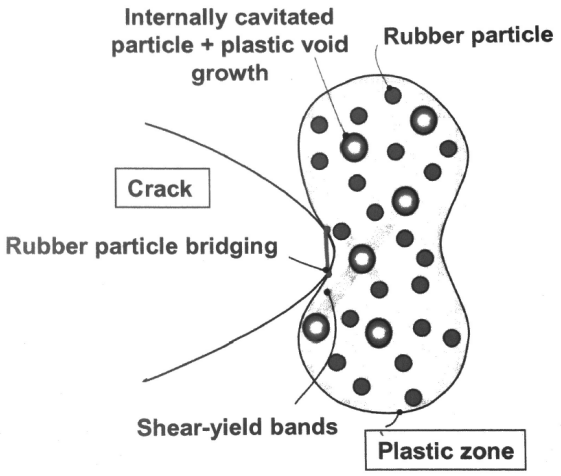

Figure 2.8: Plastic zone and rubber toughening mechanisms [15]

of William's solution and fracture toughness for determining the behavior of adhesive joints. Additionally, the use of this method requires that a crack exist in the material; therefore, when modeling the intended joints, a crack must be placed into the model [16]. In order to accurately predict the failure strength of useful joints, many researchers have turned to cohesive zone models. This type of model does not require an initial crack, can account for nonlinearity in the adhesive, and can account for the singularities generated at joint edges. The cohesive zone is modeled into FEA with either spring or contact elements. A traction - displacement relationship is created where the stress begins to relax after reaching a maximum value and the total area under the curve at fracture is equal to the critical energy release rate. This law is

matched to experimental data, where typical models are triangular, trapezoidal and exponential curve fits. The cohesive zones must be modeled along possible crack propagation paths as shown in Figure 2.9. Figure 2.10 shows the possible cohesive models.

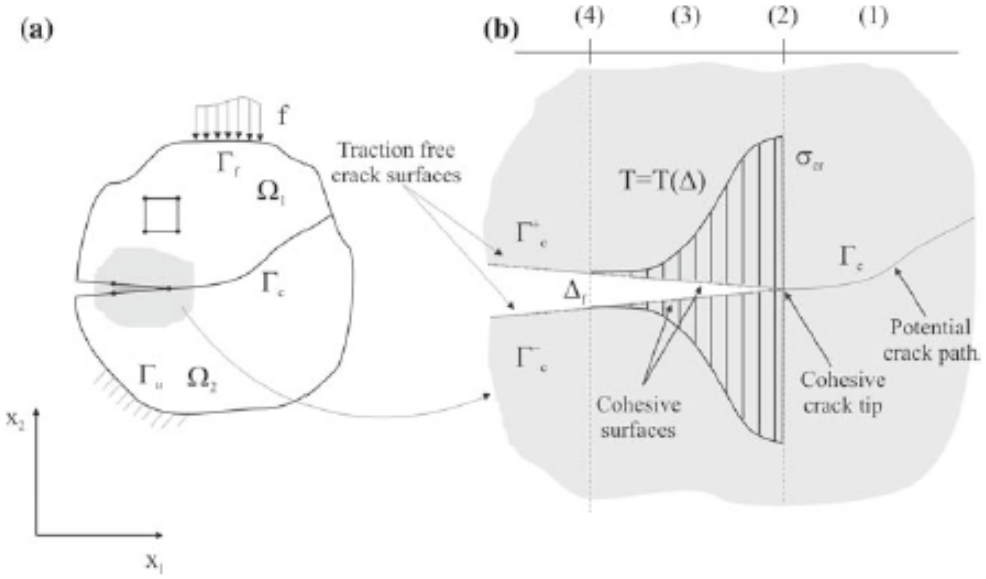

Figure 2.9: Cohesive Zone Model Concept [17]

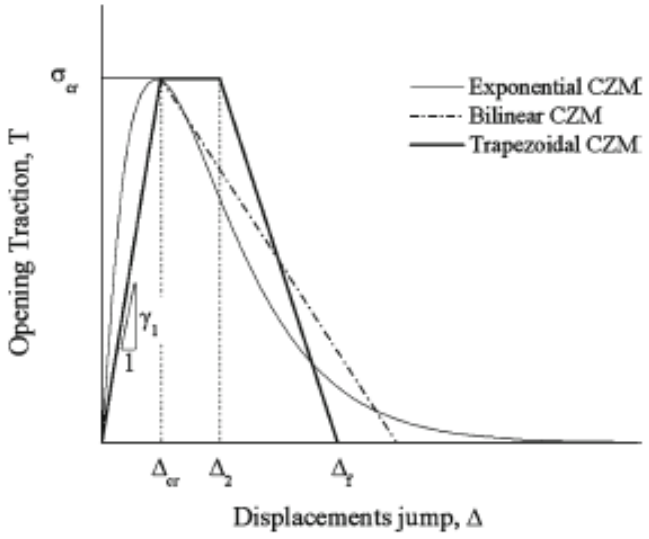

Figure 2.10: Cohesive Models [17]

There are several ways to use cohesive elements with adhesive joints. One of

the earliest methods was to model the entire adhesive layer with the cohesive zone elements. In this method the displacements represent the expected displacement across the entire adhesive layer, and the adhesive nonlinearity is modeled into the cohesive element. A second method is to use cohesive elements within the adhesive layer and along the interface. Here the adhesive layer can be modeled as linear elastic and the nonlinearity is represented with the cohesive elements. A third method is to model the joint as in method two but to model the nonlinearity in both the adhesive and substrate as well as the cohesive zone.

In order to apply this model, an appropriate displacement function must be obtained experimentally. De Moura et al. [18] describe a method for obtaining this law through measurement of the crack opening displacements and energy release rate of a DCB specimen.

$$J_I = \int_0^w \sigma(w)dw \implies \sigma(w) = \frac{dJ_I}{dw} \tag{2.1}$$

They used finite element analysis to verify the methodology, then used optical sensors to measure the COD in the DCB tests. The experimentally obtained stress functions were input back into the FE model in order estimate the load displacement curve. This was matched to the experimental data with good agreement.

On the other hand, Alfano at al. [17] used crack mouth opening displacement and load to determine the mode I traction separation model. FE analysis was used in an iterative process in order to determine the correct traction model. Exponential, bilinear and trapezoidal laws were tested. Each law was created in the FE model and run with estimates for the parameters. The resulting displacement and load data was compared to experimental results, then the parameters were adjusted and the process was repeated until satisfactory results were obtained.

Campilho et al. [19] used cohesive zone models to evaluate single lap joint strengths with different adhesives, overlap lengths and traction models. When brittle adhesive was used, increasing the adhesive length had little effect on the failure load,

while the ductile adhesive showed an increase in strength with the increased adhesive length. As for the traction laws, the trapezoidal model was the most accurate for modeling the ductile adhesive because it was capable of capturing the plastic flow which occurred after the maximum stress was reached. The different traction laws did not influence the brittle adhesive results as much except for very short joint lengths.

The cohesive zone model has also been used for Mode II loading. De Moura et al. [18] developed a cohesive zone model for mode II loading in fatigue. A triangular traction law was used where the softening of the cohesive displacements was dependent on time and number of cycles through the Paris equation. Finite element simulations were performed and compared to experimental data with good agreement. According to Chaves et al. [13] the end-notched flexure (ENF), end-loaded split (ELS) and the four-point end-notched flexure (4ENF) can be used to determine the mode II traction separation laws; however, no standard currently exists for these tests.

Blackman et al. [20] used cohesive zone models to model the delamination of fiber composites as well as adhesive joints. The researchers used a double cantilever beam with an initial delamination in order to determine the traction separation laws. Figure 2.11 shows the CFRP DCB test specimen. Several cohesive models were implemented in FEA and the resulting load displacement data were compared with experimental data. The results showed that mesh size has an effect on the load displacement results, but the results converge for sufficiently small meshes. The maximum stress in the traction law was varied, and the FE results were compared to experiment, showing how the load displacement curve changes with this parameter, see Figure 2.12.

When mixed mode conditions are present, the traction laws are often altered so that the total energy release rate, as measured experimentally, is represented by the combined area of both mode I and mode II. This is shown in Figure 2.13. In order to determine the traction law, most researchers [13] use ASTM D6671, which lays

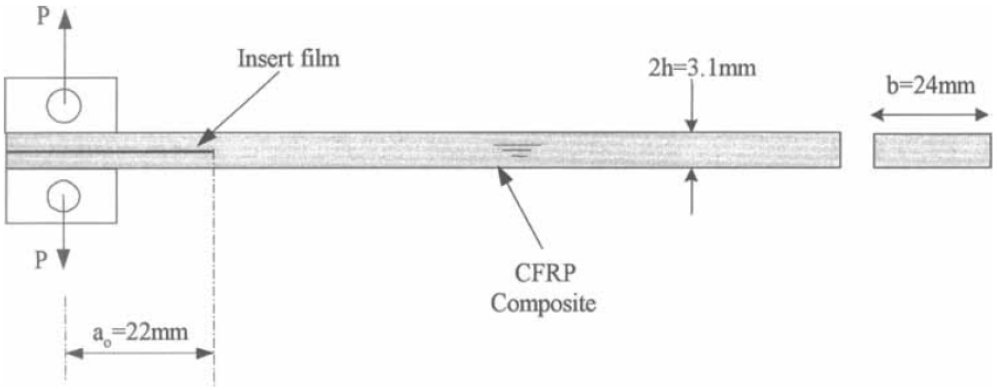

Figure 2.11: DCB test specimen for CFRP Material

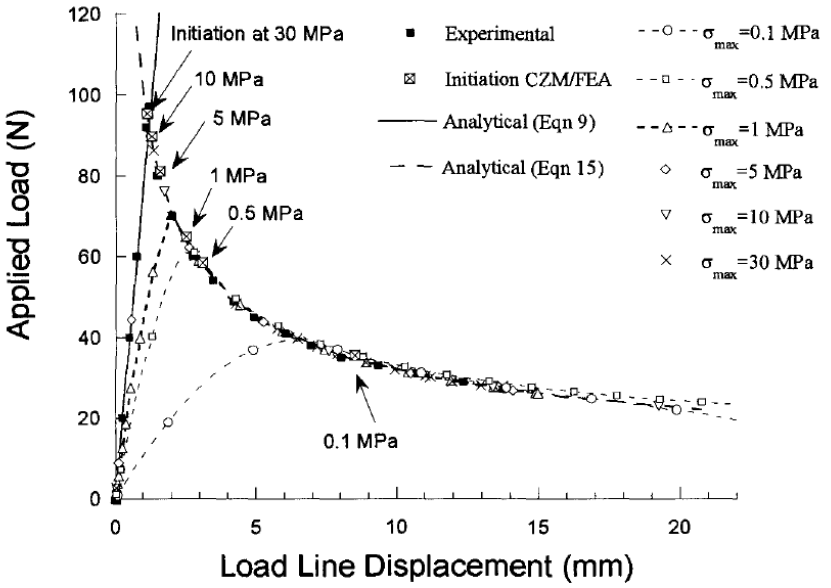

Figure 2.12: Load vs. displacement curve for CFRP DCB test [20]

out a method for obtaining the interlaminar fracture toughness of unidirectional fiber reinforced polymer matrix composites. This is a mixed mode bending test as shown in Figure 2.14. Lee et al. [21] used a mixed mode cohesive zone model where the traction separation laws were determined independently. then, the mixed mode maximum traction was determined through the following equation,

$$\left(\frac{\tau_1}{N}\right)^q + \left(\frac{\tau_2}{S}\right)^q = 1 \tag{2.2}$$

where N and S are respectively mode I and mode II failure strengths, and q de-

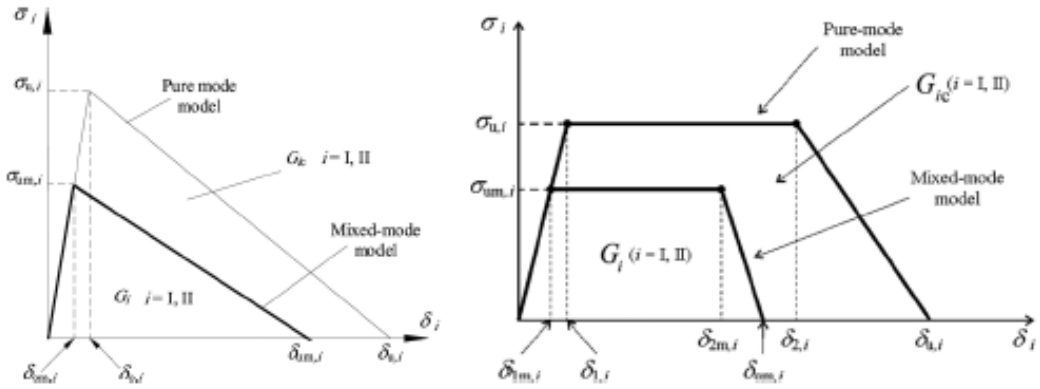

Figure 2.13: Triangular and trapezoidal softening laws for pure and mixed mode cohesive zone models [13]

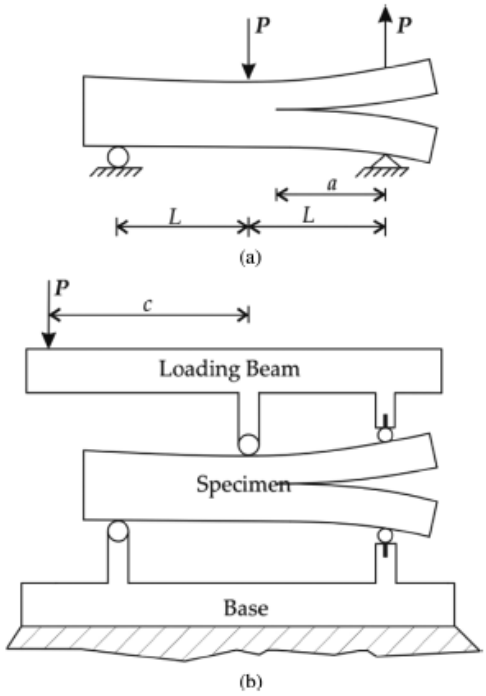

Figure 2.14: MMB specimen (a) free body diagram (b) test apparatus [13]

scribes the interaction between them. This relationship can also be visualized as in Figure 2.15.

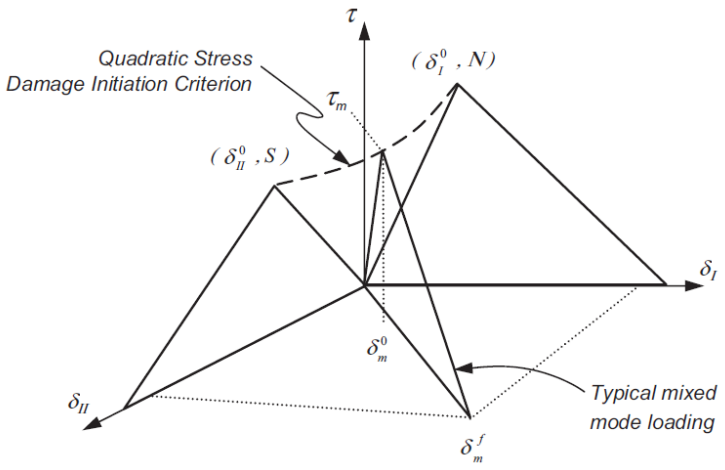

Figure 2.15: Constitutive response of a cohesive element under mixed mode loading [21]

While the cohesive zone models have been shown to be a good predictor of the behavior of real joints under static and cyclic loading, they still rely on information about the crack propagation path [22]. Also, these models cannot be used to explore the influence of adhesive thickness. The cohesive zone traction model must be determined for a particular adhesive thickness; therefore, the effects of the plastic or process zone cannot be explored. In order to overcome this limitation, some researchers have turned to continuum damage models [13]. De Moura et al. [22] applied the continuum damage model to adhesive joints in order to determine the J-R curves for various bond thicknesses. The application of this model depends on a softening relationship between stresses and strains, as opposed to a relationship between displacements and stresses, as in the cohesive zone model. This approach considers the nonlinear stress-strain relationship in the entire adhesive layer. The crack propagation path, while better than a single layer of cohesive elements, will still be mesh dependent and will require proper convergence studies before the model can be applied.

In conclusion, linear elastic fracture mechanics can be used to gather experimental data on the energy release rate for adhesive joints. This data provides a good method of comparing adhesive and adherend properties, evaluating environmental effects, or studying contamination. However, the concepts of LEFM cannot be used to predict the joint behavior. In order to make valid predictions of real adhesive joints, J-integral concepts must be used due to the high nonlinearity present in adhesive joints. Also, damage mechanics with cohesive zone and continuum damage models are typically used in order to make predictions of the behavior of joints without needing to introduce a crack. This is made possible due to the presence of singularities in the adhesive joint geometry.

2.3 Stress Singularity

A third approach which combines parts of the failure stress and fracture mechanics approaches is the generalized stress singularity approach [23] [24] [25] [26]. This approach simplifies the general equation for a stress field around a singularity, first derived by Williams,

$$\sigma = Jr^{-\lambda} \tag{2.3}$$

where J is the stress intensity, and λ is the order of the singularity. When the order of the singularity is 0.5, a sharp mode I crack, the stress intensity is equal to $K_{Ic}/\sqrt{\pi}$. As the singularity order decreases towards 0, the function can represent the stress field of an interface singularity. The value of J is determined by the applied load, as well as the geometry and elastic constants of the adherends. The value of λ is determined by the elastic constants of the adherends and the geometry near the singularity. A failure surface is generated through testing and is dependent on λ and J.

Failure occurs at critical values of J and λ. FEA can be used to determine the order of the singularity at critical locations, as well as the stress intensity for any given load. This information is used to determine the failure load. The benefit of this

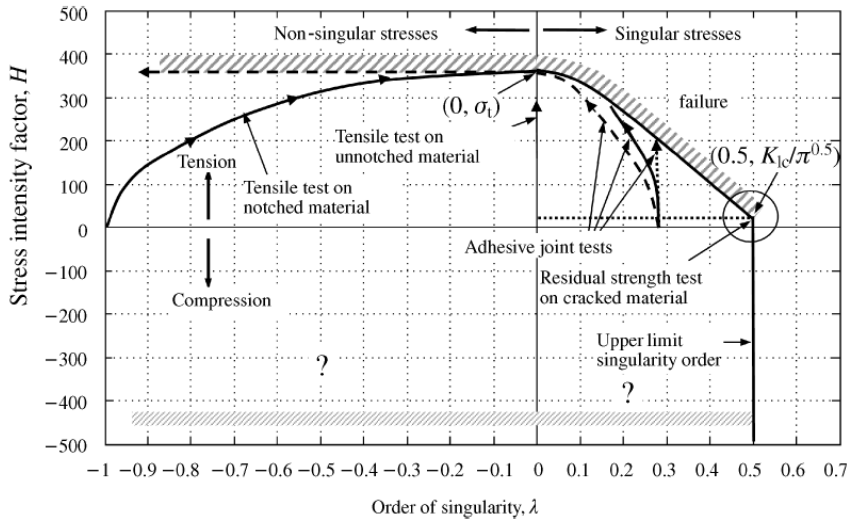

Figure 2.16: Generalized singularity approach to material failure [26]

approach is that it can be used for both problems that contain singularitites as well as uniform stress distributions. If plasticity leads to the blunting of a crack tip or other singularity, then the load line will curve as the order of the singularity changes, this is shwon in Figure 2.16. Therefore the approach is not limited to linear elestic models, and again FEA can be used to study this blunting.

Chapter 3

Nondestructive Evaluation

The section is dedicated to the introduction of some of the basics of nondestructive evaluation (NDE) and how they can be used to inspect composite joints. Ultrasonics, radiography, eddy current testing, magnetic particle inspection and dye penetrants are the five most frequently used NDE techniques, especially with metallic materials [7]. The most common technique for adhesively bonded joints is Ultrasonics; therefore, a majority of this section will discuss Ultrasonics. Thermography also has some potential for the inspection of bonded structures.

Adams [7] stated that "The objective of any form of nondestructive test is to correlate the joint strength with some physical, chemical or other parameter which can be measured without causing damage." If a correlation can be proven between an NDE parameter and a destructive measurement, then a good bond quality gauge can be determined.

There are some tests that can be performed prior to bonding, such as FTIR, water break, water drop and others, in order to evaluate the surface chemistry of the adherend. This type of testing is not discussed in this paper.

Light [3] found through an extensive literature review that no single NDE technique can solve all problems. While Segal [27] broke the inspection into four parts: detection of disbonds, evaluation of cohesive quality, detection of adhesive failure, and the prediction of combined cohesive/adhesive quality.

Method/Technique	Bond/ Debond	Bond Quality	Inclusions	Thickness
Sonics				
Coin Tap	X		X	
Mechanical Impedance	X		X	
Mechanical Resonance	X		X	X
Ultrasonics				
Pulse-echo	X		X	X
Through-Transmission	X		X	
Frequency Spectrum	X	?X*	X	X
Rayleigh Waves	X	?X*	X	X
Interface Waves	X	X	X	
Stress Wave Factor	X	?X*	X	X
Horizontally Polarized Shear Waves	X	X	X	X
Obliquely Incident Waves	X	X	X	
Acoustic Emission				
Passive	X		X	
Active	X		X	
Holography	X	?X*	X	
Radiography			X	X
Thermography	X		X	
Nuclear Magnetic Resonance	X	X		

Figure 3.1: NDE methods for the inspection of adhesive joints [7]

3.1 Visual inspection

Visual inspection is used to check the adhesive fillet and flash for voids, disbonds and cracks. A lack of adhesive can be inspected with a feeler gauge at the edge of the joint. If desired, a Verifilm can be used to ensure that the stacking, bond line thickness and curing are performed properly. This is a film adhesive with a thin release film on either side. The process is performed as usual with the exception that the entire assembly can be removed after curing.

3.2 Sonics

3.2.1 Coin tap test

The coin tap method was used for a long time to detect large disbonds. Adams and Cawley [28] extended this concept with the use of an instrumented hammer that could measure the force applied at the hammer head. The plot of the force vs. time,

shown in Figure 3.2, was used to detect disbonds. The disbonded regions result in a lower amplitude and a longer pulse duration, this leads to a lower frequency content.

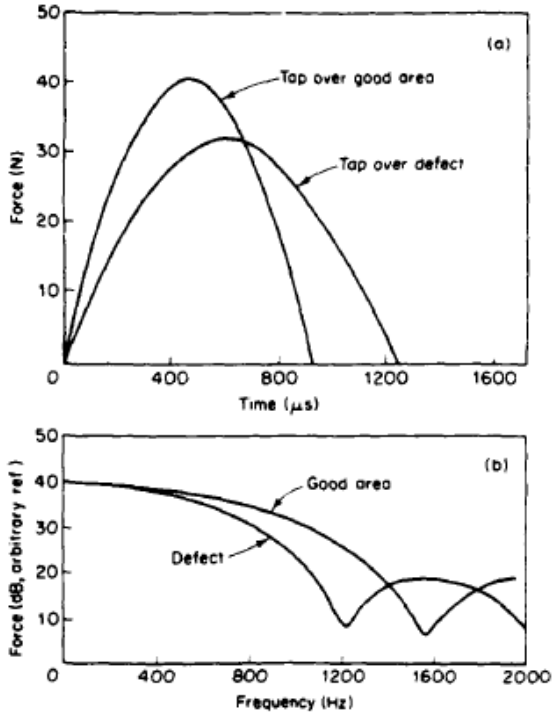

Figure 3.2: Measurements from hammer blows to a bonded assembly [28]

3.2.2 Mechanical impedance

Mechanical impedance is performed with a contact probe, and does not require couplant. The tip of the probe is held against the part and a resonating force is applied. The velocity at the probe tip is measured, providing the necessary values to calculate the mechanical impedance. Changes in the magnitude and phase are used to determine the existence and depth of flaws. This method is commonly used to detect disbonds, especially in thin structures. A variety of frequencies could be chosen depending on the application.

The method is particularly sensitive to the contact stiffness, which makes it difficult to apply to fiber reinforced composite materials

3.2.3 Mechanical resonance

The mechanical resonance method uses resonant transducers, which are coupled to the structure through a coupling agent. Changes in the structure are detected through the changes in the electrical impedance of the piezoelectric element in the transducer. This method is particularly common for honeycomb structures [7].

Many bond testers use this method, such as the Fokker bond tester.

3.3 Ultrasonics

3.3.1 Normal incidence bulk wave techniques

This technique used piezoelectric transducers to excite and transmit elastic waves into structures for inspection. There are two basic forms: pulse-echo and through transmission. The pulse-echo generally only requires a single transducer and access to only one side of the specimen. The through transmission process requires two transducers and access to the back side of the part, limiting the possible applications. A couplant is required between the transducer and the part in order to maximize the transmission of energy. Coupling is usually accomplished with either special gel or water. Occasionally other liquids, such as grease, or used for special application, such as high temperature or where rust prevention is necessary. The most reliable coupling method is the immersion of the part and transducer in a bath of water. This removes unknown variables such as pressure applied by the operator. In-service testing is almost always done with contact transducers and gel couplant. Same structures may absorb water or gel, which could lead to environmental degradation. Fiber reinforced composites are often susceptible to water absorption. Recent research has focused on non-contact methods to eliminate these problems. This could be accomplished through air-coupled transducers or electro-magnetic acoustic transducers (EMAT), although this requires a conductive material. Another new improvement is the use

of rubber wheel probes. The transducer is contained within a rubber wheel, which is filled with water. The rubber absorbs water in order to provide good coupling. A light water mist is still required, but this is an improvement to a water bath or gel application. Another option for parts which cannot be submerged in a water bath, is the use of an ultrasonic squirter, which uses jets of water as a coupler. This method allows all of the usual automated immersion techniques with a decrease in water exposure. This may be required for parts that utilize honeycomb cores, which could suffer from water intrusion.

The basic goal of the ultrasonic methods in the inspection of bonded structures was best described by Light and Kwun [3] as an "attempt to determine the quality of the bond by evaluating the interaction of the ultrasonic beam with the adhesive boundary interfaces"

Some researchers, such as Gericke [29], have found ultrasonic methods to be limited since the techniques cannot typically determine the geometry of defects that are similar in size or smaller than the beam diameter of the transducer. Williams and Zwicke [30] stated that either simple nor complicated ultrasonic approaches were able to completely assess joint quality.

Light and Kwun [3] discussed the fact that any good bond is determined from multiple variables, and the ultrasonic characteristics will also depend on several, possibly different, variables, and these can be difficult to separate.

Williams and Zwicke [30] produced a very useful table that show which ultrasonic measurements can be used to indicate the quality of certain bond variables, see Figure 3.3.

3.3.1.1 Pulse - echo

Pulse-echo is the most common ultrasonic inspection method. This technique only requires one side of the part for inspection. The method measures the reflection,

Ultrasonic Measurements	Bond Variables						
	Cure State	Chemistry	Porosity	Bondline Thickness	Etch	Surface Condition	Defects
Longitudinal Wave Velocity, V_L	S	W		S	W		
V_L vs. Wavelength			W				
Longitudinal Wave Hysteresis Atten., α_{HL}	S	S			W	W	S
Longitudinal Wave Scattering Atten., α_{SL}			S			S	S
α_{SL} vs. Wavelength			S				
Shear Wave Velocity, V_T	S	W		S	S		
V_T vs. Wavelength			W				
Shear Wave Hysteresis Atten., α_{HT}	S	S			S	W	S
Shear Wave Scattering Atten., α_{ST}			S			S	S
α_{ST} vs. Wavelength			S				

Figure 3.3: Effects of bond variables on ultrasonic measurements, S = strong dependence, W = weak dependence [30]

or echo, of the ultrasonic signal. The time of flight and amplitude of echoes provide information about the part, particularly when an echo appears where it is unexpected. Figure 3.4 shows a schematic of the pulse-echo technique, and provides an example of an adhesive disbond. The figure shows that the lack of adhesive results in multiple reflections within the top adherend. If the adherend is thin compared to the pulse width, then the reflection will appear as a long pulse, this is sometimes called the ringing effect [7]. On the other hand, the presence of the adhesive permits some of the energy to transfer to the second adherend, and the damping effect of the adhesive, particularly a thick adhesive, will reduce the amplitude of the returning wave packets. Typically echoes between the front and back wall indicate defects; however, adhesive bond lines are generally thin and the defect may appear on the interface. This eliminates this basic type of test for adhesive joints, but it is still a good method for inclusion if the acoustic impedance is very different from the host material.

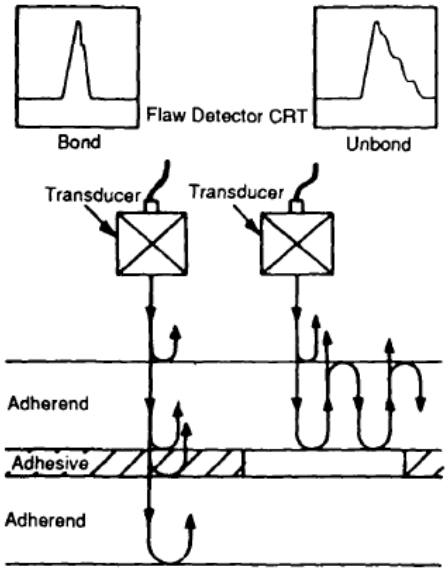

Figure 3.4: Normal incidence pulse-echo for the inspection of bonded structures [7]

A second method is to monitor the amplitude of the reflection off of the interface. An increase in the reflection will occur if the adherend is in contact with air or another gas. Additionally, a gate could be set up on the back wall of the part. If a disbond is present, then the back wall amplitude will be reduced. If the disbond is large enough to completely reflect the wave pulse, then the back wall amplitude will disappear. Generally, disbonds, delaminations and the separation of skin and core are easily detected with this technique. If the adherends are thin, then a reflection plate, or through transmission must be used because the reflections from the front wall and the interface will overlap. The absence of a fillet in honeycomb structures can also be detected from changes in the interface reflection amplitude. Finally, the amplitude and phase of the interface reflection can be used to determine the modulus and loss factor of the adhesive, but this requires several comparison samples.

Both porosity and under curing will increase the attenuation in the adhesive. Careful calibration is required to detect changes in attenuation because a reference signal is required.

Tattersall [31] investigated reflections from a weak adhesive interface and found

that the complex reflected signal continuously changed in amplitude and phase as the signal changed from a perfect bond to a vacuum. Greater differences in the acoustic impedance between the adherend and adhesive lead to greater changes.

Rose and Meyer [32] found that a good indication of bond quality was the ratio of front wall reflection divided by back wall reflection. An increasing ratio should indicate an increase in bond quality. This measurement should correlate with energy transmission through the adhesive layer, where high energy transmission will occur with good bonding.

Meyer and Rose [33] inspected 50 aluminum lap joints with a 20 MHz transducer and found that changes in surface preparation could be detected through changes in the interface reflection, with an inverse dependence. This was only observed with the 20 MHz transducer.

Chernobelskaya, Kovnovich, and Harnik [34] stated that the adhesive bond quality could be measured by comparing the effective reflection coefficient to the true reflection coefficient. Where the true reflection coefficient was derived from transit times, thickness and known densities. No strength or fracture tests were performed to verify this theory.

3.3.1.2 Through transmission

The through transmission technique requires two transducers, one to generate the wave and another to receive. This method uses similar techniques to the pulse echo, and attempts to extract information from the boundaries. In general, good bonds exhibit high transmission through the bond and a decrease in this transmission is associated with weak bonding.

3.3.2 Normal incidence spectroscopy

Normal incidence spectroscopy is perform using either pulse-echo or through transmission techniques. The reflected or transmitted signals undergoes a Fourier transform so that the frequency dependent properties can be analyzed.

Adler and Whaley [35] investigated the frequency dependence of defect reflections and found that a constructed interference occurs when waves are reflected from circular defects. The frequency is given by,

$$f_n = \frac{nv}{2d \sin a} \tag{3.1}$$

where n is an integer, d is the diameter of the circular object, v is the velocity of sound in the media and a is the angle of the transducer.

Alers, Flynn and Buckley [36] demonstrated that the pressure wave velocity and attenuation can be correlated with the strength of the adhesive joint. A Fourier transform was performed on the adhesive interface reflection and this result was divided by the Fourier transform of the front wall reflection. The minima in the signal can be related to the adhesive thickness and velocity, and the height of the minima is related to the attenuation. Figure 3.5 shows the non-linear correlation between the adhesive joint strength and attenuation, and Figure 3.6 shows the linear relationship between adhesive joint strength and velocity.

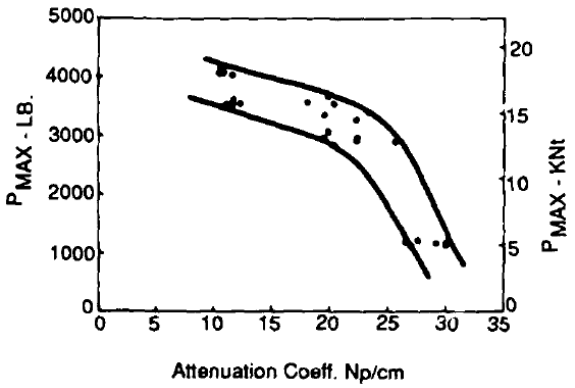

Figure 3.5: Correlation between attenuation and adhesive joint strength [36]

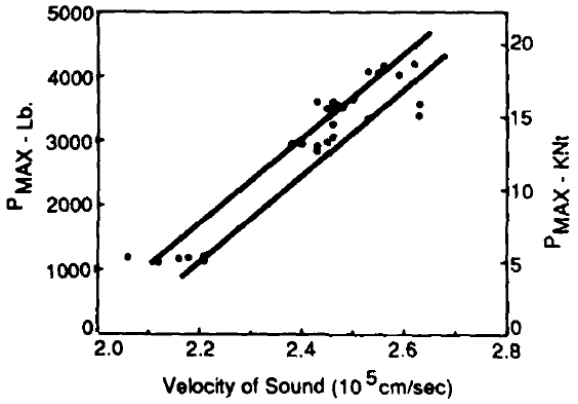

Figure 3.6: Correlation between pressure wave velocity and adhesive joint strength [36]

Chang et al. [37] found that the shape and Q-value of the maxima and minima in the spectrum correlated with the bond quality for aluminum bonded joints, with a 15 MHz transducer. Also, Chang et al. [38] used the spectral method to detect delaminations in composites through the changes in the frequency spectrum. Later, Chang et al. [39] showed a good correlation between the reciprocal of the half-power bandwidth and shear strength, see Figure 3.7. Additionally, Adams [7] showed that the normal incidence spectroscopy method could be used to detect poor matrix curing.

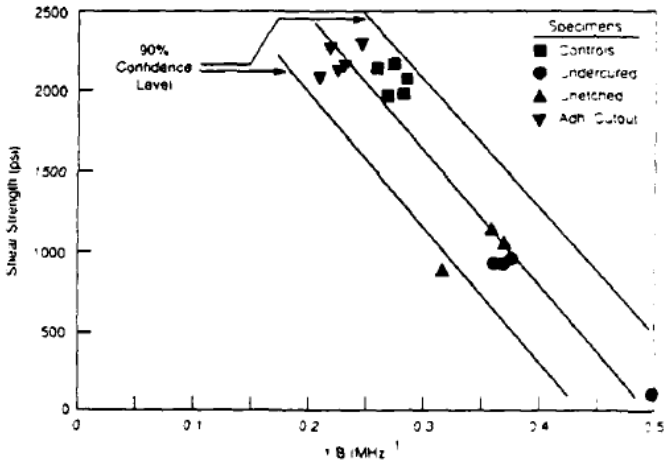

Figure 3.7: Correlation between shear strength and the reciprocal of half-power bandwidth [39]

3.3.3 Lamb and interface waves

Lamb and interface waves have been shown to be useful at determining the cohesive and adhesive properties, as well as the strength of the bond interface. A detailed discussion on this topic is provided in a subsequent chapter.

3.3.4 Oblique incidence

Oblique incidence is similar to the normal incidence methods with the addition of an oblique angle of impingement from the incident wave. This angle leads to the generation of both shear and pressure wave within the laminate, depending on the angle. Less work has been performed with this method due to the more difficult application. There is also an overlap between oblique incidence and guided wave techniques. If the wave pulse is long enough for reflections to interact, then a guided wave will be generated. These methods become particularly difficult to differentiate in composite laminates, where the thin lamina thicknesses lead to resonances with all but very short pulse widths.

3.4 Thermography

Thermography can be used to quickly find large disbonds, delaminations and inclusions with varying conductivity within adhesive joints, but this method is not as sensitive as ultrasonic techniques, which are generally preferred.

Part II

Ultrasonic Nondestructive Evaluation

Chapter 4

Fundamentals of Elastic Waves

This chapter lays the foundation for further study into the use of elastic waves in the inspection of adhesively bonded composite structures. The chapter has been broken into two sections: Isotropic and Anisotropic media. This split is due to the different approaches taken in the solution for isotropic and anisotropic material; the potential method and the partial wave method. A homogeneous media is assumed for the entire dissertation when dealing with elastic wave propagation. In the case of fiber-reinforced polymers, each ply is considered to be a homogeneous layer with elastic properties that are determined from micro-mechanics. This is a sufficient assumptions since the wavelengths of interest are much larger than the fiber diameter.

Each section has been split into bulk and guided waves. The development of equations for the bulk wave case does not impose boundary conditions, unlike the guided wave. This chapter only considers the harmonic solution to the elastic wave problem. As a result, the guided wave solution should be used when the pulse length is larger than the wave guide. If the pulse length is shorter than any dimension, the bulk wave approach can be used with satisfactory results. The term wave guide has been used deliberately to note that guided waves may exist throughout the thickness of a plate or may be confined to an adhesive layer or similar guided structure. Therefore, it is useful to describe the existence of three possible scenarios; where, p is the pulse length, t is the plate thickness, a is the thickness of an internal or external feature,

such as an adhesive bond, and n is a coefficient.

$$\begin{aligned} p &\geq nt \quad \text{plate guided wave} \\ an \leq p &\geq nt \quad \text{embedded guided wave} \\ p &\leq an \quad \text{bulk wave} \end{aligned} \tag{4.1}$$

It is expected that n will be equal to 2; although, large oblique angle will require a larger value. In general, n must be large enough that the head of the pulse bites the tail, so to speak. In the case of laminated composites, it is more difficult to predict the appropriate value of n. A final note on this subject, the generation of creeping wave, and the guided waves which consist of them, is not limited by these resonance conditions.

4.1 Isotropic media

First, consider the case of bulk wave; no boundary conditions.

4.1.1 Bulk waves

For an isotropic media, the procedure begins with the Navier-Lamé equation,

$$(\lambda + \mu)u_{j,ji} + \mu u_{i,jj} = \rho \ddot{u}_i \tag{4.2}$$

where λ is the first Laméparameter, μ is the second Lamé parameter or shear modulus, and ρ is the mass density. We will assume that the wave travels with a plane wave front such that the particle motion is,

$$\begin{aligned} \mathbf{u} &= \mathbf{A}f(\mathbf{n}\cdot\mathbf{r} - ct) \\ \frac{\partial \mathbf{u}}{\partial x_i} &= \mathbf{A}n_i f(\mathbf{n}\cdot\mathbf{r} - ct) \\ \frac{\partial \mathbf{u}}{\partial t} &= -\mathbf{A}cf(\mathbf{n}\cdot\mathbf{r} - ct) \end{aligned} \tag{4.3}$$

where $\mathbf{A}$ is the wave amplitude vector, $\mathbf{n}$ is a unit vector normal to the plane wave front and directed towards the direction of propagation for an isotropic material, $\mathbf{r}$

is the position vector describing the location of the plane wave front in Euclidean space, and c is the wave speed. Combining the two previous equations results in a system of homogeneous linear equations whose solution is nontrivial only when the determinant of the resulting matrix is singular. There are three solutions to this eigenvalue problem which result in two unique values for the wave speed and three unique wave amplitude vectors. These resulting solutions are known as the pressure wave, shear-horizontal wave and shear-vertical wave. The pressure wave travels at the pressure or longitudinal wave speed, and both shear waves travel at the shear or transverse wave speed,

$$c_P = c_L = \sqrt{\frac{\lambda + 2\mu}{\rho}} = \sqrt{\frac{1-\nu}{(1+\nu)(1-2\nu)}\frac{E}{\rho}} \tag{4.4}$$

$$c_S = c_T = \sqrt{\frac{\mu}{\rho}} = \sqrt{\frac{G}{\rho}} = \sqrt{\frac{1}{2(1+\nu)}\frac{E}{\rho}} \tag{4.5}$$

where G is the shear modulus, E is the elastic modulus and ν is the Poisson ratio. The pressure wave has particle motion which is parallel with the normal vector for the plane wave front and the shear wave has particle motion perpendicular to this vector. There are two shear waves traveling at the same speed, but with different polarizations which are orthogonal to each other. The total wave solution, as shown in Eq. (4.3), can also be expressed as the sum of the particle motions of all three wave solutions,

$$\mathbf{u} = \mathbf{u}_P + \mathbf{u}_{SH} + \mathbf{u}_{SV} \tag{4.6}$$

where the individual waves have the following solution when propagating along the x_1-axis.

$$\mathbf{u}_P = A_1 f(x_1 - c_P t)\mathbf{e}_1 \tag{4.7a}$$

$$\mathbf{u}_{SH} = A_2 f(x_1 - c_S t)\mathbf{e}_2 \tag{4.7b}$$

$$\mathbf{u}_{SV} = A_3 f(x_1 - c_S t)\mathbf{e}_3 \tag{4.7c}$$

If the waves propagate harmonically, then the particle displacement has the following form,

$$\mathbf{u}(\mathbf{r},t) = \mathbf{A}e^{i(\mathbf{k}\cdot\mathbf{r}-\omega t)} = \mathbf{A}e^{i(\xi x_1+\eta x_2+\zeta x_3-\omega t)} \tag{4.8}$$

where ξ, η and ζ are the wave numbers in the x_1, x_2 and x_3 directions, and ω is the circular frequency. If the wave propagates along the x_1 axis, then the displacements can be expressed as follows. Where the total wave solution is once again the summation of the independent wave solutions,

$$\begin{aligned} \mathbf{u}_P &= A_1 e^{i(\xi_P x_1-\omega t)}\mathbf{e}_1 \\ \mathbf{u}_{SH} &= A_2 e^{i(\xi_S x_1-\omega t)}\mathbf{e}_2 \\ \mathbf{u}_{SV} &= A_3 e^{i(\xi_S x_1-\omega t)}\mathbf{e}_3 \end{aligned} \tag{4.9}$$

where the wave number ξ_P and ξ_S are given by the following.

$$\xi_P = \frac{\omega}{c_P}\ ; \quad \xi_S = \frac{\omega}{c_S} \tag{4.10}$$

It is often convenient to express the displacements in terms of wave potentials.

$$\mathbf{u} = grad\Phi + curl\vec{H} = \vec{\nabla}\Phi + \vec{\nabla}\times\vec{H} \tag{4.11}$$

Combining Eq. (4.2) and Eq. (4.11) results in the wave equations for the scalar and vector potentials.

$$\begin{aligned} c_P^2\nabla^2\Phi &= \ddot{\Phi} \\ c_S^2\nabla^2\vec{H} &= \ddot{\vec{H}} \end{aligned} \tag{4.12}$$

It is useful to have the wave propagate along the x_1 axis as a straight crested wave with the wave crest parallel to the x_3 axis, then we can consider an x_3-invariant condition, where all derivatives with respect to x_3 are zero. Now, the displacements from Eq. (4.11) are simplified to the following.

$$\begin{aligned} u_1 &= \frac{\partial\Phi}{\partial x_1} + \frac{\partial H_1}{\partial x_2} \\ u_2 &= \frac{\partial\Phi}{\partial x_2} + \frac{\partial H_3}{\partial x_1} \\ u_3 &= \frac{\partial H_2}{\partial x_1} + \frac{\partial H_1}{\partial x_2} \end{aligned} \tag{4.13}$$

This equation indicates that it is possible to divide the solution into two parts; the solution of $u_3(H_2$ and $H_1)$ and the solution of u_1 and $u_2(\Phi$ and $H_3)$. The first solution is for displacement in the x_3 direction which corresponds to the shear horizontal wave, SH. The second solution is a combination of a pressure wave and a shear vertical wave, P + SV.

The stress-displacement relationships for linear elasticity with the small strain and x_3-invariant assumptions are shown below.

$$\begin{aligned}
\sigma_{11} &= (\lambda + 2\mu)\frac{\partial u_1}{\partial x_1} + \lambda\frac{\partial u_2}{\partial x_2} \\
\sigma_{22} &= \lambda\frac{\partial u_1}{\partial x_1} + (\lambda + 2\mu)\frac{\partial u_2}{\partial x_2} \\
\sigma_{33} &= \lambda\frac{\partial u_1}{\partial x_1} + \lambda\frac{\partial u_2}{\partial x_2} \\
\sigma_{12} &= \mu(\frac{\partial u_1}{\partial x_2} + \frac{\partial u_2}{\partial x_1}) \\
\sigma_{23} &= \mu\frac{\partial u_3}{\partial x_2} \\
\sigma_{31} &= \mu\frac{\partial u_3}{\partial x_1}
\end{aligned} \tag{4.14}$$

For SH waves, the stresses are expressed in terms of wave potentials as follows.

$$\begin{aligned}
\sigma_{23} &= \mu(-\frac{\partial^2 H_1}{\partial x_2^2} + \frac{\partial^2 H_2}{\partial x_1 \partial x_2}) \\
\sigma_{31} &= \mu(-\frac{\partial^2 H_1}{\partial x_1 \partial x_2} + \frac{\partial^2 H_2}{\partial x_1^2}) \\
\sigma_{rest} &= 0
\end{aligned} \tag{4.15}$$

For P + SV waves, the stresses are expressed in terms of wave potentials as follows.

$$\begin{aligned}
\sigma_{11} &= (\lambda + 2\mu)\frac{\partial^2 \Phi}{\partial x_1^2} + \lambda\frac{\partial^2 \Phi}{\partial x_2^2} + 2\mu\frac{\partial^2 H_3}{\partial x_1 \partial x_2} \\
\sigma_{22} &= \lambda\frac{\partial^2 \Phi}{\partial x_1^2} + (\lambda + 2\mu)\frac{\partial^2 \Phi}{\partial x_2^2} - 2\mu\frac{\partial^2 H_3}{\partial x_1 \partial x_2} \\
\sigma_{12} &= \mu(2\frac{\partial^2 \Phi}{\partial x_1 \partial x_2} - \frac{\partial^2 H_3}{\partial x_1^2} + \frac{\partial^2 H_3}{\partial x_2^2}) \\
\sigma_{rest} &= 0
\end{aligned} \tag{4.16}$$

4.1.2 Guided waves

The investigation presented in this work is not concerned with SH waves within isotropic media; therefore the solution to this type of guided wave is omitted. The following subsection solved the propagation of waves within a plate structure with in-plane displacements, often referred to as Lamb waves.

4.1.2.1 Lamb wave

We must solve the P + SV case along with boundary conditions in order to determine the Lamb wave characteristics. Assuming a harmonic solution, the wave potentials of interest can be expressed as follows, using the same form as shown in Eq. (4.7),

$$\Phi = f(y)e^{i(\xi x-\omega t)} \; ; \quad H = ih(y)e^{i(\xi x-\omega t)} \tag{4.17}$$

where H is used instead of H_x for the wave potential, and ξ is the wave number, which is the same for both potentials since the Lamb wave is the combination of the two. The corresponding derivatives are as follows.

$$\begin{aligned} \ddot{\Phi} = -\omega^2\Phi \; ; \quad \Phi' = i\xi\Phi \; ; \quad \Phi'' = -\xi^2\Phi \\ \ddot{H} = -\omega^2 H \; ; \quad H' = i\xi H \; ; \quad H'' = -\xi^2 H \end{aligned} \tag{4.18}$$

Since we are assuming that z is invariant, Eq. (4.12) can be simplified as follows.

$$\begin{aligned} \frac{\partial^2\Phi}{\partial x^2} + \frac{\partial^2\Phi}{\partial y^2} = \frac{1}{c_P^2}\ddot{\Phi} \\ \frac{\partial^2 H}{\partial x^2} + \frac{\partial^2 H}{\partial y^2} = \frac{1}{c_S^2}\ddot{H} \end{aligned} \tag{4.19}$$

Combine Eq. (4.17), 4.18 and 4.19.

$$\begin{aligned} f''(y) + (\frac{\omega^2}{c_P^2} - \xi^2)f(y) = 0 \\ h''(y) + (\frac{\omega^2}{c_S^2} - \xi^2)h(y) = 0 \end{aligned} \tag{4.20}$$

Define the following.

$$\eta_P^2 = \frac{\omega^2}{c_P^2} - \xi^2 \; ; \quad \eta_S^2 = \frac{\omega^2}{c_S^2} - \xi^2 \tag{4.21}$$

Combine equations 4.20 and 4.21.

$$\begin{aligned} f'' + \eta_P^2 f = 0 \\ h'' + \eta_S^2 h = 0 \end{aligned} \tag{4.22}$$

The solution of Eq. (4.22) can have the following form.

$$\begin{aligned} f(y) = A_1 sin\eta_P y + A_2 cos\eta_P y \\ h(y) = B_1 sin\eta_S y + B_2 cos\eta_S y \end{aligned} \tag{4.23}$$

The coefficients are determined form the boundary conditions, which are free traction on the upper and lower surfaces of the single layer. Combining Eq. (4.16) and Eq. (4.18), along with simplification, yields.

$$\begin{aligned} \sigma_{xx} &= (1(\xi^2 + \eta_S^2 - 2\eta_P^2)f - 2\xi h')\mu e^{i(\xi x - \omega t)} \\ \sigma_{yy} &= ((\xi^2 - \eta_S^2)f + 2\xi h')\mu e^{i(\xi x - \omega t)} \\ \sigma_{xy} &= (2\xi f' + (\xi^2 - \eta_S^2)h)i\mu e^{i(\xi x - \omega t)} \end{aligned} \tag{4.24}$$

The final solution consists of a system of four equations, and the final solution is found by splitting the problem into symmetric and antisymmetric systems and solving for the determinant equal to zero. This results in the Rayleigh-Lamb equation for symmetric modes.

$$\frac{tan\eta_P d}{tan\eta_S d} = -\frac{(\xi^2 - \eta_S^2)^2}{4\xi^2 \eta_P \eta_S} \tag{4.25}$$

Along with the Rayleigh-Lamb equation for antisymmetric modes.

$$\frac{tan\eta_P d}{tan\eta_S d} = -\frac{4\xi^2 \eta_P \eta_S}{(\xi^2 - \eta_S^2)^2} \tag{4.26}$$

The equations can be modified in order to express the solution in a non-dimensional form. The wavenumber can be expressed as the non-dimensional wavenumber divided by half the thickness, and the circular frequency can be expresses as the product of the non-dimensional circular frequency and the shear wave velocity divided by the half thickness.

$$\xi = \frac{\bar{\xi}}{d}\ ; \quad \omega = \frac{\Omega c_S}{d} \tag{4.27}$$

Additionally, the out of plane wavenumbers can be made non-dimensional.

$$\eta_P = \frac{\bar{\eta}_P}{d} \; ; \quad \bar{\eta}_P^2 = \frac{\Omega^2}{k^2} - \bar{\xi}^2 \; ; \quad k = \frac{c_P}{c_S} \tag{4.28}$$

$$\eta_S = \frac{\bar{\eta}_S}{d} \; ; \quad \bar{\eta}_S^2 = \Omega^2 - \bar{\xi}^2 \tag{4.29}$$

Combining the previous three equations with Eq. (4.25) results in the non-dimensional symmetric Rayleigh-Lamb equation.

$$(\bar{\xi}^2 - \bar{\eta}_S^2)^2 tan\bar{\eta}_S + 4\bar{\xi}^2\bar{\eta}_P\bar{\eta}_S tan\bar{\eta}_P = 0 \tag{4.30}$$

Utilizing the same process provides the non-dimensional antisymmetric Rayleigh-Lamb equation.

$$(\bar{\xi}^2 - \bar{\eta}_S^2)^2 tan\bar{\eta}_P + 4\bar{\xi}^2\bar{\eta}_P\bar{\eta}_S tan\bar{\eta}_S = 0 \tag{4.31}$$

4.1.2.2 Isotropic laminates

When multiple isotropic layers or lamina exist within a plate, the solution follows the same procedure as for the Lamb wave with the additional boundary conditions. Now, the stress and displacement continuity through each interface must be considered, in addition to the stress free conditions at the outer interfaces. The Lamb wave solution consisted of four coefficients which describe the stress and displacement through the thickness. The general solution will contain $4N$ coefficients and $4N$ equations for a laminate with N layers. The system of equation is solved by finding the combination of ω and ξ that result in a singular matrix. Alternatively, transfer matrix and stiffness matrix approached can be utilized.

4.2 Anisotropic media

4.2.1 Bulk waves

We begin the solution with an unbound elastic medium in a three dimensional Euclidean space, where the equation of motion for a generally anisotropic material is

shown below. Where the small strain approximation has been used in the development of the strain-displacement equations.

$$C_{ijkl}\frac{\partial^2 u_k}{\partial x_l \partial x_j} = \rho \frac{\partial^2 u_i}{\partial t^2} \tag{4.32}$$

For a generally anisotropic material, the bulk wave velocities and polarization vectors are solved by combining equations 4.32 and 4.3 to generate an eigenvalue problem. The general form is shown below, where the eigenvalue is ρc^2 and the eigenvector is $\mathbf{A}$.

$$\begin{bmatrix} G_{11}-\rho c^2 & G_{12} & G_{13} \\ G_{12} & G_{22}-\rho c^2 & G_{23} \\ G_{13} & G_{23} & G_{33}-\rho c^2 \end{bmatrix} \begin{Bmatrix} A_1 \\ A_2 \\ A_3 \end{Bmatrix} = \begin{Bmatrix} 0 \\ 0 \\ 0 \end{Bmatrix} \tag{4.33}$$

We can study the results for a few material symmetries.

4.2.1.1 Transversely isotropic symmetry

The stiffness tensor in matrix form for a transversely isotropic elastic material with symmetry along the x_1-axis is shown below.

$$\mathbf{C} = \begin{bmatrix} C_{11} & C_{12} & C_{12} & 0 & 0 & 0 \\ & C_{22} & C_{23} & 0 & 0 & 0 \\ & & C_{22} & 0 & 0 & 0 \\ & & & \frac{C_{22}-C_{23}}{3} & 0 & 0 \\ & Sym & & & C_{55} & 0 \\ & & & & & C_{55} \end{bmatrix} \tag{4.34}$$

Inserting the stiffness matrix of Eq. (4.34) into the equation of motion for a generally anisotropic material from Eq. (4.32) along with the displacement definition for a plane wave front of Eq. (4.3) results in a solution of the form seen in Eq. (4.33). Where the

G matrix components are defined as follows.

$$\begin{aligned}
G_{11} &= C_{11}n_1^2 + C_{55}(n_2^2 + n_3^2) \\
G_{12} &= (C_{12} + C_{55})n_1 n_2 \\
G_{13} &= (C_{12} + C_{55})n_1 n_3 \\
G_{22} &= C_{55}n_1^2 + C_{22}(n_2^2 + \frac{n_3^2}{2}) - C_{23}\frac{n_3^2}{2} \\
G_{23} &= \frac{C_{23} + C_{22}}{2}n_2 n_3 \\
G_{33} &= C_{55}n_1^2 + (\frac{C_{22} - C_{23}}{2})n_2^2 + C_{22}n_3^2
\end{aligned} \tag{4.35}$$

Any given normal vector will produce three wave speeds with three polarization vectors. In general, these waves can be coupled, as opposed to the pure pressure and shear waves produced in an isotropic solid. However, the waves will be uncoupled when the wavenumber vector is along a plane of symmetry. For a transversely isotropic solid with the symmetry axis along the x_1-axis, the first plane of symmetry exists when the wavenumber vector is directed along the x_1-axis, and the second symmetry plane exists for all wavenumber vectors which have a zero x_1 component.

We will again consider the invariant condition; however, we will use x_2 as the invariant axis, as is traditionally done for anisotropic materials. This reduces the complexity of the eigenvalue problem.

$$\begin{bmatrix} C_{11}n_1^2 + C_{55}n_3^2 - \rho c^2 & 0 & (C_{12} + C_{55})n_1 n_3 \\ 0 & C_{55}n_1^2 + (C_{22} - C_{23})\frac{n_3^2}{2} - \rho c^2 & 0 \\ (C_{12} + C_{55})n_1 n_3 & 0 & C_{55}n_1^2 + C_{22}n_3^2 - \rho c^2 \end{bmatrix} \begin{Bmatrix} A_1 \\ A_2 \\ A_3 \end{Bmatrix} = \begin{Bmatrix} 0 \\ 0 \\ 0 \end{Bmatrix} \tag{4.36}$$

This results in a pair of coupled waves and one uncoupled. The uncoupled wave is a pure shear wave with a polarization vector in the x_2 direction.

$$c_S^2 = \frac{C_{55}n_1^2 + [\frac{C_{22} - C_{23}}{2}]n_3^2}{\rho} \; ; \quad \vec{A} = \{0 \; 1 \; 1\}^T \tag{4.37}$$

The remaining two bulk waves are a pair of coupled quasi-longitudinal and quasi-transverse waves. The equations for these waves are omitted for brevity; however, we

will consider the special case of a bulk wave propagating in the x_3 direction, where $\mathbf{n} = \{0\ 0\ 1\}^T$.

$$\begin{bmatrix} C_{55} - \rho c^2 & 0 & 0 \\ 0 & \frac{1}{2}(C_{22} - C_{23}) - \rho c^2 & 0 \\ 0 & 0 & C_{22} - \rho c^2 \end{bmatrix} \begin{Bmatrix} A_1 \\ A_2 \\ A_3 \end{Bmatrix} = \begin{Bmatrix} 0 \\ 0 \\ 0 \end{Bmatrix} \tag{4.38}$$

For this special case, all three waves decouple into a single pure pressure wave and two pure shear waves.

$$c_P^2 = \frac{C_{22}}{\rho}\ ; \quad c_{S1}^2 = \frac{C_{55}}{\rho}\ ; \quad c_{S2}^2 = \frac{C_{22} - C_{23}}{2\rho} \tag{4.39}$$

With polarization vectors.

$$\vec{A}_P = \begin{Bmatrix} 0 \\ 0 \\ 1 \end{Bmatrix}\ ; \quad \vec{A}_{S1} = \begin{Bmatrix} 0 \\ 1 \\ 0 \end{Bmatrix}\ ; \quad \vec{A}_{S2} = \begin{Bmatrix} 1 \\ 0 \\ 0 \end{Bmatrix} \tag{4.40}$$

Once again the total wave solution is the summation of the three independent waves, which results in an equation for the particle displacement. The strain is calculated from the displacement using the small strain approximation, and the stress is calculated from the general stress-strain equations.

4.2.1.2 Orthotropic symmetry

The stiffness tensor in matrix form for an orthotropic elastic material with symmetry on the x_1x_2, x_2x_3 and x_1x_3 coordinate planes is shown below,

$$\mathbf{C} = \begin{bmatrix} C_{11} & C_{12} & C_{13} & 0 & 0 & 0 \\ & C_{22} & C_{23} & 0 & 0 & 0 \\ & & C_{33} & 0 & 0 & 0 \\ & & & C_{44} & 0 & 0 \\ & Sym & & & C_{55} & 0 \\ & & & & & C_{66} \end{bmatrix} \tag{4.41}$$

where the **G** matrix components are shown below.

$$\begin{aligned} G_{11} &= C_{11}n_1^2 + C_{66}n_2^2 + C_{55}n_3^2 \\ G_{22} &= C_{66}n_1^2 + C_{22}n_2^2 + C_{44}n_3^2 \\ G_{33} &= C_{55}n_1^2 + C_{44}n_2^2 + c_{33}N_3^2 \\ G_{12} &= (C_{12} + C_{66})n_1n_2 \\ G_{13} &= (C_{13} + C_{55})n_1n_3 \\ G_{23} &= (C_{23} + C_{44})n_2n_3 \end{aligned} \tag{4.42}$$

Again, we apply the invariant condition to the x_2-axis.

$$\begin{bmatrix} C_{11}n_1^2 + C_{55}n_3^2 - \rho c^2 & 0 & (C_{13} + C_{55})n_1n_3 \\ 0 & C_{66}n_1^2 + C_{44}n_3^2 - \rho c^2 & 0 \\ (C_{13} + C_{55})n_1n_3 & 0 & C_{55}n_1^2 + C_{33}n_3^2 = \rho c^2 \end{bmatrix} \begin{Bmatrix} A_1 \\ A_2 \\ A_3 \end{Bmatrix} = \begin{Bmatrix} 0 \\ 0 \\ 0 \end{Bmatrix} \tag{4.43}$$

Since the wave is propagating along a plane of symmetry, there is a pair of coupled waves with polarization vectors in the x_1x_3 plane, and an uncoupled shear wave with a polarization vector in the x_2 direction.

$$c_S^2 = \frac{C_{66}n_1^2 + C_{44}n_3^2}{\rho} \; ; \quad \vec{A} = \{0 \; 1 \; 0\}^T \tag{4.44}$$

The equations for the coupled quasi-transverse and quasi-longitudinal waves are omitted for brevity. Once again, we consider the special case of propagation along the x_3 direction.

$$\begin{bmatrix} C_{55} - \rho c^2 & 0 & 0 \\ 0 & C_{44} - \rho c^2 & 0 \\ 0 & 0 & C_{33} - \rho c^2 \end{bmatrix} \begin{Bmatrix} A_1 \\ A_2 \\ A_3 \end{Bmatrix} = \begin{Bmatrix} 0 \\ 0 \\ 0 \end{Bmatrix} \tag{4.45}$$

Once again all of the waves decouple into true pressure and shear waves,

$$c_P^2 = \frac{C_{33}}{\rho} \; ; \quad c_{S1}^2 = \frac{C_{44}}{\rho} \; ; \quad c_{S2}^2 = \frac{C_{55}}{\rho} \tag{4.46}$$

with polarization vectors.

$$\vec{A}_P = \begin{Bmatrix} 0 \\ 0 \\ 1 \end{Bmatrix} \; ; \quad \vec{A}_{S1} = \begin{Bmatrix} 1 \\ 0 \\ 0 \end{Bmatrix} \; ; \quad \vec{A}_{S2} = \begin{Bmatrix} 0 \\ 1 \\ 0 \end{Bmatrix} \tag{4.47}$$

4.2.1.3 Monoclinic symmetry

The stiffness tensor in matrix form for an elastic material with monoclinic symmetry coincident with the x_1x_2 plane is shown below,

$$\mathbf{C} = \begin{bmatrix} C_{11} & C_{12} & C_{13} & 0 & 0 & C_{16} \\ & C_{22} & C_{23} & 0 & 0 & C_{26} \\ & & C_{33} & 0 & 0 & C_{36} \\ & & & C_{44} & C_{45} & 0 \\ & Sym & & & C_{55} & 0 \\ & & & & & C_{66} \end{bmatrix} \tag{4.48}$$

The $\mathbf{G}$ matrix components for monoclinic symmetry are shown below.

$$\begin{aligned} G_{11} &= C_{11}n_1^2 + C_{66}n_2^2 + C_{55}n_3^2 + 2C_{16}n_1n_2 \\ G_{22} &= C_{66}n_1^2 + C_{22}n_2^2 + C_{44}n_3^2 + 2C_{26}n_1n_2 \\ G_{33} &= C_{55}n_1^2 + C_{44}n_2^2 + c_{33}N_3^2 + C_{45}n_1n_2 \\ G_{12} &= (C_{12} + C_{66})n_1n_2 + C_{16}n_1^2 + C_{26}n_2^2 + C_{45}n_3^2 \\ G_{13} &= (C_{13} + C_{55})n_1n_3 + (C_{36} + C_{45})n_2n_3 \\ G_{23} &= (C_{23} + C_{44})n_2n_3 + (C_{36} + C_{45})n_1n_3 \end{aligned} \tag{4.49}$$

Again, we apply the invariant condition to the x_2-axis.

$$\begin{bmatrix} C_{11}n_1^2 + C_{55}n_3^2 - \rho c^2 & C_{16}n_1^2 + C_{45}n_3^2 & (C_{13} + C_{55})n_1n_3 \\ C_{16}n_1^2 + C_{45}n_3^2 & C_{66}n_1^2 + C_{44}n_3^2 - \rho c^2 & (C_{36} + C_{45})n_1n_3 \\ (C_{13} + C_{55})n_1n_3 & (C_{36} + C_{45})n_1n_3 & C_{55}n_1^2 + C_{33}n_3^2 = \rho c^2 \end{bmatrix} \begin{Bmatrix} A_1 \\ A_2 \\ A_3 \end{Bmatrix} = \begin{Bmatrix} 0 \\ 0 \\ 0 \end{Bmatrix} \tag{4.50}$$

Unlike the previous cases, all three waves are coupled. Now, we consider the case of propagation along the x_3 direction.

$$\begin{bmatrix} C_{55} - \rho c^2 & C_{45} & 0 \\ C_{45} & C_{44} - \rho c^2 & 0 \\ 0 & 0 & C_{33} - \rho c^2 \end{bmatrix} \begin{Bmatrix} A_1 \\ A_2 \\ A_3 \end{Bmatrix} = \begin{Bmatrix} 0 \\ 0 \\ 0 \end{Bmatrix} \tag{4.51}$$

In this case, only the true pressure wave is uncoupled. While the quasi-transverse waves have the same phase velocity with coupled polarization vectors,

$$c_P^2 = \frac{C_{33}}{\rho} \; ; \quad c_S^2 = \frac{C_{44} + C_{55} - \sqrt{(C_{44} - C_{55})^2 + 4C_{45}^2}}{2\rho} \tag{4.52}$$

with polarization vectors.

$$\vec{A}_P = \begin{Bmatrix} 0 \\ 0 \\ 1 \end{Bmatrix} \; ; \quad \vec{A}_S 1 / \vec{A}_S 2 = \begin{Bmatrix} \frac{C_{44}+C_{55} \pm \sqrt{(C_{44}-C_{55})^2+4C_{45}^2} - 2C_{44}}{2C_{45}} \\ 1 \\ 0 \end{Bmatrix} \tag{4.53}$$

It should be noted that for all three types of material symmetry the phase velocity for a pressure wave propagating along the x_3 direction is both uncoupled and depends only on the C_{33} component of the stiffness matrix.

4.2.2 Guided waves

Beginning with Cauchy's equation of motion from Eq. (4.32), one possible solution is a plane harmonic wave; shown in index notation. Where $\mathbf{k}$ is the wavenumber and ω is the circular frequency.

$$u_i(\mathbf{x}, t) = \hat{u}_i e^{i(k_j x_j - \omega t)} \tag{4.54}$$

The desired solution is for plate guided waves; therefore, the propagation direction is assumed to be in the x_1 direction. The guided wave mode will consist of multiple partial wave vectors in the $x_1 - x_3$ plane. As a result, the x_2 component of the wavenumber vector is set to zero. The wavenumber in the x_1 direction is ξ and the wavenumber in the x_3 direction is scaled by α.

$$\mathbf{k} = \{\xi \; 0 \; \alpha\xi\}^T \tag{4.55}$$

The particle displacement from Eq. (4.54) is modified by Eq. (4.55).

$$\mathbf{u} = \hat{\mathbf{u}} e^{i(k_1 x_1 + k_3 x_3 - \omega t)} = \hat{\mathbf{u}} e^{i(x_1 + \alpha x_3 - vt)} \tag{4.56}$$

Let $\bar{\mathbf{C}}$ be the unrotated stiffness matrix in the lamina coordinate system, where $\mathbf{C}(\theta)$ is the rotated stiffness matrix in the laminate coordinate system. Combining equations 4.32 and 4.54 leads to the general solution.

$$C_{ijkl}k_l k_j u_m = \rho\omega^2 u_i \tag{4.57}$$

We will assume that the $\mathbf{C}$ matrix has at least monoclinic symmetry. Since this is the rotated matrix, this assumption requires that the un-rotated $\bar{\mathbf{C}}$ matrix must contain at least orthotropic symmetry. For many fiber reinforced materials, the transversely isotropic lamina model is sufficient. Combining Eq. (4.57) with Eq. (4.50) from the bulk wave section.

$$M_{ij}(\alpha, v, \mathbf{C})\hat{u}_1 = 0_j \tag{4.58}$$

where,

$$\mathbf{M} = \begin{bmatrix} C_{11} - \rho c^2 + C_{55}\alpha^2 & C_{16} + C_{45}\alpha^2 & (C_{13} + C_{55})\alpha \\ C_{16} + C_{45}\alpha^2 & C_{66} - \rho c^2 + C_{44}\alpha^2 & (C_{36} + C_{45})\alpha \\ (C_{13} + C_{55})\alpha & (C_{36} + C_{45})\alpha & C_{55} - \rho c^2 + C_{33}\alpha^2 \end{bmatrix} \tag{4.59}$$

The matrix $\mathbf{M}$ is dependent on the rotated stiffness matrix, $\mathbf{C}$, phase velocity, v, and partial wavenumber coefficient, α. The solution to Eq. (4.58) is posed in the form of a polynomial eigenvalue problem.

$$\mathbf{M}(\alpha) = \mathbf{A}_2\alpha^2 + \mathbf{A}_1\alpha + \mathbf{A}_0 \tag{4.60}$$

where,

$$\mathbf{A}_2 = \begin{bmatrix} C_{55} & C_{45} & 0 \\ C_{45} & C_{44} & 0 \\ 0 & 0 & C_{33} \end{bmatrix} \tag{4.61}$$

$$\mathbf{A}_1 = \begin{bmatrix} 0 & 0 & C_{13} + C_{55} \\ 0 & 0 & C_{36} + C_{45} \\ C_{13} + C_{55} & C_{36} + C_{45} & 0 \end{bmatrix} \tag{4.62}$$

$$\mathbf{A}_0 = \begin{bmatrix} C_{11} - \rho v^2 & C_{16} & 0 \\ C_{16} & C_{66} - \rho v^2 & 0 \\ 0 & 0 & C_{55} - \rho v^2 \end{bmatrix} \tag{4.63}$$

There are well known solutions for polynomial eigenvalue problems, and MATLAB provides a built in function. The solution has the following form, where α is a column matrix containing the eigenvalues, whereas $\mathbf{U}$ is a rectangular matrix containing the eigenvectors as columns. For each eigenvalue α_i, the corresponding eigenvector $\mathbf{U}_i$ represents the partial wave polarization.

$$[\mathbf{U}, \alpha] = polyeig(\mathbf{A}_0, \mathbf{A}_1, \mathbf{A}_2) \tag{4.64}$$

$$U_{ij} = \hat{u}_i^{(j)} \tag{4.65}$$

where,

$$\alpha = \{\alpha_1 \ ... \ \alpha_6\}^T \tag{4.66}$$

$$\mathbf{U} = \{\mathbf{U}_1 \ ... \ \mathbf{U}_6\}^T \tag{4.67}$$

The particle displacement equation can now be redefined with a polarization vector in terms of the x_3 component.

$$\mathbf{u} = \hat{\mathbf{u}}(x_3) c^{i(\xi x_1 - \omega t)} \tag{4.68}$$

The solution will have a summation of partial wave vectors, scaled by the participation factors, η.

$$\eta = \{\eta_1 \ \eta_2 \ \eta_3 \ \eta_4 \ \eta_5 \ \eta_6\}^T \tag{4.69}$$

The displacement polarization vector is expressed as a dot product between the displacement matrix and the participation factor vector,

$$\hat{\mathbf{u}}(x_3) = \mathbf{B}^u(x_3) \cdot \eta \tag{4.70}$$

where,

$$\mathbf{B}^u(x_3) = [\mathbf{b}_u^{(1)}(x_3) \ \ ... \ \ \mathbf{b}_u^{(6)}(x_3)] \tag{4.71}$$

$$\mathbf{b}_u^{(j)}(x_3) = \mathbf{U}^{(j)} e^{i\xi\alpha^{(j)}x_3} \tag{4.72}$$

The tractions on the $x_1 - x_2$ plane,

$$\sigma(\xi, \omega, x_3) = \hat{\sigma}(x_3) e^{i(\xi x_1 - \omega t)} \tag{4.73}$$

where the polarization vector can be described as follows.

$$\hat{\sigma}(x_3) = \begin{Bmatrix} \hat{\sigma}_{33} \\ \hat{\sigma}_{23} \\ \hat{\sigma}_{31} \end{Bmatrix} = \mathbf{B}^{\sigma}(x_3) \cdot \eta \tag{4.74}$$

$$\mathbf{B}^{\sigma}(x_3) = [\mathbf{b}_{\sigma}^{(1)}(x_3) \ \ldots \ \mathbf{b}_{\sigma}^{(6)}(x_3)] \tag{4.75}$$

$$\mathbf{b}_{\sigma}^{(j)}(x_3) = i\xi \begin{Bmatrix} C_{13}U_1^{(j)} + C_{36}U_2^{(j)} + C_{33}\alpha^{(j)}U_3^{(j)} \\ C_{45}\alpha^{(j)} + C_{44}\alpha^{(j)}U_2^{(j)} + C_{45}U_3^{(j)} \\ C_{55}\alpha^{(j)}U_1^{(j)} + C_{45}\alpha^{(j)} + C_{55}U_3^{(j)} \end{Bmatrix} e^{i\xi\alpha^{(j)}x_3} \tag{4.76}$$

Finally, Eq. (4.70) and Eq. (4.74) can be combined to form the state vector.

$$\mathbf{z}(x_3) = \begin{Bmatrix} \hat{\mathbf{u}}(x_3) \\ \hat{\sigma}(x_3) \end{Bmatrix} = \begin{Bmatrix} \mathbf{B}^{u}(x_3) \\ \mathbf{B}^{\sigma}(x_3) \end{Bmatrix} \cdot \eta = \mathbf{B}(x_3) \cdot \eta \tag{4.77}$$

For a single lamina in a vacuum, the boundary conditions are free tractions on the top and bottom surfaces.

$$\hat{\sigma}(0) = \hat{\sigma}(h) = 0 \tag{4.78}$$

This results in the following system of equations, where a non-trivial solution exists only when the matrix M is singular. This can also be expressed as an eigenvalue problem, where the solution is nonlinear with respect to the wavenumber.

$$\begin{Bmatrix} \mathbf{B}^{\sigma}(0) \\ \mathbf{B}^{\sigma}(h) \end{Bmatrix} \cdot \eta = \mathbf{0} \ \rightarrow \ \mathbf{M} \cdot \eta = \mathbf{0} \tag{4.79}$$

When multiple lamina are stacked together to form a laminate, the boundary conditions between each lamina are used to form a new system of equations. This will

result in a large matrix and subsequent eigenvalue problem. The solution in this form is called the global matrix method (GMM). Other common solution schemes are the transfer matrix method (TMM) and stiffness matrix method (SMM). These schemes reduce the size of the matrix in order to reduce the computational burden and make the solution easier to find. The TMM method has numerical issues for large wavenumbers, and sometime the SMM method can have issues at small wavenumbers.

The global matrix is shown below, where the tractions and displacements across each lamina interface are considered to be continuous.

$$\begin{bmatrix} \mathbf{B}_1^{\sigma}(0) & 0 & 0 & \cdots & 0 & 0 \\ \mathbf{B}_1(h_1) & -\mathbf{B}_2(0) & 0 & \cdots & 0 & 0 \\ 0 & \mathbf{B}_2(h_2) & -\mathbf{B}_3(0) & \ddots & \vdots & \vdots \\ \vdots & \vdots & \ddots & \ddots & -\mathbf{B}_{N-1}(0) & 0 \\ 0 & 0 & \cdots & \cdots & \mathbf{B}_{N-1}(h_{N-1}) & -\mathbf{B}_N(0) \\ 0 & 0 & \cdots & \cdots & 0 & \mathbf{B}_N^{\sigma}(h_N) \end{bmatrix} \cdot \begin{Bmatrix} \eta_1 \\ \eta_2 \\ \eta_3 \\ \vdots \\ \eta_{N-1} \\ \eta_N \end{Bmatrix} = \mathbf{0} \quad (4.80)$$

The sate vector for each lamina, or layer, will depend on $\mathbf{C}$ and ρ, as well as two of the following: ξ, ω and v.

Chapter 5

State-of-the-Art for Guided Wave Inspection

5.1 Introduction to guided waves

Guided waves are distinguished from bulk waves by the application of boundary conditions. Further more, guided waves generally require pulse lengths that are greater than the critical dimension. In particular, guided waves travel along a confining media, reducing the loss of energy to the surrounding environment. This section is concerned with the propagation of waves within thin-walled structures, such as those commonly encountered in aerospace; therefore, the term guided waves will be used exclusively to refer to the propagation of elastic waves along plate like homogeneous media.

This plate-like structure may contain a single homogeneous layer, or lamina, or it may contain multiple homogeneous layers, where each layer may be defined by a unique density, stiffness matrix or other material properties. Boundary conditions will be defined between each lamina, allowing the introduction of weak bonding or complete debonding of lamina. While any number of layers, and internal boundary conditions may be considered, the exterior boundary conditions will have two possible cases. The first option is the use of a traction free boundary condition on the outside surface, this will simulate a plate in air. The second option is a plate submerged in a liquid, typically water. The water is considered an inviscid fluid which cannot support shear stress. This scenario is useful when formulating the wave propagation within a plate undergoing immersion testing. For some materials, particularly those with

large densities, the propagation characteristics remain unchanged when immersed in fluid at standard temperature and pressure, but other materials with lower densities can exhibit considerable changes in their behavior [40].

It should be noted that there are a few types of guided waves that will be discussed in this chapter. The first type, and the most common, is the plate wave. This is the wave which exists as a result of resonance through the entire laminate thickness. When the plate is immersed in fluid, some of the propagating modes will become leaky, which means that some of the energy confined within the plate will leak into the surrounding media as bulk pressure waves. Other propagating waves will not leak energy; these are called true propagating waves. The true waves will also not be capable of excitation through immersion methods. A more detailed discussion of true and leaky wave modes will be provided in subsequent sections. The origins of the plate wave are due to the work of Lamb [41]. The second type of guided wave is the interface wave. This wave travels along an interface between two media. It may exist at the interface of two half spaces or may exist within a laminate as defined earlier. Depending on the material properties of the bounding media and the characteristics of the interface, the wave may be true, leaky or simply not exist. This characteristic makes the interface wave a good choice for inspecting bonded structures, but often it is difficult to excite and detect. The origins of the interface wave come from Rayleigh [42] and Stoneley [43] waves, but the general term âĂIJinterfaceâĂİ is a result of the broadened definition and boundary conditions. The third type of guided wave is very similar to the immersed plate wave; a wave propagating along a thin media bounded dissimilar elastic media. The difference is that the inviscid fluid is replaced by an elastic media. This type of wave will be referred to as an interphase wave. This description is due to the fact that this definition can be useful when describing an interface. The interface can be replaced by a very thin interphase region. Additionally, waves may travel along adhesive layers or other dissimilar entrapped layers. Once

again the propagating modes can be divided into leaky and true modes. The true modes will exist when the phase velocity is lower than the shear velocity in the bounding media. Jones and Whittier [44] first introduced the idea of a wave traveling within a flexible layer at an interface, Nagy and Adler [45] extended this concept to an adhesive layer.

5.2 Inspection Techniques

5.2.1 Normal incidence spectroscopy

Normal incidence spectroscopy is a frequency-dependent method that can be used to measure either the ultrasonic reflection or transmission through a layered structure. The method depends on a pulse length greater than the thickness dimension of interest, and can be applied as either a contact, immersion or non-contact method. This method is grouped with the guided wave section because the finite thickness results in a resonance and guided plate waves are resonance waves. When the method is used in an immersion tank or as a non-contact method, the transducer is generating guided waves with zero phase velocity, similar to the Leaky Lamb Wave (LLW) method.

Schindel [46] used air-coupled transducers to inspect multi-layered aluminum-adhesive structures. The transducers were arranged in a pitch-catch arrangement through the thickness with a normal incidence angle. A gated tone burst was used to excite the transmitter, and the frequency was varied from 0.2 to 2 MHz. The amplitude of the received signal was plotted against frequency resulting in resonance peaks. The frequency of these peaks was used to measure the adhesive thickness by comparing theoretical and experimental values.

5.2.2 Leaky Lamb wave (LLW) method

The LLW method has been used in both immersion tanks and with air-coupled transducers. The method can be used in a pitch-catch configuration where one transducer

excites the wave and a second transducer receives the signal, or in a double transmission set-up with a single transducer. The transducer excites a bulk wave in the surrounding fluid medium, water or air, which impinges onto one surface of the plate at an oblique angle. Following the commonly called Snell's law, the wavenumber vector component which is tangential to the plane surface will generate a guided wave if there is a solution at this combination of frequency and wavenumber. Due to the finite radiator dimensions and finite pulse width a range of frequencies and wavenumbers will be present within the impinging wave and all guided waves within this region will be excited. Some energy will be leaked into the surrounding medium as bulk pressure waves, and within a finite distance of the impingement zone these leaky waves will combine with the specular reflected bulk waves. This will create a null region, where the specularly reflected wave and leaky waves destructively interfere (Figure 5.1).

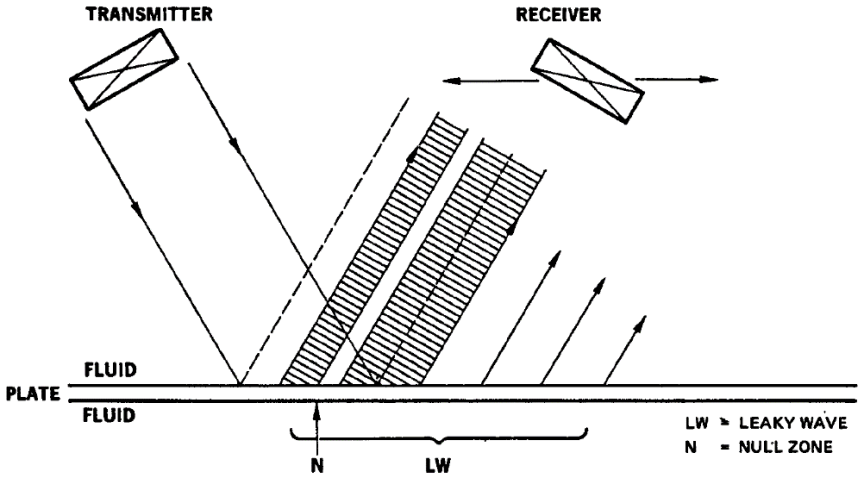

Figure 5.1: LLW Method [47], the null zone exists in a region of destructive interference between the specular reflection and the leaky wave

If the second transducer is placed within this null zone, then the Fourier transform of the received signal will reveal the guided wave modes as the troughs in the frequency spectrum. Additionally, the receiver can be placed further down range, beyond the region of specular reflection, where only the leaky waves are present, or the pair can be moved closer to the plate surface so that the transducer is defocused, accomplishing

the same goal (Figure 5.2). The Fourier transform of this signal will have regions of increased amplitude at the guided wave mode frequencies.

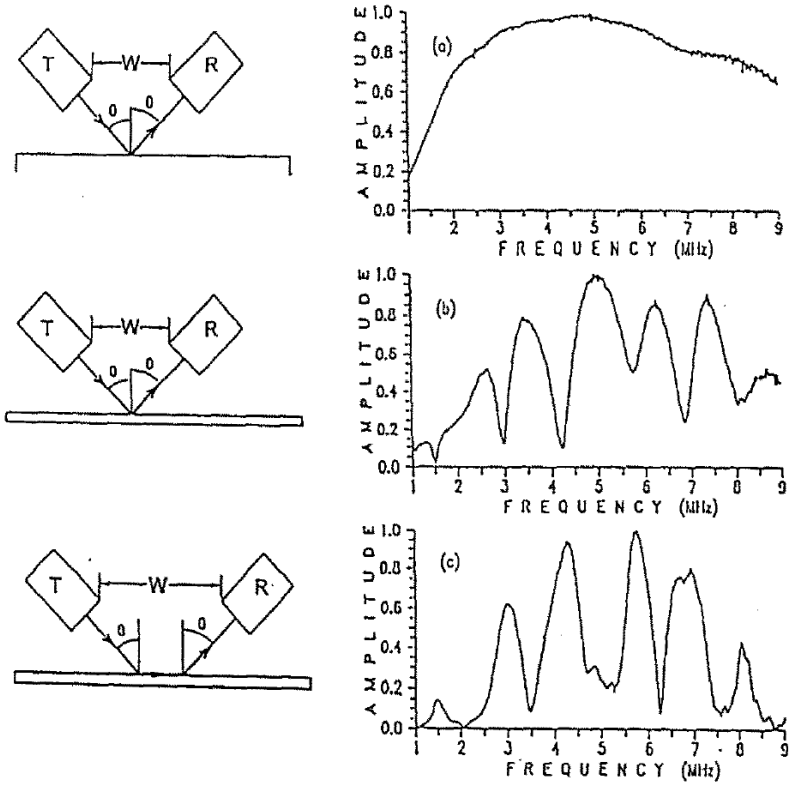

Figure 5.2: Interpretation of LLW results [48]; (a) specular reflection from a half space, (b) reflection from a plate within the null zone, (c) reflection from a plate within the leaky wave zone

Bar-Cohen [47] [49] first pioneered the use of the LLW method for the inspection of fiber reinforced laminates, where common defects, such as delaminations and matrix cracking, could be detected. Also, Bar-Cohen used the received amplitude to generate C-scan images of the composite laminates, referred to as L-scans.

Later, Bar-Cohen et al. [50] used the LLW method to inspect rubber-to-metal bonded structure, stainless steel and neoprene seals, at a frequency range of 1 to 10 MHz. The Lamb wave modes were not selected a priori, but were found through experimentation until a mode was identified which was close to the resonant frequency of the transducer. Three types of specimens were manufactured for the test;

a good bond specimen, a specimen with a clear disbond and a specimen with partial disbonding. This technique was employed while scanning over the entire specimen. The amplitude of the specified Lamb wave frequency was monitored and C-scan data was produced for each specimen. Frequencies were identified by broad-bandwidth, frequency-modulated tone burst (FM chirp), and Fourier transform was used to separate the frequencies. The L-scan was generated from the signal amplitude at the frequency identified to be a Lamb wave mode, where larger amplitude indicates destruction of the resonant mode.

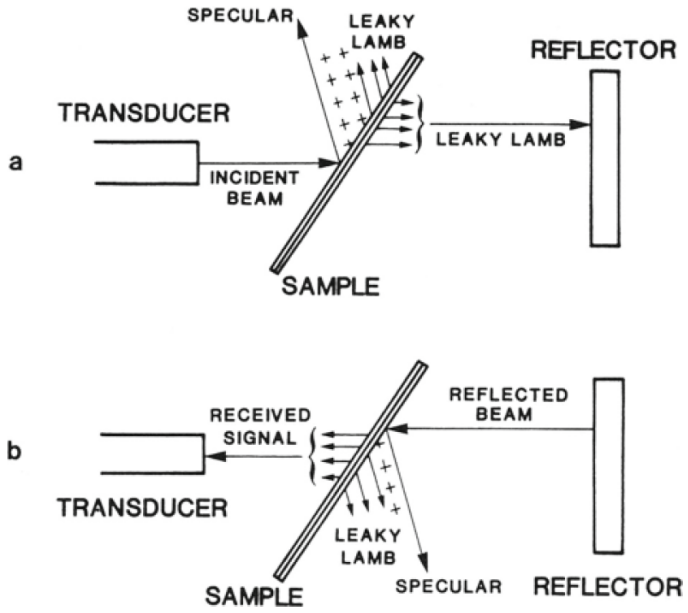

Figure 5.3: Double through transmission LLW technique [51], can also be used for leaky interface waves; (a) wave pulse traveling from the transducer to the reflector, (b) wave pulse traveling from the reflector back to the transducer

Nagy and Adler [45] [51] proposed the double transmission of leaky Lamb waves through a laminate, A2024 aluminum and FM300 adhesive, submerged in a water tank (Figure 5.3). The first returning wave packet contains frequency dependent interface information on the leaky interface wave. Experimental results from good bonds, partial disbonds, and porosity showed that the interface wave results were easier to interpret and in general more sensitive to adhesive defects as compared to

the full leaky Lamb wave information. Lamb mode distribution in an adhesive joint is only slightly affected by bond defects, although low frequency modes can be used to determine the shear modulus of the adhesive. It should be clear that this method is best used with the interface waves which decay very rapidly; otherwise, the leaked energy will be small and difficult to detect.

When the pulse length of the wave is shorter than the thickness of the laminate, it is possible to generate interface waves separately independent of the plate waves (Figure 5.4). It should be noted that the interface waves will still exist when the pulse length is long, but they are coupled to the plate wave modes.

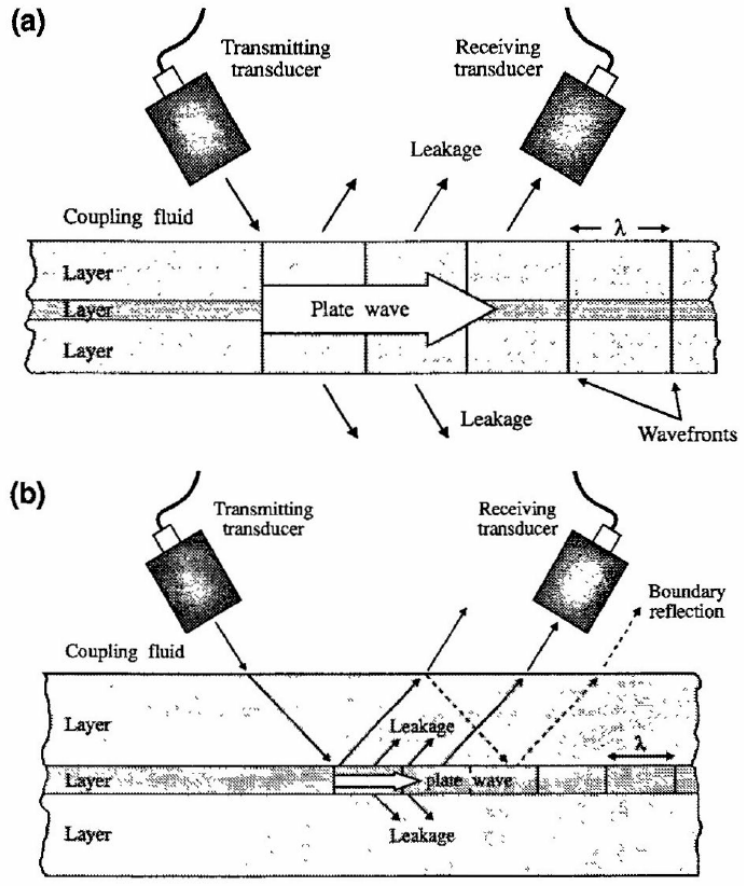

Figure 5.4: LLW method for a plate mode vs. LLW method for an interphase mode [52]; (a) plate wave, (b) interphase wave

Rokhlin, Wang and Wang [53] used an ultrasonic goniometer to reflect focused, obliquely-incident waves. They considered bonded structures, aluminum and aluminum-

oxide. The semi-circular reflector ensured that the bulk waves were reflected back through the specimen without the need to readjust for each incident angle (Figure 5.5). The transducer was focused onto the adhesive layer. The frequency dependent amplitude was used to differentiate weak and good bonds. If a short wave pulse is used then plate modes should not be generated, only adhesive interphase modes.

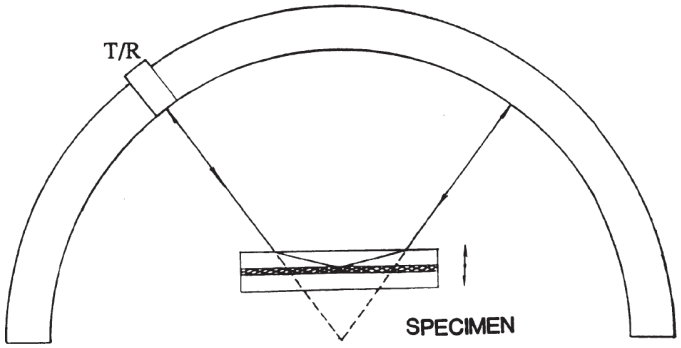

Figure 5.5: Ultrasonic goniometer for the inspection of adhesive joints [53]

Mal, Xu and Bar-Cohen [54] investigated the use of immersion LLW to determine the adhesive properties and thickness of bonded aluminum plates.

Bar-Cohen and Mal [55] discussed theoretical and experimental results in the use of ultrasonic oblique insonification for the inspection of composite materials. They used the immersion LLW technique to determine the C matrix through an inversion procedure. Also, they used the time-of-flight method, with the same experimental set-up, to find the elastic constants. The leaky Lamb wave method can provide the complex C values, while the time-of-flight only provides real values. Additionally, they used time of flight to find delaminations and matrix cracking.

Lowe and Cawley [52] investigated the applicability of plate wave techniques for adhesive and diffusion bonded joints in aluminum. Several ultrasonic inspection techniques were reviewed, such as the detection of leaky guided waves, both plate and embedded waves. Also they considered the excitation of true embedded waves through Rayleigh mode conversion in immersion or direct excitation at the joint boundary. The use of embedded modes was considered to be the most promising technique for

both cohesive and adhesive inspection of bond lines. However, the authors showed that the minimum technique, the detection of leaky guided waves within the null zone by finding the frequency minimums, used with leaky embedded modes does not necessarily coincide with the dispersion curves, but it could still be useful in the inspection of the joints. The most promising technique is the excitation and detection of true embedded modes; although, this requires access to the boundary of the joint or mode conversion from surface waves.

Mal, Lih and Bar-Cohen [56] used leaky Lamb wave techniques to measure phase velocity. They used the null frequencies in the reflected amplitude spectra, and this could be used to derive the dispersion curves. They examined a bonded aluminum plate, and a multi-layered graphite epoxy composite laminate at a 20-degree incidence angle. The techniques successfully found delaminations and matrix cracking.

Kundu and Maslov [57] investigated the interface between glass plates under hydraulic pressure. Then they inspected bonded glass plates with LLW and generated L-scans.

Kundu et al. [48] used the leaky Lamb wave technique in immersion on glass plates. They used a tone burst excitation with continuously varied frequency. Investigated two options for detecting the guided waves; (a) use the null zone to find Lamb modes at null frequencies, or (b) move the transducer-receiver pair closer and defocus, causing the Lamb wave modes to exist at the peaks.

Karpur, Kundu and Ditri [58] used the leaky Lamb wave method in an immersion tank to generate L-scans. They tested aluminum and copper adherends with an epoxy adhesive.

Fan et al. [59] discussed air-coupled LLW generation and detection, specifically analyzing secondary reflections in the air gap. FEA was used to understand these types of reflections and the effect on the received signal. Experiments were carried out on a 1 mm thick polycarbonate plate.

Mezil et al. [60] investigated zero-group velocity (ZGV) Lamb modes. They excited the waves with a Q-switched Nd:YAG laser and detected on the opposite side of the plate with an interferometer. They studied a bonded aluminum epoxy plate, and looked for changes in interfacial stiffness. Fourier transform was used to interpret the results.

5.2.3 Double mode conversion (DMC) method

I have not found an inclusive term for the present ultrasonic method; therefore, I have given the term double mode conversion (DMC) method, as follows (Figure 5.6). A guided wave is generated in a single plate or fiber reinforced laminate; the wave travels and encounters an adhesive joint where the wave is reflected and transmitted after mode conversion. The transmitted waves travel the length of the joint, where the wave packet is once again mode converted back into a single plate or laminate.

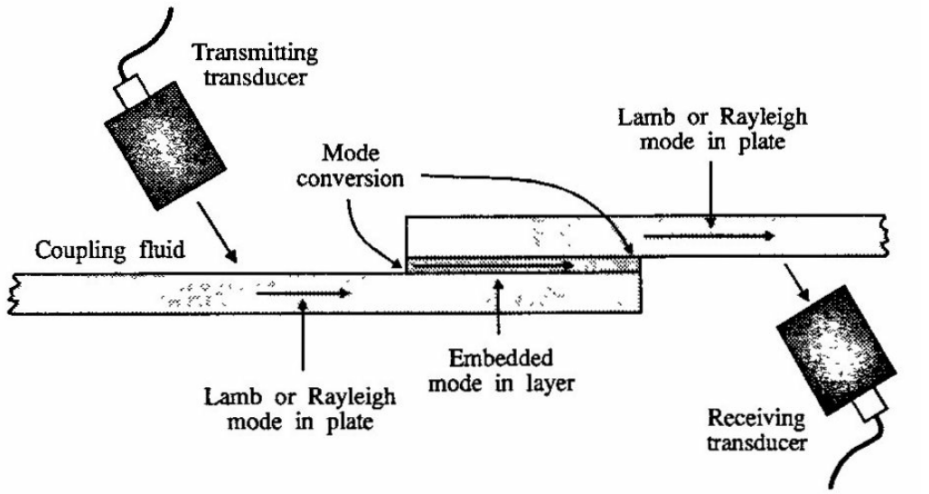

Figure 5.6: Schematic diagram of the double mode conversion method [52]

Commonly the joint is a doubler or overlap, but this could include more complicated joints such as stringers or regions of bonded honeycomb. The method is commonly used to generate interface or true interphase modes which cannot be excited through the oblique bulk wave technique (Figure 5.7).

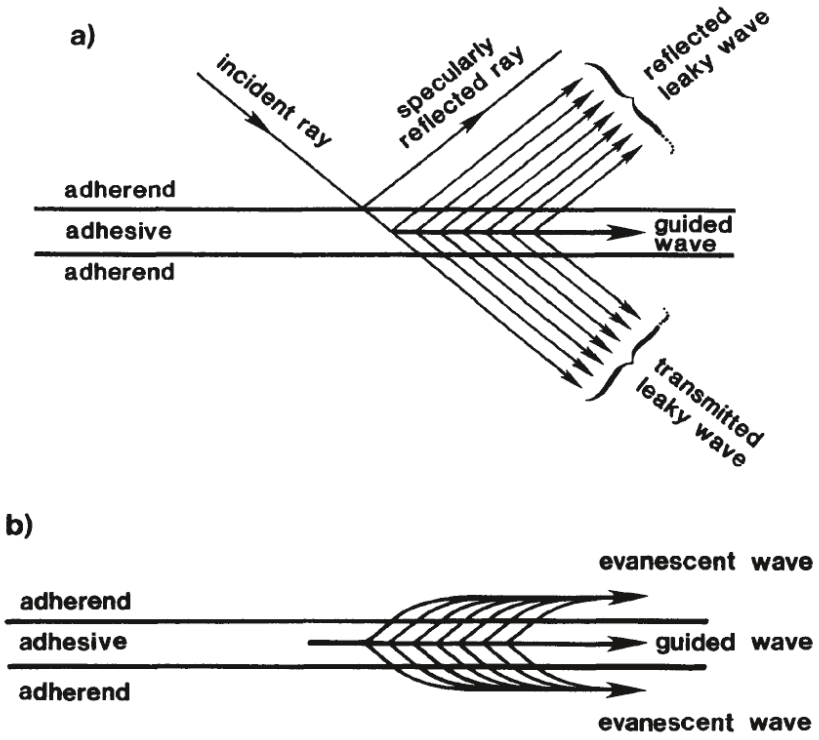

Figure 5.7: Geometric acoustic interpretation of (a) leaky interphase waves and (b) trapped interphase waves [61]

Claus and Kline [62] used 8 and 9 MHz SAW wedge transducers to excite Rayleigh waves, which were mode converted into Stoneley waves at the intersection with a doubler. The plates were made of Pyrex and differential interferometric were used to measure wave amplitudes.

Rokhlin, Hefets and Rosen [63] [64] used laboratory constructed wedge-type transducers to excite and receive Rayleigh waves; interface waves were mode converted. The carrier frequency was 1.2 MHz. They measured velocity with the signal-overlap method, while group velocity was determined by the signal delay, and variation in phase velocity were measured by relative phase changes of the high frequency signal filling the pulse. These studies were performed on isotropic substrates.

Nagy and Adler proposed using the double transmission and mode conversion of Rayleigh waves for the excitation of true propagating interface modes [45].

Lourme, Hosten and Brassier [65] used air-coupled transducers to transmit A0

Lamb waves through an aluminum-adhesive lap joint. Altering the position of the receiver allowed for the use of 2D-FFT to separate the modes.

Ren and Lissenden [66] investigated the transmission of a guided wave into an adhesive doubler from a single plate in order to inspect for interface defects. The test structure was composed of two $[0/45/90/-45]_{S2}$ plates bonded with epoxy. Teflon film was used to simulate adhesive defects. They used the pitch-catch arrangement to generate and detect surface waves, which are mode converted to the desired Lamb waves.

Alers and Thompson [67] used EMATs to excite waves in an aluminum plate, where they traveled through an adhesive lap joint and were picked up by another EMAT; the carrier frequency was 2.25 MHz. They used time of flight to measure the group velocity of trapped modes within the overlap region. They also considered normal incidence immersion resonance.

Lanza di Scalea, Rizzo and Marzani [68] performed an experimental study on the transmission of Lamb wave modes through an aluminum - epoxy lap joint, concentrating on the a_0 mode. A Q-switched, Nd:YAG puled laser (1024 nm and 8 ns pulse duration) was used as the excitation source, and a 10-mm broad band air-coupled capacitive transducer was used as the receiver, with a relatively flat frequency response below 1.5 MHz for lift-off distances below 25 mm. The Gabor Wavelet Transform was used to extract the energy and group velocity for each mode. The energy transfer through the lap joint was plotted with frequency. The angle was chosen to maximize sensitivity to a particular mode.

5.2.4 Edge generation (EG) method

The edge generation (EG) method is used to generate true interface or true interphase modes at the edge of an adhesive joint or laminate (Figure 5.8). This method avoids the complexity of the DMC method, and can be used in either pitch-catch or pulse

echo configurations.

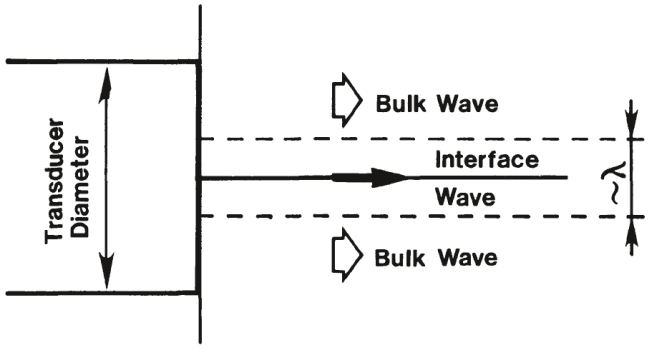

Figure 5.8: Edge generation method [69]

Nagy and Adler [69] excited true interface waves by contact transducers placed on the edge of the adhesive joint; this is different from the typical method of exciting Rayleigh waves which mode convert into interface waves at the transition into the joint. Different interface modes can be excited through the use of longitudinal and shear polarized transducers. Both bulk and interface waves are generated. Another transducer is used to detect the signal at the back wall. If the sample is long and the interface mode is not too dispersive, then the signals will arrive separately, otherwise, spectrum analysis is used to get velocity and amplitude information. The authors considered aluminum dry contact and aluminum adhesive bond.

Lowe and Cawley [52] used the edge generation method to excite and detect true embedded modes in order to avoid the mode conversion technique. However, they found that the method was restrictive, given that access to the edge of the joint is generally limited.

5.2.5 Laser Doppler Vibrometry (LDV)

The LDV method uses a laser beam to measure the out-of-plane motion of a surface by utilizing the Doppler effect (Figure 5.9). This is a non-contact method that has

been separated from the other methods, since it does not depend on the acoustics within a bounding media.

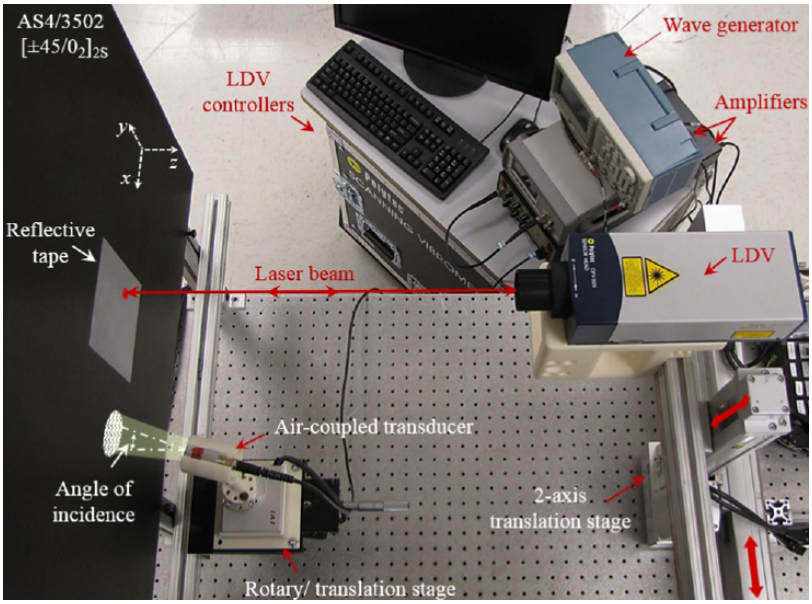

(a) Equipment set-up

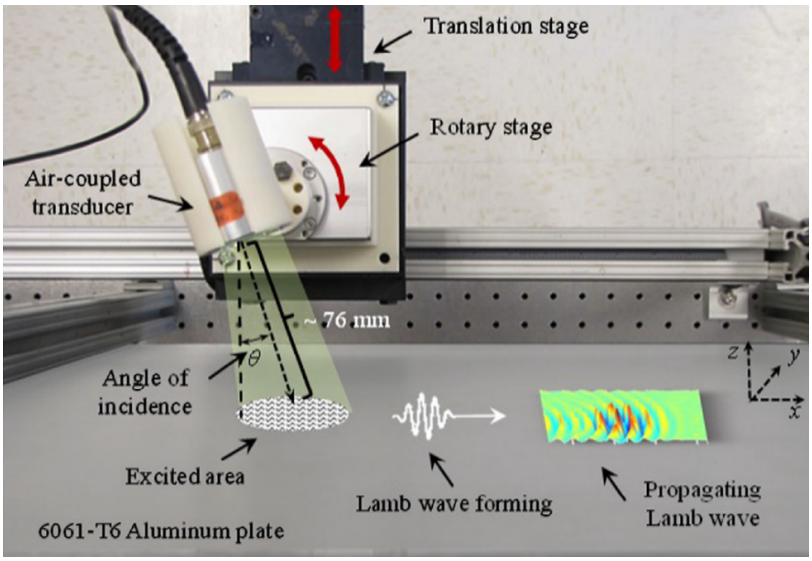

(b) Schematic of the excitation and propagation of guided wave modes

Figure 5.9: LDV experimental set-up for determining dispersion curves on (a) composite and (b) aluminum plates [70][71]

Harb and Yuan [70] used a hybrid system to generate Lamb wave dispersion curves, specifically the a0 mode in aluminum, using air-coupled transducers and Laser Doppler Vibrometry (LDV). The air-coupled transducer was mounted to a rotary

motor, and the LDV was mounted onto a 2D gantry, so that the reception point could be moved. The ideal incident angle with respect to frequency was determined for exciting the a0 mode. With only a single receiving point, the phase and group velocity vs. frequency dispersion curves are calculated. The phase velocity is calculated by varying the incident angle and using the most efficient angle, then converting angle into wavenumber through Snell's law. 2D-FFT can also be used to find the dispersion curves. The 1D method is found to be more accurate than the 2D-FFT and the Morlet wavelet transform. Later, Harb and Yuan [71] extended the work to composite plates.

Heller, Jacobs and Qu [72] used a laser source to excite Lamb waves in a single aluminum plate, a single plate with adhesive on one side and bonded plates. A second laser was used to measure the surface velocity with the Doppler affect. A 2D-FFT was used to generate the experimental frequency-wavenumber dispersion curves. However, It is difficult to make any interpretations at frequencies below one MHz based on the figures provided. Also, the wavenumber information depends on increasing the propagation distance which will lead to amplitude losses and possible misinterpretation of results.

Later, Seifried, Jacobs and Qu [73] extended the work to develop the analytical model of the dispersion curves observed in the previous work. The results matched the experimental work and showed that the experiment could not detect the modes that were specific to the adhesive layer.

Juarez and Leckey [74] used multi-frequency local wavenumber analysis and ply correlation to detect composite ply delamination due to an impact. They excited the damaged plate with a chirp signal from bonded transducer. The received signal was from a 2D gantry scan with a 1D LDV.

Castaings and Le Crom [75] used SH guided waves to infer the shear stiffness of adhesive bonds. A contact shear transmitter was used to generate SH guided waves in an aluminum, epoxy, composite plate, along a plane of symmetry. LDV was used

to measure the displacement, utilizing a skew angle to measure in-plane displacement in addition to the usual out-of-plane displacement. The 2D-FFT was used to measure the phase velocities of each propagating mode.

5.3 Theoretical modeling and prediction

While Lamb [41] and Rayleigh [42] developed the first models for guided waves along plates and half spaces, respectively, the first theoretical model with application to bonded joints came from Stoneley [43] when he studied the propagation of continuous plane harmonic waves along the interface between two elastic homogeneous isotropic half-spaces. The solution provided by Stoneley has a limited existence, depending on the material properties of the half-spaces, and the result is non-dispersive with respect to frequency.

In 1947, J. G. Scholte [76] wrote a paper considering the range of existence of Stoneley waves. In this paper, Scholte is able to determine a set of equations and figures which describe the regions where a real Stoneley wave may exist. These existence ranges are expressed in terms of the ratio of mass density and the ratio of shear modulus. For particular combinations of these parameters, it is possible for a true propagating mode to exist. This still leaves only a very limited number of cases where this mode exists, and adhesive joint interfaces for many material combinations are not included in this group.

Then in 1972, Walter Pilant [77] produced a work which discussed the determination of complex roots to the Stoneley wave equation, and revealed that it was possible to have 16 independent roots for the equation. The paper discussed two scenarios; (a) the denser material has a transverse phase velocity greater than the less dense material, and (b) the denser material has a transverse phase velocity less than the less dense material. Since the second case does not apply to the study of adhesive joints, only the first case is discussed here. For this case, there is a very small range where

real propagating modes exist when the transverse phase velocities are very close (Figure 5.10). Above this zone only leaky modes exist, which are called Interface waves. These interface waves exist in a range that begins at the Stoneley wave range and extends up to the point where the transverse phase velocity of the denser material almost 4 to 6 times greater than the less dense material. Also, beginning around the three-fold velocity mark, a Rayleigh mode begins to exist on the interface.

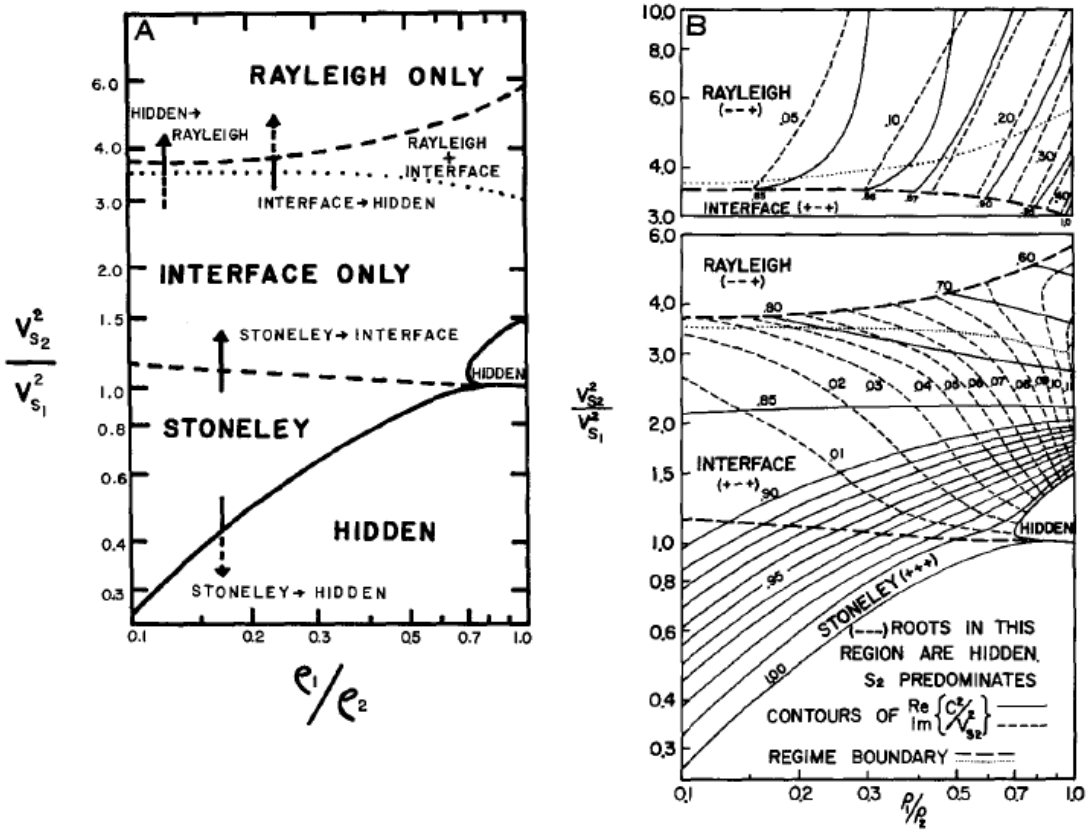

Figure 5.10: Existence of Interface Modes [77]

While Stoneley considered two elastic solids joined by a perfect interface, Jones and Whittier [44] extended this theory to include an elastic interface condition. They consider a model where the two isotropic half-spaces are joined together by an inertia less layer with a thickness, b, which is small compared to the wavelength. Since the layer is inertia less, the tractions on the top surface are equal to the tractions on the lower surface of the layer, and the stresses are assumed to be proportional to the

relative displacements. This relationship is still valid for an anisotropic layer between two isotropic half-spaces since the equations do not require that G be related to E through Poisson's ratio.

$$\sigma_{xz} = \frac{G}{b}(u^1 - u^2) \; ; \quad \sigma_{zz} = \frac{E}{b}(u^1 - u^2) \; ; \quad at \; z = 0 \tag{5.1}$$

Combining the new boundary conditions with the typical equations for plane harmonic elastic waves in two isotropic half-spaces then solving for the 4 by 4 determinant results in the characteristic equation for waves traveling along a flexible interface. The equations reveal that when the stiffnesses are sufficiently large the solution approaches the Stoneley wave solution, and when the stiffnesses are zero the solution leads to two independent Rayleigh waves one each surface. Jones and Whittier go on to discuss the real solutions to the equation between these two extremes, and they come to four major conclusions (Figure 5.11).

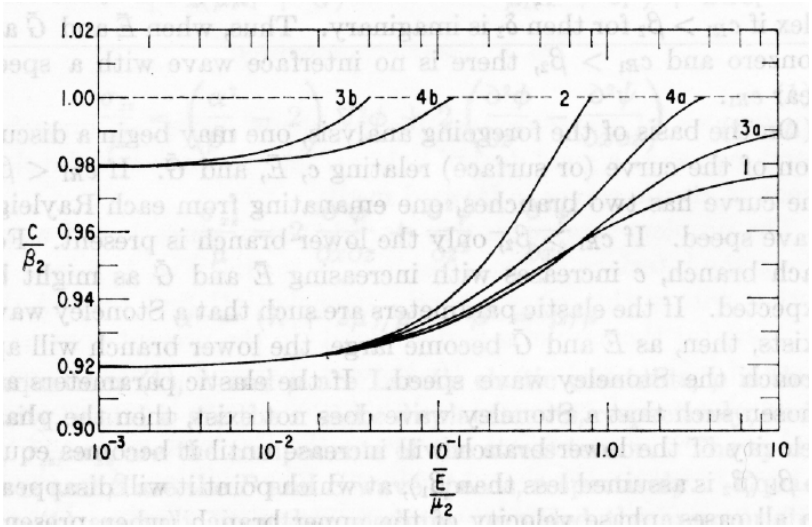

Figure 5.11: Dispersive behavior of waves at a flexible interface [44]

First, two independent Rayleigh waves exist when the effective stiffness of the interface layer is equal to zero. Second, if the faster Rayleigh wave velocity is greater than the smallest transverse phase velocity then this Rayleigh wave will only exist when the effective interfacial stiffness is zero. The remaining Rayleigh wave will increase velocity as the effective interfacial stiffness increases and will eventually become

a Stoneley wave, if a real solution is permitted, otherwise it will eventually reach the transverse phase velocity and become a complex wave. Third, if both Rayleigh wave speeds are below the minimum transverse phase velocity, then both waves will exist and behave as described in the previous sentence. The final conclusion is that the solution to the problem is dispersive due to the changing wave speed with changes in interfacial stiffness. This is the first result to show that the velocity of an interface wave can be used to infer interfacial stiffness properties.

Alers and Thompson [67] computed the Lamb wave propagation for a three-layer sandwich with a compliant adhesive layer between two stiff aluminum plates, utilizing the global matrix method. The dispersion curve for real wavenumbers and frequency was calculated for the proposed geometry, where all layers were homogeneous linear isotropic materials. The authors were particularly interested in the trapped modes, and these modes were easily identified in the phase velocity vs. frequency plot, where all modes below the bulk shear velocity of the aluminum adherend are trapped by the adhesive layer. A weak interface was simulated by relating the displacements on each side of the weak interface through a stiffness parameter. After applying this new boundary condition, the change in phase velocity with respect to frequency was plotted for two of the trapped modes, showing that there was a maximum around 4 MHz in terms of the change in phase velocity. Other modes showed large changes in phase velocity in the highly dispersive regions, or when large stresses were present at the interface. Additionally, several of the zero wavenumber modes displayed a sensitivity to the weak interface. The results show that the measurement of adhesive bond strength is possible if a particular mode is excited at a particular frequency, which takes great care and precision.

Rokhlin, Hefets and Rosen [63] developed the characteristic equation for an interface wave which travels along a thin viscoelastic film at the interface between two identical elastic half-spaces. All of the materials were considered to be homogeneous

and isotropic, while the thin layer was assumed to be viscoelastic through the use of complex Lame constants. Additionally, it was assumed that the shear modulus of the half-spaces are greater than the shear modulus of the thin film. It was shown how the velocity and attenuation of the interface wave depend on the elastic and viscoelastic properties of the half-space and film.

Nagy and Adler [45] studied the possibility of using guided interface waves for nondestructive evaluation of adhesive joints. In this paper, guided interface waves are the name given to waves which propagate in an adhesive layer surrounded by two elastic half-spaces. This type of wave has three general solutions; non-propagating, true propagating and leaky guided modes. The authors used numerical techniques to predict the frequency dependent transmission coefficient for a perfectly bonded leaky interface wave, but did not predict the response from a defective structure. Experimental results from good bonds, partial disbonds, and porosity showed that the interface wave results were easier to interpret and in general more sensitive to adhesive defects as compared to the full leaky Lamb wave information. The authors only considered isotropic adhesive and adherend and the experimental work was performed on epoxy bonded aluminum joints.

Nagy and Adler [51] found that Lamb mode distribution in an adhesive joint is only slightly affected by bond defects, although low frequency modes can be used to determine the shear modulus of the adhesive, and that while the amplitudes of different modes are altered, they are very complicated and difficult to evaluate. Instead, they propose using leaky interface waves, phase velocity greater than the shear velocity of the adherend. The initial wave packet transmitted through the structure consists of the leaky interface waves. It should be clear that this method is best used with the interface waves which decay very rapidly; otherwise, the leaked energy will be small and difficult to detect. They go on to show that the interface waves are more sensitive to small changes in the interfacial conditions of the bond, and that some

Lamb waves are sensitive but overall the interface waves are more easily distinguished between the different cases.

Nagy and Adler [45] also investigated the use of true propagating interface waves for adhesive inspection. They utilize the inertia less interfacial stiffness technique to simulate interfacial bond defects. The true interface waves are excited by contact transducers placed on the edge of the adhesive joint; this is different from the typical method of exciting Rayleigh waves which mode convert into interface waves at the transition into the joint. Different modes can be excited through the use of longitudinal and shear polarized transducers. Experimental study of an aluminum-epoxy joint showed that the measured velocity of the interface wave was dependent on frequency, dispersive, and was very close to theoretical predictions. Based on the theoretical predictions for the interfacial stiffness technique, the dispersion curve of the interfacial waves is also dependent on the stiffness at the interface; therefore, the dispersion curve can be used to evaluate the quality of the adhesive interface.

Rokhlin, Wang and Wang [53] used the obliquely incident resonance to inspect an aluminum joint for a weak interphase layer. The inspection technique is a single transducer pulse-echo method. The reflection coefficients are calculated through a matrix technique by Solyanik [78]. The layered structure includes aluminum half spaces, aluminum oxide layers, primer, adhesive and a weak boundary layer. The substrates are modeled as half spaces because the wave pulse is small compared to the substrate thickness. The weak boundary layer was modeled as a thin isotropic viscoelastic layer. The theoretical results show that the minimums in the frequency spectrum of the weak bond specimen are different from the good bond results. The authors show that as the frequency relaxation time parameter is varied, the frequency minimums vary. The frequency relaxation time parameter is used to change the layer from liquid to a near solid state. The experiments match fairly well with the theoretical work except for an unexpected branch that is very similar to a free guided

wave in the adhesive. This could possibly be caused by a trapped air bubble.

Mal, Xu and Bar-Cohen [54] used LLW to evaluate adhesive bonds. A weak bonding condition was simulated by relating the displacement jump across this zero thickness interface to the interface traction. Two models are considered; the first is an adhesive with perfect stress and displacement continuity, and the second is a zero thickness adhesive layer called the flexibility matrix. Comparing theoretical and experimental results, the authors found that the aluminum plate matched well, but that the aluminum-epoxy sandwich structure did not.

Huang and Rokhlin [79] presented first and second order asymptotic boundary conditions with the transfer matrix approach to describe interface waves in an anisotropic layer between two anisotropic solids. The approximations were compared to the exact transfer matrix solution, which is based on the Stroh formalism, with good results for small thickness to wavelength ratio of the interfacial layer and lower order modes. The second order asymptotic boundary condition maintains the energy balance, unlike the lower order approximations. The article also presents a method of calculating the reflection coefficients for an oblique wave incident onto the interface layer. A study into the interface wave velocity along different directions could provide the anisotropy of an interface. The main argument for this type of approach is the simplified mathematics of the transfer matrix approach; there is no consideration of the wave behavior within the interfacial layer. The authors do not present any results for the reduction in computational resources thought the use of the approximation method; therefore, it is hard to justify this method over the exact solution, especially with the computational resources available today.

Rokhlin and Huang [80] developed an approximate transfer matrix for relating stresses and displacements across an orthotropic interphase layer of general orientation between two generally anisotropic solids. The approximation is valid when the wavelength is much smaller than the interphase thickness. This method includes both

inertial and coupling terms, which are not present in the simple spring models. The coupling terms allow more conversion across the interphase. The authors use this transfer matrix to model an interface wave.

Bar-Cohen and Mal [55] discussed theoretical and experimental results in the use of ultrasonic oblique insonification for the inspection of composite materials. They found that their theoretical guided wave solution was not accurate for high frequency; possibly scattering from fibers and viscoelastic resin. They showed that a transversely isotropic material can be described by 5 unique bulk phase velocities. Introduced damping function to account for both viscoelastic and fiber scattering. They used a method of using 3 scalar potentials for a transversely isotropic material. This method includes the use of the 5 complex bulk wave speeds, made complex through the use of the damping function. Examined the effect of a 20% reduction in C matrix components on the dispersion curves, and found that the resin dependent properties had the greatest effect. When multi-directional laminates are used, an extra variable is introduced because of the bonding between lamina. This bonding is best modeled as a thin region of resin. Also, introduced a time-of-flight method for determining the C values since the reflection coefficient method depends on a non-linear regression. Experimentation was performed to validate the theory. Also, delaminations and matrix cracking were inserted into some samples. The delaminations were easily found due to the change in the dispersion, and the height was easily calculated by considering the delamination traction free. The matrix cracking was studied by considering the lamina as having a decrease in the stiffness.

Mal, Lih and Bar-Cohen [56] used the LLW technique to investigate the effects of adhesive properties and interfaces on the phase velocity of guided waves. Theoretical calculations of the frequency spectrum of the reflected wave from a 20-degree incident wave onto two aluminum plates bonded with adhesive are performed. It is shown that a 20% decrease in adhesive thickness and a 20% decrease in shear modulus of the

adhesive result in measurable changes in the frequency spectrum, and a disbond results in dramatic changes to the spectrum. Next, a $[0, 90]_{2S}$ cross-ply graphite/epoxy laminate is studied. Theoretical predictions and experimental data are gathered for the reflected frequency spectrum up to 5 MHz. The initial predictions appear to be frequency shifted for the higher frequency modes with a good match for the lowest order mode. The authors believe that this is due to resin rich layers between the individual laminae. A model is derived for 5 micrometer layers of resin between each laminate. The resulting predictions provide a closer match to the experimental data, but still not perfect for the higher frequencies.

Karpur, Kundu and Ditri [58] used displacement, stress and energy distribution to select appropriate Lamb wave modes and frequencies for the inspection of adhesively bonded plates. The plates were made of aluminum or copper with epoxy adhesive. The modes were selected to be sensitive to the interfaces, and the leaky Lamb wave techniques was used to generate L-scans of each plate. It was showed that different images were generated for different modes, indicating the sensitivity of the modes to different defects.

Kundu and Maslov [57] continued the investigation of an interface between glass plates by also considering a bonded plate. Once again dispersion curves were calculated and measured for a thick glass plate, a two plate laminate with a water layer under hydraulic pressure and a two plate laminate bonded with adhesive. The shear and normal stress distribution was used to validate the appropriate mode and frequency selection for detecting slip bonds or defects near the interface. The transfer matrix method was used to calculate the dispersion curves and mode shapes. This set of papers shows that the mode and frequency must be properly selected through a theoretical investigation in order to find the desired defects.

Later, Seifried, Jacobs and Qu [73] extended the work to develop the analytical model of the dispersion curves observed in the previous work. The results matched

the experimental work and showed that the experiment could not detect the modes that were specific to the adhesive layer. However, the provided mode shapes have some errors and the dispersion curve results appear to be flawed.

Lanza di Scalea, Rizzo and Marzani [68] calculated mode shapes through the Global Matrix Method (GMM). Poorly cured epoxy simulated by halving the longitudinal and shear velocities. Slip interface simulation used water as the adhesive layer with the epoxy density, but the longitudinal wave speed of water and a nearly zero value for the shear velocity. Experimental results were collected using a fully cured epoxy, an improper mix of hardener to resin, and a water layer trapped between the plates with a silicone barrier. The Gabor Wavelet Transform was used to extract the energy and group velocity for each mode. The energy transfers completely through the lap joint and from the single adherend onto the joint is plotted with frequency. The graphs show how the mode conversions and transfer efficiency change with frequency. The analytically derived mode shapes, GMM, are compared in order to justify the observed mode conversions. A few frequency ranges are found that may provide a good indication of bond quality. The results apply only to the specific geometry used in this study. I have some concerns about the method of evaluating the mode conversion, because the laser source most likely excited more than just the A_0 mode; therefore, there is no good way telling the difference between modes converted from an A_0 incident wave or another mode. The work only considered isotropic, lossless media, and is only valid for the specific geometry considered.

Cho and Rokhlin [81] used the finite difference time-domain (FDTD) method to model the propagation and edge conversion of an interphase wave between two isotropic half-spaces. Phase spectrum analysis was used to estimate the phase velocity and wavelet transformation with the Gabor function was used for the group velocity. Along the interface, symmetric and antisymmetric interface waves cause constructive and destructive interference which results in noticeable dips and peaks

in the frequency spectra for the top and bottom interface surfaces. The symmetric and antisymmetric waves are separated through subtraction and addition of the waves at the top and bottom interfaces. The separated frequency spectra do not contain the interference patterns like the combined spectrum. The frequency spectrum of the through transmitted Rayleigh wave showed noticeable interference dips due to the different velocities of the two interface modes. These dips could potentially be used to infer interphase layer properties.

Delrue and Abeele [82] used 3D FEA to simulate the non-linear air coupled emission from a Lamb wave interacting with a delamination. Performed a FE analysis and modeled the delamination with virtual spring and damper forces. Above a threshold, the surfaces are stress free and below that threshold the forces are applied. The authors characterize the defect with nonlinear air-coupled emission (NACE) and using local defect resonances (LDR). The air-coupled emission is detected and the subharmonic and harmonic frequencies are used to detect the defect. The best method of detection is to utilize the resonance of the defect by performing a frequency sweep.

Koreck, Valle, Qu and Jacobs [83] used numerical methods to quantify the material properties of an adhesive layer hidden from traditional inspection techniques. The authors used the GMM and FE simulation to determine the dispersion and slowness curves. The dispersion curve for a given adhesive - aluminum joint mode moves between the different modes for a single layer of aluminum and/or a single layer of adhesive. When calculating the frequency - wavenumber dispersion from the outside layer of a FE simulation, the modes "disappear" from the plot when they are transferring between single layer modes. These areas are then used as sensitive points for identifying changes in the adhesive material. A parametric study was performed on the adhesive thickness, Young's modulus, and Poisson's ratio. Graphs in the paper show how these sensitive points vary in frequency for each property. Finally, an inverse problem algorithm was devised to calculate the adhesive properties form the

frequency of the sensitive points.

Hauck, Rose and Moose [84] used FEM to model the bondline of a steel to composite scarf joint. Used Both GMM and SAFE for the calculation of the dispersion curves. Examination of the mode shapes revealed a possible inspection mode with high shear stress at the interface. ABAQUS simulations were used to verify the guided wave modes. A steel wave guide template is used to make the transducer parallel to the bondline.

Lourme, Hosten and Brassier [65] used FEM to study the sensitivity of guided waves to adhesion in lap joints. The model included aluminum substrates, an adhesive layer with complex Young's modulus and normal and shear springs on the interface to simulate weak interfacial adhesion. Absorbing regions at the ends of the substrate where used to eliminate reflections. An energy balance of the incident, reflected and transmitted energy was performed as a model validation. A 3D-FFT in time and space was used to find the amplitudes of each mode through the surface displacements in a region before and after the lap joint. The transverse spring stiffness for good bonding is set to $1e\hat{6}$ GPA/mm and is reduced to nearly zero to simulate a contaminated joint. The FE model shows that the reflected and transmitted A0 mode is sensitive to the simulated contamination, especially around 400 kHz. Experimentation was performed on two samples; one with ideal bonding and a second with silicone contamination. Air-coupled transducers were used to excite and receive the guided waves. The a_0 incident experiment resulted in some correlation with FEM and confirmed the general trend of changes in the reflection and transmission with surface contamination.

Kannajosyula, Lissenden and Rose [85] looked into the relationship between inhomogeneous (decaying, not true waves; evanescent or complex) interface waves in a thin layer embedded between two half spaces and Lamb waves. Inhomogeneous interface waves could be useful for adhesive joint inspection since they do not require a mode conversion technique to be generated. They considered the isotropic

case with aluminum substrates and an epoxy adhesive. The authors show that the interface waves are a special type of Lamb wave that is present in the general Lamb wave model above certain frequencies, and that the inhomogeneous interface waves are not necessarily inhomogeneous in a real plate. The regions where an inhomogeneous interface waves coincides with a Lamb wave mode could be useful for adhesive inspection since this type of Lamb wave can be excited by surface impingement and will not attenuate as quickly as the interface model suggests.

Castaings and Le Crom [75] used SH guided waves to infer the shear stiffness of adhesive bonds. A 1-D SAFE model is used to predict the dispersion curves for the first three SH guided waves. The direction of propagation is directed along a plane of symmetry, hence the separation of SH from the P and SV waves. The stacking sequence consists of a 3 mm aluminum plate, a 0.2 mm viscoelastic epoxy adhesive and a 1.2mm thick, 8 ply $[0, 90]_{2S}$ carbon epoxy patch. A shear spring model is implements at the interface between the adhesive and aluminum. COMSOL was used to implement SAFE. Numerical studies are performed to find the sensitivity to different changes in properties. Small changes in the density for each layer did not result in significant changes in the dispersion. Also, 15% changes in the bond thickness did not have a very significant impact. However, the thickness of the composite patch did have a significant impact on the SH2 mode between 0.7 and 1 MHz. Similarly, there was some sensitivity to the aluminum plate thickness. The SH2 mode is also highly sensitive to the aluminum and composite material properties, hindering the possible use for adhesive properties. In general, all of the SH modes are more sensitive to the aluminum and composite properties than the adhesive properties. The low frequency SH0 modes and the SH1 modes near the cut-off frequency are more sensitive to the adhesive properties. Experimental characterization was performed on a curing plate, and an inversion process was used to determine the adhesive properties.

Puthillath et al. [86] examined the existence of mode-pairs when a Lamb wave

is mode converted across a step, a doubler or lap joint for isotropic, aluminum adherends. The authors provided a good literature survey of the methods for understanding mode conversion and transmission at a step lap joint. This article also uses the wave structure matching coefficient to find good through transmission pairs. This is based on matching the mode shape and the phase velocity and frequency. The matching pairs are found by identifying two modes (one from each waveguide) which overlap on the phase velocity - frequency plot. Then the mode shapes are compared, finally identifying modes that have nearly identical mode shapes in the common layer. A hybrid conversion model is discussed which combines SAFE and normal mode expansion. SAFE is used to find the normal modes that exist at a given frequency for each wave guide. Then the normal mode expansion technique is used to find the modifying coefficient for each mode. Only modes which carry energy away from the junction are considered. The hybrid model showed that most of the energy goes into the matched-pair when they exist.

Puthillath et al. [87] investigated mode pairs for transmitting guided waves into bonded metal structures. The authors first compared the phase and group velocities of the guided waves in each waveguide at the same frequencies. If the velocities are close, then this forms a potential mode-pair. Next a correlation coefficient was used to evaluate the mode-pair potential.

$$\rho_{A_i B_j}|_{f,\Gamma} = \sum_{k=1}^{3} \frac{cov(u_k^{A_i}, u_k^{B_j})}{\sigma_{A_i}\sigma_{B_j}} \tag{5.2}$$

When unsymmetrical adhesive joints are considered, the number of mode-pairs tends to decrease. The transmission coefficients were calculated for the identified mode pairs; this was done using the method outlined in the author's own reference [86]. There was a good correlation between the transmission coefficients and the correlation coefficients.

Ren and Lissenden [66] investigated the transmission of a guided wave into an adhesive doubler from a single plate in order to inspect for interface defects. The

test structure was composed of two $[0/45/90/-45]_{2S}$ plates bonded with epoxy. The authors hypothesize that a guided mode with large in-plane displacement at the adhesive interface should be sensitive to interface defects, such as disbonds or kissing bonds. The phase velocity - frequency dispersion curve was calculated for the laminate and the curve color was varied with the intensity of the in-plane displacement at the two interfaces. Several modes were selected with large in-plane displacements, mode 8 at 0.75 MHz and mode 12 at 0.95 MHz. These modes must be generated through mode conversion from the single lamina outside of the doubler. In order to find appropriate modes for conversion, the phase velocities are compared so that the single lamina mode has a similar phase velocity to the desired laminate mode. Normal mode expansion and semi-analytical FE method are mentioned for finding the transmission coefficients, but no discussion or references are supplied. The authors use a wave structure matching scheme to find the best modes for mode conversion into the desired modes. The method works in the desired frequency âĂŞ phase velocity region, but not outside, when compared to the normal mode expansion. An effectiveness index is devised to compare the possible modes. The results shown only apply to the specified materials and geometry. Possibly interested in the wave structure matching scheme.

Chapter 6

Solution to Guided Wave Dispersion Equation

The analytical solution of guided waves in multi-layered isotropic and anisotropic media is derived in Chapter 4. The Chapter implements the GMM for solving guided waves in laminates, but the solution methods are also valid for the TMM, SMM and hybrid methods. The final system of homogeneous equations can be simplified to the form,

$$\mathbf{M}(\omega, \xi) \cdot \mathbf{x} = \mathbf{0} \tag{6.1}$$

where, $\mathbf{M}$ is the matrix that is dependent on the circular frequency, ω, and the wave number, ξ; $\mathbf{x}$ is a vector that may contain participation factors of potentials or coefficients, depending on the model; $\mathbf{0}$ is a vector of zeros as a result of the homogeneous equations.

A non-trivial solution to Eq. (6.1) exists when the matrix $\mathbf{M}$ is singular. Or, as is often taught, when the determinant is zero. There are several indicator for the existence of a singular matrix, and these are discussed in the next section.

One of the challenges in the solution to guided waves, is that the solution contains many modes. As a result, the full solution cannot be solved by a simple numerical root solving techniques; instead, an algorithm must be implemented in order to determine all roots in a desired domain. The first couple of sections discuss numerical methods for finding the roots of the analytical model. The third section derives a method of approximating Eq. (6.1) as a polynomial eigenvalue problem that is valid within a trust region. 'The fourth section derives an alternate approach based on the finite element method. The last two sections discuss the algorithms that can be used to

find all of the roots in a given domain.

6.1 Singular Matrix Indicators

The most direct solution is to determine the roots of the equation. The problem consists of a system of equations arranged in a matrix format. The roots exist when this matrix is singular, or when the determinant of the matrix is zero. For small matrices (2 - 4 rows), the determinant can be expanded analytically to generate an analytical equation. This is common in the Rayleigh-Lamb solution, interface wave solution, and any model that can be reduced to four or less boundary conditions.

When there are more than four boundary conditions, the analytical solution to the determinant becomes unwieldy. In this case, the numerical solution to the determinant is the best approach. The downside to this approach is that the numerical algorithm for expanding the determinant is undefined for a singular matrix; however, the root solving technique will not find the exact root, in which case the determinant is still defined. Care must be taken to ensure the matrix is balanced and normalized or the numerical solution can give inaccurate results. Additionally, the value of the determinant around a root may have very large values leading to the classic problem in numerical methods of small differences between large numbers.

There are alternative indications of a singular matrix that may be used in place or in addition to the determinant. The singular value decomposition (SVD) provides the singular values of the matrix, which are all positive real values. If one of the singular values is zero, the matrix is singular. The indicator is the minimum singular value. Additionally, the condition number can be used as an indicator. The 1-norm condition number may be used, but the 2-norm should be more stable because it used the SVD instead of inverse. The 2-norm condition number is defined below,

$$\kappa(\mathbf{M}) = \frac{\sigma_{max}(\mathbf{M})}{\sigma_{min}(\mathbf{M})} \tag{6.2}$$

where, σ_{max} is the maximum singular value and σ_{min} is the minimum singular value. When the matrix is singular, the condition number is infinite; therefore, it is best to use the reciprocal of the condition number so that the value approaches zero as the matrix tends towards a singular condition.

Also, the LU decomposition can also be used to find the singular matrix, although most of the numerical implementation are undefined for a singular matrix. The LU decomposition algorithm decomposes the matrix into the product of two triangular matrices. The determinant of this matrix product is the product of the determinant of each matrix. Additionally, the determinant of a triangular matrix is the product of the diagonal elements. The lower diagonal matrix has all ones along its diagonal; therefore, the determinant is one. As a result, the determinant of the initial matrix is calculated as the product of the diagonal elements of the upper triangular matrix. Again, if one of these diagonal elements is zero, the matrix is singular. Another approach is to calculate the product of the diagonal elements, but this is equivalent to calculating the determinant. The goal is to avoid the very large values generated by the determinant algorithm; often this is caused by very large elements within the LU decomposition. Using the smallest value can help to minimize this issue.

A final approach is to pose the problem as a linear eigenvalue problem. If the matrix is singular, at least one of the eigenvalues will be zero. In this case the minimum of the absolute value of the eigenvalues is used. In this case, there will be no zero crossings.

In the application of the methods above, the minimum of the absolute value is used as the indication. If a zero exists, then the minimum of the absolute value will be zero; however, this method does not give a positive or negative values.

6.2 Root Solving Schemes

6.2.1 Bracketing Method

Bracketing methods depend on finding the zero-crossing of the function. There are several techniques within this broad category, but they all depend on the existence of positive and negative values within the domain. The bracketing method also has the advantage that bounds are easily applied to the search, but the method is generally slower than open methods.

6.2.2 Newton's Method

Newton's method (or Newton-Raphson method) is an open method that depends on an initial guess. If the initial guess is not the root, then the slope at the initial guess is used to generate the next guess. This process is repeated until a sufficiently small function value is determined. The disadvantages of this method are that the search is not restricted to a given domain and local extrema can trap the search. The advantage is that the method is not restricted to zero crossings and can find double roots or roots to functions that do not contain negative values.

6.2.3 Modern Methods

Modern methods and root solving algorithms combine the bracketing and open methods, as well as implement optimization techniques. The MATLAB function fzero used bracket methods along with open methods to quickly converge on a solution; however, this function still requires zero crossings and is limited to one dimension problems.

The trust region-dogleg algorithm combines open methods with optimization techniques, and it does not require zero crossings. This algorithm is fast and efficient but requires a square system. This means that the number of dependent variable and the number of function outputs must be equal. For example, a two dimensional search

requires two function outputs.

If a non-square system must be used, the Levenberg-Marquardt algorithm is a suitable option. This type of algorithm is essentially the same as those used in optimization routines, but the algorithm checks the function to ensure that the result is not a local minimum.

Both of these algorithms are implemented in the MATLAB function fsolve. If a square system is input, then the trust region-dogleg algorithm is implements, otherwise the Levenberg-Marquardt algorithm is used. Fsolve has the advantage that no zero-crossings are required, non-square systems can be utilized, and complex outputs can also be handled. The disadvantage is that only an initial guess is provided, so the solution can move outside the desired domain.

6.2.4 Optimization Methods

As mentioned in the previous subsection, many modern methods use optimization techniques to search for roots. As a result, one option is to directly use optimization to find the roots of non-linear functions. Care must be taken to ensure that the solution is a root and not a minimum, but this is easily implements as a threshold.

6.3 Considerations for Complex Values

One important consideration that must be discussed is that the matrix elements are generally complex values; at times they may be purely real or imaginary. As a result, the effect of this on the singularity indicators must be considered. The SVD will only provide real values; while the remaining indicators provide complex values. The complex values can either be converted to an absolute value, or separated into real and imaginary components. Both the real and imaginary values must be zero for the existence of a singular matrix. If the absolute values is used, then there will be no zero-crossings. Also, some of the root solving algorithms can directly handle complex

values. If the complex value is separated into real and imaginary components, then the function will have two outputs. Another alternative is to use the phase of the complex value; there is greater discussion on this method in the coming sections.

6.4 Specific Approaches for Multi-dimensional Searches

This sections provides a bit more details as to how the root solving schemes can be used to find roots when the domain is one, two or three dimensions. If desired, many of the methods can be extended to n-dimension searches.

6.4.1 One Dimension

The one dimensional approach is required when searching along a single variable or when searching for either the real or imaginary component of one of the input variables. This problem poses a challenge for traditional root finding methods, since the function outputs a complex number while the input is a single real number. In other words, the function has two outputs but only one input.

The trust region-dogleg approach can be used for any of the singular matrix indicators that return either a real or complex value. A general optimization can be used if the indicators are converted to real values. If a bracket method is desired, there are two options that both depend on using the determinant. First, the problem is split up into two root searches; one for the real determinant and another for the imaginary determinant. Then, the solutions are compared and the matching solutions are the true solutions. Second, the complex determinant is expressed as magnitude and phase, and the change in phase is used as the "zero-crossing". In fact, the change in sign for real valued functions is a sub set of the change in phase method.

To prove this method, I will demonstrate the following four possible scenarios; a change in sign for a real or imaginary number, the change of a number from real to imaginary or imaginary to real, the change in sign of one component of a complex

number, and the change in sign of both components of a complex number. First, consider the change in sign of a real or imaginary number. In both cases there will be a phase difference of 180 degrees, as shown in Figure 6.1.

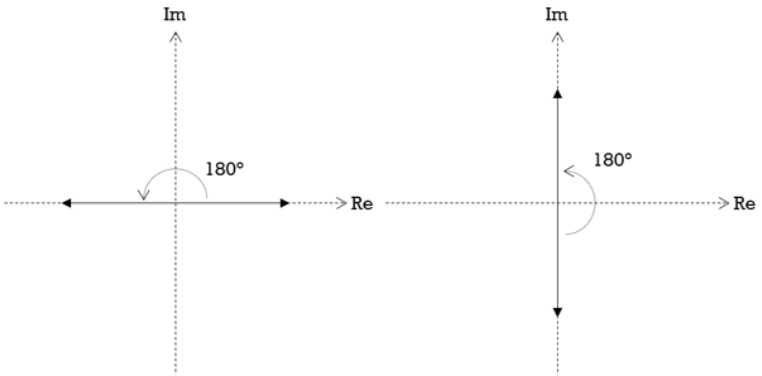

Figure 6.1: Phase change when the sign of a real or imaginary number changes

Next, consider the phase difference when a number changes from a real number into an imaginary number, and vice-verse. There will be a 90-degree difference between the phase of each vector, see Figure 6.2.

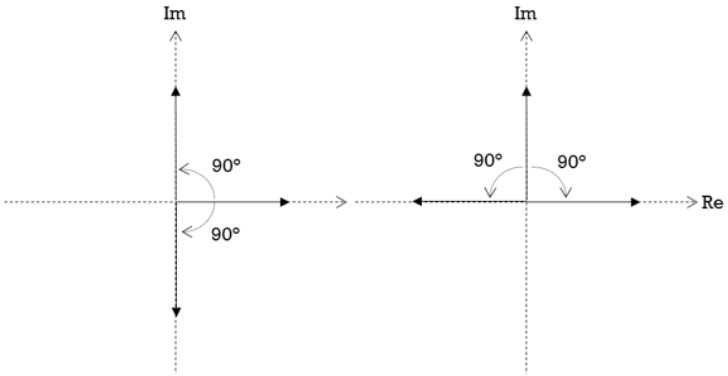

Figure 6.2: Phase change when an imaginary or real number changes into a real or imaginary number, respectively

The third scenario is when either the real or imaginary component of a complex number changes sign. Both cases result in a 90-degree phase change, as shown in Figure 6.3.

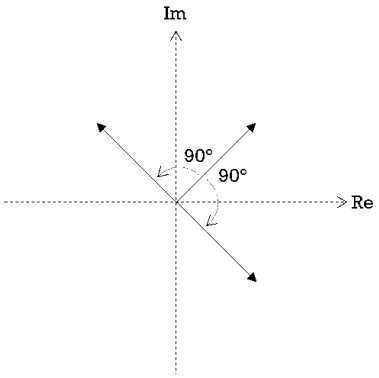

Figure 6.3: Phase change when a complex number changes the sign of either the real or imaginary component

The last scenario is when both components of a complex number change sign. This, or course, leads to a 180-degree phase shift, which is graphically demonstrated in Figure 6.4.

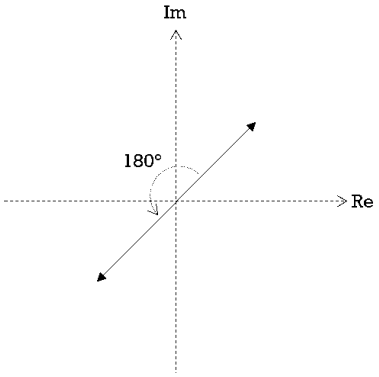

Figure 6.4: Phase change when both components of a complex root change sign

The change in sign of a number that is only real or imaginary and the change in sign of both real and imaginary components represent the obvious root existence scenarios, and they correspond to either a 180 degree phase shift or a movement to the opposite quadrant. The scenario of a real number changing to an imaginary number is less obvious, but it is still an indication of a root. This case is a 90 degree shift. Lastly, the change in sign of only one of the complex components does not indicate the presence of a root, unless this is a double root. In practice, this scenario is indicated by the shift of the value into an adjacent quadrant.

The challenge in applying this method is that both a change into the opposite quadrant, as well as a 90 or 180 degree phase shift are indicators of a root. This method could still be applied, but the previous techniques will be more reliable.

6.4.2 Two Dimensions

In two dimensions, the trust-region-dogleg algorithm requires an indicator with two outputs. This is accomplished by converting a complex indicator into real and imaginary components, or by using two indicators. The Levenberg-Marquardt algorithm can be used with any number of indicators, and a general optimization approach must have the indicators reduced to a single real value.

Again, if a bracketing method is desired the problem must be split into two separate root finding problems. Now a two dimensional array of points must be generated, and a sign change between any two points indicates a possible root. Poddar [88] devised an algorithm that generates a smooth plot between the node points and finds the intersection of the real and imaginary plots, then the process is repeated at the intersection with a more dense domain.

6.4.3 Three Dimensions

For a three dimension search, the trust region-dogleg, Levenberg-Marquardt or general optimization algorithms can be used. Poddar's [88] method could be extended to three dimensions, where the lines would be replaced by surfaces. However, the application of this approach may be prohibitively complicated with the intersecting surfaces.

6.5 Exploration of Partial Waves

In Chapter 4 the partial wave method of modeling guided waves in a plate was introduced, where it was shown that the general solution to Cauchy's momentum

equation can be expressed in the following form.

$$C_{ijkl}k_l k_j u_m = \rho\omega^2 u_i \tag{6.3}$$

We seek the solution for a guided wave along the x_1 direction, where the x_2 component is considered invariant. Therefore, we introduce the following expressions for the wavenumber vector, $\mathbf{k}$, and propagating direction phase velocity, v_p. This asssumes that we know the wavenumber vector component in the propagating direction, ξ_p, and the circular frequency, ω, and leaves the unknown scaling parameter, α, for the x_3 component.

$$\mathbf{k} = \xi_p \begin{Bmatrix} 1 & 0 & \alpha \end{Bmatrix}^T \tag{6.4}$$

$$v_p = \frac{\omega}{\xi_p} \tag{6.5}$$

Assuming at least monoclinic symmetry, combine Eq. (6.3), Eq. (6.4) and Eq. (6.5) and express in matrix form.

$$\begin{bmatrix} C_{11} - \rho v_p^2 + C_{55}\alpha^2 & C_{16} + C_{45}\alpha^2 & (C_{13} + C_{55})\alpha \\ C_{16} + C_{45}\alpha^2 & C_{66} - \rho v_p^2 + C_{44}\alpha^2 & (C_{36} + C_{45})\alpha \\ (C_{13} + C_{55})\alpha & (C_{36} + C_{45})\alpha & C_{55} - \rho v_p^2 + C_{55}\alpha^2 \end{bmatrix} \begin{Bmatrix} \hat{u}_1 \\ \hat{u}_2 \\ \hat{u}_3 \end{Bmatrix} = \begin{Bmatrix} 0 \\ 0 \\ 0 \end{Bmatrix} \tag{6.6}$$

This equation can be simplified into the following expression.

$$\left(\mathbf{A}_2\alpha^2 + \mathbf{A}_1\alpha + \mathbf{A}_0 - \mathbf{D}v_p^2\right) \cdot \hat{\mathbf{u}} = \mathbf{0} \tag{6.7}$$

where,

$$\mathbf{A}_2 = \begin{bmatrix} C_{55} & C_{45} & 0 \\ C_{45} & C_{44} & 0 \\ 0 & 0 & C_{33} \end{bmatrix} \tag{6.8}$$

$$\mathbf{A}_1 = \begin{bmatrix} 0 & 0 & C_{13} + C_{55} \\ 0 & 0 & C_{36} + C_{45} \\ C_{13} + C_{55} & C_{36} + C_{45} & 0 \end{bmatrix} \tag{6.9}$$

$$\mathbf{A}_0 = \begin{bmatrix} C_{11} & C_{16} & 0 \\ C_{16} & C_{66} & 0 \\ 0 & 0 & C_{55} \end{bmatrix} \tag{6.10}$$

$$\mathbf{D} = \begin{bmatrix} \rho & 0 & 0 \\ 0 & \rho & 0 \\ 0 & 0 & \rho \end{bmatrix} \tag{6.11}$$

If α is known, then the phase velocity, v_p, can be determined by solving the following linear eigenvalue problem, where there will be three solutions for v_p.

$$(\mathbf{M}_\alpha - \lambda \mathbf{I}) \cdot \hat{\mathbf{u}} = \mathbf{0} \tag{6.12}$$

where,

$$\begin{aligned} \lambda &= \rho v_p^2 \\ \mathbf{M}_\alpha &= \mathbf{A}_2\alpha^2 + \mathbf{A}_1\alpha + \mathbf{A}_0 \end{aligned} \tag{6.13}$$

Additionally, if the phase velocity, v_p, is known then α can be determined by solving the following polynomial eigenvalue problem, which has well known solutions. There will be six solutions for *alpha*, with three unique results with positive and negative terms.

$$\left(\mathbf{A}_2\alpha^2 + \mathbf{A}_1\alpha + \mathbf{M}_v\right) \cdot \hat{\mathbf{u}} = \mathbf{0} \tag{6.14}$$

where,

$$\mathbf{M}_v = \mathbf{A}_0 - \mathbf{D}v_p^2 \tag{6.15}$$

We can now find the v_p and α for a guided wave, but we also want to explore how these values affect the partial waves that combine to form the guided waves. Let's begin by revisiting the wavenumber vector. Eq. (6.4) represents the wavenumber vector in terms of the propagating wavenumber, ξ_p and scaling factor, α. We also know from section (insert reference) that the wavenumber vector for a bulk wave can be expressed as the wavenumber, ξ_b, multiplied by the normal vector of the wavefront.

$$\mathbf{k} = \xi_b \, \mathbf{n} \tag{6.16}$$

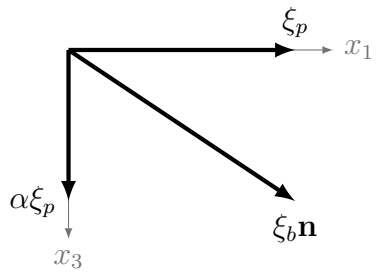

Figure 6.5: Wavenumber vector

Additionally, we defined the phase velocity of the bulk wave in the direction of the wavefront normal.

$$v_b = \frac{\omega}{\xi_b} \tag{6.17}$$

The two expressions for the wavenumber vector must be equivalent.

$$\xi_b \ \mathbf{n} = \xi_p \begin{Bmatrix} 1 & 0 & \alpha \end{Bmatrix}^T \tag{6.18}$$

In order for this expression to be true, the normal vector must have the following form.

$$\mathbf{n} = \frac{\begin{Bmatrix} 1 & 0 & \alpha \end{Bmatrix}^T}{\| \begin{Bmatrix} 1 & 0 & \alpha \end{Bmatrix}^T \|} = \frac{\begin{Bmatrix} 1 & 0 & \alpha \end{Bmatrix}^T}{\sqrt{1 + \alpha\bar{\alpha}}} \tag{6.19}$$

where,

$$\alpha\bar{\alpha} = |\alpha|^2 \tag{6.20}$$

Combining Eq. (6.18) and Eq. (6.19) with the phase velocity definitions.

$$\frac{\omega}{v_b} \frac{\begin{Bmatrix} 1 & 0 & \alpha \end{Bmatrix}^T}{\sqrt{1 + |\alpha|^2}} = \frac{\omega}{v_p} \begin{Bmatrix} 1 & 0 & \alpha \end{Bmatrix}^T \tag{6.21}$$

Reducing and rearranging terms results in the following equations for α and v_b.

$$\begin{aligned} |\alpha| &= \sqrt{\frac{v_p^2}{v_b^2} - 1} \\ v_b &= \sqrt{\frac{v_p^2}{|\alpha|^2 + 1}} \end{aligned} \tag{6.22}$$

Therefore,

$$\frac{v_p^2}{v_b^2} \geq 1$$
$$v_p \geq v_b \tag{6.23}$$

This implies that the bulk waves are not present when the propagating velocity is below the bulk velocity. However, the eigenvalue problem does not change, i.e. still has the same number of results. Therefore, a new type of wave must exist for these velocities.

One option is to use Eq. (6.14) to solve for all value of α for a given v_p in order to calculate v_b through Eq. (6.22). This will lead to ever smaller bulk velocities as the propagating phase velocity decreases. This result is incorrect, because the phase velocity was defined for a real wavenumber vector, not a complex one. Therefore, the derivation of phase velocity must be revisited.

Reintroduce the harmonic wave solution,

$$\mathbf{u} = \mathbf{p}e^{i(\mathbf{k}\cdot\mathbf{r}-\omega t)} \tag{6.24}$$

The definition of phase velocity is a constant phase,

$$e^{i\theta} = constant \rightarrow \theta = constant \tag{6.25}$$

and there is no change in phase over time,

$$\frac{d\theta}{dt} = 0 = \frac{d(\mathbf{k}\cdot\mathbf{r})}{dt} - \omega \tag{6.26}$$

The wavenumber vector is constant; therefore,

$$\frac{d(\mathbf{k}\cdot\mathbf{r})}{dt} = \mathbf{k}\cdot\frac{d\mathbf{r}}{dt} \tag{6.27}$$

Wavenumber vector can be expressed as a normal vector, called the wavefront normal, multiplied by a scaling factor, k, the wavenumber.

$$\mathbf{k} = k\mathbf{n} \tag{6.28}$$

Combining these equations,

$$\mathbf{n} \cdot \frac{d\mathbf{r}}{dt} = \frac{\omega}{k} \tag{6.29}$$

Introduce a term for the projection of the distance of wave travel onto the wave normal.

$$\xi = \mathbf{n} \cdot \mathbf{r} \tag{6.30}$$

Now, we have the definition of phase velocity,

$$v_p = \frac{d\xi}{dt} = \frac{\omega}{k} \tag{6.31}$$

What if the wavenumber vector is complex?

$$\mathbf{k} = \mathbf{k}^R + i\mathbf{k}^I \tag{6.32}$$

Again, introduce the wavefront normal.

$$\mathbf{k} = k^R\mathbf{n}^R + ik^I\mathbf{n}^I \tag{6.33}$$

The complex wavenumber vector slightly changes the harmonic wave solution.

$$\mathbf{u} = \mathbf{p}e^{-k^I\mathbf{n}^I\cdot\mathbf{r}}e^{i(k^R\mathbf{n}^R\cdot\mathbf{r}-\omega t)} \tag{6.34}$$

It should be clear from this equation that only the real component of the wavenumber vector contributes to the phase in the equation. The imaginary components only modify the amplitude as a function of position. Therefore,

$$\theta = k^R\mathbf{n}^R \cdot \mathbf{r} - \omega t \tag{6.35}$$

Following the same procedure, and adding the new definition of ξ,

$$\xi = \mathbf{n}^R \cdot \mathbf{r} \tag{6.36}$$

The phase velocity for a complex wavenumber is determined.

$$v_p = \frac{d\xi}{dt} = \frac{\omega}{k^R} \tag{6.37}$$

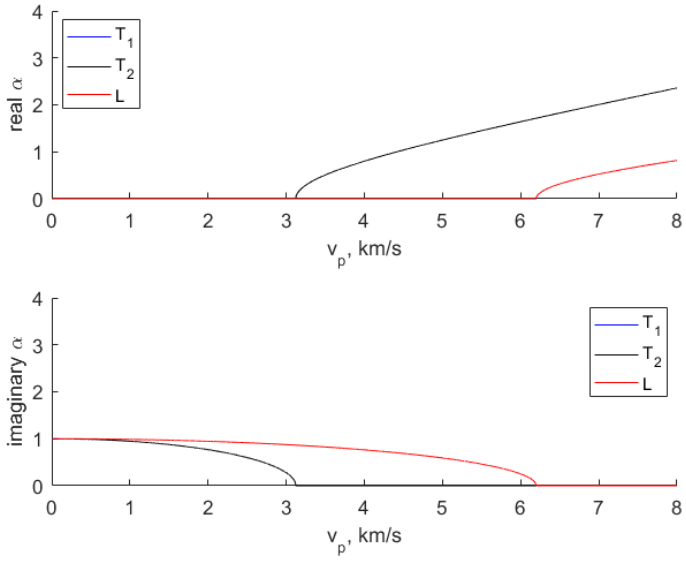

Figure 6.6: Positive α values for an isotropic material with respect to v_p

Revisiting the guided wave problem, when the propagating phase velocity is less than at least one of the bulk phase velocities, at least one unique value for α becomes imaginary. As a result, the phase velocity of this new "bulk" wave is equal to the propagating phase velocity of the guided wave. This discussion should serve as proof that a new unique set of "bulk" waves exist when the wavenumber vector components are allowed to contain complex values.

Let's explore this relation by calculating the alpha values for an isotropic media. The material properties are as follows.

$$E = 70 \text{ GPa}$$

$$\nu = 0.33$$

$$\rho = 2700 \ \frac{\text{kg}}{\text{m}^3}$$

Figure 6.6 shows the variation of the α values with v_p. Only the positive values are shown. There are two results for the transverse waves that are identical. The results are as expected, where α is imaginary when $v_p < v_b$ and real when $v_p > v_b$. Also, the alpha values match the equation from the Rayleigh-Lamb solution.

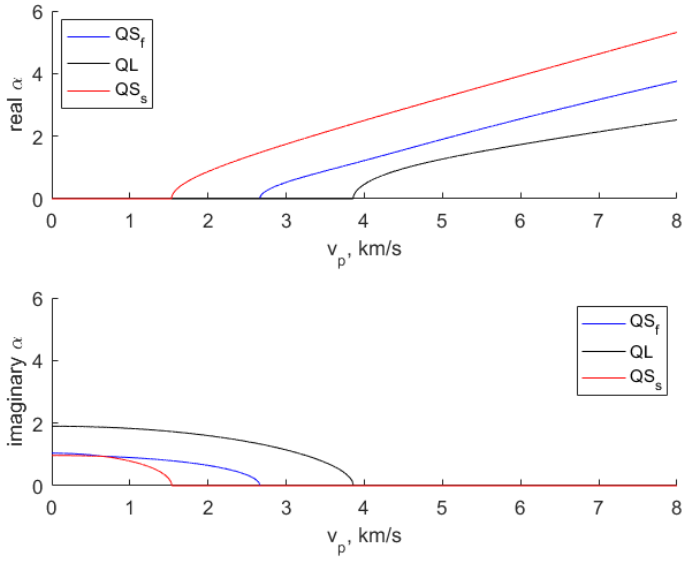

Figure 6.7: Positive α values for a monoclinic material with respect to v_p

Now, will this trend continue for a monoclinic material. At the beginning of this section it was stated that these equations work for materials with at least monoclinic symmetry. In order to test this trend, let's consider an orthotropic material with the following properties.

$$\mathbf{C} = \begin{bmatrix} 143.8 & 6.2 & 6.2 & 0 & 0 & 0 \\ & 13.3 & 6.5 & 0 & 0 & 0 \\ & & 13.3 & 0 & 0 & 0 \\ & & & 3.4 & 0 & 0 \\ & & & & 5.7 & 0 \\ & & & & & 5.7 \end{bmatrix} \text{ GPa}$$

$$\rho = 1560 \ \frac{\text{kg}}{\text{m}^3}$$

These properties correspond to a unidirectional fiber reinforced plastic. The fibers are oriented along the $\bar{x}_1$ direction. The monoclininc symmetry is formed by rotating $\bar{x}_3$ $+70°$ so that a $70°$ angle is formed between $\bar{x}_1$ and x_1. The stiffness matrix in the unbarred coordinate system is used, where the new stiffness components are

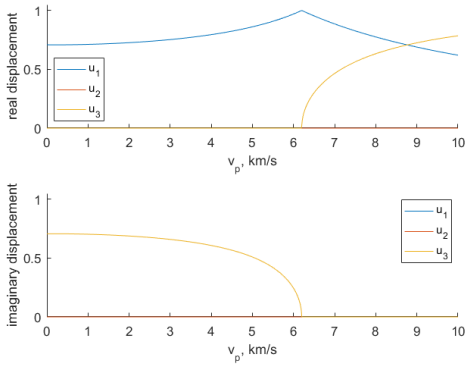

(a) pressure wave

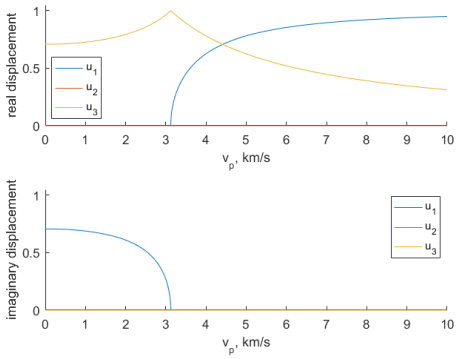

(b) shear vertical wave

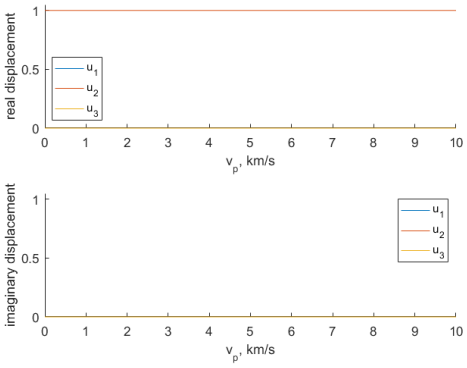

(c) shear horizontal wave

Figure 6.8: particle displacement, u, with respect to v_p

calculated through a transformation. Since the propagating wave is not traveling along a plane of symmetry, we expect to see three unique alpha values.

Figure 6.7 shows the variation of the α values with v_p for the monoclinic media. The black lines correspond to the quasi-longitudinal wave, QL; the red lines correspond to the slow quasi-shear wave, QS_s; and the blue lines correspond to the fast quasi-shear wave, QS_f.

The behavior of these waves can be better understood through the analysis of the particle displacement vectors. The displacement vectors for each type of wave have been plotted against the propagating velocity for the isotropic media. Figure 6.8 shows the pressure, shear vertical and shear horizontal wave displacement vectors.

These figures prove that the wavefront normal definition in Eq. (6.19) is correct.

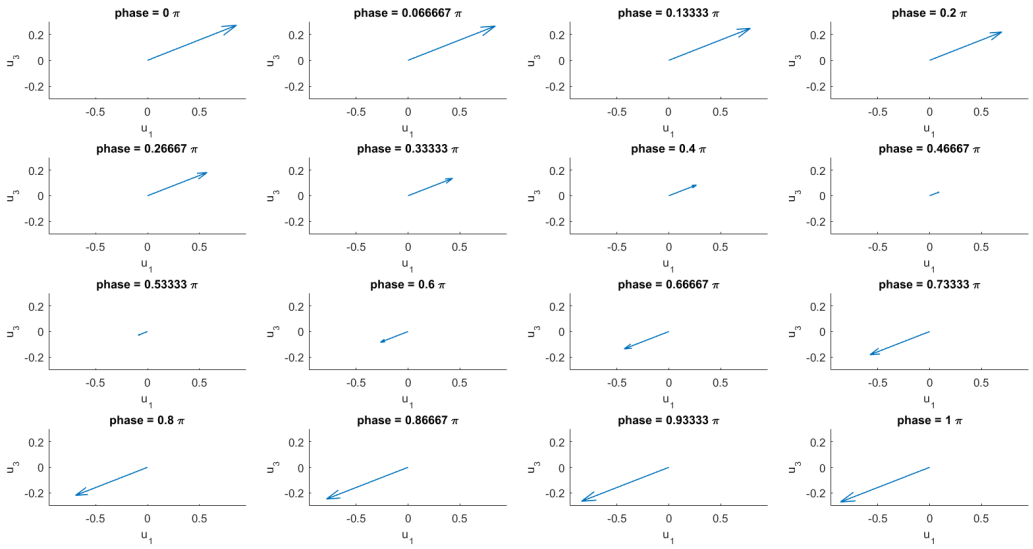

Figure 6.9: Isotropic pressure wave particle displacement with varying phase, $v_p = 6.5$ km/s, $\alpha = 0.316$

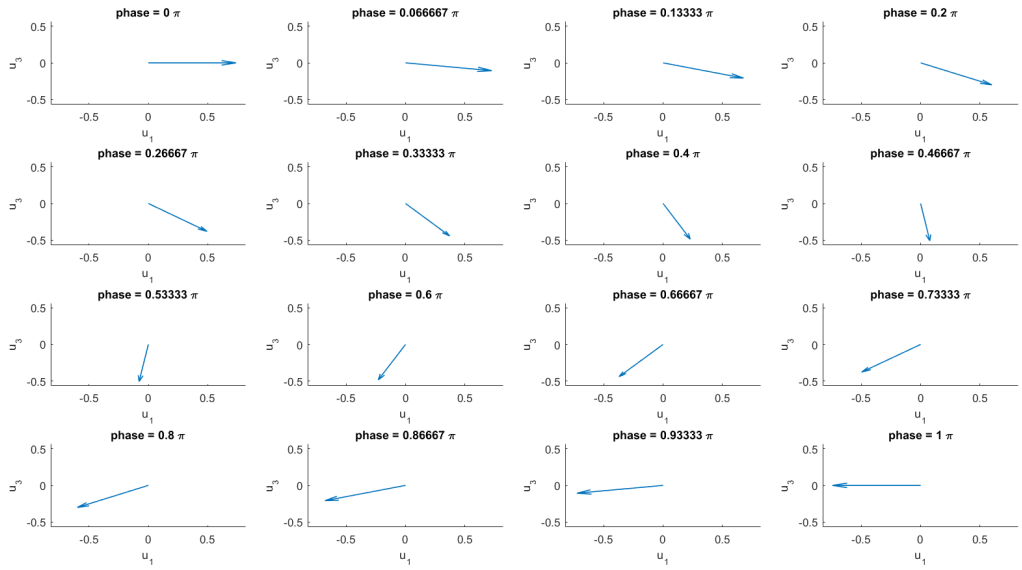

Figure 6.10: Isotropic pressure wave particle displacement with varying phase, $v_p = 4.5$ km/s, $\alpha = 0.6876$i

The alpha values can be used to find the wavefront normal vector, which is used in the eigenvalue equation to determine the bulk velocity, v_b. They also show that one of the displacement components becomes imaginary for the P and SV waves when v_p is less than c_b. This will lead to rotation of the displacement vector, as opposed to a vibration. As the imaginary α increases the motion becomes more of a rotation with less vibration. This change is demonstrated in Figure 6.9 and Figure 6.10.

6.6 Semi-Analytical Solution (Trust Region Scheme)

There are major difficulties encountered in the previous approach: the numerical calculation of the determinant of a large, poorly conditioned matrix; and distinguishing between multiple closely spaced or overlapping modes. One way of avoiding the use of determinants is to use the Taylor's series to approximate the exponential as a second order polynomial. This will allow the problem to be expressed as a polynomial eigenvalue problem, which has well known solutions. The solution of eigenvalue problem provides both the location of the root and the mode shape in a single operation. The eigenvalue solution also provides all of the solutions when roots overlap, or double roots. The following sub-sections discuss the development of this approach for several classes of problems.

6.6.1 Searching along a given phase velocity

Since the problem of guided waves in layered orthotropic plates can be divided into two sequential eigenvalue problems, see Chapter 4, it is possible to separate the two unknowns. The phase velocity, v, must be specified in the first eigenvalue problem. This will provide α and $\mathbf{U}$ for each lamina. The second eigenvalue problem now only depends on either ξ or ω. In the following derivation, phase velocity and wavenumber are selected as the independent variables. In order to derive this method, the state vector must be redefined in a new more compact description. First, define a new

matrix,

$$\mathbf{F}(\xi, \boldsymbol{\alpha}, x_3) = \begin{bmatrix} e^{i\xi\alpha_1 x_3} & 0 & 0 \\ 0 & \ddots & 0 \\ 0 & 0 & e^{i\xi\alpha_6 x_3} \end{bmatrix} \tag{6.38}$$

which is a diagonal matrix of exponential functions with the x_3 component of the partial waves. Now, the field matrix, from Chapter 4 can be redefined. First the displacement field matrix,

$$\mathbf{B}^u(x_3) = \mathbf{U} \cdot \mathbf{F}(x_3) = \hat{\mathbf{B}}^u \cdot \mathbf{F}(x_3) \tag{6.39}$$

Similarly, the traction field matrix,

$$\mathbf{B}^\sigma(x_3) = i\xi \left[\mathbf{S}_1 \cdot \mathbf{U} + \mathbf{S}_2 \cdot \mathbf{U} \cdot \mathbf{A}\right] \cdot \mathbf{F} = \hat{\mathbf{B}}^\sigma \cdot \mathbf{F}(x_3) \tag{6.40}$$

where,

$$\mathbf{S}_1 = \begin{bmatrix} C_{13} & C_{36} & 0 \\ 0 & 0 & C_{45} \\ 0 & 0 & C_{55} \end{bmatrix} \tag{6.41}$$

$$\mathbf{S}_2 = \begin{bmatrix} 0 & 0 & C_{33} \\ C_{45} & C_{44} & 0 \\ C_{55} & C_{45} & 0 \end{bmatrix} \tag{6.42}$$

$$\mathbf{A} = \begin{bmatrix} \alpha_1 & 0 & 0 \\ 0 & \ddots & 0 \\ 0 & 0 & \alpha_6 \end{bmatrix} \tag{6.43}$$

Finally, redefine the complete state vector.

$$\mathbf{z}(x_3) = \begin{Bmatrix} \hat{\mathbf{u}}(x_3) \\ \hat{\boldsymbol{\sigma}}(x_3) \end{Bmatrix} = \begin{bmatrix} \mathbf{B}^u(x_3) \\ \mathbf{B}^\sigma(x_3) \end{bmatrix} \cdot \boldsymbol{\eta} = \begin{bmatrix} \hat{\mathbf{B}}^u \\ \hat{\mathbf{B}}^\sigma \end{bmatrix} \cdot \mathbf{F}(x_3) \cdot \eta = \hat{\mathbf{B}} \cdot \mathbf{F}(x_3) \cdot \boldsymbol{\eta} \tag{6.44}$$

The new definition of the state vector is used to redefine the global matrix, as shown in Chapter 4, Eq. (4.80).

$$\begin{bmatrix} \hat{\mathbf{B}}_1^{\sigma} \cdot \mathbf{F}_1(0) & 0 & 0 & \cdots & 0 & 0 \\ \hat{\mathbf{B}}_1 \cdot \mathbf{F}_1(h_1) & -\hat{\mathbf{B}}_2 \cdot \mathbf{F}_2(0) & 0 & \cdots & 0 & 0 \\ 0 & \hat{\mathbf{B}}_2 \cdot \mathbf{F}_2(h_2) & -\hat{\mathbf{B}}_3 \cdot \mathbf{F}_3(0) & \ddots & \vdots & \vdots \\ \vdots & \vdots & \ddots & \ddots & -\hat{\mathbf{B}}_{N-1} \cdot \mathbf{F}_{N-1}(0) & 0 \\ 0 & 0 & \cdots & \cdots & \hat{\mathbf{B}}_{N-1} \cdot \mathbf{F}_{N-1}(h_{N-1}) & -\hat{\mathbf{B}}_N \cdot \mathbf{F}_N(0) \\ 0 & 0 & \cdots & \cdots & 0 & \hat{\mathbf{B}}_N^{\sigma} \cdot \mathbf{F}_N(h_N) \end{bmatrix} \cdot \boldsymbol{\eta} = \mathbf{0} \quad (6.45)$$

There is currently no analytical solution to this eigenvalue problem. This is due to the fact that there will be infinite solutions because of the harmonic nature of the problem. However, there are solutions for polynomial eigenvalue problems. If we restrict the solution to a finite range of wavenumbers, then Taylor's series can be used to approximate the exponential in this range. The approximation to this exponential is shown below for a second order approximation near the given wavenumber, a.

$$\begin{aligned} e^{i\xi\alpha_n x_3} &= e^{i\alpha_n x_3 a}\left[1 + i\alpha_n x_3(\xi - a) - \tfrac{\alpha_n^2 x_3^2}{2}(\xi - a)^2\right] \\ &= e^{i\alpha_n x_3 a}\left[1 - i\alpha_n x_3 a - \tfrac{\alpha_n^2 x_3^2 a^2}{2} + (i\alpha_n x_3 + \alpha_n^2 x_3^2 a)\xi - \tfrac{\alpha_n^2 x_3^2}{2}\xi^2\right] \end{aligned} \quad (6.46)$$

Redefine $\mathbf{F}$ as a polynomial in terms of ξ with initial guess a,

$$\mathbf{F}(x_3) \approx \hat{\mathbf{F}}(x_3, a) = \hat{\mathbf{F}}^{(0)} + \hat{\mathbf{F}}^{(1)}\xi + \hat{\mathbf{F}}^{(2)}\xi^2 \quad (6.47)$$

where the new sub-matrices are shown below.

$$\hat{\mathbf{F}}^{(0)}(x_3, a) = \begin{bmatrix} e^{i\alpha_1 x_3 a}(1 - i\alpha_1 x_3 a - \frac{\alpha_1^2 x_3^2 a^2}{2}) & 0 & 0 \\ 0 & \ddots & 0 \\ 0 & 0 & e^{i\alpha_6 x_3 a}(1 - i\alpha_6 x_3 a - \frac{\alpha_6^2 x_3^2 a^2}{2}) \end{bmatrix} \quad (6.48)$$

$$\hat{\mathbf{F}}^{(1)}(x_3, a) = \begin{bmatrix} e^{i\alpha_1 x_3 a}(i\alpha_1 x_3 + \alpha_1^2 x_3^2 a) & 0 & 0 \\ 0 & \ddots & 0 \\ 0 & 0 & e^{i\alpha_6 x_3 a}(i\alpha_6 x_3 + \alpha_6^2 x_3^2 a) \end{bmatrix} \quad (6.49)$$

$$\hat{\mathbf{F}}^{(2)}(x_3,a)=\begin{bmatrix} e^{i\alpha_1 x_3 a\left(\frac{-\alpha_1^2 x_3^2}{2}\right)} & 0 & 0 \\ 0 & \ddots & 0 \\ 0 & 0 & e^{i\alpha_6 x_3 a\left(\frac{-\alpha_6^2 x_3^2}{2}\right)} \end{bmatrix} \tag{6.50}$$

The state vector is now redefined in terms of the new Taylor's series approximation.

$$\boldsymbol{z}(x_3)=\hat{\mathbf{B}}\cdot(\hat{\mathbf{F}}^{(0)}+\hat{\mathbf{F}}^{(1)}\bar{\xi}+\hat{\mathbf{F}}^{(2)}\bar{\xi}^2)\cdot\boldsymbol{\eta}=(\hat{\mathbf{B}}\cdot\hat{\mathbf{F}}^{(0)}+\hat{\mathbf{B}}\cdot\hat{\mathbf{F}}^{(1)}\xi+\hat{\mathbf{B}}\cdot\hat{\mathbf{F}}^{(2)}\xi^2)\cdot\boldsymbol{\eta} \tag{6.51}$$

The new method can be applied to the GMM approach; combining Eq. (6.45) and Eq. (6.51),

$$(\mathbf{M}_0+\mathbf{M}_1\xi+\mathbf{M}_2\xi^2)\cdot\boldsymbol{\eta}=\mathbf{0} \tag{6.52}$$

where the sub matrices of $\mathbf{M}$ are defined as follows.

$$\mathbf{M}_k=\begin{bmatrix} \hat{\mathbf{B}}_1^{\sigma}\cdot\hat{\mathbf{F}}_1^{(k)}(0) & 0 & 0 & \cdots & 0 & 0 \\ \hat{\mathbf{B}}_1\cdot\hat{\mathbf{F}}_1^{(k)}(h_1) & -\hat{\mathbf{B}}_2\cdot\hat{\mathbf{F}}_2^{(k)}(0) & 0 & \cdots & 0 & 0 \\ 0 & \hat{\mathbf{B}}_2\cdot\hat{\mathbf{F}}_2^{(k)}(h_2) & -\hat{\mathbf{B}}_3\cdot\hat{\mathbf{F}}_3^{(k)}(0) & \ddots & \vdots & \vdots \\ \vdots & \vdots & \ddots & \ddots & -\hat{\mathbf{B}}_{N-1}\cdot\hat{\mathbf{F}}_{N-1}^{(k)}(0) & 0 \\ 0 & 0 & \cdots & \cdots & \hat{\mathbf{B}}_{N-1}\cdot\hat{\mathbf{F}}_{N-1}^{(k)}(h_{N-1}) & -\hat{\mathbf{B}}_N\cdot\hat{\mathbf{F}}_N^{(k)}(0) \\ 0 & 0 & \cdots & \cdots & 0 & \hat{\mathbf{B}}_N^{\sigma}\cdot\hat{\mathbf{F}}_N^{(k)}(h_N) \end{bmatrix} \tag{6.53}$$

Now the wavenumbers in the desired range are found through the polynomial eigenvalue function,

$$[\mathbf{I},\boldsymbol{\xi}]=polyeig(\mathbf{M}_0,\mathbf{M}_1,\mathbf{M}_2) \tag{6.54}$$

where $\mathbf{I}$ is a matrix containing the participation factors for each layer and eigenvalue, and $\boldsymbol{\xi}$ is a vector of the eigenvalues, which are the potential values of ξ.

6.6.2 Thickness-wise standing waves

In the previous section, the phase velocity is first given before the wavenumbers can be found. This method will not produce the modes when the wavenumber is zero, which results in an infinite phase velocity. As a result, a similar process has been devised for this special case. First the wavenumber vector must be defined.

$$\mathbf{k}=\begin{Bmatrix} 0 & 0 & k_3 \end{Bmatrix} \tag{6.55}$$

Combine Eq. (4.57) and Eq. (6.55).

$$\left(\begin{bmatrix} C_{55} & C_{45} & 0 \\ C_{45} & C_{44} & 0 \\ 0 & 0 & C_{33} \end{bmatrix} k_3^2 - \begin{bmatrix} \rho\omega^2 & 0 & 0 \\ 0 & \rho\omega^2 & 0 \\ 0 & 0 & \rho\omega^2 \end{bmatrix} \right) \begin{Bmatrix} \hat{u}_1 \\ \hat{u}_2 \\ \hat{u}_3 \end{Bmatrix} = \begin{Bmatrix} 0 \\ 0 \\ 0 \end{Bmatrix} \tag{6.56}$$

Introduce β as a scaling coefficient for the wavenumber.

$$k_3^{(j)} = \beta^{(j)}\omega \rightarrow \beta^{(j)} = \frac{k_3^{(j)}}{\omega} \tag{6.57}$$

Combine Eq. (6.56) and Eq. (6.57) then rearrange the terms,

$$(\mathbf{A}_0 + \beta^2 \mathbf{A}_2) \cdot \hat{\mathbf{u}} = \mathbf{0} \tag{6.58}$$

where,

$$\mathbf{A}_2 = \begin{bmatrix} C_{55} & C_{45} & 0 \\ C_{45} & C_{44} & 0 \\ 0 & 0 & C_{33} \end{bmatrix} \tag{6.59}$$

$$\mathbf{A}_0 = \begin{bmatrix} -\rho & 0 & 0 \\ 0 & -\rho & 0 \\ 0 & 0 & -\rho \end{bmatrix} \tag{6.60}$$

Follow Eq. (6.38) and redefine in terms of β and ω.

$$\mathbf{F}(x_3) = \begin{bmatrix} e^{i\beta_1\omega x_3} & 0 & 0 \\ 0 & \ddots & 0 \\ 0 & 0 & e^{i\beta_6\omega x_3} \end{bmatrix} \tag{6.61}$$

Define the independent displacement and traction field matrices.

$$\hat{\mathbf{B}}^u = \mathbf{U} \tag{6.62}$$

$$\hat{\mathbf{B}}^\sigma = i\omega \begin{bmatrix} 0 & 0 & C_{33} \\ C_{45} & C_{44} & 0 \\ C_{55} & C_{45} & 0 \end{bmatrix} \cdot \mathbf{U} \cdot \begin{bmatrix} \beta_1 & 0 & 0 \\ 0 & \ddots & 0 \\ 0 & 0 & \beta_6 \end{bmatrix} \tag{6.63}$$

Once again use a second order Taylor's series to approximate the exponentials.

$$e^{i\beta_n \omega x_3} = e^{i\beta_n x_3 a}\left[1 + i\beta_n x_3(\omega - a) - \tfrac{\beta_n^2 x_3^2}{2}(\omega - a)^2\right] \tag{6.64}$$

Redefine Eq. (6.61) in terms of Eq. (6.64),

$$\mathbf{F}(x_3) \approx \hat{\mathbf{F}}(x_3, a) = \hat{\mathbf{F}}^{(0)} + \hat{\mathbf{F}}^{(1)}\omega + \hat{\mathbf{F}}^{(2)}\omega^2 \tag{6.65}$$

where,

$$\hat{\mathbf{F}}^{(0)}(x_3, a) = \begin{bmatrix} e^{i\beta_1 x_3 a}(1 - i\beta_1 x_3 a - \frac{\beta_1^2 x_3^2 a^2}{2}) & 0 & 0 \\ 0 & \ddots & 0 \\ 0 & 0 & e^{i\beta_6 x_3 a}(1 - i\beta_6 x_3 a - \frac{\beta_6^2 x_3^2 a^2}{2}) \end{bmatrix} \tag{6.66}$$

$$\hat{\mathbf{F}}^{(1)}(x_3, a) = \begin{bmatrix} e^{i\beta_1 x_3 a}(i\beta_1 x_3 + \beta_1^2 x_3^2 a) & 0 & 0 \\ 0 & \ddots & 0 \\ 0 & 0 & e^{i\beta_6 x_3 a}(i\beta_6 x_3 + \beta_6^2 x_3^2 a) \end{bmatrix} \tag{6.67}$$

$$\hat{\mathbf{F}}^{(1)}(x_3, a) = \begin{bmatrix} e^{i\beta_1 x_3 a}(\frac{-\beta_1^2 x_3^2}{2}) & 0 & 0 \\ 0 & \ddots & 0 \\ 0 & 0 & e^{i\beta_6 x_3 a}(\frac{-\beta_6^2 x_3^2}{2}) \end{bmatrix} \tag{6.68}$$

The GMM approach is again used with a polynomial expression for the circular frequency. The sub-matrices are equivalent to those in Eq. (6.53).

$$(\mathbf{M}_0 + \mathbf{M}_1\omega + \mathbf{M}_2\omega) \cdot \boldsymbol{\eta} = \mathbf{0} \tag{6.69}$$

The final solution is determined through the polynomial eigenvalue function.

$$[\mathbf{I}, \boldsymbol{\omega}] = polyeig(\mathbf{M}_0, \mathbf{M}_1, \mathbf{M}_2) \tag{6.70}$$

6.7 Finite Element Scheme

Another numerical approach which avoids the issues of root solving is to use the finite element method. The plane harmonic wave is described with the use of an

exponential. When applying boundary conditions through the thickness of the plate, the exponentials often become either very large or very small leading to numerical issues in the calculation of the determinant. The finite element method can be used to describe the displacements and stresses through the thickness of the plate, avoiding the problems with the exponentials. In order for the solution to be accurate, the number of elements must be sufficiently large.

We begin with Cauchy's equation where we have ignored the contribution from body forces.

$$\frac{\partial \sigma_{ij}}{\partial x_j} = \rho \ddot{u}_i \tag{6.71}$$

Once again we consider a harmonic guided wave propagating along the x_1 direction. The wave front is plane with the x_2 invariant condition; Therefore, we can simplify Eq. (6.71).

$$\begin{aligned} \frac{\partial \sigma_{11}}{\partial x_1} + \frac{\partial \sigma_{13}}{\partial x_3} &= \rho \ddot{u}_1 \\ \frac{\partial \sigma_{12}}{\partial x_1} + \frac{\partial \sigma_{23}}{\partial x_3} &= \rho \ddot{u}_2 \\ \frac{\partial \sigma_{31}}{\partial x_1} + \frac{\partial \sigma_{33}}{\partial x_3} &= \rho \ddot{u}_3 \end{aligned} \tag{6.72}$$

The solution has the following form.

$$\begin{aligned} u_i(\mathbf{x}, t) &= \hat{u}_i(x_3) e^{i(\xi x_1 - \omega t)} \\ \frac{\partial u_i}{\partial t} &= -i\omega \hat{u}_i e^{i(\xi x_1 - \omega t)} \\ \frac{\partial u_i}{\partial x_1} &= i\xi \hat{u}_i e^{i(\xi x_1 - \omega t)} \\ \frac{\partial u_i}{\partial x_2} &= 0 \\ \frac{\partial u_i}{\partial x_3} &= \frac{d\hat{u}_i}{dx_3} e^{i(\xi x_1 - \omega t)} \end{aligned} \tag{6.73}$$

We can now convert this system of equations into a weighted residual statement.

$$\begin{aligned} \int_{x_A}^{x_B} w \left[\tfrac{\partial \sigma_{11}}{\partial x_1} + \tfrac{\partial \sigma_{13}}{\partial x_3} - \rho \ddot{u}_1 \right] dx_3 = 0 \\ \int_{x_A}^{x_B} w \left[\tfrac{\partial \sigma_{12}}{\partial x_1} + \tfrac{\partial \sigma_{23}}{\partial x_3} - \rho \ddot{u}_2 \right] dx_3 = 0 \\ \int_{x_A}^{x_B} w \left[\tfrac{\partial \sigma_{31}}{\partial x_1} + \tfrac{\partial \sigma_{33}}{\partial x_3} - \rho \ddot{u}_3 \right] dx_3 = 0 \end{aligned} \tag{6.74}$$

We wish to transfer part of the derivation to the weighting function. This will provide two benefits. First, it will reduce the requirements on the weighting function. Second, this will impart boundary conditions into the weighted residual statement. This is accomplished by applying integration by parts.

$$\begin{aligned}
&\int_{x_A}^{x_B} -\frac{dw}{dx_3}\sigma_{13} + w[\frac{\partial \sigma_{11}}{\partial x_1} - \rho\ddot{u}_1]dx_3 + w(x_B)\sigma_{13}(x_B) - w(x_A)\sigma_{13}(x_A) = 0 \\
&\int_{x_A}^{x_B} -\frac{dw}{dx_3}\sigma_{23} + w[\frac{\partial \sigma_{12}}{\partial x_1} - \rho\ddot{u}_2]dx_3 + w(x_B)\sigma_{23}(x_B) - w(x_A)\sigma_{23}(x_A) = 0 \\
&\int_{x_A}^{x_B} -\frac{dw}{dx_3}\sigma_{33} + w[\frac{\partial \sigma_{31}}{\partial x_1} - \rho\ddot{u}_3]dx_3 + w(x_B)\sigma_{33}(x_B) - w(x_A)\sigma_{33}(x_A) = 0
\end{aligned} \tag{6.75}$$

Each lamina has at least monoclinic symmetry, where $\mathbf{C}$ is the fiber orientation dependent stiffness matrix. The stress-strain equations with x_2 invariance is shown below.

$$\begin{Bmatrix} \sigma_{11} \\ \sigma_{22} \\ \sigma_{33} \\ \sigma_{23} \\ \sigma_{31} \\ \sigma_{12} \end{Bmatrix} = \begin{bmatrix} C_{11} & C_{12} & C_{13} & 0 & 0 & C_{16} \\ & C_{22} & C_{23} & 0 & 0 & C_{26} \\ & & C_{33} & 0 & 0 & C_{36} \\ & & & C_{44} & C_{45} & 0 \\ & Sym & & & C_{55} & 0 \\ & & & & & C_{66} \end{bmatrix} \begin{Bmatrix} u_{1,1} \\ 0 \\ u_{3,3} \\ u_{2,3} \\ u_{3,1} + u_{1,3} \\ u_{2,1} \end{Bmatrix} \tag{6.76}$$

Combining Eq. (6.75) and Eq. (6.76).

$$\begin{aligned}
&\int_{x_A}^{x_B} -\frac{dw}{dx_3}(C_{55}\frac{\partial u_1}{\partial x_3} + C_{45}\frac{\partial u_2}{\partial x_3} + C_{55}\frac{\partial u_3}{\partial x_1}) \\
&+ w[\frac{\partial}{\partial x_1}(C_{11}\frac{\partial u_1}{\partial x_1} + C_{16}\frac{\partial u_2}{\partial x_1} + C_{16}\frac{\partial u_3}{\partial x_3}) - \rho\ddot{u}_1]dx_3 \\
&+ w(x_B)\sigma_{31}(x_B) - w(x_A)\sigma_{31}(x_A) = 0
\end{aligned} \tag{6.77}$$

$$\begin{aligned}
&\int_{x_A}^{x_B} -\frac{dw}{dx_3}(C_{45}\frac{\partial u_1}{\partial x_3} + C_{44}\frac{\partial u_2}{\partial x_3} + C_{45}\frac{\partial u_3}{\partial x_1}) \\
&+ w[\frac{\partial}{\partial x_1}(C_{16}\frac{\partial u_1}{\partial x_1} + C_{66}\frac{\partial u_2}{\partial x_1} + C_{36}\frac{\partial u_3}{\partial x_3}) - \rho\ddot{u}_2]dx_3 \\
&+ w(x_B)\sigma_{23}(x_B) - w(x_A)\sigma_{23}(x_A) = 0
\end{aligned} \tag{6.78}$$

$$\begin{aligned}
&\int_{x_A}^{x_B} -\frac{dw}{dx_3}(C_{13}\frac{\partial u_1}{\partial x_1} + C_{36}\frac{\partial u_2}{\partial x_1} + C_{33}\frac{\partial u_3}{\partial x_3}) \\
&+ w[\frac{\partial}{\partial x_1}(C_{55}\frac{\partial u_1}{\partial x_3} + C_{45}\frac{\partial u_2}{\partial x_3} + C_{55}\frac{\partial u_3}{\partial x_1}) - \rho\ddot{u}_3]dx_3 \\
&+ w(x_B)\sigma_{33}(x_B) - w(x_A)\sigma_{33}(x_A) = 0
\end{aligned} \tag{6.79}$$

Combining Eq. (6.77) to Eq. (**??**) and Eq. (6.73), and assuming that the stiffness matrix does not change with r, and dividing in through by the exponential.

$$\begin{aligned}
&\int_{x_A}^{x_B} \frac{dw}{dx_3}(C_{55}\frac{d\hat{u}_1}{dx_3} + C_{45}\frac{d\hat{u}_2}{dx_3} + i\xi C_{55}\hat{u}_3) + w[\xi^2(C_{11}\hat{u}_1 + C_{16}\hat{u}_2) - i\xi C_{13}\frac{d\hat{u}_3}{dx_3} - \rho\omega^2\hat{u}_1]dx_3 \\
&\qquad - w(x_B)\sigma_{31}(x_B) + w(x_A)\sigma_{31}(x_A) = 0 \\
&\int_{x_A}^{x_B} \frac{dw}{dx_3}(C_{45}\frac{d\hat{u}_1}{dx_3} + C_{44}\frac{d\hat{u}_2}{dx_3} + i\xi C_{45}\hat{u}_3) + w[\xi^2(C_{16}\hat{u}_1 + C_{66}\hat{u}_2) - i\xi C_{36}\frac{d\hat{u}_3}{dx_3} - \rho\omega^2\hat{u}_2]dx_3 \\
&\qquad - w(x_B)\sigma_{23}(x_B) + w(x_A)\sigma_{23}(x_A) = 0 \\
&\int_{x_A}^{x_B} \frac{dw}{dx_3}(i\xi(C_{13}\hat{u}_1 + C_{36}\hat{u}_2) + C_{33}\frac{d\hat{u}_3}{dx_3}) + w[-\xi(C_{55}\frac{d\hat{u}_1}{dx_3} + C_{45}\frac{d\hat{u}_2}{dx_3}) + \xi^2 C_{55}\hat{u}_3 - \rho\omega^2\hat{u}_3]dx_3 \\
&\qquad - w(x_B)\sigma_{33}(x_B) + w(x_A)\sigma_{33}(x_A) = 0
\end{aligned} \tag{6.80}$$

Introduce the approximation of displacement.

$$\hat{u}_i(x_3) \approx U_i(x_3) = \sum_{j=1}^{N} \bar{u}_i^j \Psi_j(x_3) \tag{6.81}$$

In matrix format,

$$\mathbf{U}(x_3) = \mathbf{\Psi} \cdot \mathbf{\Delta} \tag{6.82}$$

where,

$$\mathbf{\Psi} = \begin{bmatrix} \Psi_1 & 0 & 0 & \cdots & \Psi_N & 0 & 0 \\ 0 & \Psi_1 & 0 & \cdots & 0 & \Psi_N & 0 \\ 0 & 0 & \Psi & \cdots & 0 & 0 & \Psi_N \end{bmatrix} \tag{6.83}$$

$$\underset{\sim}{\Delta} = \begin{Bmatrix} \bar{u}_1^1 & \bar{u}_2^1 & \bar{u}_3^1 & \cdots & \bar{u}_1^N & \bar{u}_2^N & \bar{u}_3^N \end{Bmatrix}^T \tag{6.84}$$

We assume the Galerkin, or Ritz, form.

$$\begin{aligned}
w_i(x_3^i) &= \Psi_I(x_3^i) \\
\Psi_j(x_3^i) &= \delta_{ij}\mathbf{w} = \mathbf{\Psi}
\end{aligned} \tag{6.85}$$

Combine Eq. (6.80), Eq. (6.82) and Eq. (6.85),

$$\left(\mathbf{K}_1^e + i\xi\mathbf{K}_2^e + \xi^2\mathbf{K}_3^e - \omega^2\mathbf{M}^e\right)\boldsymbol{\Delta}^e = \boldsymbol{Q}^e \tag{6.86}$$

where,

$$\begin{aligned}
\mathbf{K}_1^e &= \int_0^{h_e} \frac{d\boldsymbol{\Psi}}{dx_3}\mathbf{B}_1\frac{d\boldsymbol{\Psi}}{dx_3}dx_3 \\
\mathbf{K}_2^e &= \int_0^{h_e} \frac{d\boldsymbol{\Psi}}{dx_3}\mathbf{B}_{21}\boldsymbol{\Psi}dx_3 - \int_0^{h_e} \boldsymbol{\Psi}\mathbf{B}_{22}\frac{d|\boldsymbol{\Psi}}{dx_3}dx_3 \\
\mathbf{K}_3^e &= \int_0^{h_e} \boldsymbol{\Psi}\mathbf{B}_3\boldsymbol{\Psi}dx_3 \\
\mathbf{M}^e &= \int_0^{h_e} \boldsymbol{\Psi}\mathbf{D}\boldsymbol{\Psi}dx_3 \\
\mathbf{Q}^e &= \begin{Bmatrix} -\hat{\sigma}_{31}(0) & -\hat{\sigma}_{23}(0) & -\hat{\sigma}_{33}(0) & 0 & \cdots & 0 & \hat{\sigma}_{31}(h_e) & \hat{\sigma}_{23}(h_e) & \hat{\sigma}_{33}(h_e) \end{Bmatrix}^T
\end{aligned} \tag{6.87}$$

and,

$$\begin{aligned}
\mathbf{B}_1 &= \begin{bmatrix} C_{55} & C_{45} & 0 \\ C_{45} & C_{44} & 0 \\ 0 & 0 & C_{33} \end{bmatrix} \\
\mathbf{B}_{21} &= \begin{bmatrix} 0 & 0 & C_{55} \\ 0 & 0 & C_{45} \\ C_{13} & C_{36} & 0 \end{bmatrix} \\
\mathbf{B}_{22} &= \begin{bmatrix} 0 & 0 & C_{13} \\ 0 & 0 & C_{36} \\ C_{55} & C_{45} & 0 \end{bmatrix} \\
\mathbf{B}_3 &= \begin{bmatrix} C_{11} & C_{16} & 0 \\ C_{16} & C_{66} & 0 \\ 0 & 0 & C_{55} \end{bmatrix} \\
\mathbf{D} &= \begin{bmatrix} \rho & 0 & 0 \\ 0 & \rho & 0 \\ 0 & 0 & \rho \end{bmatrix}
\end{aligned} \tag{6.88}$$

If a quadratic element is used, then the shape function takes the following form for nodes placed at the midpoint.

$$\begin{aligned}\Psi_1^e(\bar{x}_3) &= (1-\frac{\bar{x}_3}{h_e})(1-\frac{2\bar{x}_3}{h_e}) \\ \Psi_2^e(\bar{x}_3) &= 4\frac{\bar{x}_3}{h_e}(1-\frac{\bar{x}_3}{h_e}) \\ \Psi_3^e(\bar{x}_3) &= -\frac{\bar{x}_3}{h_e}(1-\frac{2\bar{x}_3}{h_e})\end{aligned} \tag{6.89}$$

Now, the stiffness matrices are expressed as follows.

$$\mathbf{K}_1^e = \frac{1}{3h_e}\begin{bmatrix} 7\mathbf{B}_1 & -8\mathbf{B}_1 & \mathbf{B}_1 \\ -8\mathbf{B}_1 & 16\mathbf{B}_1 & -8\mathbf{B}_1 \\ \mathbf{B}_1 & -8\mathbf{B}_1 & 7\mathbf{B}_1 \end{bmatrix} \tag{6.90}$$

$$\mathbf{K}_2^e = \frac{1}{6}\begin{bmatrix} -3\mathbf{B}_{21} & -4\mathbf{B}_{21} & \mathbf{B}_{21} \\ 4\mathbf{B}_{21} & 0\mathbf{B}_{21} & -4\mathbf{B}_{21} \\ -\mathbf{B}_{21} & 4\mathbf{B}_{21} & 3\mathbf{B}_{21} \end{bmatrix} - \frac{1}{6}\begin{bmatrix} -3\mathbf{B}_{22} & 4\mathbf{B}_{22} & -\mathbf{B}_{22} \\ -4\mathbf{B}_{22} & 0\mathbf{B}_{22} & 4\mathbf{B}_{22} \\ \mathbf{B}_{22} & -4\mathbf{B}_{22} & 3\mathbf{B}_{22} \end{bmatrix} \tag{6.91}$$

$$\mathbf{K}_3^e = \frac{h_e}{30}\begin{bmatrix} 4\mathbf{B}_3 & 2\mathbf{B}_3 & -\mathbf{B}_3 \\ 2\mathbf{B}_3 & 16\mathbf{B}_3 & 2\mathbf{B}_3 \\ -\mathbf{B}_3 & 2\mathbf{B}_3 & 4\mathbf{B}_3 \end{bmatrix} \tag{6.92}$$

$$\mathbf{M}^e = \frac{h_e}{30}\begin{bmatrix} 4\mathbf{D} & 2\mathbf{D} & -\mathbf{D} \\ 2\mathbf{D} & 16\mathbf{D} & 2\mathbf{D} \\ -\mathbf{D} & 2\mathbf{D} & 4\mathbf{D} \end{bmatrix} \tag{6.93}$$

The element equations are then combined to form the global equations in the usual manner, such that the following equation is generated.

$$\left(\mathbf{K}_1^G + i\xi\mathbf{K}_2^G + \xi^2\mathbf{K}_3^G - \omega^2\mathbf{M}^G\right)\boldsymbol{\Delta}^G = \boldsymbol{Q}^G \tag{6.94}$$

There is now the choice of solving for wavenumbers with a given frequency or solving for frequencies for a given wavenumber. If a wavenumber is chosen, then a polynomial eigenvalue is created to solve for complex wavenumbers. However, if a wavenumber is chosen, then a linear eigenvalue can be used to solve for the squared frequency.

6.8 Brute Force Algorithm

As mentioned at the beginning of the chapter, an algorithm is required, since the domain consists of many roots. The algorithm will generate the initial guesses and/or sub-domains, depending on the type of root finding method. The most basic approach is to divide the global search domain into a number of sub-domains and/or initial guesses; this is referred to as a brute force algorithm. The most important decision, when implementing a brute force algorithm, is the choice of mesh density. If the mesh is not sufficiently dense, some of the roots may be missed; however, an increase in mesh density is computationally expensive. A modified brute force technique may be used, in which an initial global mesh is first used to find the location of possible roots followed by more dense sub-domains. This process is continued until a sufficiently accurate solution is found. The challenge still remains in that the initial domain must be sufficiently dense to not miss a root.

The following three sub-sections discuss the possible brute force routines that can be employed for the one, two and three dimension searches.

6.8.1 One Dimension

When searching along a single dimension, the global domain is broken into a number of sub-domains. The size of the sub-domains depends on the function, and the programmer or user must make this decision. One of the single dimension root solving schemes is chosen and run in each sub-domain. The final result is the collection of roots from each sub-domain; many sub-domains will not provide a solution.

6.8.2 Two Dimensions

There are two options for a two dimensional search. First, the domain can be divided into a number of one dimension problems. In this method, each one dimension problem is solved with the method mentioned in the previous sub-section. This approach

is useful when the guided wave modes form lines plots within the chosen two dimensions. If the root exists as a single point, this method is not recommended. This type of root exists when the mode travels through the two dimensional plane.

The second method is to divide the global domain into a number of two dimensional sub-domains. Each sub-domain uses one of the two dimensional root searching methods. This is similar to the one dimension algorithm. This method is required when the single point roots exist in the domain.

6.8.3 Three Dimensions

A number of approaches can be used for a three dimension problem. Once again, the problem may be discretized into a number of reduced dimension problems; in this case two dimensions. From there, the solution follows the two dimension algorithm, and the same considerations must be given.

Another approach is to divide the three dimension global domain into a number of three dimension sub-domains. This technique would utilize the three dimension search methods.

One issue with a three dimensional guided wave search is that the solution is sparse, such that most of the domain will not contain roots. This makes the computation very costly because of the mesh density required to obtain a valuable result.

6.9 Behavioral Algorithm

An algorithm that more efficiently searches the sparse domain is desired. One possible solution is to build an algorithm that takes advantage of the common observed behavior of guided waves. The following observations have been made through the generation of complex dispersion curves for multiple models, using the brute force algorithm.

- All the real mode curves begin on the frequency axis with zero wavenumber

- All the imaginary modes begin at the frequency axis with zero wavenumber
- All the complex modes begin at a local maximum of an imaginary or real mode, move in the positive frequency direction and end at a local minimum of an imaginary or real mode
- All bifurcation points contain four separate paths, and each path is separated by 90 degrees

These observations are consistent for the single material results as well as when multiple materials and multiple layers are present in the model.

A refined algorithm has been devised based on the previous observations about the nature of the dispersion curve. These observations and the corresponding algorithm allow for a more efficient and robust approach to finding the roots for guided waves, and are based on the observed behavior of the dispersion curves. The flow chart for the algorithm is shown in Figure 6.11.

First, the roots along the frequency axis are determined. These are referred to as the resonance roots, since they correspond to the resonance frequency for pressure and shear waves through the thickness of the plate, without wave propagation. Next, the initial roots for the fundamental modes are found. The fundamental modes are the modes which exist at zero frequency. Due to the numerical instability at very low frequencies, a minimum frequency is set within the code and the roots are found along a line extending from the minimum frequency along the real wavenumber axis.

Now that the initial roots are known, the search process begins. First, a guess must be generated for the fsolve function. This is accomplished through the use of a second order polynomial extrapolation. Then, the guess is fed into the fsolve function. For each initial guess, the program iterates through the previous process until the calculated root moves outside of the domain. Once this occurs, the last found root is compared to the initial roots of other modes. If the roots match, then

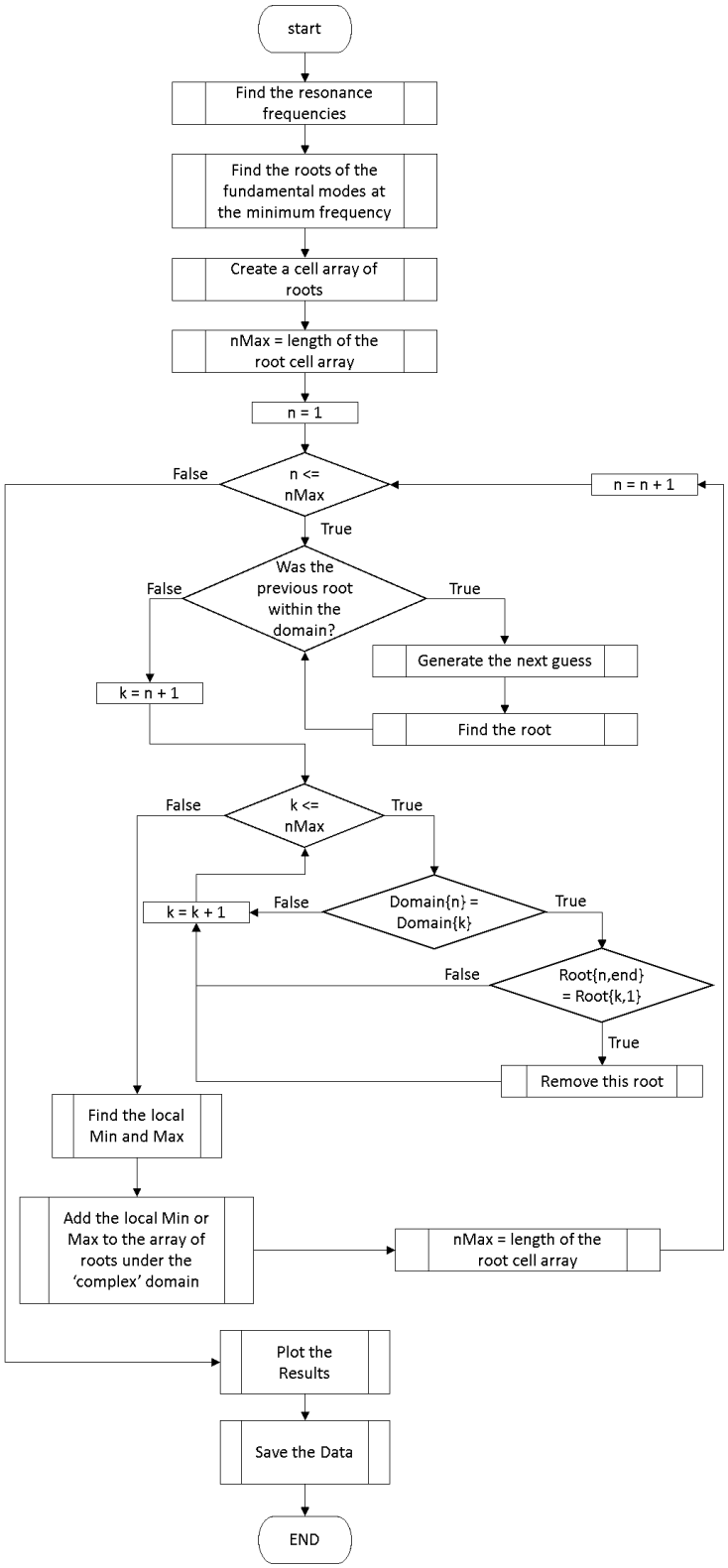

Figure 6.11: Behavioral algorithm

that set is deleted. This is used to prevent duplicate searches. As a note, the root is only deleted if the domain of the curve is the same. In other words, if the domain is real, imaginary or complex.

After this step, the local maximums and minimums are calculated if the curve was real or imaginary. If a local min or max is found, then this becomes another initial guess. This process continues until all initial guesses are exhausted. Finally, the results are plotted and the data saved.

6.10 Algorithm Verification

The following two subsections verify the proposed root solving algorithms by comparing the output to the well know Rayleigh-Lamb solution for a single isotropic plate with traction free surfaces.

6.10.1 Brute Force Algorithm

The flow chart for the specific brute force algorithm used in this section is shown in Figure 6.12. After the program has discretized the domain and performed the root finding method for each initial guess, the roots are filtered before plotting the results and saving the data. The exit status from each iteration is saved, and this information is used to decide if the calculated root is correct. Additionally, if the roots fall outside of the domain then they are discarded. Finally, the roots are sorted into real, imaginary and complex results. This is accomplished by setting a tolerance on the definition of a zero value for the real or imaginary component.

In order to verify that this algorithm will work for a multilayer laminate, two test scenarios are constructed and compared. First, the non-dimensional Rayleigh-Lamb solution of equations 4.25 and 4.26 are used in the brute force algorithm. Next, the three-layer non-dimensional solution is implemented with all three layers having the

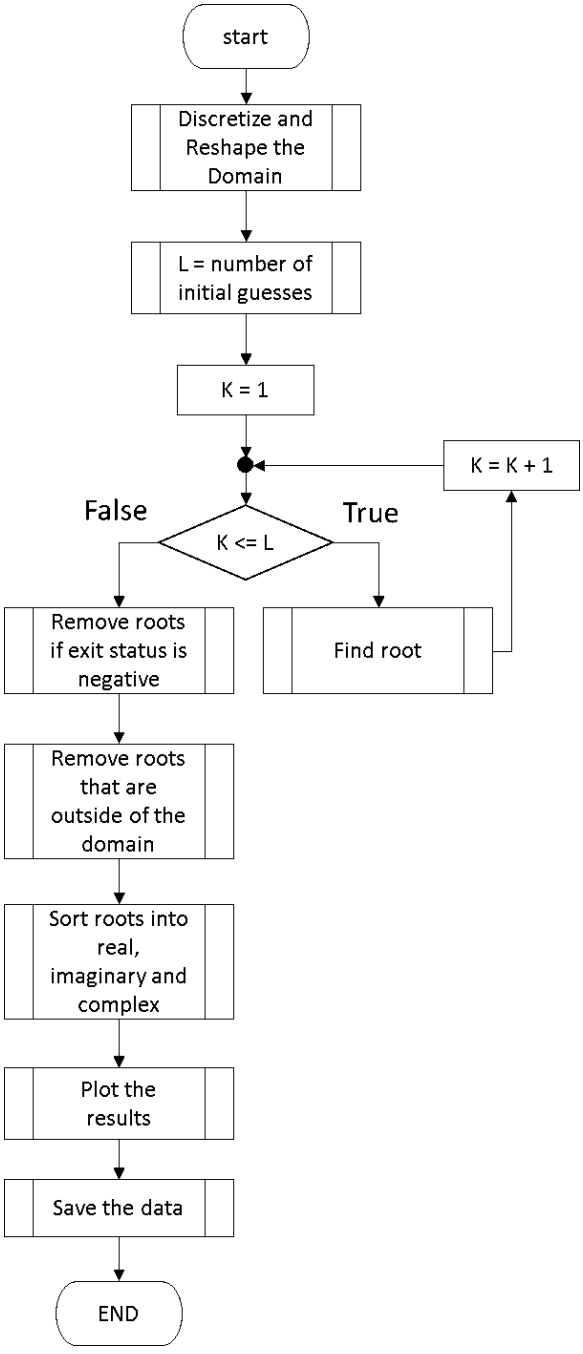

Figure 6.12: Flow chart for the brute force algorithm

same material properties. If the algorithm is correct, then both solutions should be the same.

Figure 6.13 shows the real and imaginary non-dimensional wavenumber solutions. Since the root solving method is unconstrained, some curves have a dense collection of roots, while others are missing point along part of the curve. Each approach seems to be good in one section and poor in another, generally these weaknesses and strengths are not the same. Overall, it appears that the multilayer solution has been successfully implemented. The bulk shear wave solution is not fully resolved, but this is partly due to the close proximity of the fundamental modes and the bulk wave mode at low frequencies.

The complex wavenumber perspective view is shown in Figure 6.14. Overall there is a good match. The Rayleigh-Lamb solution does not include the bulk pressure and shear waves, while the laminate model does include parts of this solution. The laminate model provides a more consistent solution along the imaginary root curves, but the Rayleigh-Lamb spears to be clearer along the complex curves.

These results show that the brute force algorithm has been successfully implemented and can solve for the roots for multi-layered isotropic laminates; however, some improvements can be made to this basic forceful approach.

6.10.2 Behavioral Algorithm

Again, the same verification process was performed. This time the Raleigh-Lamb equation was not used. Instead only the three-layer setup was implemented with all three layers containing the same material properties, and the previous results can be used for comparison.

The real-imaginary wavenumber view is shown in Figure 6.15. The calculation of this set of roots took about one twenty fifth of the time that was required in the brute force algorithm. Additionally, the domain in these results is much larger than

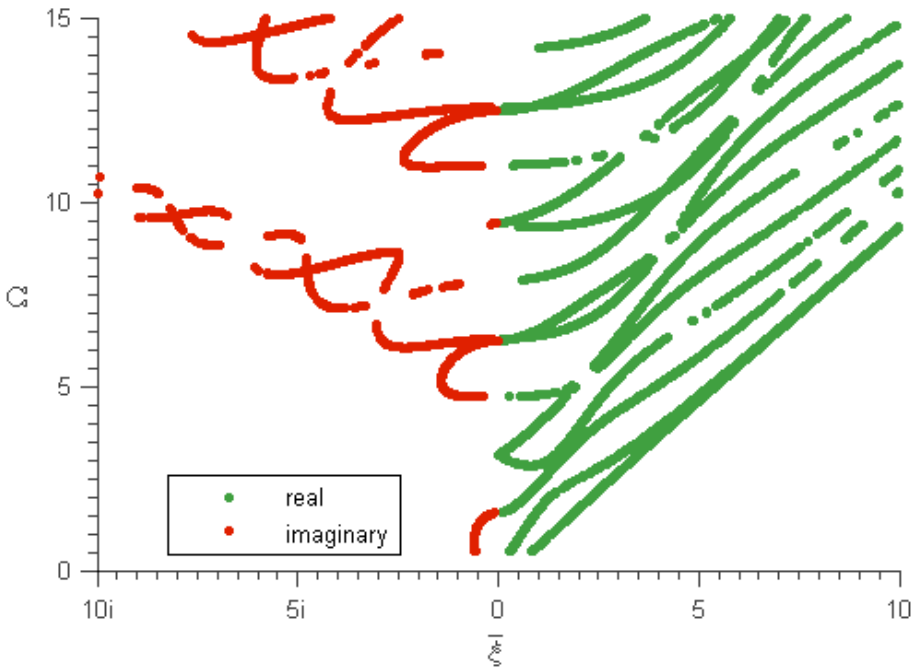

(a) Rayleigh-Lamb solution

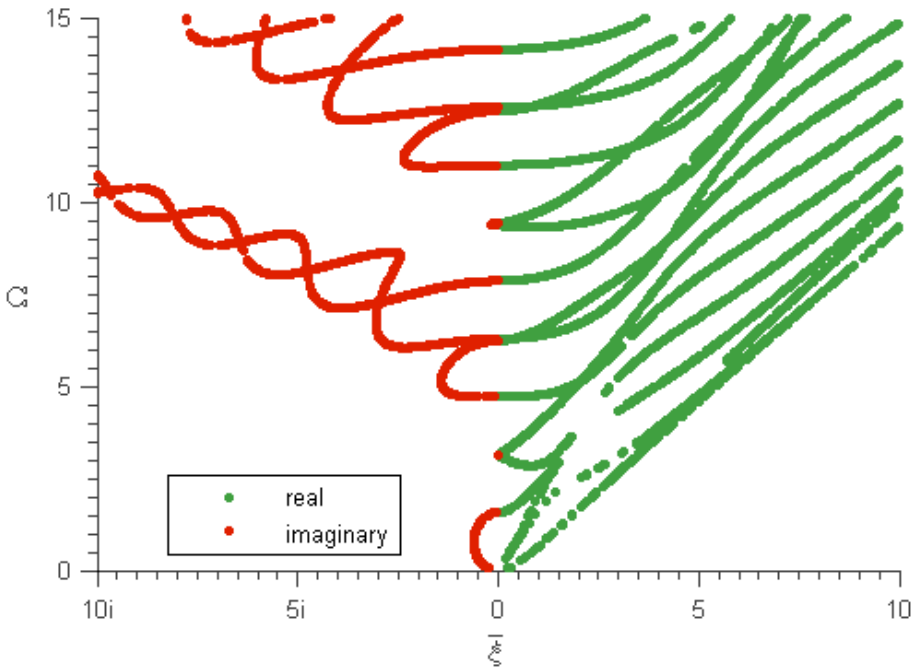

(b) Isotropic laminate model with identical plies

Figure 6.13: Brute force algorithm

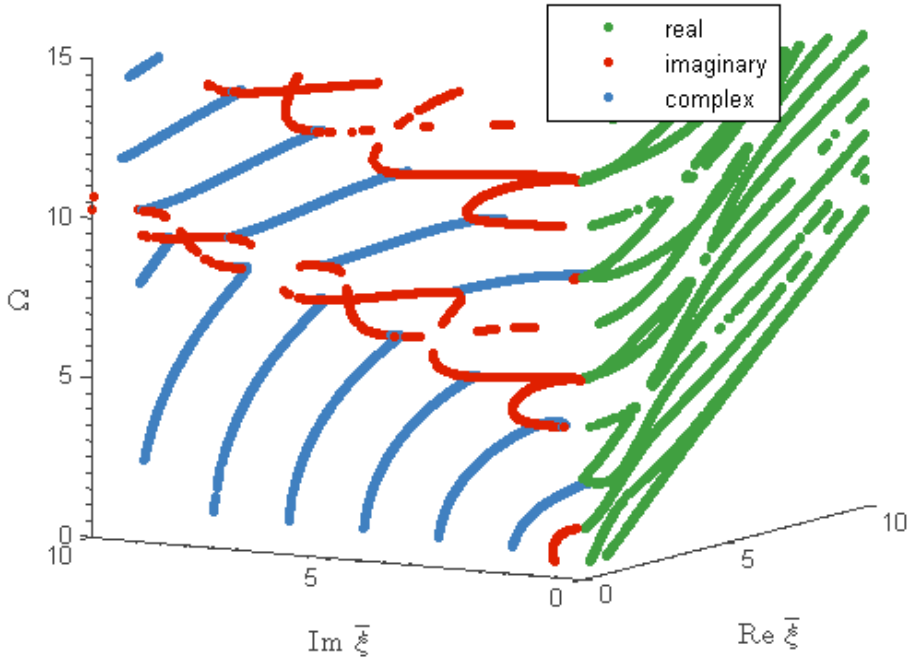

(a) Rayleigh-Lamb solution

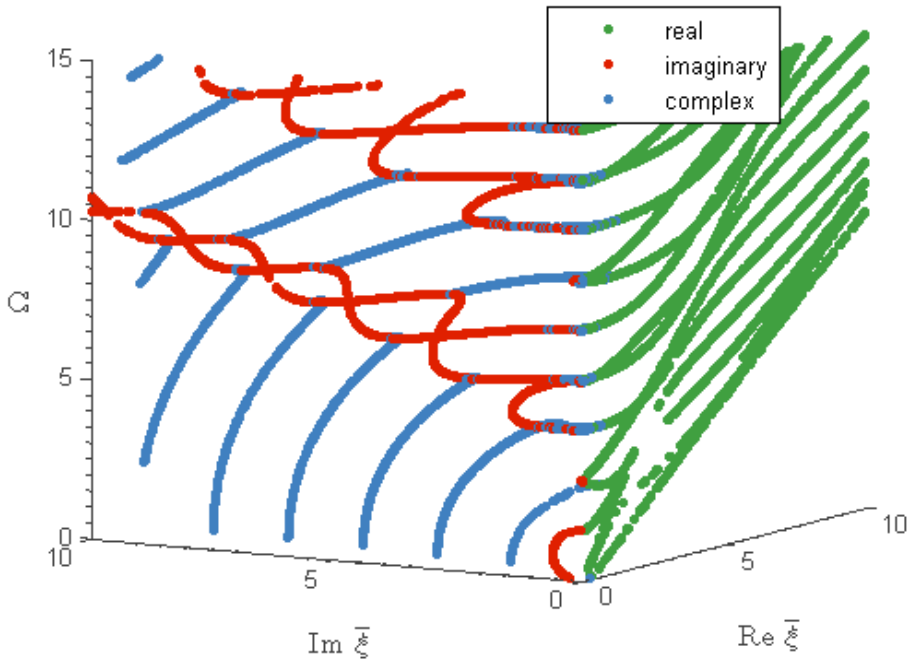

(b) Isotropic laminate model

Figure 6.14: Perspective view of brute force algorithm results

the results presented previously. Another major improvement over the brute force algorithm is that the curve for each mode is knows, as opposed to a random collection of points.

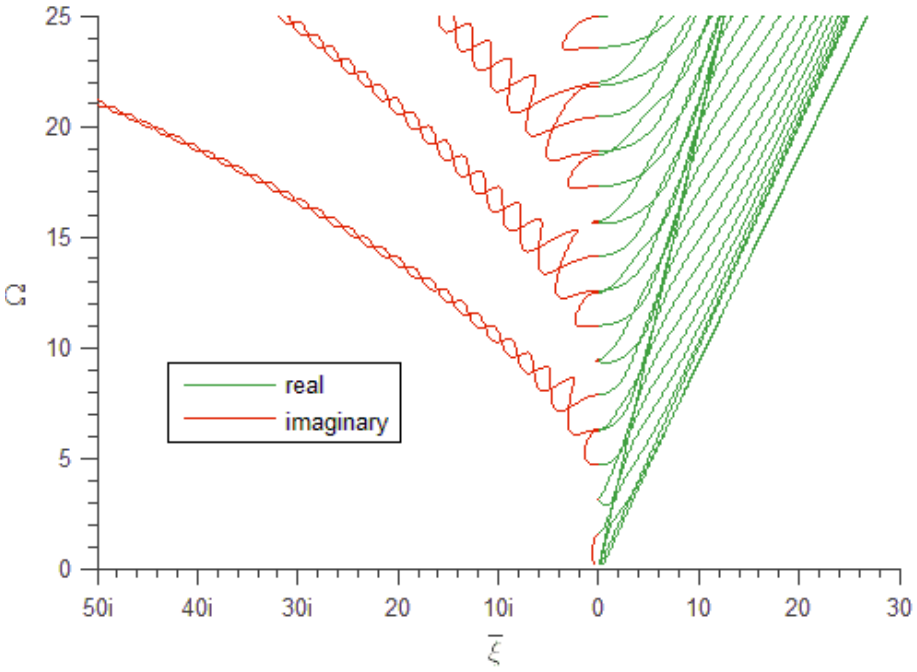

Figure 6.15: Single material, three lamina model solution using the behavioral algorithm

The complex wavenumber view of the solution is shown in Figure 6.16. The behavioral algorithm provides clean plot lines for each real mode. It is clear how the fundamental modes converge to the Rayleigh wave speed, while the resonance modes converge on the shear wave speed. Also, the figure shows clearly how the complex modes begin at local maximum and move in the positive frequency direction to a local minimum.

The algorithm was also used to calculate the dispersion curves for a two material and three-layer model. This is the scenario encountered when an adhesive is bonded between two identical isotropic plates. The real-imaginary plot of the solution is shown in Figure 6.17. This solution has some similar properties to the single material model, but changes dramatically at higher frequencies and wavenumbers.

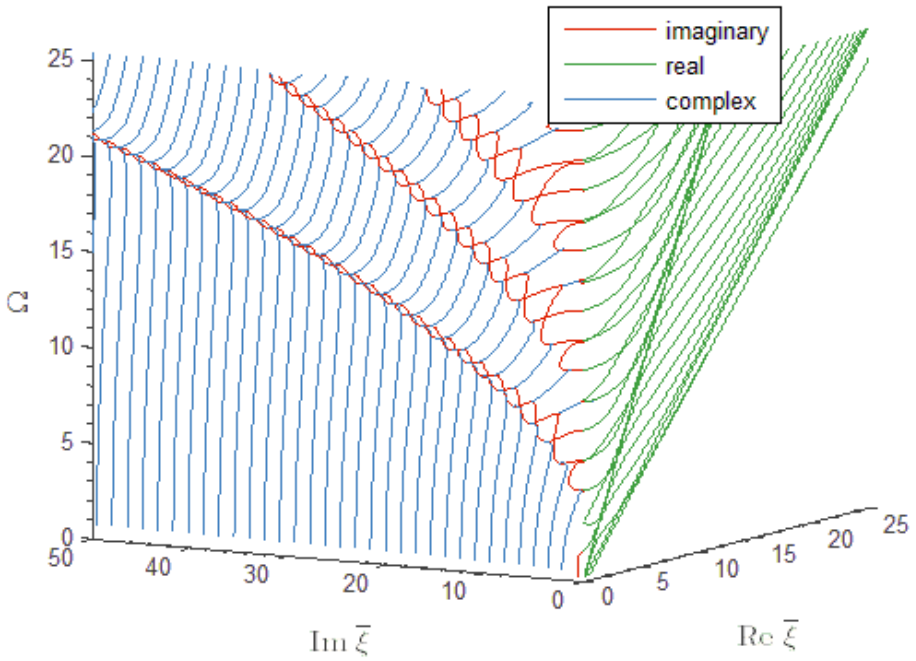

Figure 6.16: Perspective view of the complex single material, three lamina model solution using the behavioral algorithm

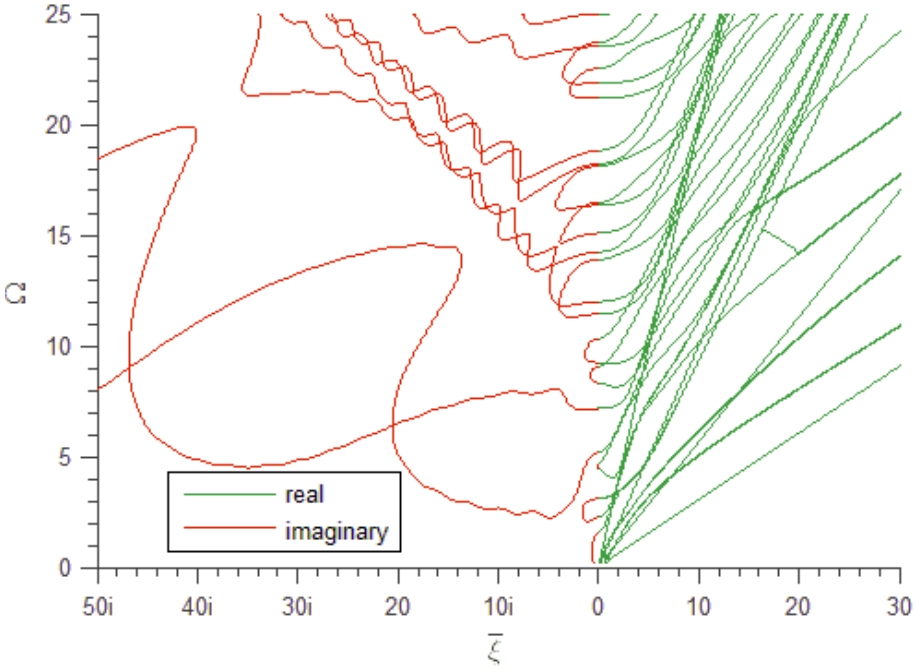

Figure 6.17: Two material, three lamina model solution using the behavioral algorithm

The complex wavenumber view of the solution is shown in Figure 6.18. There are some clear differences from the single material case. The fundamental modes do not converge to the Rayleigh wave speed; in fact, they do not converge towards each other. The solution also contains the solution for both of the pressure and shear waves. It appears that many of the higher modes will converge towards the shear speed of the outer material, while multiple modes have wavenumbers below the shear speed of the outside material, these are most likely interface modes. There also appears to be an error were one curve jumps from one mode to another. This could possibly be corrected by using a higher order backward difference method.

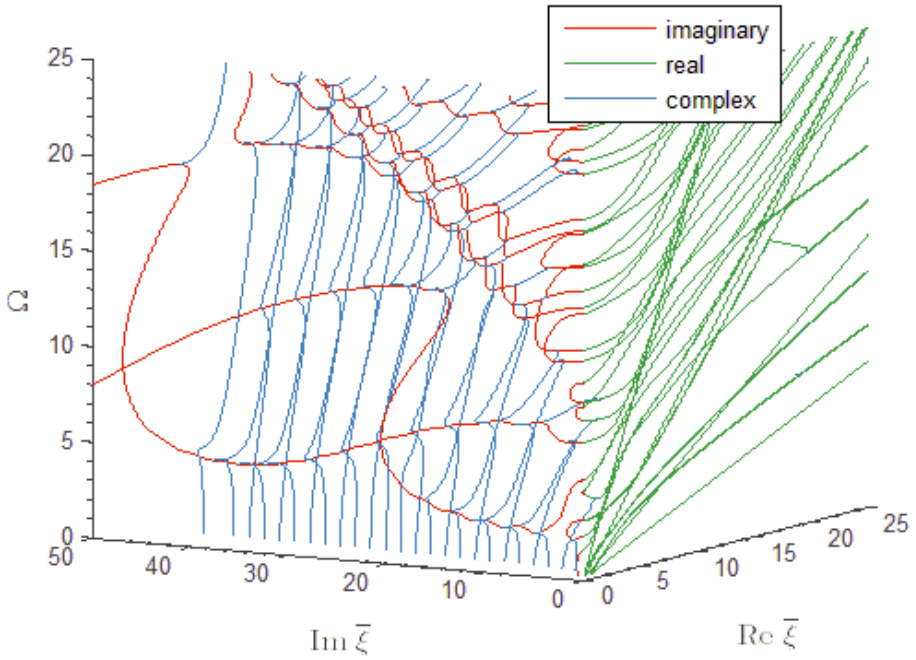

Figure 6.18: Real perspective view of the complex two material, three lamina model solution using the behavioral algorithm

There are two groups of imaginary curves in this figure. There is a set of curves which form very large peaks and troughs as they move in the imaginary wavenumber direction, and there is a group that forms much tighter and more frequent fluctuations. The curves with large variation most likely correspond to the thickness resonance of the thin inside layer representing the adhesive, while the tighter variations correspond

to the resonances of the outside layers representing the adherends.

In order to give a closer look into the two material results, the solution has been replotted with a smaller domain size in Figure 6.19. In these figures, the lower order modes are easily distinguishable. It is clear how the fundamental modes have changed from the Rayleigh-Lamb solution. Also, from this perspective two of the imaginary modes appear to be nearly horizontal with a wide range of wavenumber solution for limited range of frequencies.

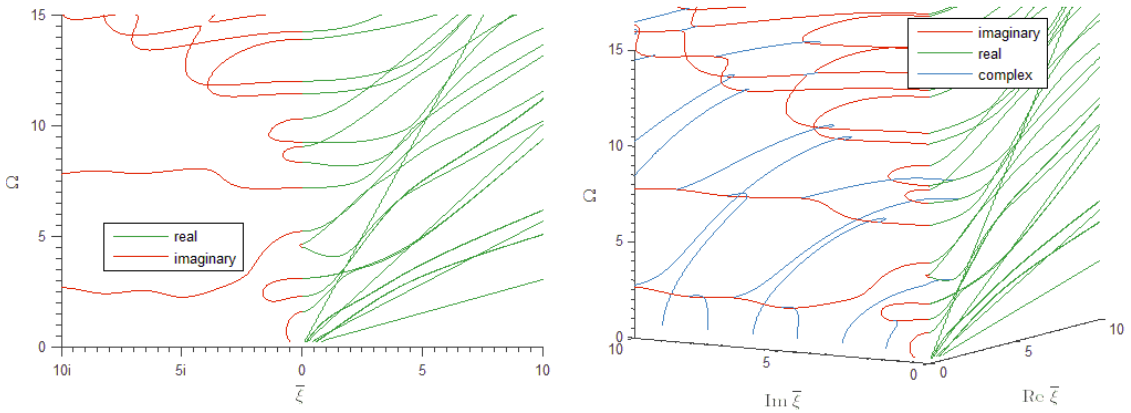

(a) (b)

Figure 6.19: Close up view of the two material, three lamina model solution using the behavioral algorithm; (a) real and imaginary solution; (b) full complex solution

6.11 Conclusion

Two methods for finding the solution to guided plate waves have been presented. The brute force method is capable of solving any type of problem but is slow, bulky and requires post processing to group the roots into the proper modes. The behavioral algorithm uses the observed behavior of the guided wave roots to quickly and efficiently solve the equation and simultaneous group the roots by mode. This method also provides an easy way to calculate the roots for any frequency, since interpolation can be used between the calculated points for each curve. The backwards difference scheme which is used to determine the initial guess for root calculation could be im-

proved by increasing the order. Another possible source of errors is the calculation of the local minimums and maximums for each curve. Additional work could be carried out in this area.

Chapter 7

Guided Wave Inspection

7.1 Weak Interfacial Bonding

7.1.1 Definition of weak bonding and "kissing" bonds

According to Bode et al. [8] "weak bonds can be defined in many ways, but for the purpose of developing NDI methods to assess bond strength, consensus among researchers has generally evolved into a common set of characteristics that center on failure of the adherend/adherent interface." Additionally, Bode [8] stated that the adhesives are selected for the specified application, and as a result bond failure at the interface will be the most important failure mode to prevent. Throughout this work weak bonding will refer to a bond which fails at or near the bonding interface.

Some researchers discuss the detection of the so called "kissing" bond. This is generally thought of as an extreme case of weak bonding, were the interfaces remain in close contact but there is only slightly more strength than the case of complete disbonding. Bode at al. [8] defined kissing bonds as follows, "the term 'kissing' bond has been adopted by the research community to describe a bonded structure for which contact is intimate between both adherends and the adhesive, but there is no residual bond strength for at least one interface." While Marty et al. [89] provided a quantitative description with the following requirements: the bond strength in peel must be less than 20% of the full strength, the failure mode must be 100% adhesive, and a normal incidence UT longitudinal wave must not exhibit low signal attenuation through the joint, must transmit across the joint as if there was no disbond present.

The last requirement eliminates the cases of improper adhesive mixing and incomplete curing, which will ultimately lead to an increase in damping and signal attenuation. This paper will primarily discuss weak bonding or weak interface bonding, leaving the term kissing bond as a special case that will only be used when the strength is particularly low.

7.1.2 When does weak bonding occur

One way to understand how a weak bond may occur in practice is to study the methods used to purposely creating weak bonds. Bode et al. [8] wrote a good review article on weak adhesive bond fabrication and showed that the primary variables that undergo alterations in the process of weak bond creation are surface contamination, mixing ratios, adhesive application, bond line thickness variation and processing or cure deviations from an optimum.

Kumar et al. [90] used poly vinyl alcohol (PVA) to create weak bonds in a two-part epoxy bonding GFRP. The PVA reduces the degree of polymerization, and several different amounts of PVA were applied. The use of the PVA decreased the through transmission amplitude and increased the reflection coefficient. Additionally, the measured density and velocity decreased with an increase in PVA content. This process altered the bulk properties of the adhesive and could not be considered a decrease in interface strength.

Brotherhood et al. [91] investigated the reflection of longitudinal and shear waves from a dry contact interface under increasing pressure, and variations in surface roughness. As the contact pressure was increased the reflection coefficient approached the expected value for a perfect contact. Where an increase in initial surface roughness required an increase in pressure to approach the perfect contact condition. This paper shows that the size of small surface voids influences the reflection and transmission coefficients.

Brotherhood et al. [91] also looked into the reflection from contaminated adhesive bonds. The surface was contaminated prior to bonding with the following: petroleum jelly, carbonated grease, sapphire-bearing grease, lithium grease and Frekote. The detectability depended on the adhesive, where for a 2-part room cure adhesive all but the Frekote were detected, while the heat cured adhesive was more difficult with defect signs present for the carbonated grease and sapphire-bearing grease. The authors also considered the effect of compression loading on the detectability, once again showing that an increase in pressure reduces the reflection coefficient towards the expected perfect contact condition.

7.1.3 Adhesion theories

There is no universal theory for adhesive bonding, instead there are multiple theories that each contribute a part to the total adhesion, and the contributions depend on the materials and conditions involved in the specific system. The list includes; mechanical interlocking, electrostatic, diffusion, wettability, chemical bonding and weak boundary layer [92].

The mechanical interlocking theory depends on the penetration of the adhesive into the cavities, pores and other surface irregularities. It is this 'mechanical interlocking' that provides the strength to resist shear stresses, and it is thus posited that an increase in surface roughness will increase adhesive strength. Will in some cases increasing surface roughness may lead to an increase in strength, this theory is often neglected for most scenarios. It is possible that this theory could play an important role in the bonding of porous media.

The electrostatic theory depends on the formation of an electrical double layer at the interface. The transfer of electrons between the adhesive and adherend creates an electrostatic force across the interface. This theory could contribute to polymer-metal bonding or other incompatible materials, but this is unlikely in the adhesive bonding

of polymer composites.

The diffusion theory results from the observation of inter-diffusion of the molecules between the adhesive and adherend. This reaction is known to create an interphase region or transition zone between the two materials. This condition only exists for compatible materials and proper bonding conditions. Seferis et al. [93] investigated the interphase properties of co-cured and secondary bonded composite materials. The authors found that when chemically compatible adhesives where used in co-cured structures there were clear signs of resin intermingling, leading to a gradual change in resin properties. However, when secondary bonding was performed, there was no sign of diffusion and there was a clear demarcation between the resin and adhesive. That lack of intermingling resulted in a significant loss of fracture toughness. Diffusion will also exist in the welding of thermoplastics. An advantage to the diffusion or intermingling of resin systems is that there is a gradual change in material properties, which reduces the stress concentration between the layers.

The wetting theory states that adhesion results from the molecular forces between the two contacting surfaces. Wetting is the name given to a fluid which forms an intimate contact with a solid. In order for complete wetting to occur, the adhesive should have a much lower surface tension compared to the solid, the large surface tension of the solid overcomes the intermolecular forces of the adhesive. This theory provides the motivation behind the surface treatment and careful handling of adherends to increase and/or maintain a high level of surface energy. Similar to the mechanical interlocking theory, poor wetting will result in the adhesive bridging surface cavities and decreasing the total contact area. Incomplete wetting will generate interfacial defects, while complete wetting is necessary for a high bond strength.

The chemical bonding theories consider the formation of hydrogen, covalent and ionic bonds between the adhesive and adherend. According to Maguire et al. [94] chemical bonding occurs over a distance or 1 to 3 angstroms of the surface. While

the chemical bonding theories may contribute to part of the adhesive strength, the length scales are too small for a reasonable nondestructive inspection. Additionally, the chemical bonding theories will lead to theoretical strengths that are several orders of magnitude larger than observed in real materials. This observation led to the development of fracture mechanics in the early 20th century, which is also used in the study of adhesive joint failure.

The acid-base theory is a specific interaction between an acid and base where the base donates an electron pair to the acid in a similar manner to the electrostatic theory. This theory will not be of much use in the study of polymer composites.

The weak boundary layer theory, as proposed by Bikerman, states that adhesive failure at the interface is either due to a cohesive flaw or a weak boundary layer. These boundary layers can occur in the adhesive or adherend. This theory comes from the observation that even complete adhesive failures still leaves a very thin layer of adhesive on the substrate; therefore, the failure must occur in a weak layer just below the interface. An example of a weak boundary layer originating in the adherend is the formation of an oxide layer that is weakly attached to the base metal. The introduction of some types of surface contaminates prior to bonding can result in reactions with the adhesive leading to the formation of a weak adhesive layer. As discussed in previous theories, if the adhesive does not fully wet the substrate then small voids will form along the interface also leading to a weak interface layer. According to Bikerman [95], the weak boundary layers are formed from either air pores, impurities at the interface or reactions between components and medium.

There has been some criticism of Bikerman's theory; particularly from the argument that the stress distribution across the adhesive layer and around an adhesive crack tip will lead to a crack that propagates close to the interface [96]. Despite this criticism, there has been a renewed interest in the concept of interphase layers near the adherend interface. This interphase layer could be caused by multiple factors.

Delong et al. found that graphite-polymer interphase can have a thickness up to 10 microns [97]. Maguire et al. found that the small to medium scale phenomena, such as surface chemistry and morphology, were often not enough to explain the much larger interphase region [94]. Also, Maguire et al. showed that there is a formation of ordered structures in adhesives near surfaces and the presence of this surface causes a perturbation in the local density. The authors also stated that this perturbation is likely the 'nucleus' that the interphase 'skin' most likely grows; however, current theories can only explain density variation for up to 30 angstroms.

7.1.4 Modeling weak interfacial bonding

Brotherhood et al. [91] used a spring model for dry contact reflection coefficients.

Rokhlin and Wang [98] modeled a layer of circular voids with plane strain as an effective layer acting as an anisotropic layer with properties depending on the micro-structure. This method can be used for voids, inclusions and micro-cracks.

Rokhlin and Huang [80] introduced a transfer matrix approach to relate the boundary conditions across an anisotropic layer between two generally anisotropic solids. The approximation works well for small thickness to wavelength ratios. This method improves upon the simple zero-thickness string models by including inertia effects and coupling terms.

Rose et al. [99] modeled weak bonding with a thin homogeneous interface layer with particular density, elastic constants, and thickness. The particular case of a kissing bond was simulated by treating the interface layer as an inviscid fluid with zero shear velocity.

Nagy [61] investigated the ultrasonic bulk wave reflection from an adhesive interface and showed that the kissing bond could not be modeled simply as a transverse slip. He considered the interface issues to be resolved into three types of conditions; slip bond, kissing bond and partial bond. He showed that the reflection coefficient is

frequency dependent, this should be expected if the interface contains thin defects. Nagy felt that the shear wave was more effective at detecting interface issues. He used the finite boundary stiffness approach more modeling interface defects, where the tractions are continuous across the interface but the displacements are related through a zero-thickness spring. He only considered an isotropic and homogeneous materials.

Modeling the weak interface as a very thin homogeneous layer with unique density and stiffness matrix has shown to be the most comprehensive method. This will allow a wide range of possible defects to be included, not just a single case such as a kissing bond.

7.2 Inspection Methodology

Three inspection schemes are demonstrated in this chapter. They consist of a normal incidence technique and guided wave techniques. The normal incidence technique and one of the guided wave techniques are performed immersed in water.

7.2.1 Normal incidence ultrasonic inspection

This technique uses a single transducer to inspect the part. The wave is generated through water as the coupling medium and impinges onto the part at a zero degree incident angle, or normal to the part surface. Some of the energy from the wave pulse is reflected, while the remaining energy is transmitted into the material. This process is repeated at each new interface; additionally, every reflected wave re-encounters the interfaces, resulting in an every growing number of wave packets. Analyzing each packet as a ray, we can see that the first three reflections are of most interest, with the remaining reflections exhibiting a significant decrease in amplitude from multiple refractions and material damping. These will be the reflection from the top surface of the laminate, the reflection from the adhesive layer (the adhesive thickness will

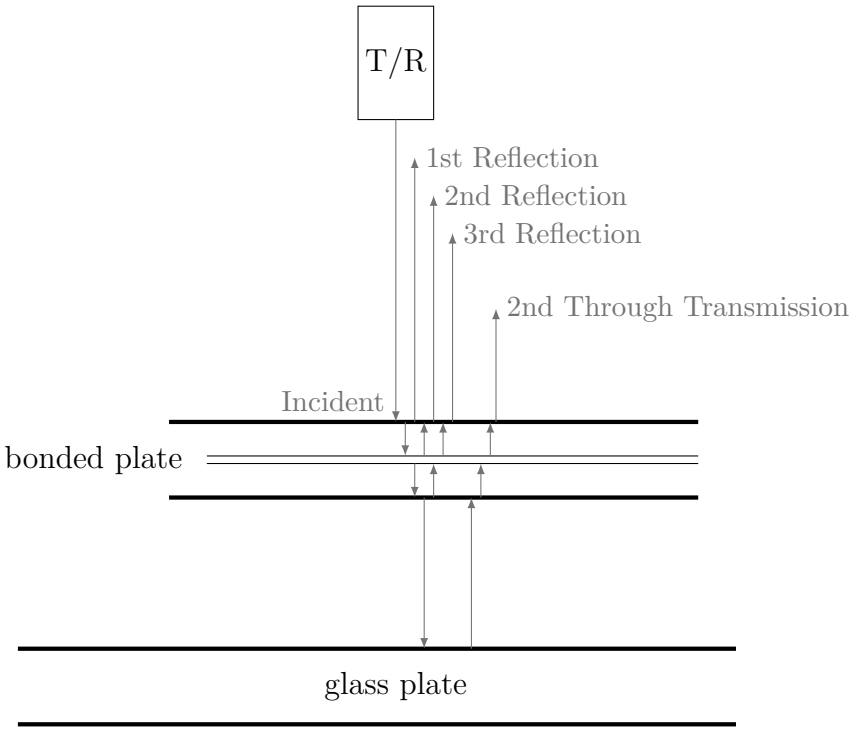

Figure 7.1: Normal UT inspection technique

be small compared to the wavelength for all frequencies considered in this report), and finally the reflection from the back interface. The ray trace of these reflections is shown in Figure 7.1. If the frequency is high, each of these reflections will be visible as separate wave pulses; however, at lower frequencies each reflection overlaps resulting in a single long pulse. In the case of overlapping pulses, the frequency content can be used to analyze the laminate; for high frequencies, the frequency content of the second reflection is sued to investigate the adhesive properties. Additionally, phase shifts are used to find changes to the bondline.

A second feature is used in this setup: a glass plate is utilized to reflect the transmitted signal. In this way, a single transducer can be used to perform a through-transmission inspection, now called double through-transmission. This is also shown in Figure 7.1. Both the transmitted amplitude and frequency content are used to

inspect the laminate.

7.2.2 Contact guided wave inspection

Two techniques are used to investigate guided waves in this report. The first is called the contact method because it utilized contact wedges, as opposed to immersing the laminate in a fluid. This requires a transmitter and a receiver. The transmitter, in this case, is an adjustable angle wedge with piezoelectric transducer. Adjusting the angle of the wedge results in the excitation of varying ranges of phase velocities. The resulting guided waves travel along the laminate and are picked up again by a fixed angle wedge with phased array transducer, see Figure 7.2. A focal law is generated which allows the separation of signals based on the incident angle of the wavefront, which directly corresponds to phase velocity. Following the schematic in Figure 11.3, a straight crested wavefront is assumed. This wavefront travels through the wedge at the known pressure wave velocity, c_P, at the angle, α, with respect to the array. Knowing all these parameters, along with the element pitch, a time delay is applied to each element for every desired value of alpha. Knowing the angle of the fixed wedge, leads to a focal law which finds the signal for a set array of phase velocity values. This leads to a time domain signal for each phase velocity. Applying an FFT to the time domain signal, the signal can now be plotted as phase velocity and frequency, or the dispersion curve.

7.2.3 Immersion guided wave inspection

The immersion method for performing guided wave inspection uses two transducers in a pitch catch arrangement. The transmitter is an unfocused transducer which excited a pressure wave within the fluid. The receiver detects the pressure waves which are leaked away from the plate as the guided wave phase velocity remains faster than the bulk velocity in water. The incident angle is controller by rotating

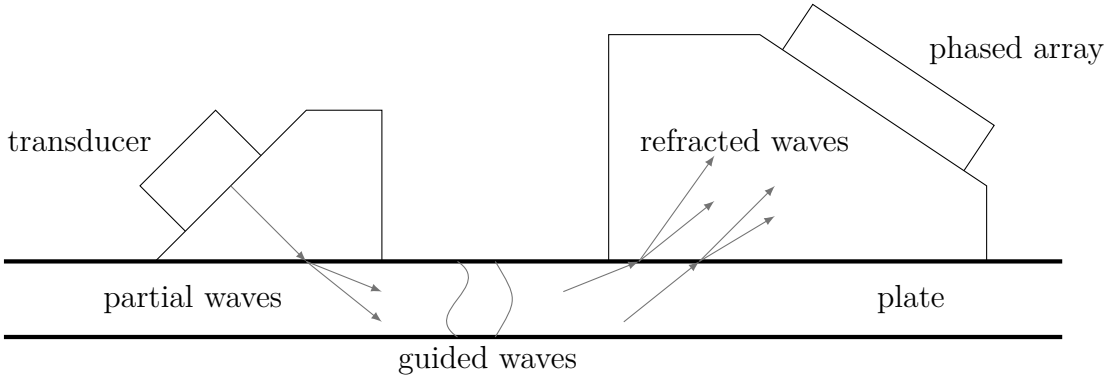

Figure 7.2: Contact guided wave inspection technique

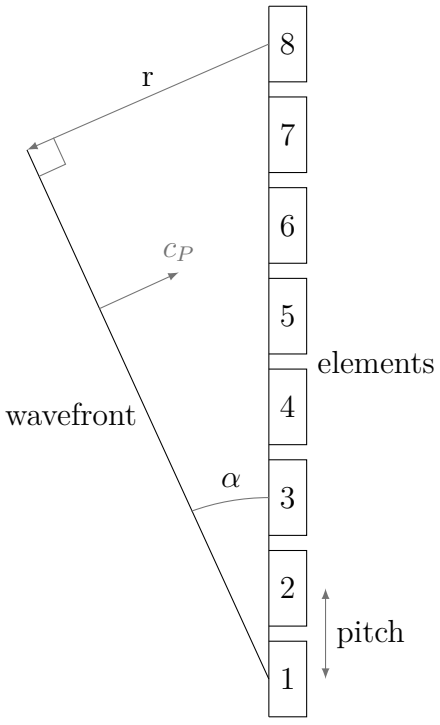

Figure 7.3: Straight crested wave phased array focal law

the plate to be inspected; additionally, the receiver can be translated to find the peak amplitude of the leaked wave. A diagram is shown in Figure 7.4, which provided a clearer description of the technique.

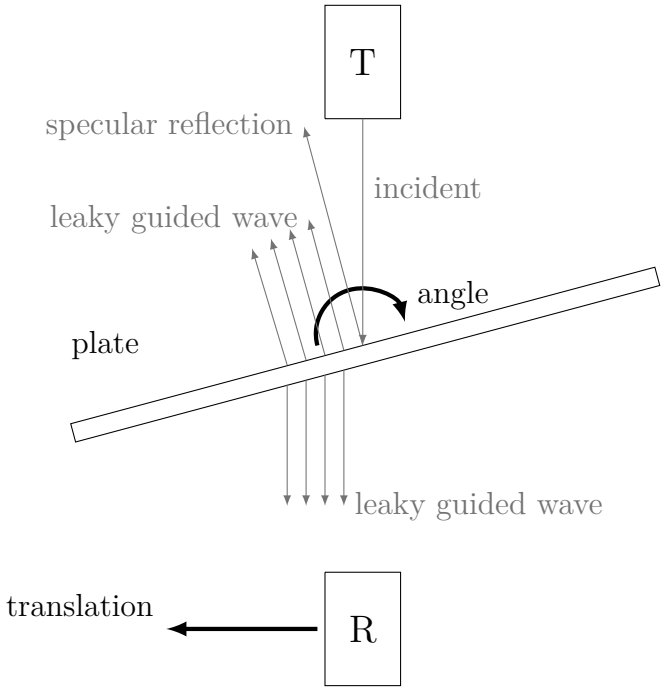

Figure 7.4: Immersion guided wave inspection technique

7.3 Predictive Modeling

7.3.1 Mode shape analysis

7.3.1.1 Mode sensitivity

As discussed in the review chapter, several authors have used the mode shape, displacement and stress, as a method of assessing the sensitivity of a guided wave mode to an adhesive and/or adhesive interface defect. The idea is fairly straight forward; mode shapes with large displacements, stresses and strains across the interface, as compared to the maximum displacement or stress, should be sensitive to a defect at the interface. First, the dispersion curve and corresponding mode shapes are gener-

ated for the pristine model within a predetermined domain. Next, an approach must be taken to search through the mode shapes and rank the relative sensitivity.

Since the mode shapes are eigenvectors, they must be normalized. In this dissertation, the mode shapes (displacement, stress and strain) are normalized by the greatest magnitude of the vectors. As an example, consider a simple bonded structure. Two 1.6 mm 2024 aluminum plate bonded with an epoxy adhesive. The adhesive is 0.08 mm thick, and has a Young's modulus of 2.8 GPa and a Poisson's ratio of 0.36. First, consider the displacement, and find modes that exhibit relatively large displacements at the bonded interface (Figure 7.5 and Figure 7.6).

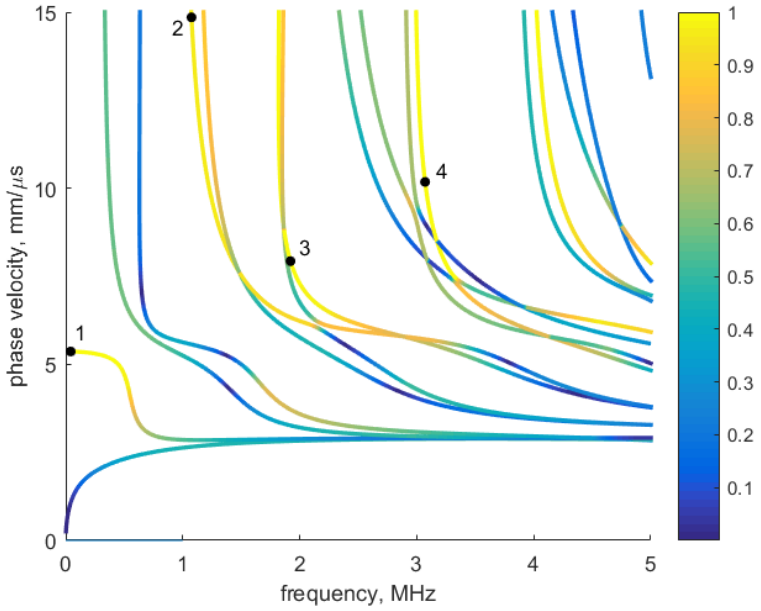

Figure 7.5: Dispersion curve for the bonded aluminum structure; the color corresponds to the normalized u_1 displacement at the interface

Similarly, the process is repeated for the u_3 displacement (Figure 7.7 and Figure 7.8).

Displacement may not be the best way to rank the sensitivity of the mode shape to a defect at the interface. Instead, the shear stress, σ_{31}, may be used. Again, the dispersion curve is plotted with the color mapping corresponding to the normalized

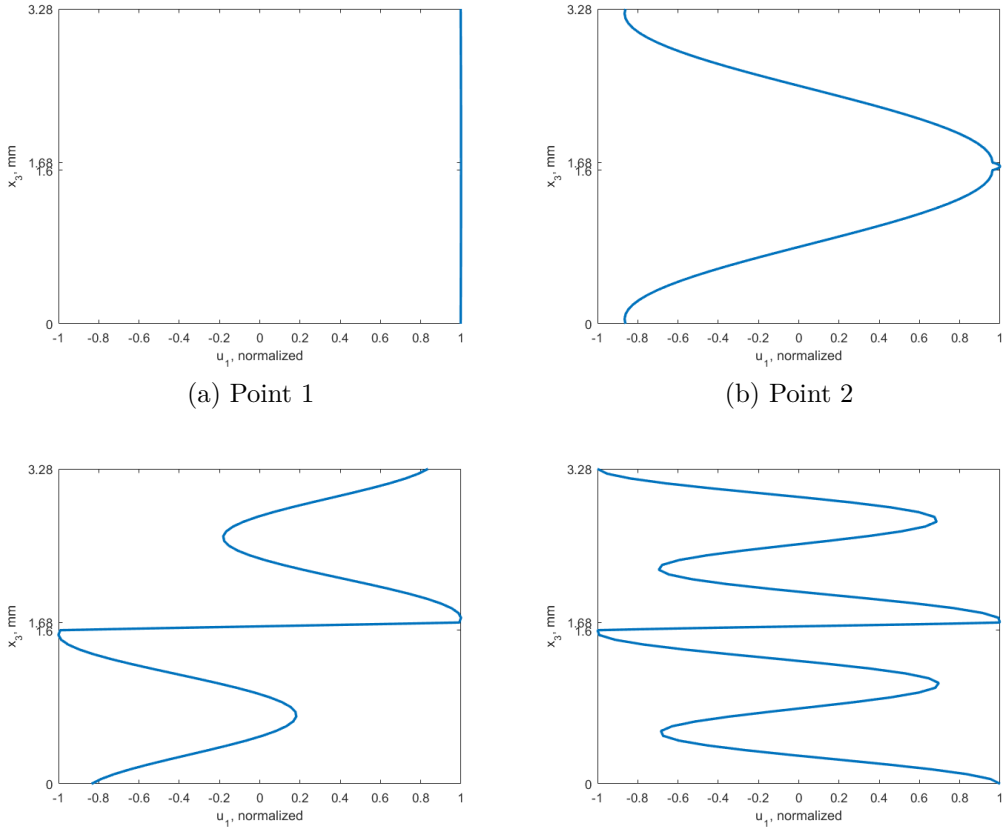

(a) Point 1

(b) Point 2

(c) Point 3

(d) Point 4

Figure 7.6: Bonded aluminum structure; u_1 displacement mode shapes

σ_{31} at the interface (Figure 7.9). Several points on the dispersion curves were selected to demonstrate the displacement and stress mode shapes (Figure 7.10).

7.3.1.2 Mode tracing and the intermediate zone

As discussed in the review chapter, many authors have considered using either interface or interphase waves, while others have considered plate waves. The interface and interphase waves are modeled with half spaces and the plate waves are modeled with traction free surfaces. Some others discuss the trapped interphase waves that exist when the phase velocity is below the shear velocity of the adherend, but the authors do not discuss how this wave mode transitions between the two regimes or discuss that this single mode can act as all three wave types depending on the frequency.

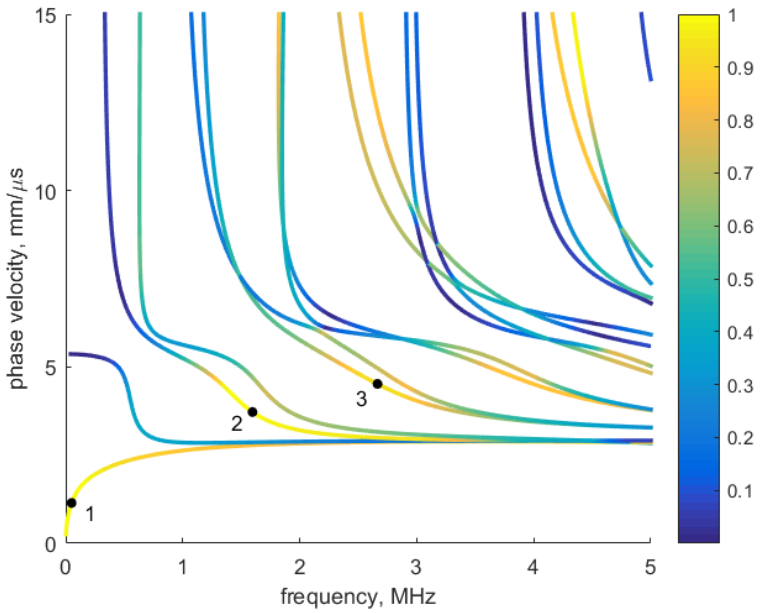

Figure 7.7: Dispersion curve for the bonded aluminum structure; the color corresponds to the normalized u_3 displacement at the interface

The analysis of this transition reveals potential inspection modes. I will demonstrate this in the following pages.

I will use the same aluminum-epoxy joint geometry discussed previously, with two 1.6 mm aluminum adherends and a 0.2 mm epoxy layer. Figure 7.11 shows the non-dimensional dispersion plot, and the bulk shear velocity for aluminum and the S_0 and A_0 modes are marked on the figure. It is clear in the figure where the modes cross over the aluminum shear velocity line and become trapped within the adhesive layer.

First, the A0 mode was discretized so that the displacement mode shape could be calculated for a variety of frequencies. The normalized particle displacement for the x_1 component is shown in Figure 7.12, Figure 7.13 and Figure 7.14. These figures show how the displacement morphs from the expected first anti-symmetric mode of a single plate into an interface mode at each interface. At the higher frequencies, the maximum displacement is on the interface, and this displacement decays towards the

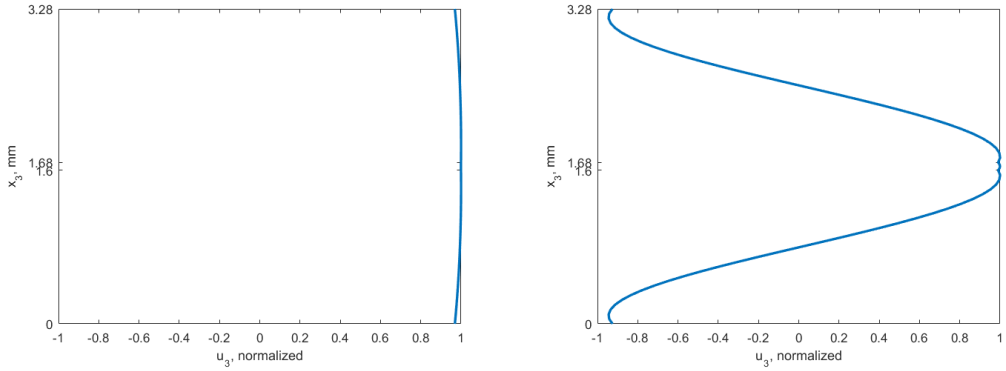

(a) Point 1

(b) Point 2

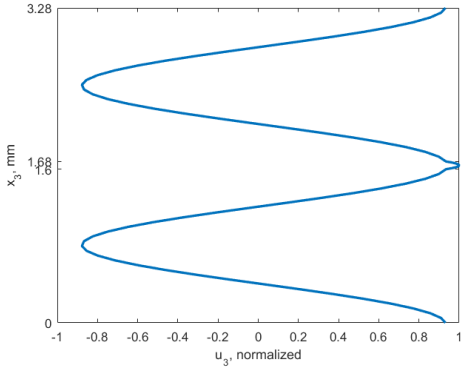

(c) Point 3

Figure 7.8: Bonded aluminum structure; u_3 displacement mode shapes

exterior surfaces, which show zero displacement. Examination of these figures shows that there are three distinct zones. The first zone occurs at the lowest frequencies where the wave behaves as if there were no adhesive layer. The third zone occurs at the higher frequencies where the wave behaves as an interface or interphase wave with large displacements within the adhesive and on the interface and zero displacements on the laminate surface. The second zone is a transitional zone between adhesively dominated behavior and plate or adherend dominated behavior. This zone has both large displacements at the interface and displacements on the plate surface. This zone should be useful for adhesive inspection because the wave mode could still be excited by surface forces.

Additionally, it should be noted that the A_0 mode exists almost entirely below the

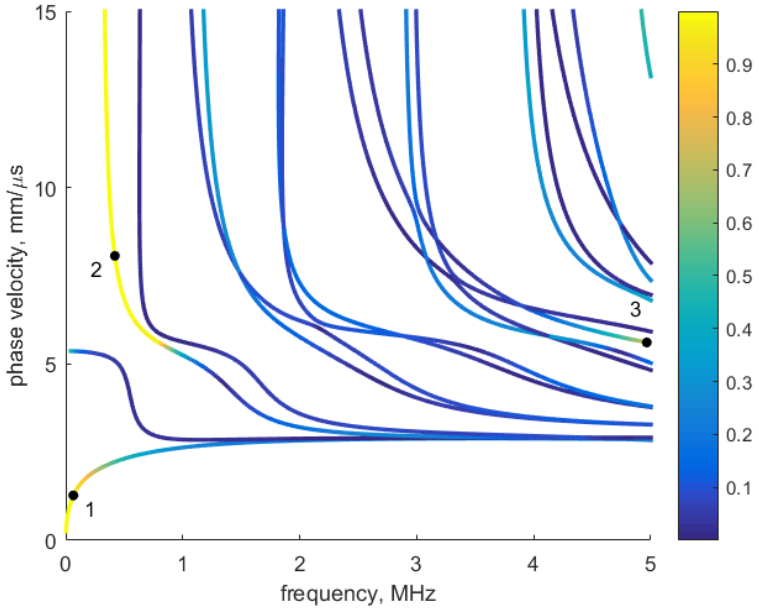

Figure 7.9: Dispersion curve for the bonded aluminum structure; the color corresponds to the normalized σ_{31} displacement at the interface

aluminum shear velocity. Despite this being an indication of a trapped mode, there is still a very large region of surface displacements. This should show that each mode should be analyzed to determine when the transition into a trapped mode occurs.

The next set of three figures show the x_2 component of displacement for the A_0 mode. Again the transition between the three zones is clear with the last zone showing large displacement at in the adhesive and decaying towards the plate surfaces.

The second and last guided mode considered here is the S_0 mode. The displacement mode shapes are shown in the following six figures. We again see the same behavior. However, the mode shape very quickly transitions from the plate zone into the transitional zone, and this 2^{nd} zone extends into a higher frequency than the A_0 mode. This should be due to the fact that the S_0 mode does not cross the aluminum shear speed until a non-dimensional frequency of around 2 or 3.

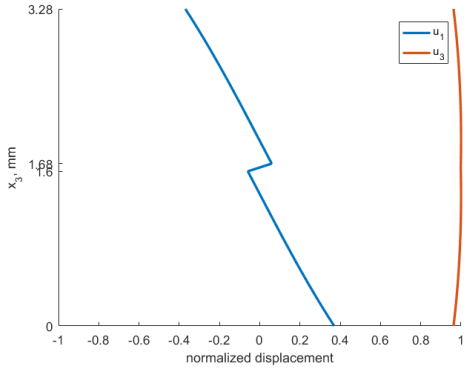

(a) Point 1; displacement

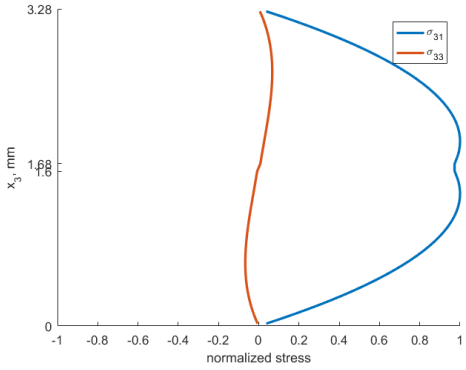

(b) Point 1; stress

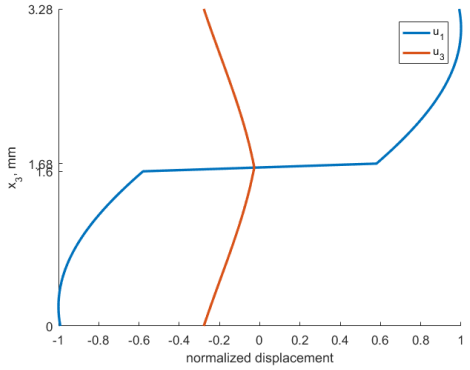

(c) Point 2; displacement

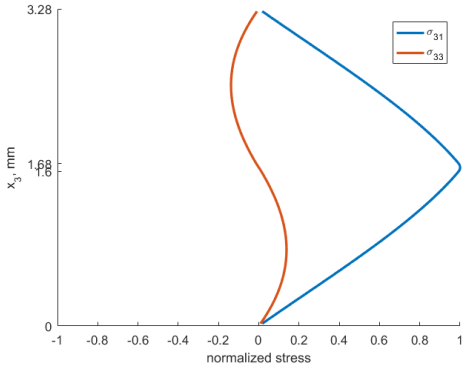

(d) Point 2; stress

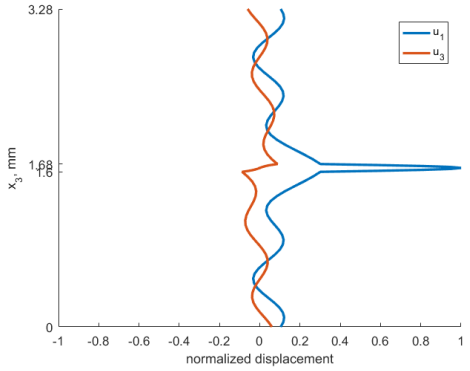

(e) Point 3; displacement

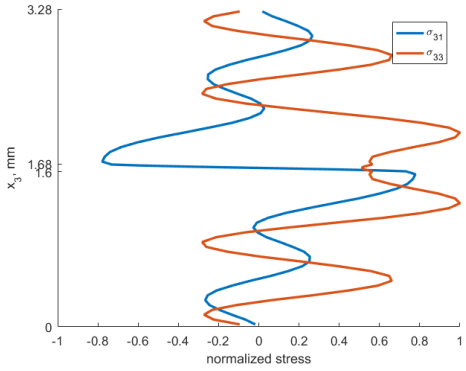

(f) Point 3; stress

Figure 7.10: Bonded aluminum structure; u_3 displacement mode shapes

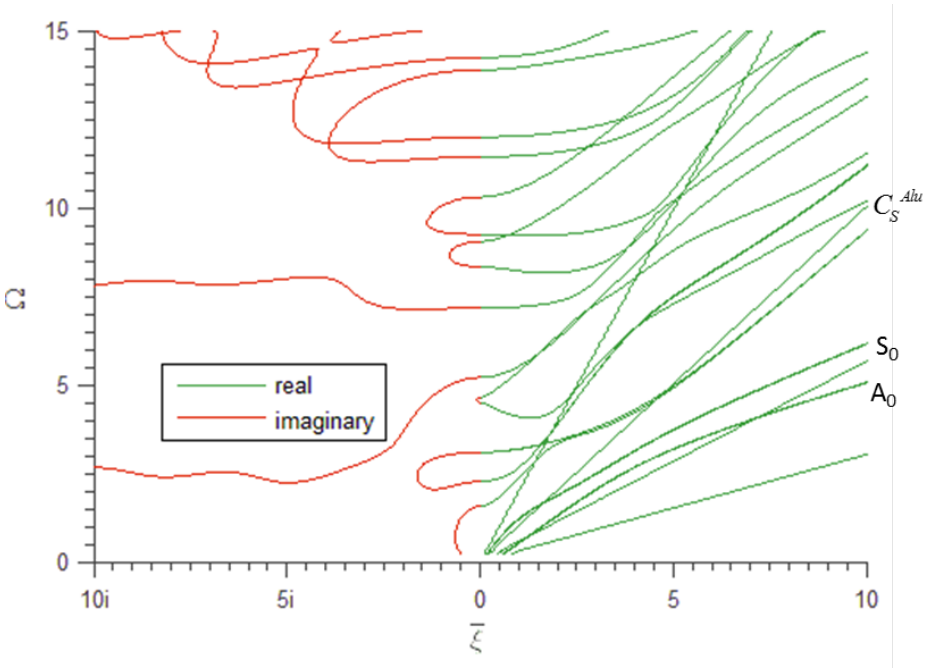

Figure 7.11: Non-dimensional frequency-wavenumber plot

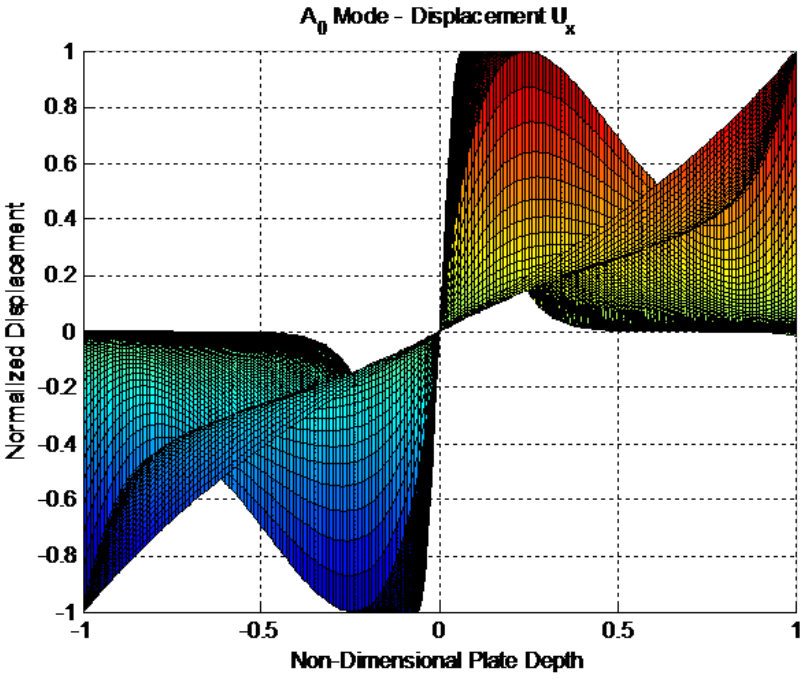

Figure 7.12: A_0 mode x_1 particle displacement component, view 1

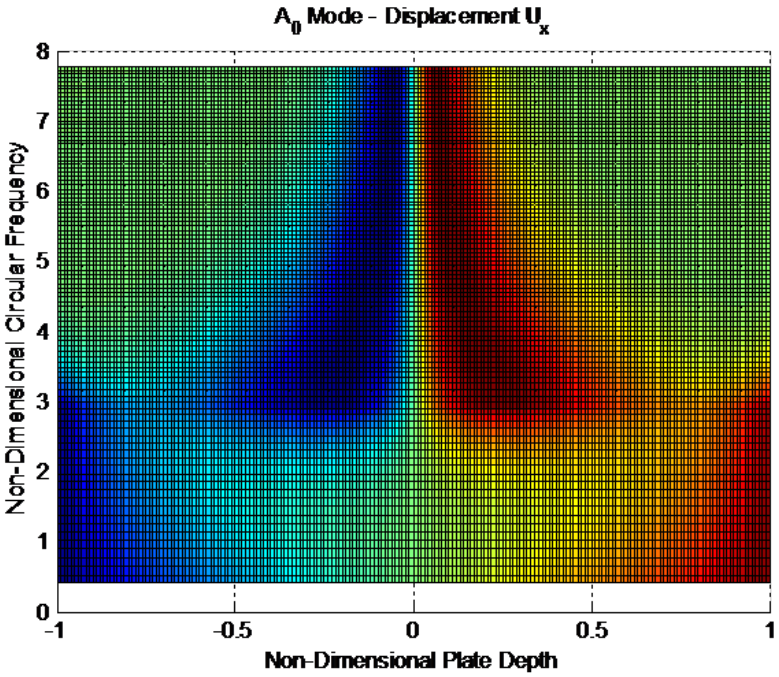

Figure 7.13: A_0 mode x_1 particle displacement component, view 2

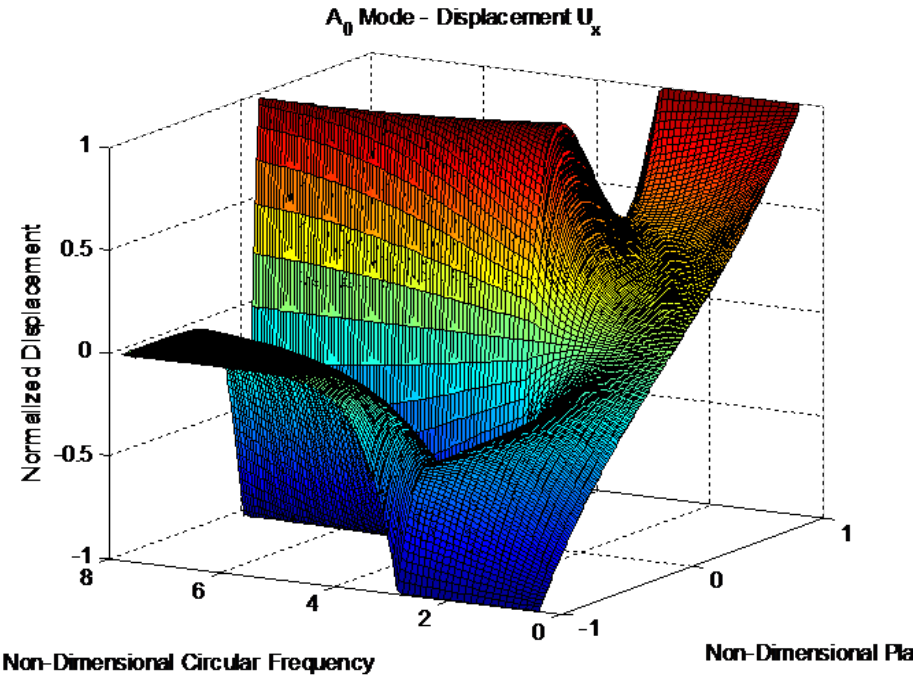

Figure 7.14: A_0 mode x_1 particle displacement component, perspective view

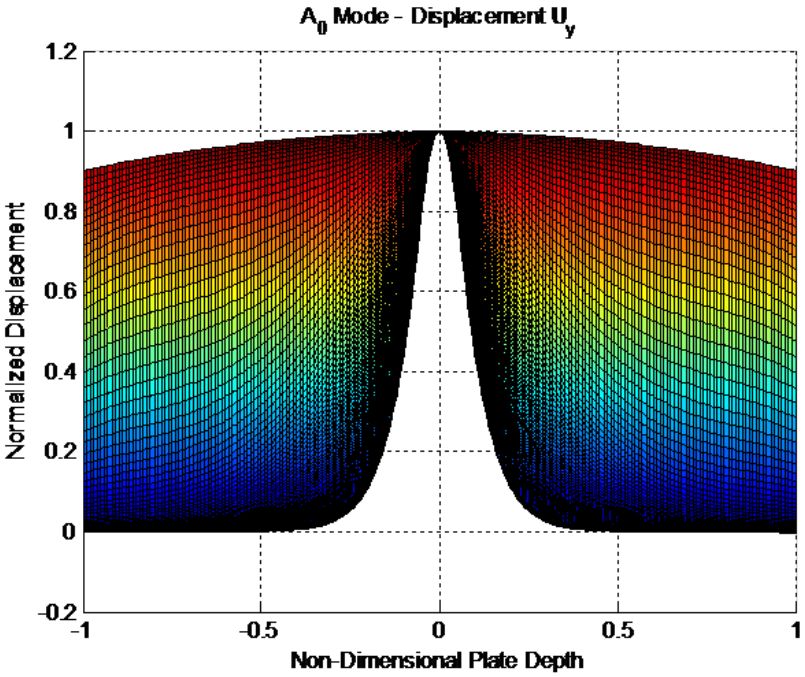

Figure 7.15: A_0 mode x_2 particle displacement component, view 1

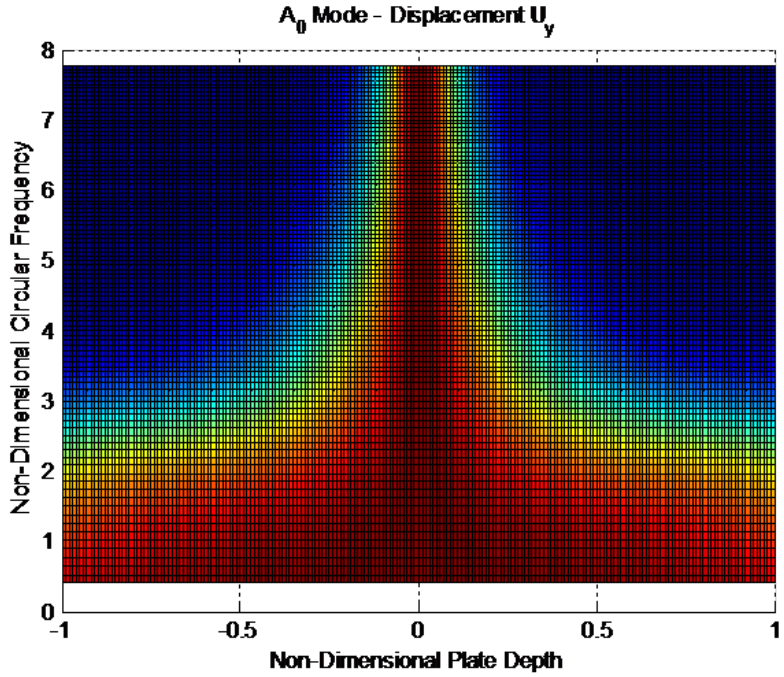

Figure 7.16: A_0 mode x_2 particle displacement component, view 2

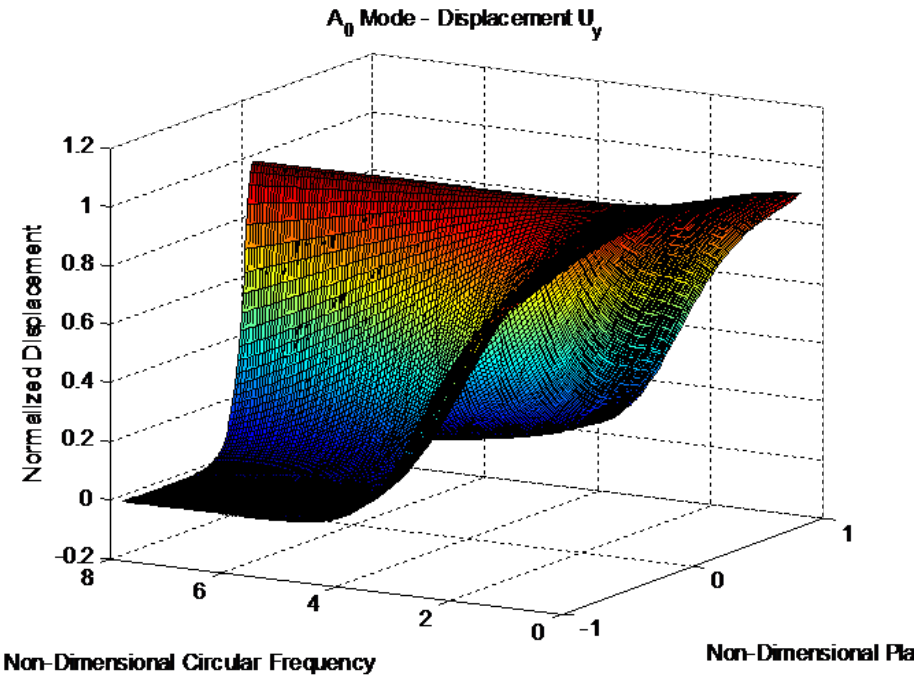

Figure 7.17: A_0 mode x_2 particle displacement component, perspective view

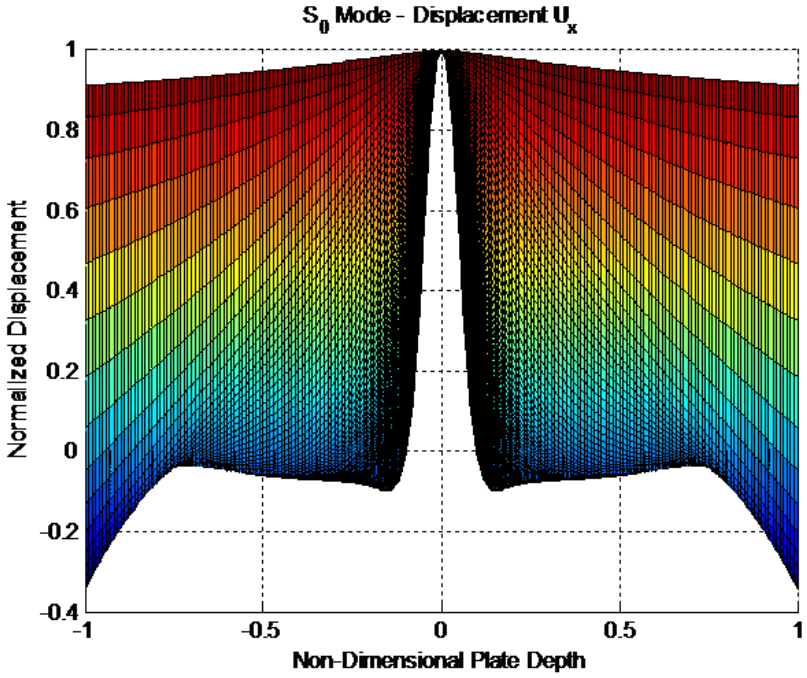

Figure 7.18: S_0 mode $x_1$particle displacement component, view 1

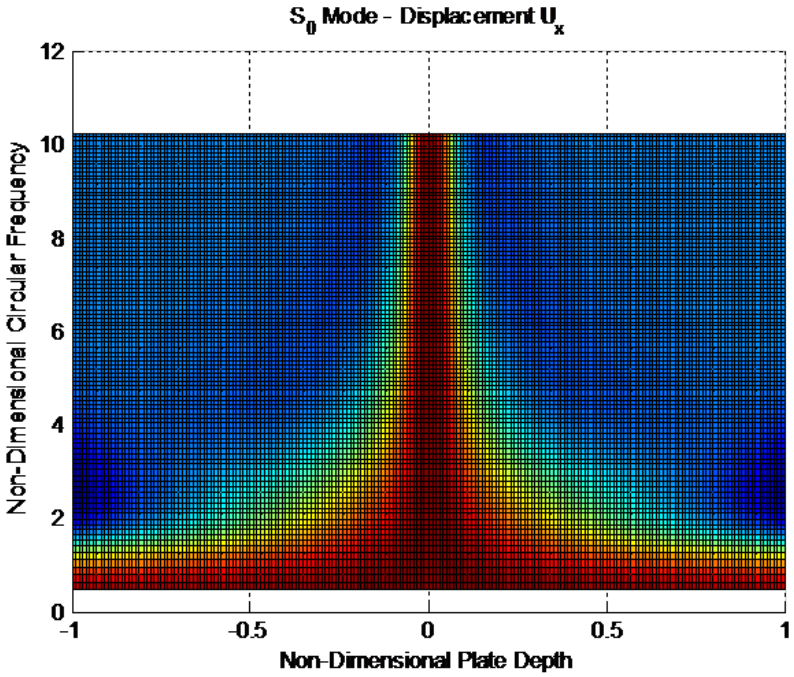

Figure 7.19: S_0 mode x_1 particle displacement component, view 2

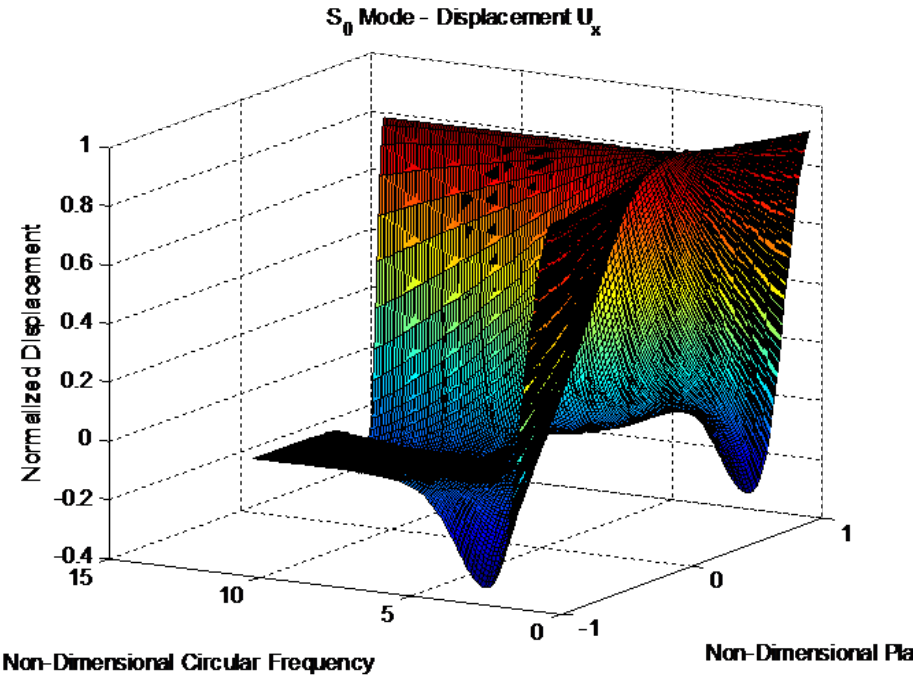

Figure 7.20: S_0 mode x_1 particle displacement component, perspective view

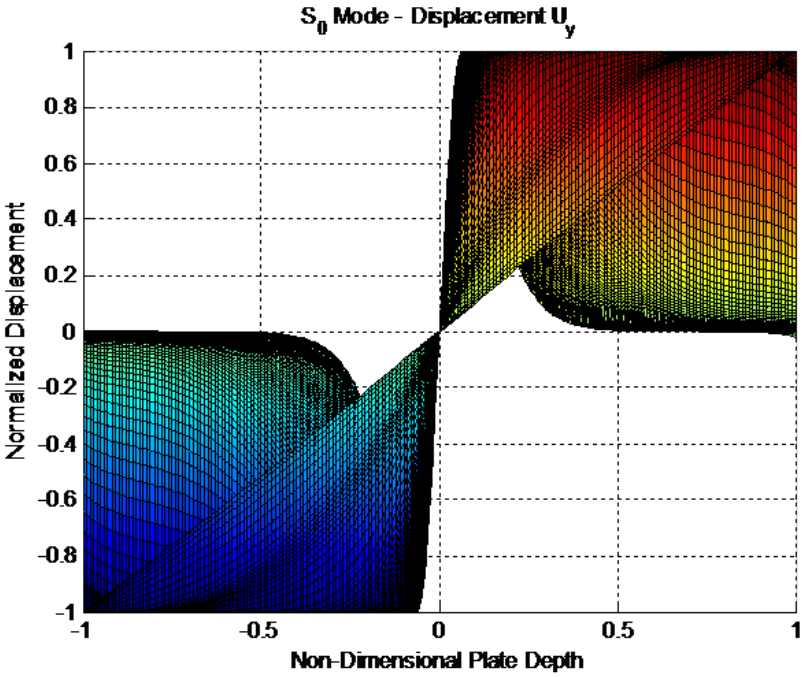

Figure 7.21: S_0 mode x_2 particle displacement component, view 1

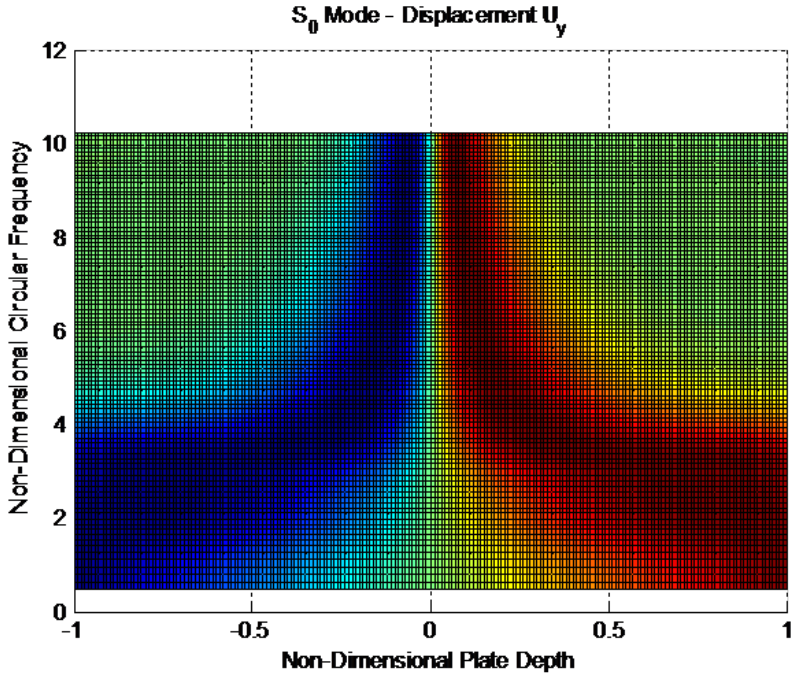

Figure 7.22: S_0 mode x_2 particle displacement component, view 2

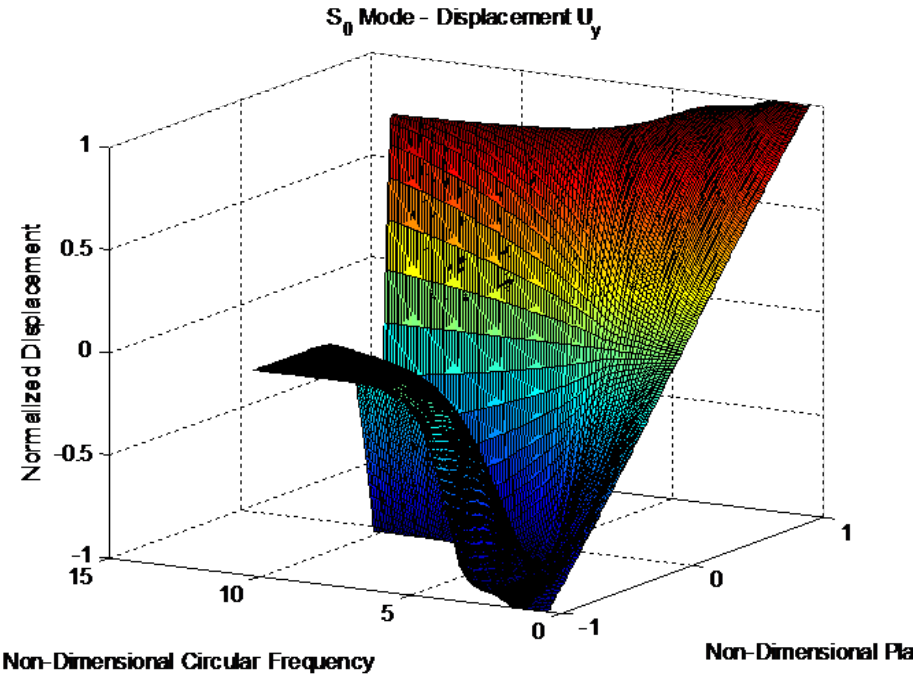

Figure 7.23: S_0 mode x_2 particle displacement component, perspective view

7.3.2 Damage modeling

7.3.2.1 Influence of weak bonding

A better method for finding the sensitive modes is to generate dispersion curves and mode shapes from a laminate model that includes damage. For a weak bonding layer, this is accomplished by modeling a very thin layer which contains a unique stiffness matrix and/or density. In order to demonstrate we will consider two composite laminates with a layup of $[0, 45, -45, 90]_S$ with a total thickness of 1 mm. The lamina stiffness matrix is shown in Eq. (7.1). There is an epoxy adhesive bonding the two laminates with a total thickness of 200 microns. The epoxy is modeled as an elastic material with a Young's modulus of 3.5 GPa, a Poisson's ratio of 0.3 and a density of 1250 $\frac{kg}{m^3}$. The weak boundary layer is placed on the upper interface, and the thickness is modeled as a fraction of the total adhesive thickness. The weak layer is given a Young's modulus of 1 GPa and the same density and Poisson's ratio, and the

thickness is 10 microns.

$$\mathbf{C} = \begin{bmatrix} 143.8 & 6.2 & 6.2 & 0 & 0 & 0 \\ & 13.3 & 6.5 & 0 & 0 & 0 \\ & & 13.3 & 0 & 0 & 0 \\ & & & 3.4 & 0 & 0 \\ & Sym & & & 5.7 & 0 \\ & & & & & 5.7 \end{bmatrix} GPa \tag{7.1}$$

The dispersion curve was calculated using the finite element approach where the frequency was discretized and a polynomial eigenvalue problem was solved for the complex wavenumbers. Both the pristine and weak boundary layer solutions were calculated, and the real values are shown in Figure 7.24. It clear from inspection of the dispersion curve that the weak boundary layer has altered the curves for some of the mode shapes. The crowded regions on the graph are a bit misleading, but it clear that the trapped modes have large differences. We know that these should be trapped modes because they occur below the smallest shear velocity for the bounding composite laminate; however, the previous subsection showed that the modes go through a transitional period before they become trapped. Therefore, only an analysis of the mode shapes will reveal the true state. The slower red curve is the shear velocity in the bounding 0-degree layer. Another observation is that even though the phase velocity of the trapped modes are very different when the boundary layer is introduced, the group velocity will be similar, making it difficult to detect through the double mode conversion method.

In order to provide a better interpretation of the results, the weak boundary layer dispersion has been plotted in Figure 7.25. The color of the plots has is based on the distance to the nearest pristine mode, in terms of wavenumber. So the red colors in the figure show modes which have undergone large shifts in wavenumber due to the existence of the weak boundary layer. We can clearly see the changes in the

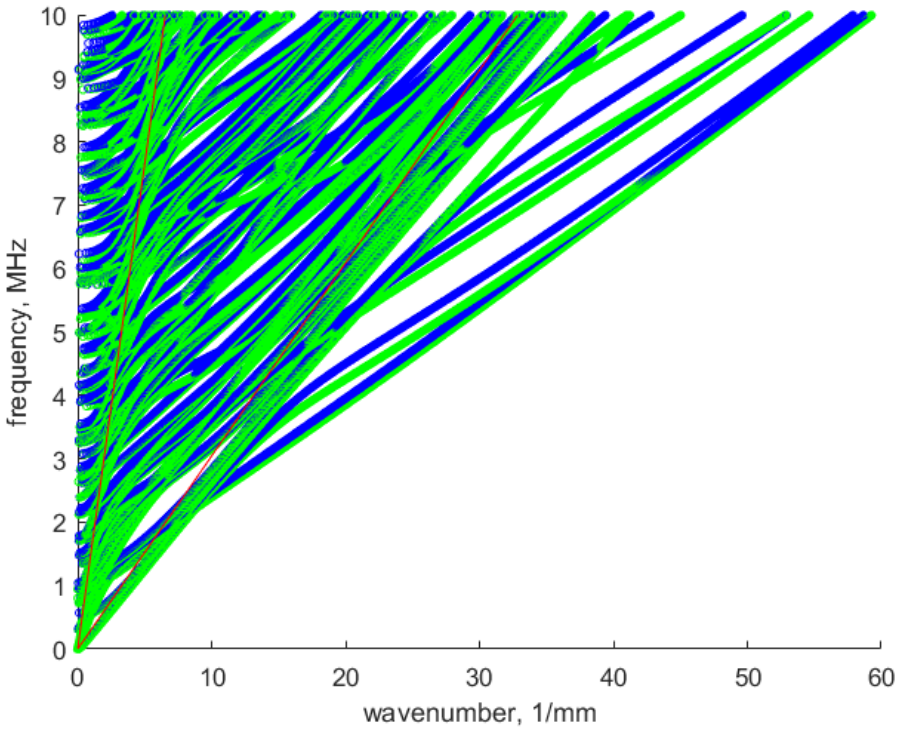

Figure 7.24: Pristine vs. Weak Boundary Layer

trapped modes, but it is also clear that some of the other higher order modes have been shifted. We can also see that there is some shifting near the frequency axis.

In order to take a closer look at the higher order modes that are near the frequency axis, a second plot was generated as shown in Figure 7.26. For this figure, the real wavenumbers were discretized and the eigenvalue problem was used to calculate the frequency. This provides a more data points near the frequency axis. It appears that several of the higher order modes have been shifted in the frequency domain, especially close to zero wavenumber. Once again a second plot was generated to study the frequency shift, see Figure 7.27. This time the amplitude corresponds to the frequency shift, and the curves are from the weak boundary layer model. Several of the higher modes at zero wavenumber have frequency shifts of over 100 kHz. This could be used in a normal incident spectroscopy inspection to indicate a weak boundary layer. Additionally, there is a propagating mode with over 200 kHz

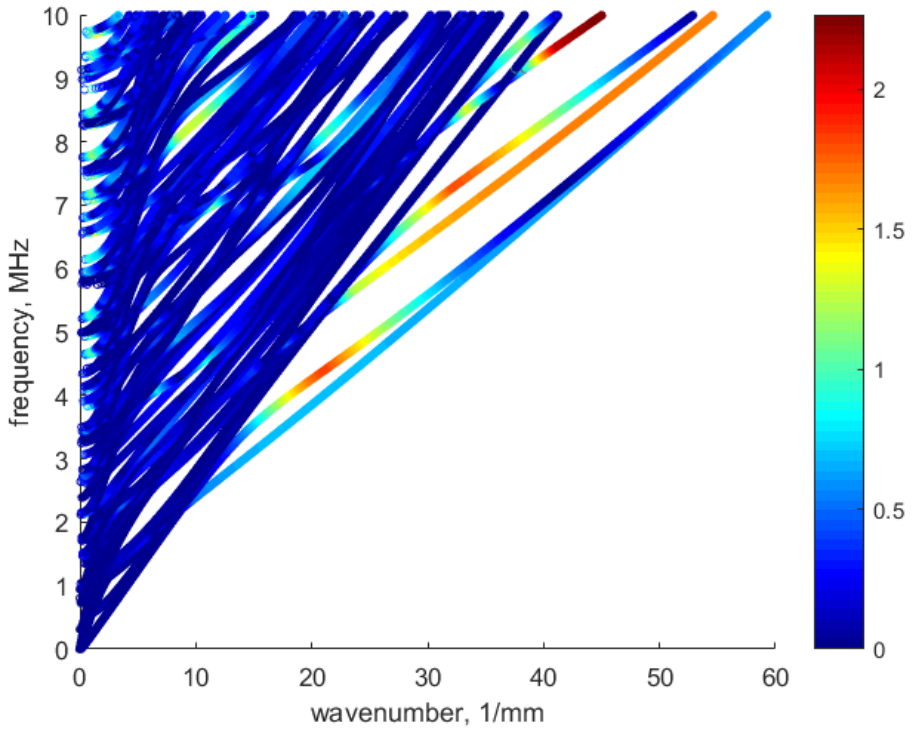

Figure 7.25: Wavenumber shift

frequency shift from the nearest pristine mode.

In order to understand why some of the modes exhibit large differences between the damaged and pristine model, the displacement mode shape for the most sensitive mode has been plotted in Figure 7.28. This mode is the dark red region of the previous figure. This mode shape was taken at a frequency of 7.9 MHz and a wavenumber of 7.6 mm^{-1}. There are several interesting observations from this figure. The first is that there are very large displacements around the adhesive zone. In fact, it appears that the shear stress will be a maximum at the interfaces. This could explain part of the sensitivity. The second observation is that all three displacement components are present in this mode. This indicates that the weak boundary layer has destroyed the symmetry that was previously present in the structure. This fact could be exploited in an inspection scheme, where a wave is excited along a symmetry plane and shear displacements are measured in the direction that we would expect there to be zero

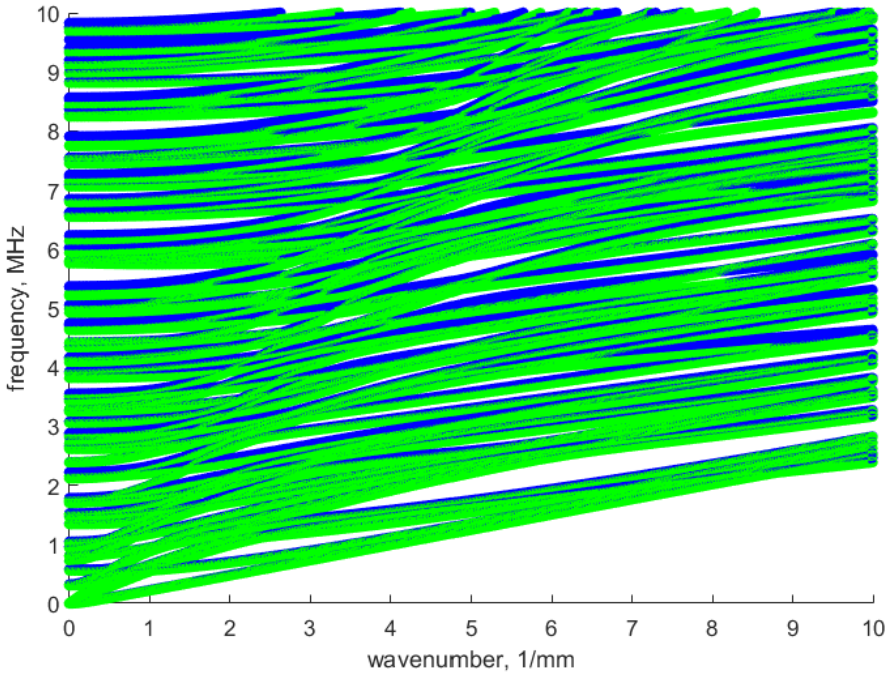

Figure 7.26: Pristine vs. weak boundary layer

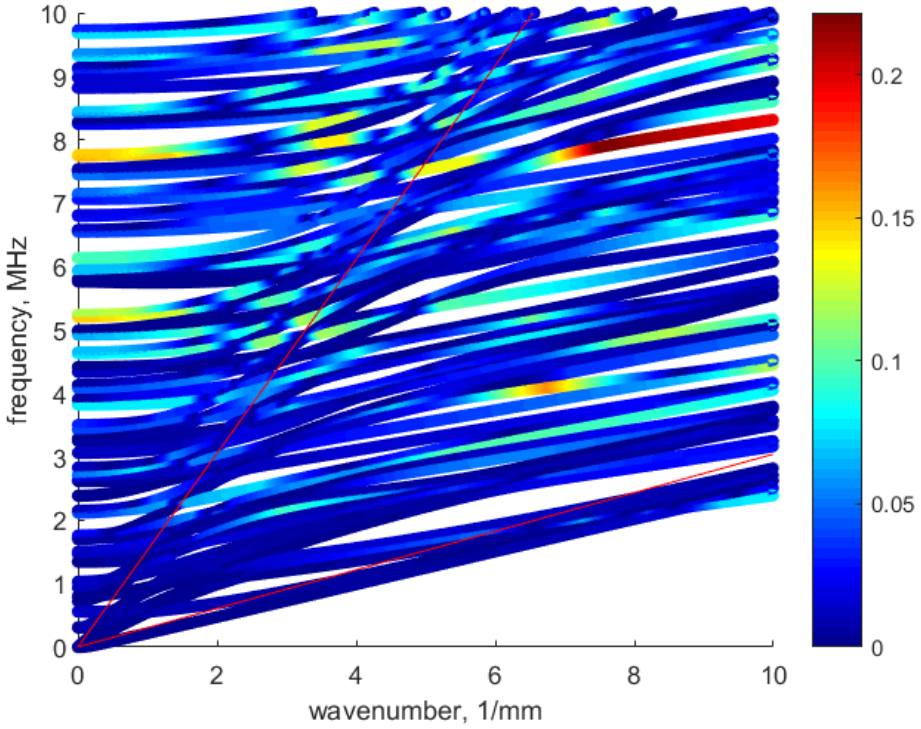

Figure 7.27: Frequency shift

displacements. The last observation is that the mode shape does not exhibit symmetry through the thickness of the structure. It is clear that the displacements on one of the interfaces is greater than the other. This must be due to the weakened single interface.

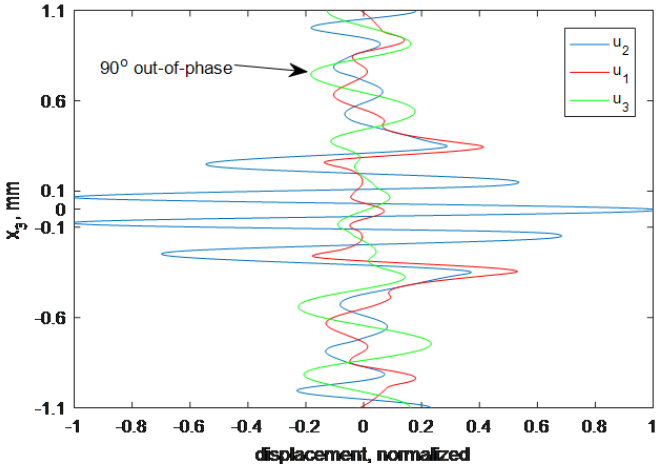

Figure 7.28: Displacement mode shape

7.3.2.2 Influence of all factors

As discussed in the review chapter, many authors have considered using either interface or interphase waves, while others have considered plate waves. The interface and interphase waves are modeled with half spaces and the plate waves are modeled with traction free surfaces. Some others discuss the trapped interphase waves that exist when the phase velocity is below the shear velocity of the adherend, but the authors do not discuss how this wave mode transitions between the two regimes or discuss that this single mode can act as all three wave types depending on the frequency. The analysis of this transition reveals potential inspection modes.

Some authors investigate the mode shape of guided waves in order to determine the sensitive modes. A better method for finding the sensitive modes is to generate dispersion curves and mode shapes from a laminate model that includes damage.

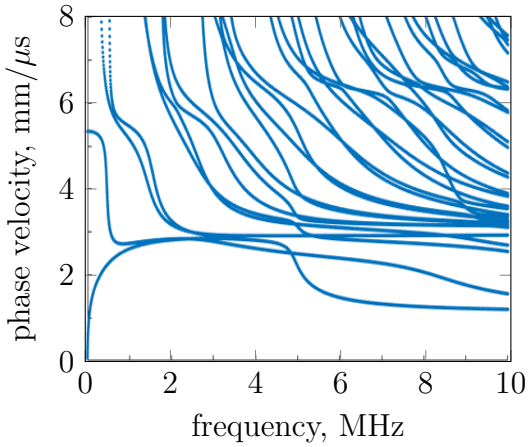

(a) Initial dispersion curve

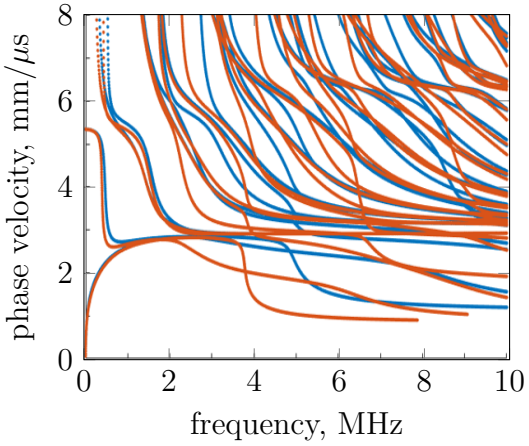

(b) Decreasing adhesive modulus

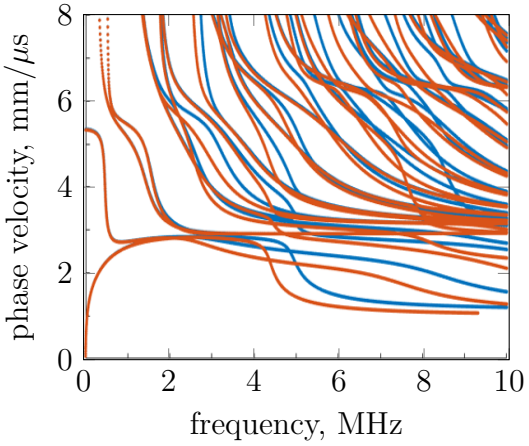

(c) Decreasing adhesive density

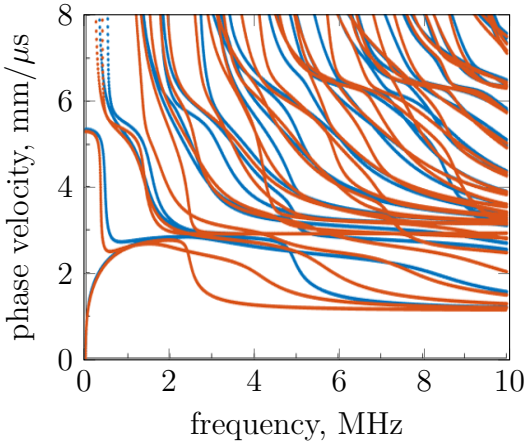

(d) Increasing adhesive thickness

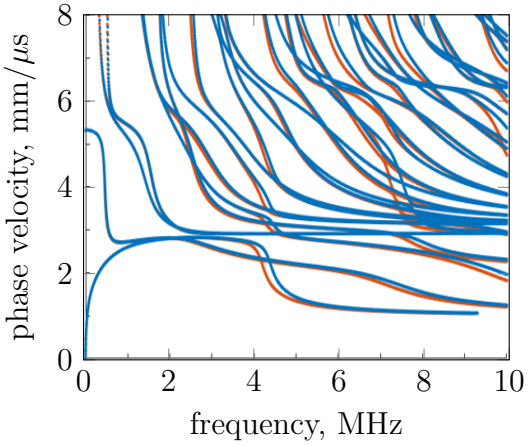

(e) Addition of a weak interphase layer

Figure 7.29: Calculated dispersion curves from the immersion technique, 2.25 MHz transducer

For a weak bonding layer, this is accomplished by modeling a very thin layer which contains a unique stiffness matrix and/or density. Changes in the behavior of the damaged mode can be detected through experimental methods. This is a direct or primary method for detecting damage, a secondary method is to utilize mode conversion, reflection and refraction at transitions between damaged and undamaged regions of the structure.

The considerable challenge in using the primary method for detecting a weak interphase is the large shifts in the guided wave behavior due to changes in the bondline properties. Figure 7.29 shows numerically calculated dispersion curves for a bonded aluminum plate. The dispersion curves have been calculate with a custom one-dimension (through-thickness) finite element scheme, ensuring convergence in the desired phase velocity - frequency domain. The blue curve corresponds to the original laminate, while the orange curve corresponds to the altered laminate. Four alternate scenarios have been considered; a decrease in the adhesive Young's modulus, a decrease in the adhesive density, an increase in the adhesive thickness and the addition of a weak interphase layer. The laminate consists of a 200 μm adhesive between two 1.6 mm thick aluminum layers. The weak interphase layer is added to a single interface and is 10 μm thick with half the modulus of the adhesive material. The total adhesive thickness is maintained when the weak interphase is added to the laminate.

7.3.2.3 Best inspection methods

Two major observations can be drawn from Figure 7.29. First, changes to material properties of a very thin layer near the interface result in changes in the behavior of guided waves. Second, changes to the entire bond line result in larger changes in the guided wave behavior. In order for the small changes due to a weak interphase layer to be detected, the bondline characteristics must first be well known.

This can be resolved in two ways.

- Normal incidence spectroscopy and/or low frequency (in context) guided waves are used to determine the properties of the adhesive layer. Next, changes in higher frequency guided waves, as compared to the expected nature, are used to find areas of weak adhesion.
- A large area of the dispersion curve is calculated at once and the properties of the bondline and the weak interphase layer are determined in a single optimization routine. The difference between the properties of the interphase layer and the bulk adhesive will indicate damage at the interface.

7.3.3 Finite element analysis

In order to verify the contact guided wave method, finite element simulations have been performed of the excitation of guided waves through a angled wedge. Two different incident angles have been chosen to highlight the importance of creeping waves in the generation of plate guided waves. The first incidence angle is 30 degrees, which is less than the second critical angle. At this angle shear waves are generated in the aluminum, which reflect and refract to create guided waves. The second angle is 60 degrees, this is greater than the second critical angle. Traditionally, an wave at an angle greater than the 2nd critical angle is fully reflected. This explanation ignores the creeping wave. Instead creeping waves are generated, which make up the partial waves that form guided waves at this low phase velocity.

The model consists of a bonded aluminum plate with two rexolite wedges. The wave is generated on the wedge border by a forced displacement of a single count tone burst, followed by propagation through the domain. A dense mesh was used due to the high frequencies and corresponding short wavelengths; element length of 25 μm.

Figure 7.30 shows a series of snap shots of the model at various time increments at the 30 degree incidence angle. The frame is centered on the excitation wedge,

and the color plot corresponds to the magnitude of the von Mises stress. Following each frame; the wave is excited; the wave reflects and refracts at the interface; waves continue to reflect and refract at each interface; a guided wave is formed; the guided waves continues away from the wedge. This angle is less than the second critical angle; therefore, at least one of the refracted waves is a bulk wave with a clear wavefront that is expected from Snell's law.

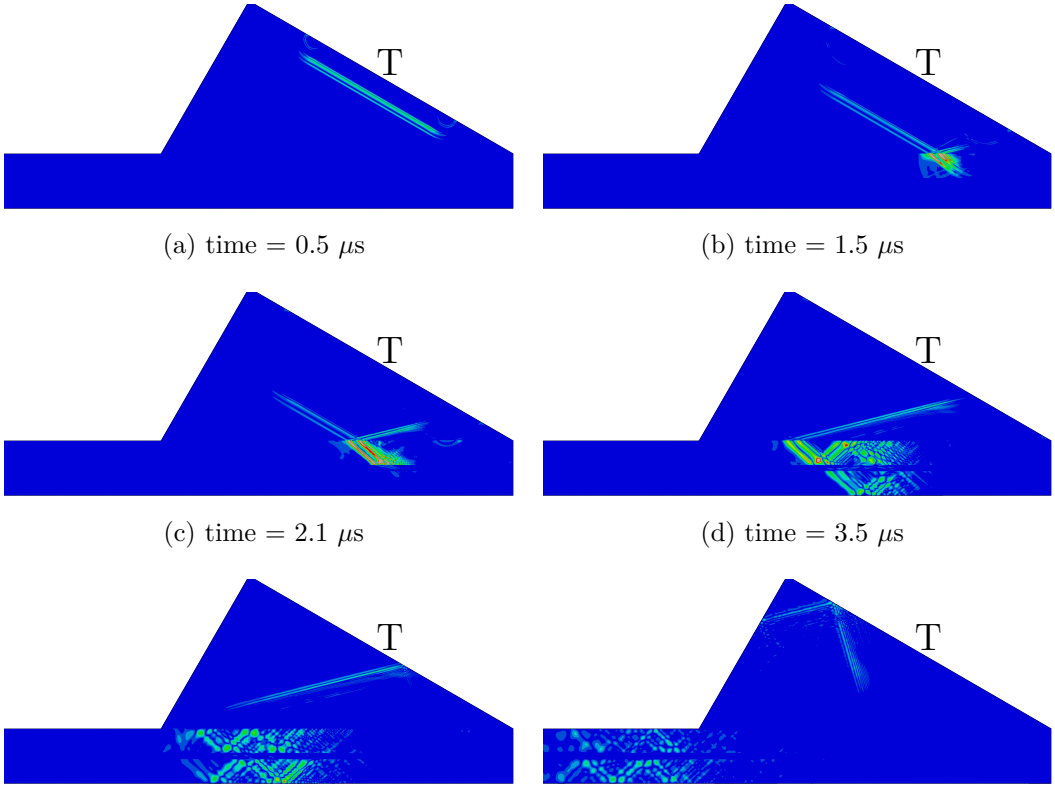

(a) time = 0.5 μs (b) time = 1.5 μs

(c) time = 2.1 μs (d) time = 3.5 μs

(e) time = 5.0 μs (f) time = 10.0 μs

Figure 7.30: FEA simulation of a 30 degree wedge generating a guided wave in a bonded aluminum structure, single count 5 MHz tone burst

The second series of pictures corresponds to the 60 degree incidence angle wedge, Figure 7.31. This angle is greater than the second critical angle, typically represented as total reflection. These time shots follow a similar series, except that the refracted wave at the top interface is a creeping wave. This can be determined from two clues. First, the wavefront is along the plate or propagation direct, instead of at an angle

as in Figure 7.30. Second, the amplitude decreases in the direction normal to the interface. Clearly the wave is not completely reflected back into the wedge, and guided wave is still generated. This should be clear since Rayleigh waves are known to have a phase velocity just below the bulk shear velocity.

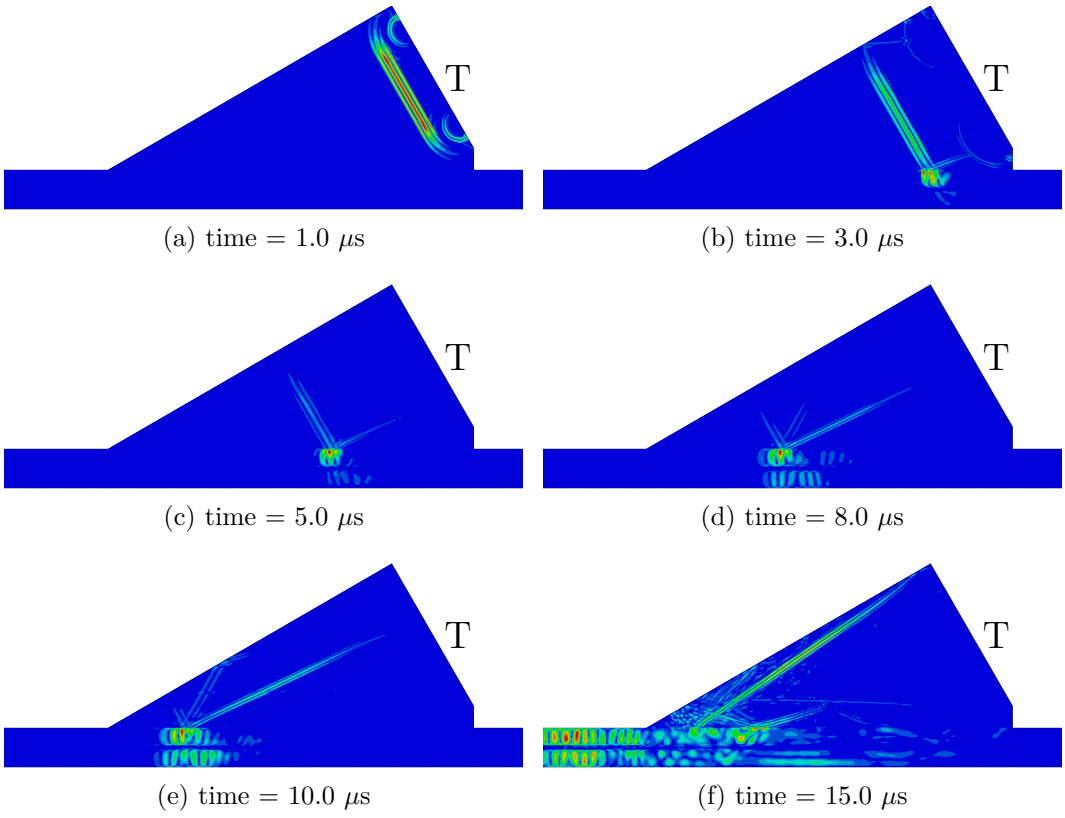

(a) time = 1.0 μs (b) time = 3.0 μs

(c) time = 5.0 μs (d) time = 8.0 μs

(e) time = 10.0 μs (f) time = 15.0 μs

Figure 7.31: FEA simulation of a 60 degree wedge generating a guided wave in a bonded aluminum structure, single count 2 MHz tone burst

Figure 7.32 shows a long guided wave packet propagate along the plate between the two wedges. The guided waves are excited from the short pulse in the wedge and form long dispersive guided waves in the laminate. These figures further prove that the wedge method can generated guided waves, even at angles greater than the second critical angle.

The last set of snap shots, Figure 7.33, shows the guided waves refracting into pressure and shear waves in the receiving wedge. It is shown that the pressure waves are normal to the 60 degree line, while the shear waves have a lower incidence angle.

(a) time = 1 μs

(b) time = 10 μs

(c) time = 15 μs

(d) time = 25 μs

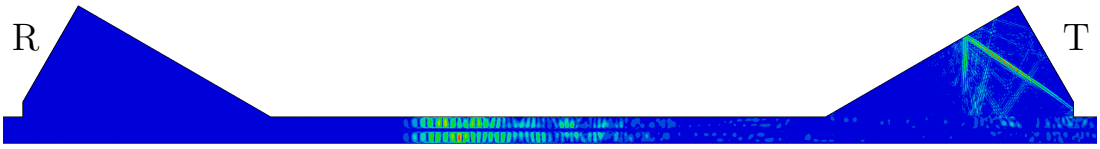

(e) time = 30 μs

(f) time = 35 μs

(g) time = 45 μs

Figure 7.32: FEA simulation of a 60 degree wedge generating a guided wave in a bonded aluminum structure and propagation along the plate to a receiving wedge, single count 2 MHz tone burst

There are some secondary reflections from the top surface of the wedge; this could be reduces by using a 90 degree angle at the leading edge of the wedge. Clearly the receiving wedge can detect the guided waves and accurately predict the phase velocity.

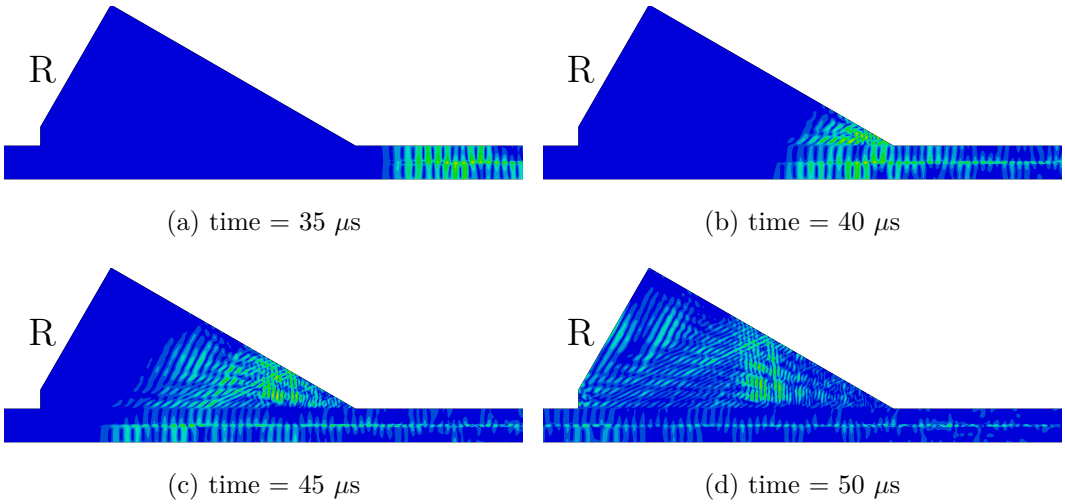

(a) time = 35 μs (b) time = 40 μs

(c) time = 45 μs (d) time = 50 μs

Figure 7.33: FEA simulation of a 60 degree wedge detecting a guided wave in an bonded aluminum structure, single count 2 MHz tone burst

7.4 Experimental Verification

The following section discusses the experimental verification of the inspection techniques earlier in the chapter. The guided wave inspection method is contrasted with the conventional normal incidence inspection scheme. A bonded aluminum test specimen was manufactured with defects for proof-of-concept testing of the guided wave concepts. The test specimen was first subjected to nondestructive testing using (a) conventional ultrasonic inspection, and (b) guided wave inspection. Subsequently, the specimen was cut up into coupons for mechanical testing to evaluate the pristine and defect bonding areas. Future work will use carbon fiber reinforced plastic (CFRP) substrates with similar film adhesives.

7.4.1 Manufacturing Coupons

The proof-of-concept test specimen was made from two 1.6 mm thick 2024-T3 aluminum plates. These plates were bonded with a single layer of 3M AF 555M .05wt in a compression molding machine with the recommended cure cycle. An attempt was made to limit squeeze out, but a good amount of adhesive was lost from the bond line. Three different artificial defects were introduced into the part. An artificial disbond was created by leaving the protective film on one side of the film adhesive over the desired region. Two types of contaminates were used to create "kissing bond" defects: Frekote and silicone oil. Each contaminate was wiped onto the defined surface with a sterile gauze pad. Each of these defects were only applied to a single interface. The dimensions of the test specimen are shown in Figure 7.34, along with the defect locations.

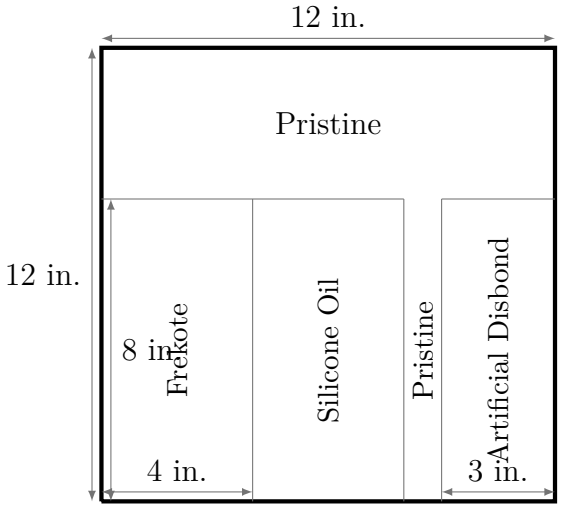

(a) Schematic

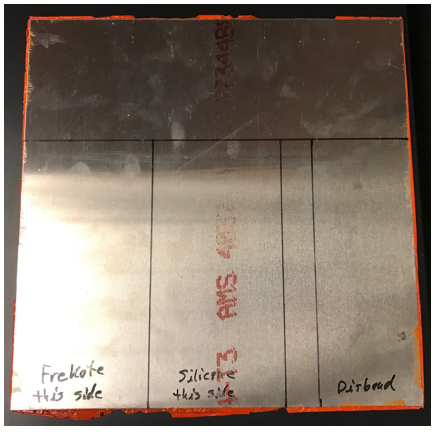

(b) Picture following adhesive curing cycle

Figure 7.34: Proof-of-concept test specimen with artificial defects; Frekote contamination, silicone oil contamination and a disbond

7.4.2 Conventional Ultrasonic Inspection

The conventional UT inspection follows the general techniques outlined in Chapter 3. The best way to detect a disbond in an adhesively bonded structure, especially with thin substrates and a fast longitudinal wave velocity, is the through transmission method. Utilizing the double through transmission technique, the entire test specimen was scanned in the immersion tank with an un-focused 2.25 MHz transducer. The root mean square value of the double through transmission wave packet can be used to give an indication of the power of the signal that was transmitted through the structure, see Figure 7.35 for a surface plot of the RMS power magnitude. The darker blue color corresponds to the low end of the magnitude spectrum. There is a clear indication of the disbond, but it is not clear that there is a weak bond. Some features can be seen, including over the weak bond areas, but this is more likely to be variations in the adhesive thickness.

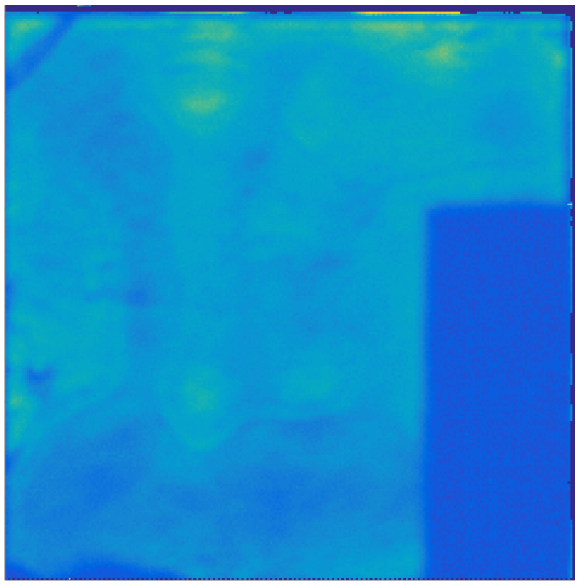

Figure 7.35: Double through transmission, RMS Power, 2.25 MHz transducer

The second technique utilized the phase shift of the wave pulse. Changes with respect to a known good region can be an indication of a difference at the bond line. The phase shifts are detected by measuring the change in amplitude at a set

time delay from the front wall surface. Two different transducers were used for this inspection; an unfocused 2.25 MHz transducer and a focused 20 MHz transducer. The results are shown in Figure 7.36.

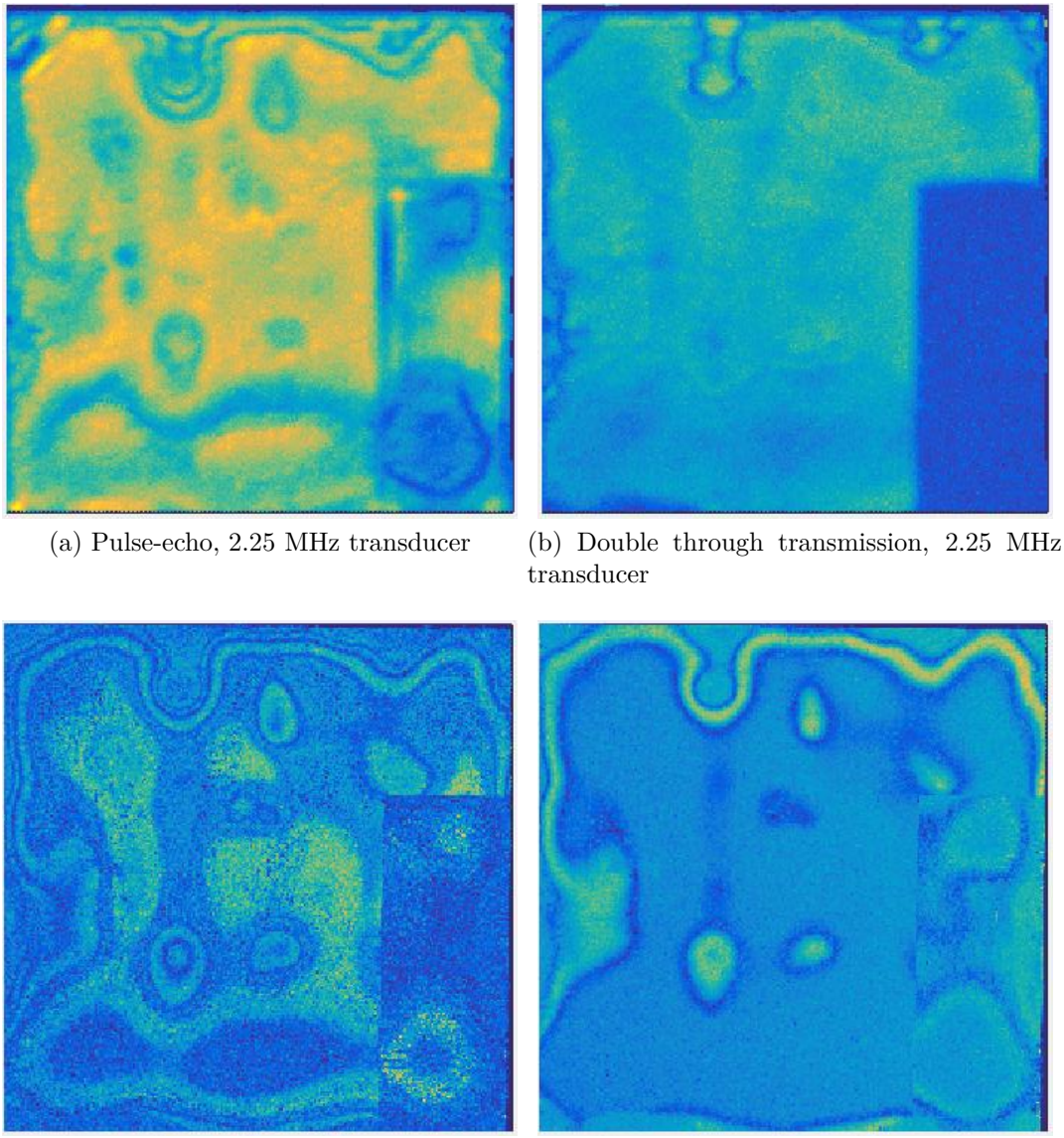

(a) Pulse-echo, 2.25 MHz transducer

(b) Double through transmission, 2.25 MHz transducer

(c) Pulse-echo from the adhesive layer, 20 MHz transducer

(d) Pulse-echo from the adhesive layer, 20 MHz transducer

Figure 7.36: Normal incidence ultrasonic phase shift analysis of the bonded aluminum plate

7.4.3 Guided Wave Inspection

7.4.3.1 Contact method

The contact guided wave technique was described in Chapter **??**. In this section, the experimental results are analyzed to determine the usefulness of the approach. In order to verify that the method generates the correct dispersion curves, the first test was performed on an aluminum plate (1.6mm thick 2024-T3). The excitation transducer has a center frequency of 2.25 MHz. The results are shown in Figure 7.37, where plot (a) contains just the experimental result and plot (b) has the numerically determined dispersion curve overplayed onto the experimental results. The numerical results match very well with the experimental results, verifying that the procedure works as intended.

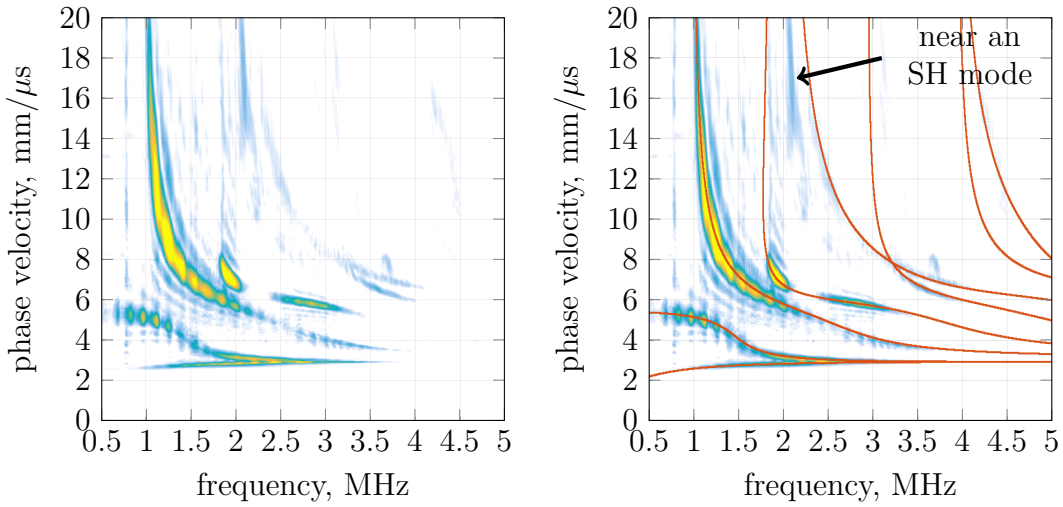

Figure 7.37: Dispersion curve for a single layer of 2024 aluminum

With the techniques verifies, the same procedure was performed on the proof-of-concept test specimen. The dispersion curves were calculated for four regions; the good bond region, the Frekote contaminated region, the silicone oil contaminated region, and the disbonded region. Figure 7.38 shows the results for each region. The

most dramatic change is in the disbonded region where the guided wave experiences high attenuation. Some changes can be observed to the contaminated regions, but not significant or obvious.

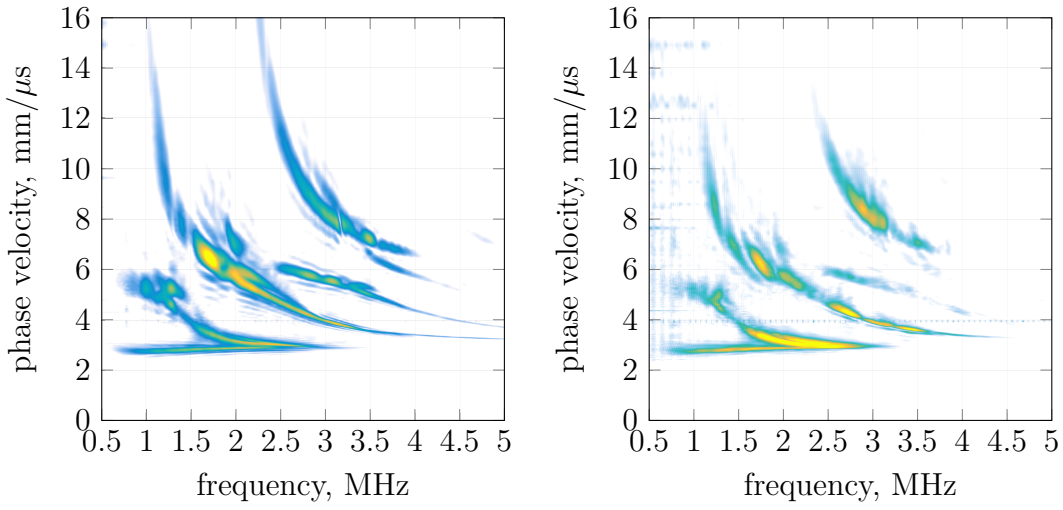

(a) good bond

(b) Frekote

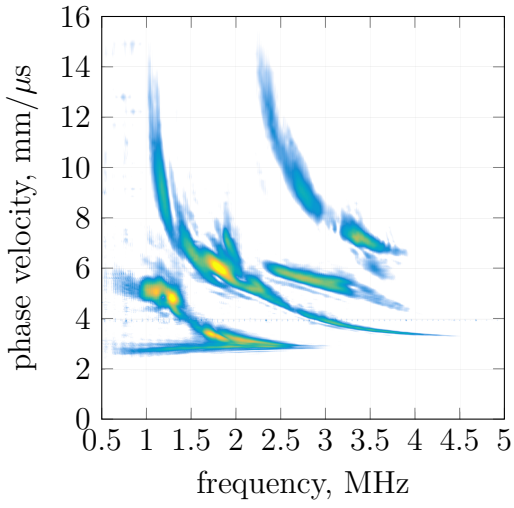

(c) Silicone Oil

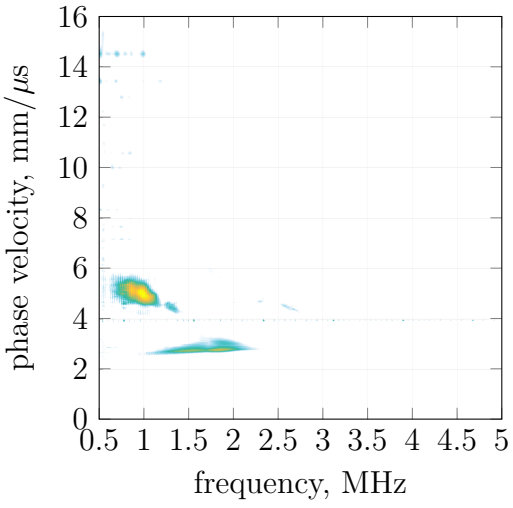

(d) Disbond

Figure 7.38: Dispersion curves from the aluminum bonded plate through the contact method

In order to better highlight the changes to the dispersion in the contaminated region, the numerical dispersion curve was calculated for the bonded structure with the expected material properties and thickness for the adhesive.

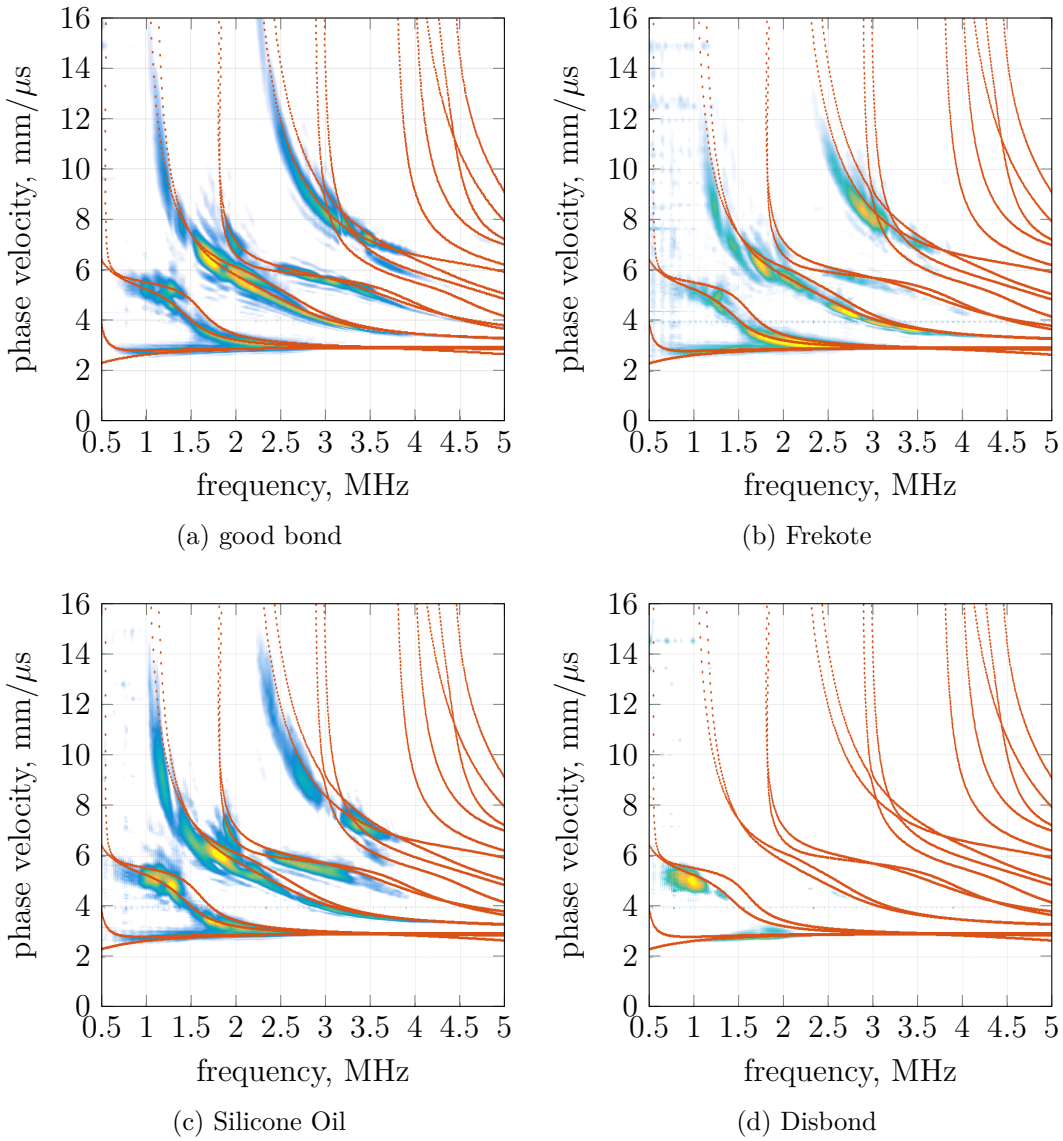

(a) good bond

(b) Frekote

(c) Silicone Oil

(d) Disbond

Figure 7.39: Dispersion curves from the aluminum bonded plate through the contact method with an overlay of the estimated dispersion curve for the pristine structure

Figure 7.39 again shows the experimental results with the addition of the numerical dispersion curve. Plot (a) shows the dispersion in the uncontaminated region. The numerical results match the low frequency region well, but the higher frequencies begin to shift away from the expected behavior. This could be caused by changes to the bondline and/or changes at the interface. Future work will explore the use of an optimization scheme to match the dispersion curve with material properties. Plots

(b) and (c) show increased shifting from the ideal curve. This can be attributed to changes at the interface and changes to the bondline properties as a result of the reaction to the contaminates. Plot (d) shows the disbonded dispersion curve. The small portion of the experimental dispersion curve that was found is clearly different from the bonded structure dispersion curve.

7.4.3.2 Immersion method

The techniques for the immersion method were outlined at the beginning of this chapter.. This section explores the experimental results. This experimental method generates a large amount of data that reveals interesting facts about the nature of guided waves. A fixture is used to rotate the inspected plate inside of the water tank. This fixture has a limit on the size plate that can be manipulated; therefore, the plate was cut into inspection coupons. A total of nine coupons were created, see Figure 7.40. Four pristine coupons, two Frekote contaminated coupons, two silicone oil contaminated coupons and one disbond coupon.

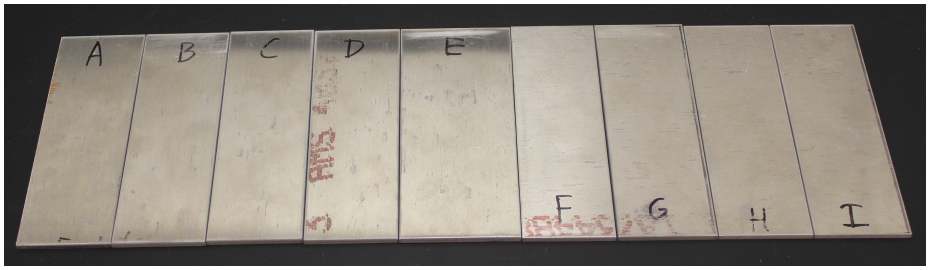

(a) All nine inspection coupons

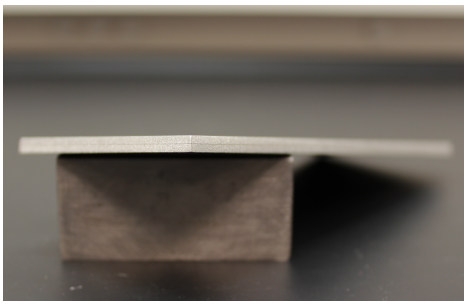

(b) Coupon C, close up of bondline

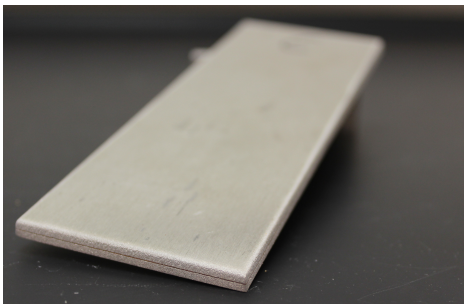

(c) Coupon C

Figure 7.40: Inspection Coupons

A schematic diagram was provided at the beginning of this chapter of the immersion guided wave technique. The experimental setup is shown in Figure 7.41, which follows the schematic. Additionally this fixture provided an additional rotational axis, which is useful for anisotropic materials.

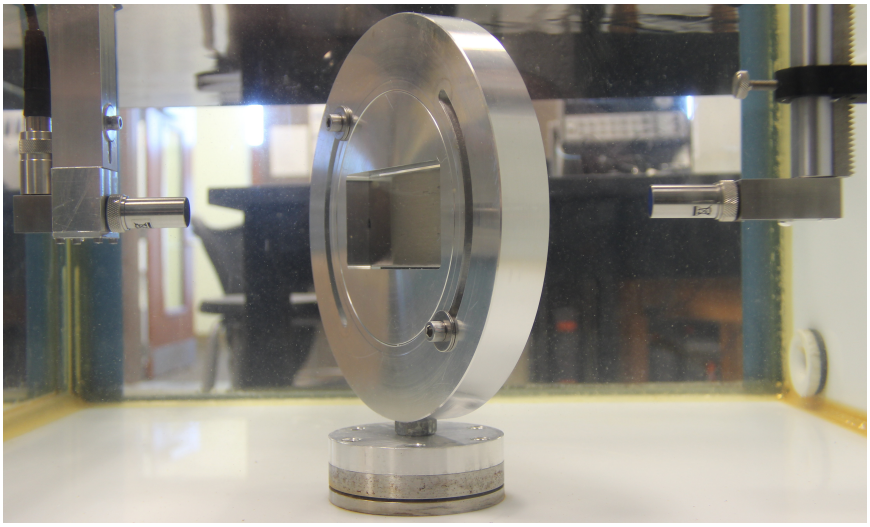

Figure 7.41: Experimental immersion guided wave apparatus

At first, coupon I, pristine, is analyzed over a large frequency range. Three sets of experiments were performed using 2.25, 5 and 10 MHz transducers. The two lower sets used all unfocused transducers, while the 10 MHz experiment used a focused excitation transducer coupled with an unfocused receiver. The incident angle was controlled by the immersion scanner turn table axis. The angle varied between -36 and 36 degrees with 0.1 degree increments. For each incident angle, the receiver position was translated from -1.65 and 1.65 inches with 0.015 inch increments. The zero position was aligned with the transmitter. At each 2 dimensional location, the time domain signal was recorded.

The first set of plots generated for this case is shown in Figure 7.42, where the absolute peak amplitude APA of each time domain signal is shown with respect to position. At a zero degree incident angle, the amplitude decreases in each direction as the receiver is translated. This is due to the beam profile of the transmitter. As

the incident angle is varied, the peak amplitude is expected to shift slightly, but the peak amplitude is shifted further than expected due to the creation of guided waves. Additionally, in some regions the guided wave travels a long distance as it leaks energy into the fluid medium. This is seen as the unsymmetrical tails at certain incident angles. These longer propagating waves are less dispersive than the waves at incidence angles with narrow widths. The first and second critical angles are observed as the regions where the amplitude nearly or fully disappears. The first critical angle is more clear in all three of the frequency plots. The guided waves near the critical angles are less dispersive; this can be observed in frequency - phase velocity plots where the modes tend to flatten out around the bulk wave velocities. The Rayleigh wave mode is visible in the 2.25 MHz plot as the large amplitude at an angle above 30 degrees, past the second critical angle. The Rayleigh wave is not visible at the higher frequencies because the creeping waves do not penetrate into the substrate far enough to be visible from the back side of the laminate. At 5 MHz, some waves are observed below the second critical angle, but at 10 MHz no waves are seen above this angle. Another important observation is that the guided wave modes tend to decay faster as the frequency is increased. This is clear from the difference between plots (b) and (c).

Next, the dispersion information was extracted from this data set. This was accomplished by performing a Fourier analysis of the time domain signal at the transducer location of maximum amplitude. The incidence angle is converted to phase velocity with the bulk wave velocity of the water. The results form the same three experiments on coupon I, along with the combined results, are shown in Figure 7.43. The 10 MHz results are not as clear as the lower frequency results. This could be caused by two factors; first, the large number of modes and higher attenuation decreases the amplitude of any given wave; second, the unfocused transducer is not ideal for exciting guided waves, future experiments will use an unfocused transducer.

The technique was repeated for all nine coupons with the 2.25 MHz transducer, the dispersion results are shown in Figure 7.44. Small changes in the dispersion can be observed across all nine coupons. The disbonded region, coupon E, required a large amplification of the signal in order to extract results; this is the reason for the grainy nature of the figure. Future work will use an optimization routine to extract the material properties of the adhesive from these results.

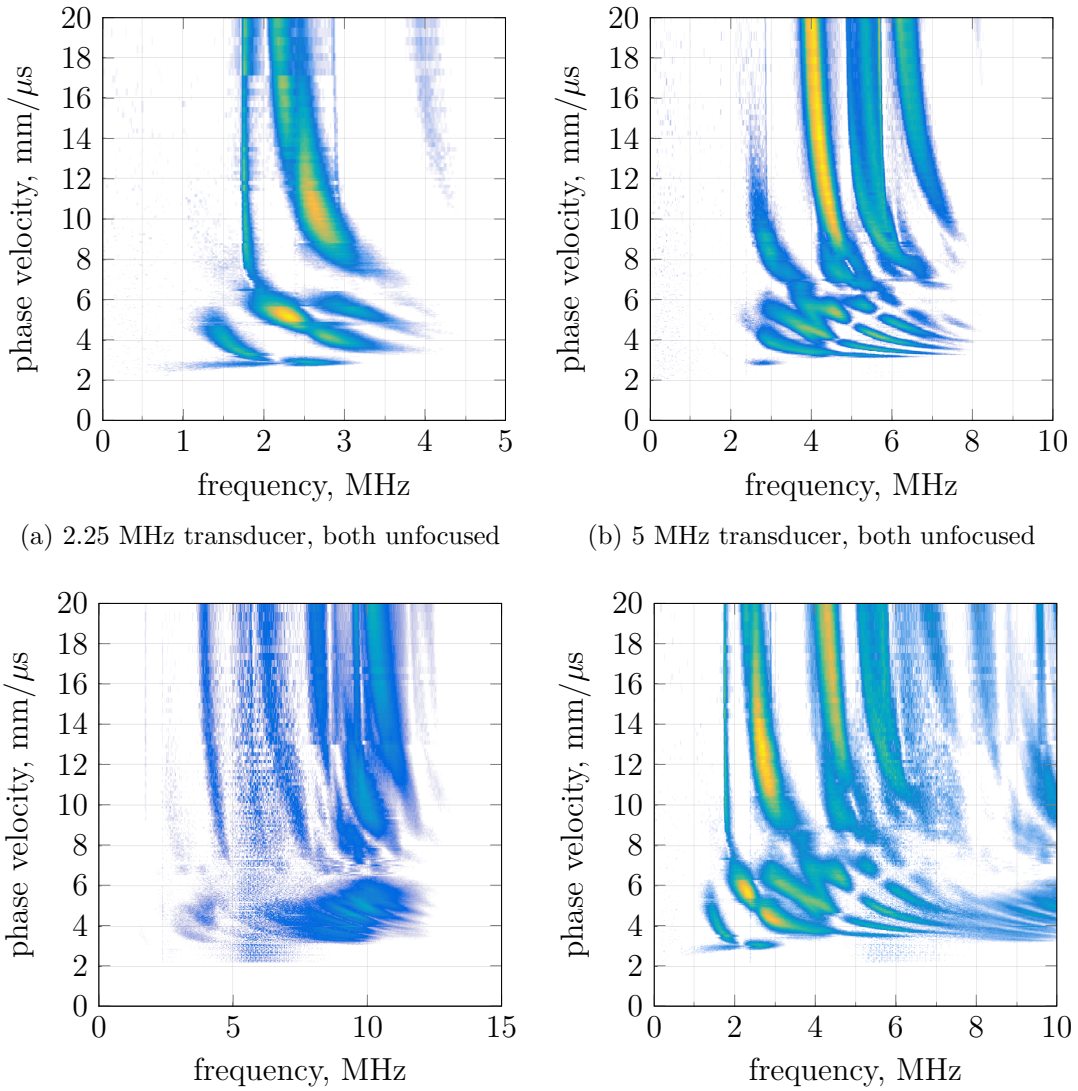

(a) 2.25 MHz transducer, both unfocused

(b) 5 MHz transducer, both unfocused

(c) 10 MHz transducer, focused transmitter, unfocused receiver

(d) combined results

Figure 7.43: Experimental dispersion curves from the immersion technique, coupon I

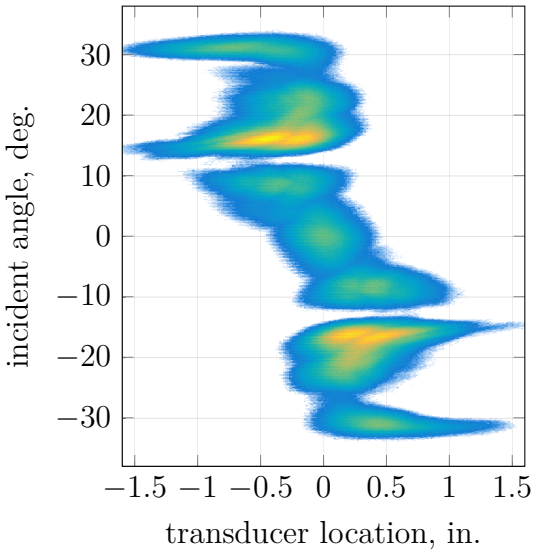

(a) 2.25 MHz transducer, both unfocused

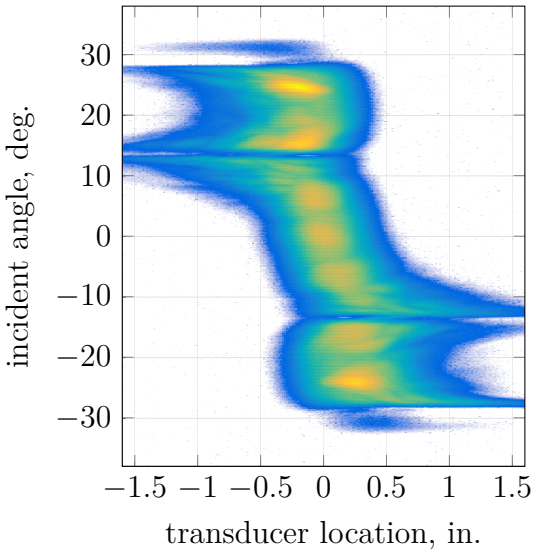

(b) 5 MHz transducer, both unfocused

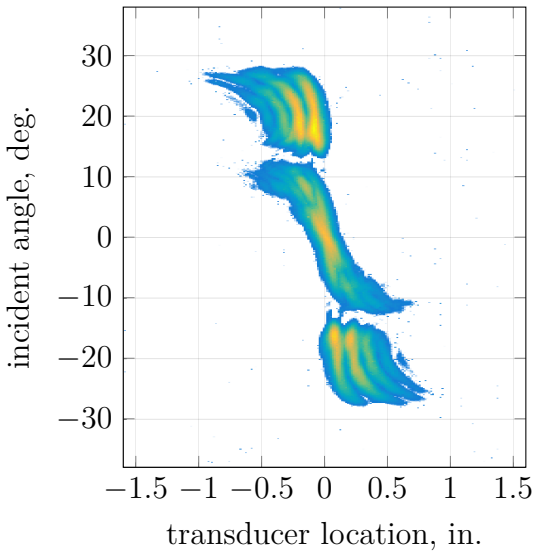

(c) 10 MHz transducer, focused transmitter, unfocused receiver

Figure 7.42: Absolute peak amplitude of the transmitted wave packet with varying incident angle and transducer location, coupon I

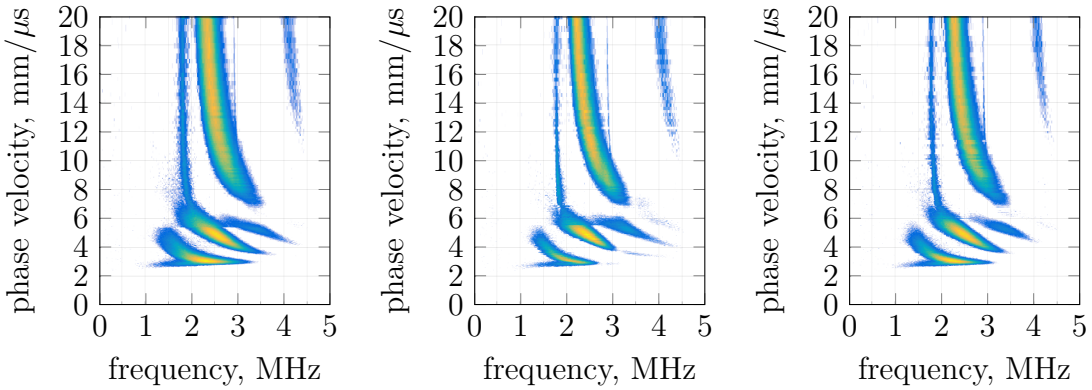

(a) coupon A, frekote (b) coupon B, frekote (c) coupon C, silicone

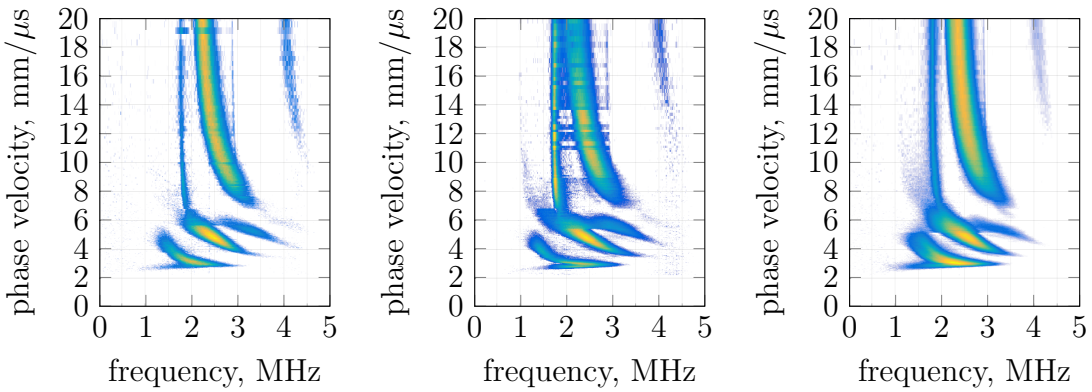

(d) coupon D, silicone (e) coupon E, disbond (f) coupon F, pristine

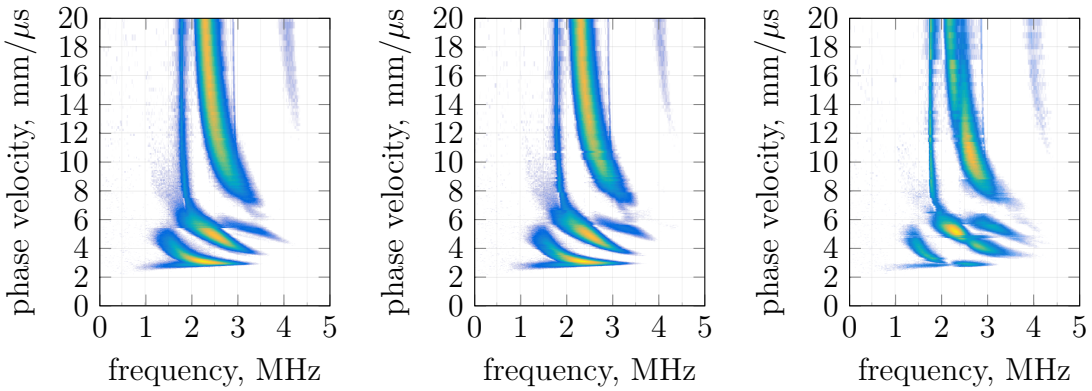

(g) coupon G, pristine (h) coupon H, pristine (i) coupon I, pristine

Figure 7.44: Experimental dispersion curves from the immersion technique, 2.25 MHz transducer

The results for the pristine coupons at 5 MHz is shown in Figure 7.45. Future reports will contain the results for all coupons at this frequency. The 5 MHz results are expected to have greater changes in dispersion due to the interface conditions. Considerable changes in the dispersion can be observed for all of the pristine coupons. This change is also likely due to the changes in adhesive thickness detected by the normal incidence UT inspection.

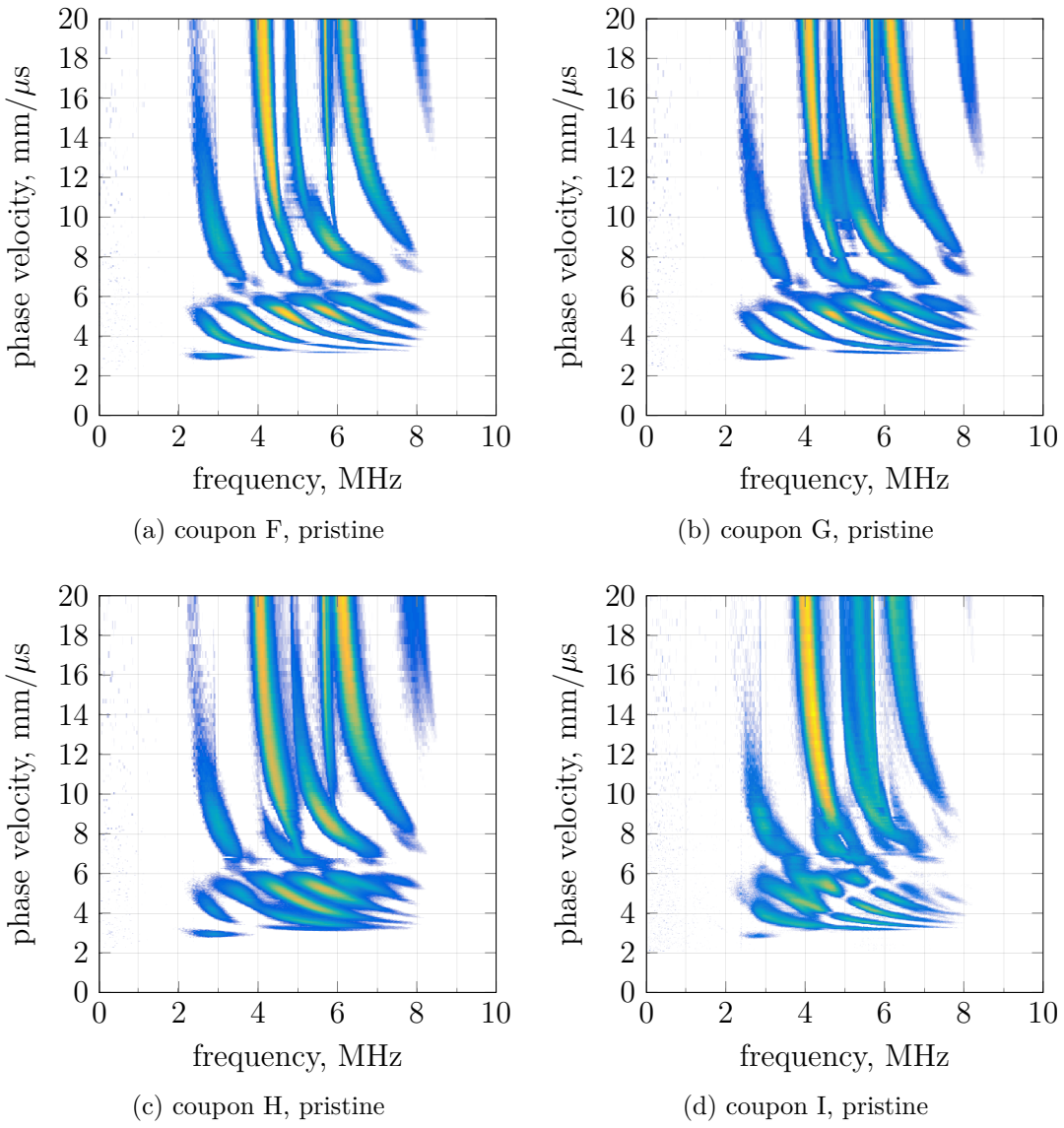

(a) coupon F, pristine

(b) coupon G, pristine

(c) coupon H, pristine

(d) coupon I, pristine

Figure 7.45: Experimental dispersion curves from the immersion technique, 5 MHz transducer

7.4.4 Mechanical Testing

The immersion coupons will be cut in half and subject to double cantilever beam (DCB) testing to analyze the failure mode and measure the critical energy release rate for the adhesive layer. These results will show how the contaminates affected the strength and durability of these joints. These results will be reported after all inspections have been completed on these coupons. In the meantime, a scrap strip of the plate was subject to the Boeing wedge test so that the fracture surfaces could be analyzed. This test gives good qualitative results on the strength of the interface.

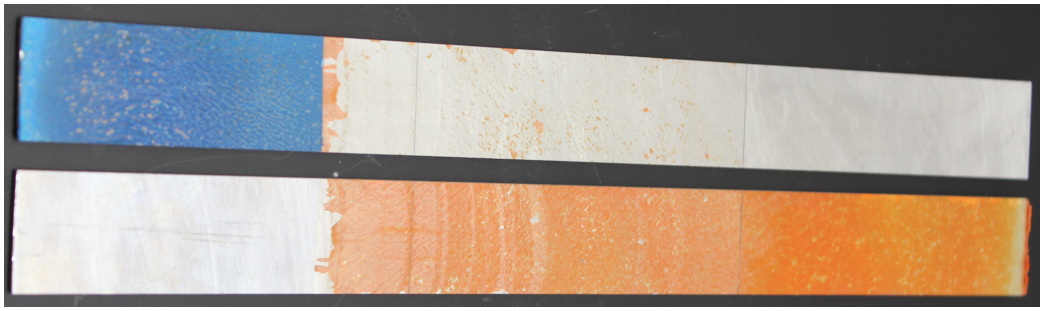

(a) Inspection of the adhesive failure mode

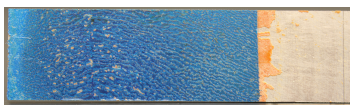

(b) Surface adjacent to the artificial disbond

(c) Surface with the silicone oil application

(d) Surface with the Frekote application

(e) Surface with the artificial disbond

(f) Surface adjacent to the silicone oil contamination

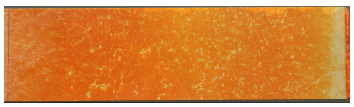

(g) Surface adjacent to the Frekote contamination

Figure 7.46: Analysis of the adhesive failure mode through the wedge test

This specimen was cut across the disbond, silicone contaminated and Frekote contaminate regions. The disbond was easy to separate and the wedge was inserted here and driven into the bond line. Pictures of the fracture surfaces are shown in Figure 7.46. The disbond and Frekote contaminated surfaces contain to traces of the adhesive. The silicone oil contaminated surface has a trace amount of adhesive

residue. The adhesive color is also different for the silicone and Frekote regions. The Frekote and disbond behaved as expected, preventing good bonding to those surfaces. The silicone clearly acted as a contaminate because the failure was primarily adhesive, but the trace amounts of contaminate indicate a greater strength as compared to the Frekote. It should be noted that the very thin bondline used in this specimen make a true cohesive failure less likely.

7.5 Optimization

As discussed in section 7.3.2, the influence of the bulk elastic properties of each lamina can dominate the guided wave behavior; therefore, optimization is one of the potential methods for determining these unknown influences, so that the desired interface parameters may be determined. The resulting problem is a multidimensional constrained optimization. It is multidimensional because more than one material property must be determined simultaneously, and it is constrained because there are physical constraints on some of the properties, such as Poisson's ratio. Additionally, the optimization is nonlinear; this should be clear from the chapters covering guided wave solutions. In this work, the MATLAB function fmincon() is implemented to solve this nonlinear constrained optimization problem. There are multiple algorithms embedded in this function, but the most commonly used algorithm is the trust region method based on interior point techniques. The algorithms in this section are similar to the optimization and nonlinear root finding algorithms covered in chapter 6.

The overall program architecture (Figure 7.47) goes as follows. A set of initial guesses for the desired properties are generated, along with the remaining constant properties and the experimental incident angles. These parameters are fed into the guided wave dispersion algorithm, which outputs the frequencies at which guided waves exist for each incident angle. The calculated frequencies are compared to the experimental frequencies through least squares, generating a single value as the

output of the objective function. This process is iterated until a global minimum is located, generating the final reconstructed properties.

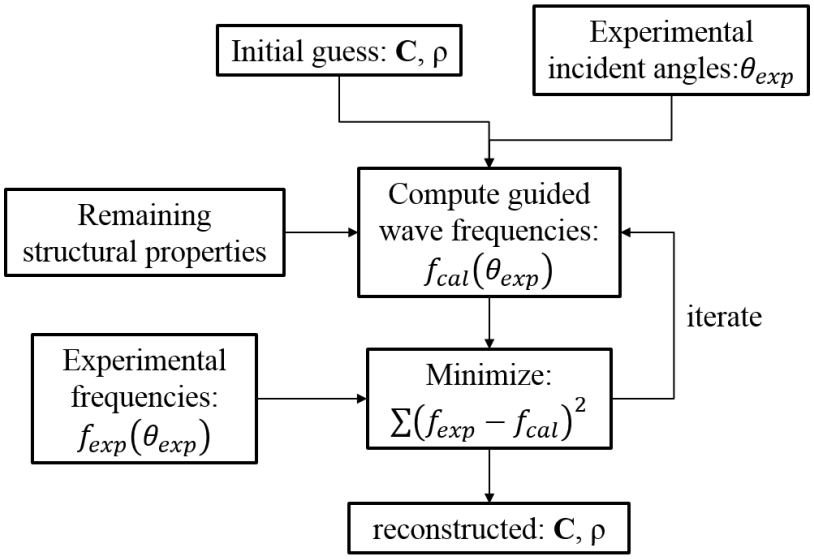

Figure 7.47: Optimization program architecture

There is still a hurdle to overcome in this process. The experimental results for the guided wave dispersion result in color contour plots, not the desired scatter plot. This is accomplished through the following method. A one dimensional plot can be generated for a given phase velocity. This plot will have frequency along the x-axis and the signal amplitude as the y-axis. By searching for the location of the peak amplitudes, this continues plot is reduced to a few frequency points for a given phase velocity, exactly what is required for the optimization algorithm. In order to successfully implement this technique, care must be taken to insure that the peaks have a significant prominence and minimum amplitude, or other factors, such as noise, may contribute to incorrect peak selection. The program was tuned to accept the rejection of valid results in order to eliminate the possibility of generated a false point. The immersion method results are shown in Figure 7.48 for both the 2.25 MHz and 5 MHz transducers.

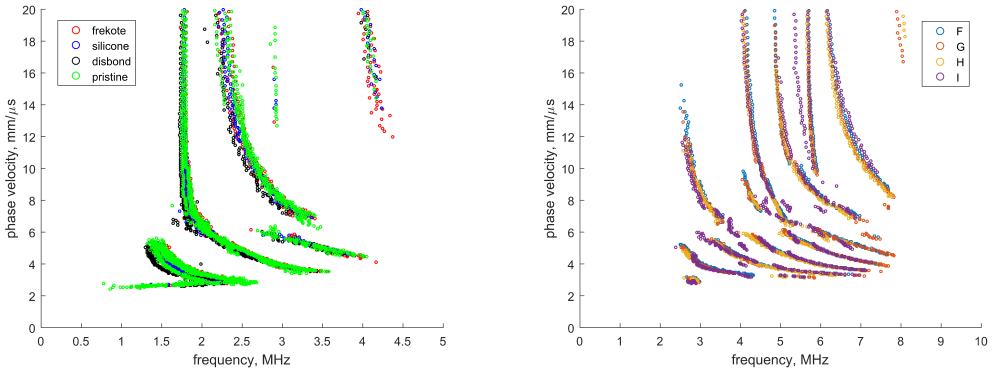

(a) 2.25 MHz (b) 5 MHz

Figure 7.48: Experimental dispersion data converted into scatter point data

The revised programming flow chart is shown in Figure 7.49 with the transformation from the color contour plot to scatter results.

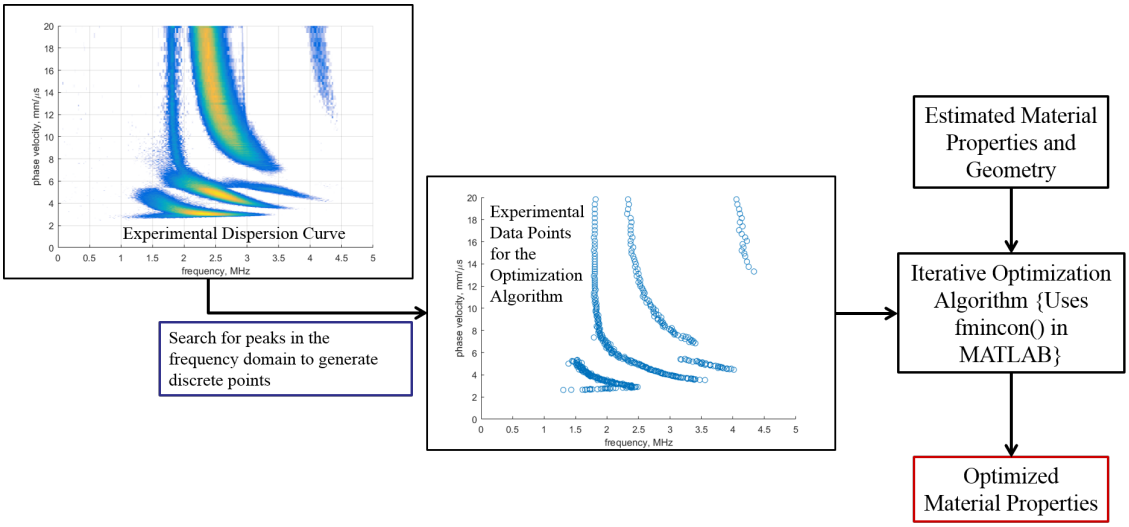

Figure 7.49: Flow chart for inserting the experimental dispersion data into the optimization algorithm

A demonstration of the optimization of material properties is shown in Figure **??**: figure (a) shows the calculated dispersion curve over the experimental scatter plot for the estimated material properties; figure (b) shows a similar plot with the optimized material properties; and figure (c) compares the dispersion curves for the estimated and optimized material properties along with the color contour plot of the

experimental results.

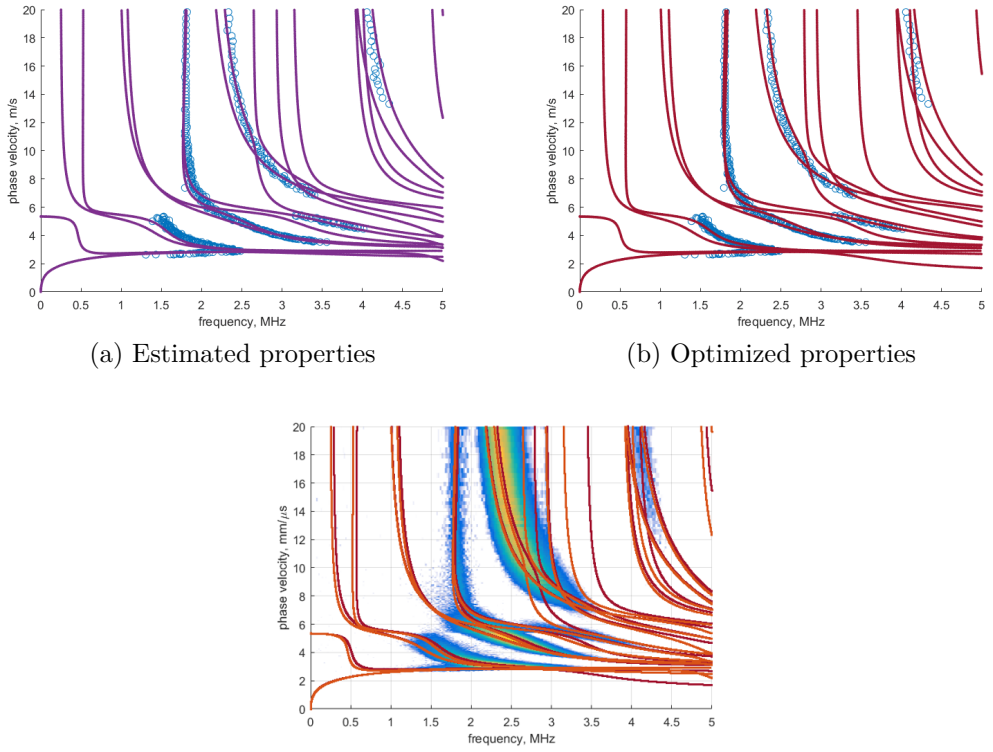

(a) Estimated properties

(b) Optimized properties

(c) Comparison

Figure 7.50: Optimization of the 2.25 MHz experimental dispersion results for coupon A

This optimization problem only optimized the adhesive properties, while the relatively well know substrate properties were left constant. The initial an final properties are shown in Table 7.1. One important observation of these results is that the density was significantly increased up to the constraint boundary. It is hypothesized that this is due to the fact that the true independent variables in the guided wave equation are the bulk wave speeds, which are a function of both elastic properties and density. Subsequent optimization routines have used the bulk wave speeds as the design vector since any combination of material properties can generate the same wave speeds.

The shear velocities for the adhesive layer of all nine coupons, following optimization, are shown in Table 7.2. The smallest shear velocity calculation is for coupon A, Frekote contamination, but several of the pristine coupons also have small shear

Table 7.1: Estimated and optimized adhesive properties based on the experimentally determined guided wave dispersion of an adhesively bonded aluminum structure

	Estimated	Optimized
Young's modulus, GPa	3.5	2.35
Poisson's ration	0.38	0.364
density, g/cm^3	1	2
adhesive thickness, mm	0.20	0.095

velocities. It should also be mentioned that after sitting in the lab for several months coupon A exhibited a disbond that had growth to nearly half of its length. This disbond was not present during dispersion testing, and it likely grew under the residual stress generated from cold rolling the aluminum and high temperature curing of the adhesive.

Table 7.2: Shear velocity from the optimization of the guided wave dispersion curves

Coupon	c_s, m/s	Condition
A	705	Frekote
B	1044	Frekote
C	1101	Silicone oil
D	1196	Silicone oil
E	1187	Artificial disbond
F	837	Pristine
G	861	Pristine
H	936	Pristine
I	1262	Pristine

The remaining coupons were subjected to the traveling wedge test in order to quantitatively evaluate the interface strength. An adhesive failure, where the adhesive remains on one interface, is considered to be an unacceptable bond. While a cohesive failure, adhesive remains on both interfaces, is an acceptable failure mode becasue the strength is primarily determined by the adhesive chemistry, curing condition, adhesive thickness, and adhesive fillet, which are all easily monitored and inspected with conventional ultrasonics.

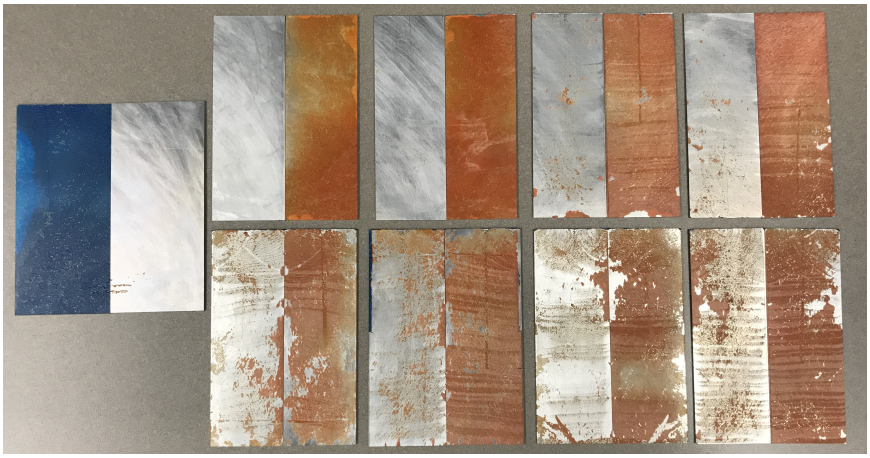

(a) Both interfaces

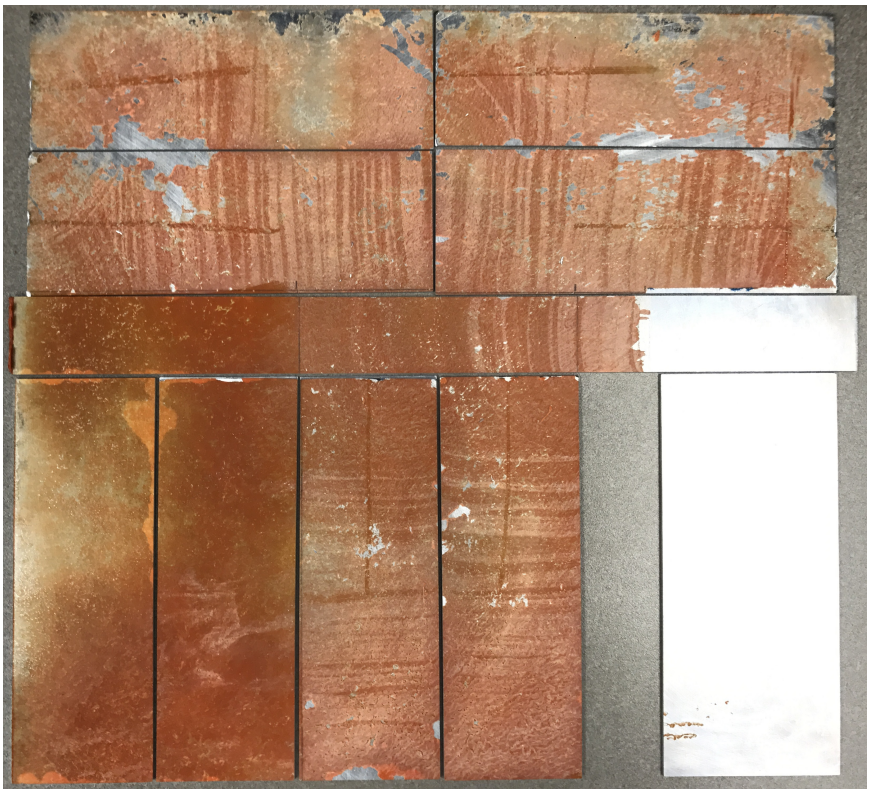

(b) Uncontaminated interfaces in the original orientation

Figure 7.51: Traveling wedge test failure modes for all coupons

The resulting failure modes are shown in Figure 7.51. Examination of the bond interface provides a clear indication of each type of contamination, or lack there of. In Figure 7.51(a) the coupons are arranged in order, where A - D are shown in the upper row starting from the left. E is the far left coupon, and coupons F - I begin on the left

of the bottom row. Coupons A and B are contaminated with Frekote and have very clean surfaces with no adhesive residue. Coupons C and D were contaminated with silicone oil and contain a trace amount of adhesive on the weak interface, indicating improved but not satisfactory interface strength. Coupon E contains a large artificial disbond, which is clearly indicated. Coupons F - I were not contaminated. All of these coupons exhibit a large amount of adhesive residue on both interfaces, along with deep, clear patterns where the crack front moved from one interface to the next from the unsymmetrical loading. Rearranging the coupons back into there orientation when they were cut from the bonded specimen clearly indicates how the contaminates were applied prior to bonding (Figure 7.51(b)). Close examination of the adhesive indicates that porosity may have contributed to the reduction in shear speed in the adhesive.

Chapter 8

Material Characterization

8.1 Setup

This technique for measuring the elastic properties of an anisotropic material depends on the change in the time-of-flight for a wave pulse through the material at various angles. The length of this pulse must be sufficiently small compared to the thickness of the sample to prevent the formation of guided waves. Some guided waves will be generated at the critical angles; this is unavoidable. Since the material is assumed to be anisotropic, two angles are required to completely describe the phase velocity in the material (Figure 8.1). Two angles are used to describe the direction of the incident wave. θ_i is the incident angle, or deviation from the surface normal, and ϕ is the angle of the plane of incidence measured from the fiber direction. θ_r is the angle of the refracted wave measured from the negative surface normal. In the refracted ray, the direction of the energy velocity differs from the direction of phase velocity by the angle γ. This angle can further be broken into an α component that is in the incident plane, and a β component that is normal to this plane. A last note on this figure, there is a primed and unprimed coordinate system. The unprimed coordinate system is the material coordinate system, and the elastic properties will be defined in this coordinate system. The primed coordinate system has been rotated so that $x_1^{'}$ is aligned with the plane of incidence. This technique greatly simplifies the calculation of phase velocities.

The technique presented in this paper seeks to determine the elastic properties

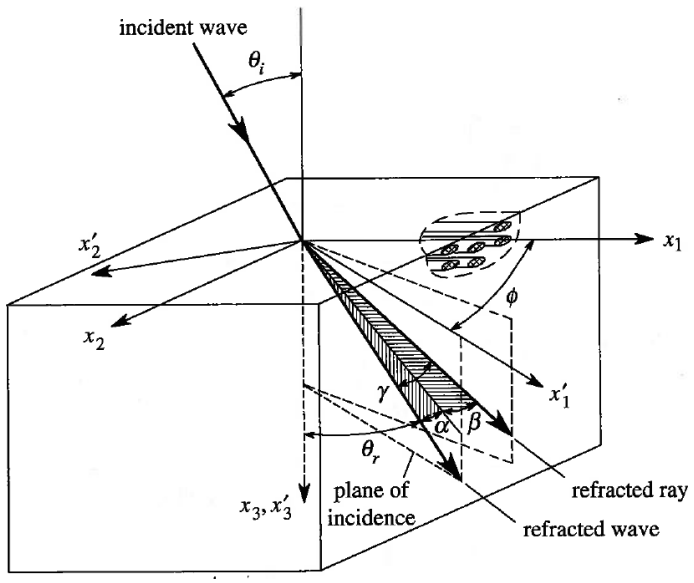

Figure 8.1: Refracted wave and ray directions in a unidirectional composite plate [?]

of fiber reinforced composite materials, which have been shown [?] to be sufficiently transversely isotropic.

$$\mathbf{C} = \begin{bmatrix} C_{11} & C_{12} & C_{12} & 0 & 0 & 0 \\ & C_{22} & C_{23} & 0 & 0 & 0 \\ & & C_{22} & 0 & 0 & 0 \\ & & & \frac{C_{22}-C_{23}}{2} & 0 & 0 \\ & & & & C_{55} & 0 \\ & & & & & C_{55} \end{bmatrix} \tag{8.1}$$

Utilizing the symmetry of the material, see equation 8.1, the components that are required for determining the phase velocities within the material for a given θ_i and ϕ = 0 are the following: C_{11}, C_{22}, C_{12} and C_{55}. That leaves one unknown component. Switching ϕ to 90 degrees, the dependent components are as follows: C_{22} and C_{23}. Therefore, all of the unknown can be determined for two values of ϕ that lie along planes of symmetry. This greatly simplifies the experimental method.

If the stiffness matrix is inverted into the compliance matrix, a larger number of

unknowns can be solved for a single value of ϕ.

$$C_{11} = \frac{S_{22}^2 - S_{23}^2}{S} \tag{8.2}$$

$$C_{22} = \frac{S_{11}S_{22} - S_{13}^2}{S} \tag{8.3}$$

$$C_{12} = \frac{S_{12}S_{23} - S_{12}S_{22}}{S} \tag{8.4}$$

$$C_{23} = \frac{S_{12}^2 - S_{11}S_{23}}{S} \tag{8.5}$$

$$C_{55} = \frac{1}{S_{55}} \tag{8.6}$$

$$S = S_{11}S_{22}^2 - S_{11}S_{23}^2 - 2S_{22}S_{13}^2 + 2S_{23}S_{12}^2 \tag{8.7}$$

For the case of $\phi = 0$, the unknowns are S_{11}, S_{22}, S_{12}, S_{23} and S_{55}. This is all of the unknown components for a transversely isotropic material. For the case of $\phi = 90$ degrees, the unknowns are S_{11}, S_{22}, S_{12} and S_{23}. Only S_{55} is missing for this case. Furthermore, the compliance matrix components can be converted into engineering constants, such that the phase velocities are calculated directly from the following engineering constants: E_1, E_2, ν_{12}, ν_{23} and G_{23}. For a thourough discussion of wave speed and the stiffness matrix refer to Chapter 4. Also, additional information on material symmetry can be found in Appendix A, and analytical calculations for bulk wave speeds of various material symmetries and directions can be found in Appendix B.

The experimental procedure requires measuring the transmitted wave over a range of incident angles, see Figure E.1. The receiving transducer is translated in order to detect the wave pulse as the angle changes. The angle ϕ is varied between 0 and 90 degrees through the use of a specialty built fixture. Figure E.2 shows an experimental fixture immersed in the water tank. The coupon is within the fixture, which is bolted to the turntable. The transmitter and receiver are shown on opposite sides of the fixture. The rotation of ϕ and θ_i is controlled by the fixture and turntable, which is illustrated in Figure E.3. The translation of the receiving transducer is controlled

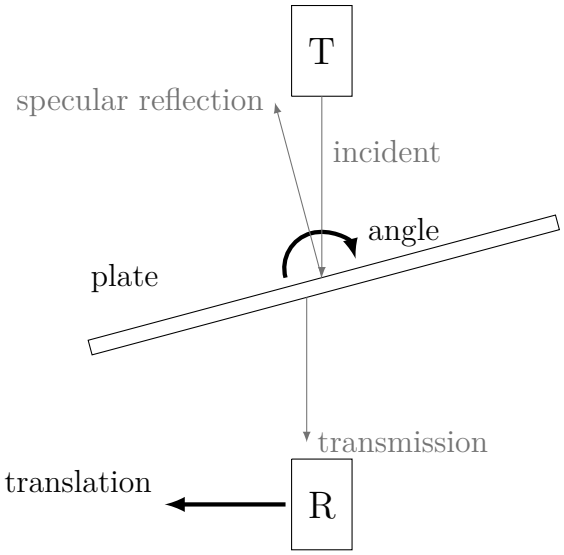

Figure 8.2: Through transmission technique

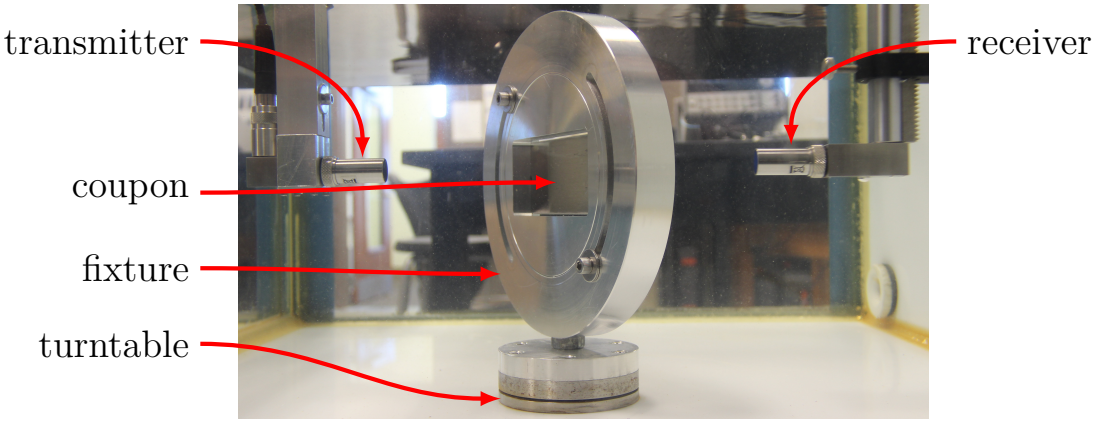

Figure 8.3: Experimental setup

by the y-axis motor of the immersion scanner, see Figure E.4. The receiver distance from the coupon is controlled by the x-axis motor; while the transmitter distance is controlled by the position of the crossbar, which travels on the x-axis rails. The position of the transmitter along the z-axis is set, but the z-axis position of the receiver is controlled by varying the height of the search tube.

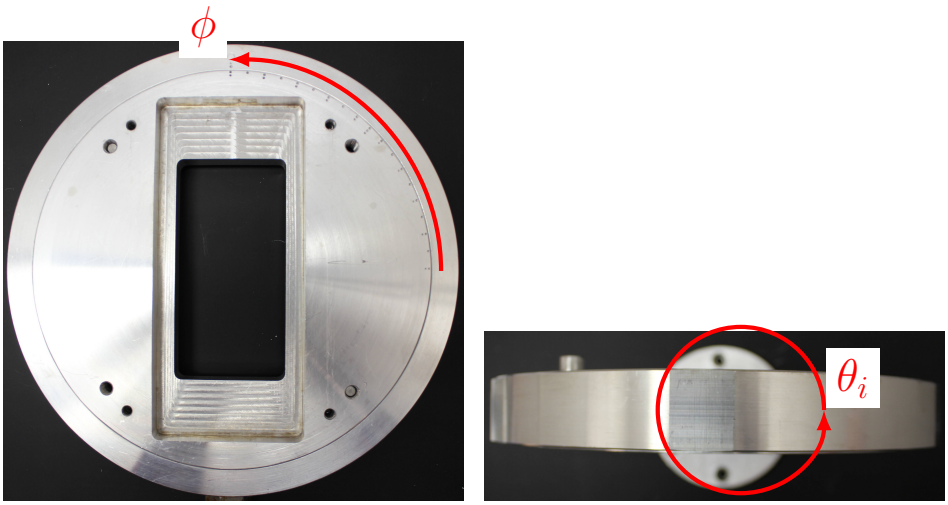

(a) Rotating ϕ from 0 to 90 degrees (b) Rotating θ_i from 0 to 360 degrees

Figure 8.4: The fixture is used to vary the angles for (a) ϕ and (b) θ_i

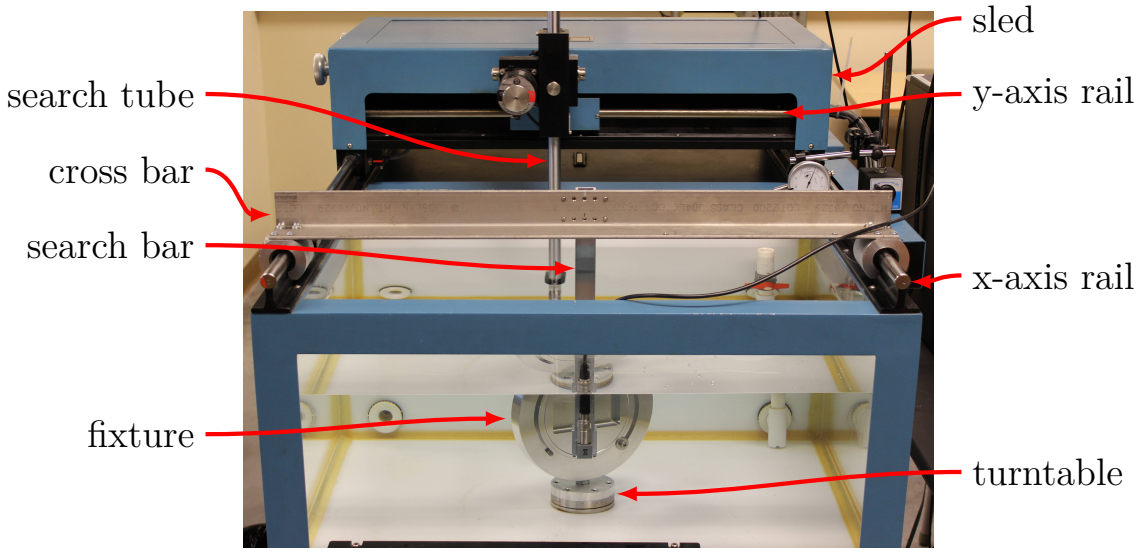

Figure 8.5: Immersion tank with 4 DOF

8.2 Procedure

Once the coupon, fixture and all supporting equipment have been loaded into the water tank, the following steps must be taken to ensure the collection of relevant and correct data.

8.2.1 Find θ_0

The first step is to orient the turntable so that the incident angle, herein referred to as θ, is at zero degrees. This is accomplished by using a pulse echo technique. The transmitter transducer both emits and receives the acoustic wave pulse. A gate is set up around the first incoming pulse so that the absolute peak amplitude (APA) of the pulse is measured. A scan is preformed where the angle of the turntsable is varied through several degrees from the estimated θ_0. The angle at which the peak amplitude occurs is the θ_0.

8.2.2 Find y_0 and z_0

Next, the origin of the receiver position is determined. This is accomplished with a two dimensional through transmission scan. Again, a gate is set up to find the APA of the first wave pulse. The receiver is scanned in the y and z directions. The resulting C-scan is shown in Figure E.5. The datum is located at the center of the circle.

8.2.3 Collect data

The data for each ϕ angle is collected as a two dimensional scan. A new gate is set up to collect all of the time data within the gate boundaries. This is called a waveform gate. This gate is set to the absolute scale, instead of using a follower gate. This is required because the absolute time is needed for the correct calculation of the phase velocity. The scan is performed with the turntable and y-axis. A total distance of

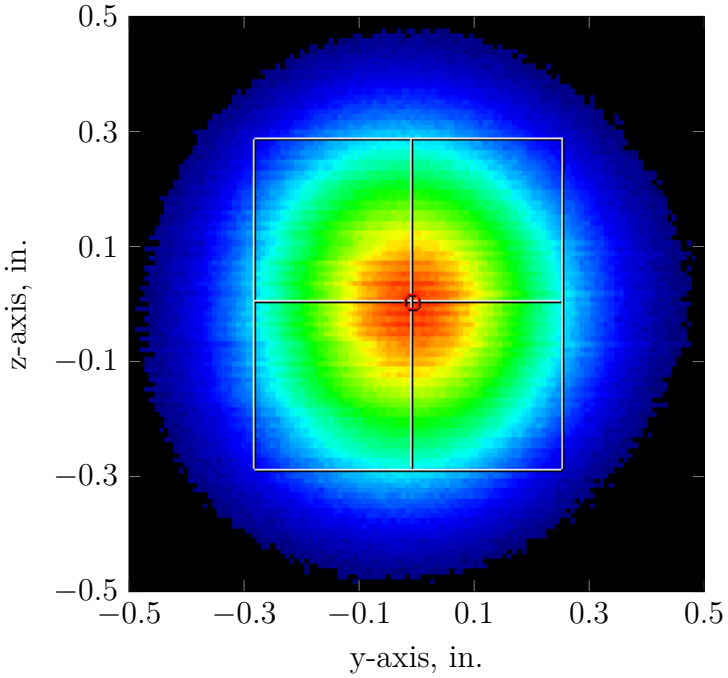

Figure 8.6: APA of the through transmission

2-2.4 inches is selected for the y-axis. The turntable is swept through a total range of 120-140 degrees. The resulting data is extracted for post-processing.

8.3 Data Processing

The data processing is necessary to convert the raw waveforms into a phase velocity measurement for every θ. The first step is to further refine the datum location.

8.3.1 Find Datum

The accuracy of the datum location, when using the machine setup, is limited to the step size of the rotary encoder, and it is vulnerable to operator interpretation. The first step in data processing is to refine this measurement through calculations. Figure E.6 is a visual guide to the required process. The process begins with a two dimensional array of absolute peak amplitude, as shown in Figure E.6a as a surface plot. In order to find θ_0, the maximum amplitude along the y-axis for every incident

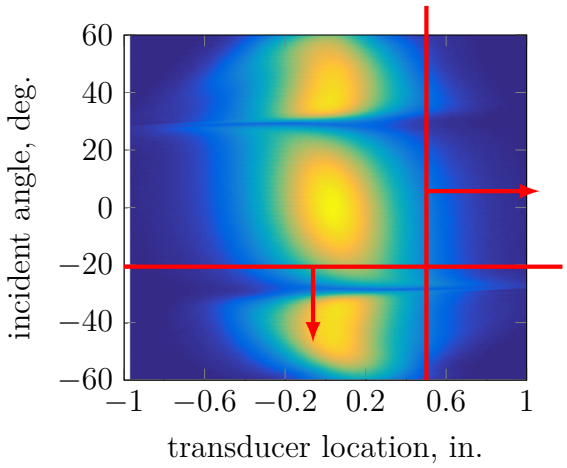

(a) Original absolute peak amplitude (APA)

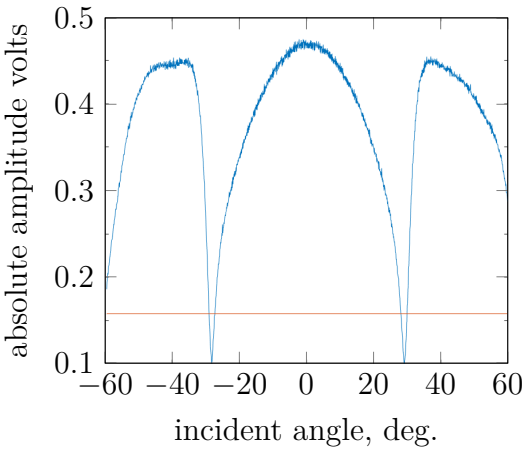

(b) Maximum APA along the transdcuer location for each incident angle

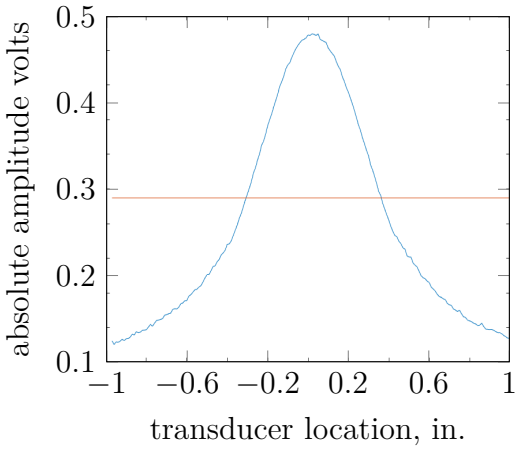

(c) Maximum APA along the incident angle for each transducer location

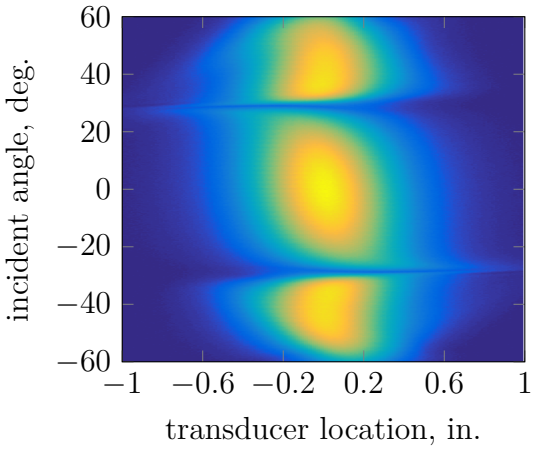

(d) APA with the correct datum

Figure 8.7: Determining the datum

angle is collected. The resulting data is plotted inFigure E.6b. Instead of finding the peak of the plot, the x-axis is shifted up and the roots, or zero crossing, are determined. It is the averaged half-way point between these roots that is used as the θ_0. The same process is followed to determine the y_0, see Figure E.6c. The corrected APA data is shown in Figure E.6d.

8.3.2 Find Time-of-Flight

The time-of-flight at every angle must be determined. The first step is to select a single transducer location for each incident angle. This is accomplished by finding the location of the APA for each incident angle, see Figure 8.8(a). The waveform at each location undergoes a Hilbert transform, see Figure 8.8(b). The location of the peak amplitude of the first wave packet is used as the time-of-flight. The Hilbert transform is used to provide a more accurate estimation of the peak amplitude of the wave packet. This process is performed for each incident angle, generating a plot of time vs. incident angle, see Figure 8.9.

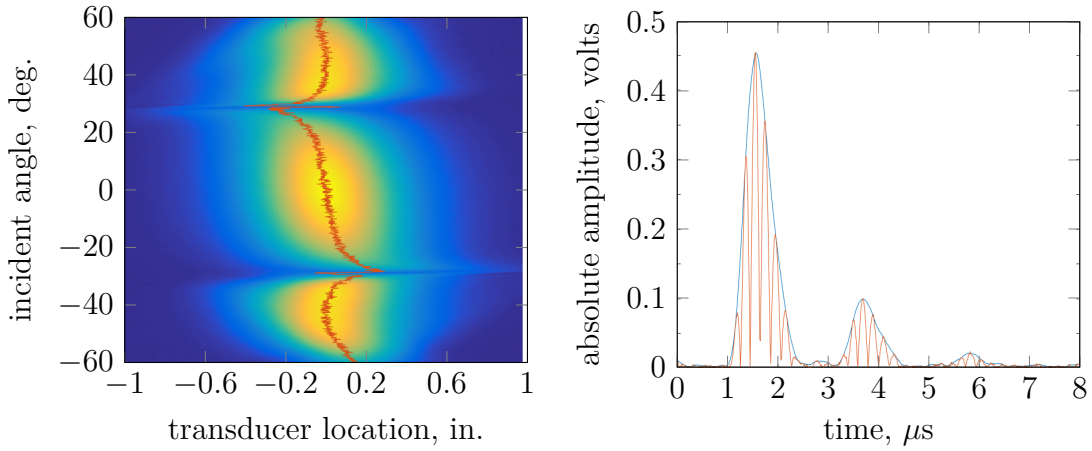

(a) The location of maximum APA for each incident angle

(b) Absolute amplitude vs. time with Hilbert transform

Figure 8.8: Method for finding the time-of-flight

8.3.3 Find Reference Time

In order to calculate the phase velocity, the time-of-flight must be converted into a change in time-of-flight from the reference case of no coupon, or only water between the transducer and receiver. Instead of removing the coupon, and potentially disturbing the orientation of the transducers, the phase velocity of through the thickness of the coupon at an incident angle of zero degrees is calculated from the pulse-echo data.

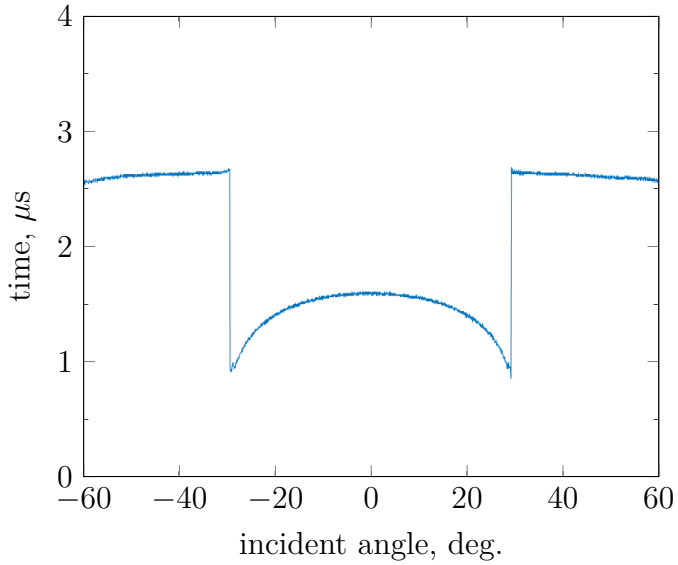

Figure 8.9: Time-of-flight for all incident angles; the starting time is the beginning of the gate

This data is shown in Figure 8.10. The raw signal undergoes a Hilbert transform, and the location of the peak for each wave packet is determined. In this case, three pulses were detected. The average time-of-flight between the pulses is calculated. Since the

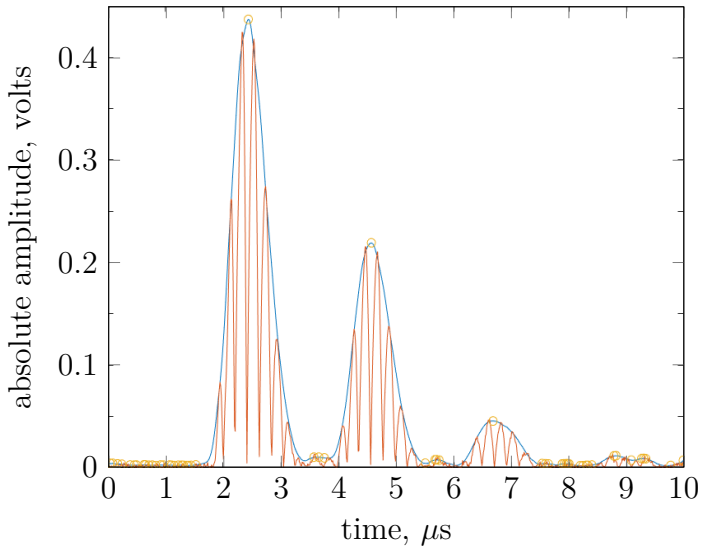

Figure 8.10: Pulse-echo at zero incident angle

thickness of the coupon is known, the phase velocity is easily determined,

$$c = \frac{2h}{t_{avg}} \tag{8.8}$$

where t_{avg} is the average time-of-flight between the pulses for the pulse-echo data. Now, the change in time-of-flight, or Δt, can be calculated for the zero incident angle case,

$$\Delta t = \frac{h}{c_w} - \frac{h}{c} \tag{8.9}$$

where c_w is the wave velocity in water. The reference time, corresponding to the time-of-flight without the coupon, is determined from the Δt,

$$t_0 = t - \Delta t \tag{8.10}$$

where t is the time-of-flight to the first peak in the through transmission data at zero incidence angle. The reference time is then used to calculate the Δt at every incident angle, see Figure 8.11.

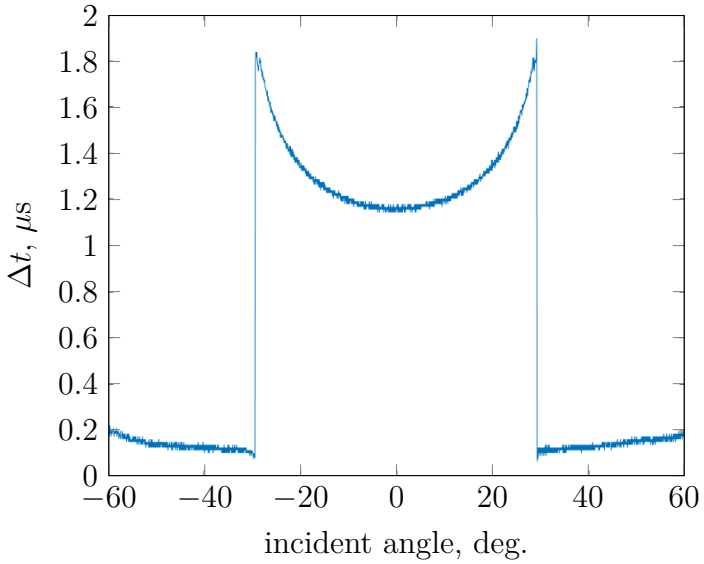

Figure 8.11: Change in the time-of-flight from the reference value for all incident angles

8.3.4 Convert to Phase Velocity

The final step is to convert the Δt values into phase velocities. Using the equation from Rokhlin (insert reference), the phase velocities are determined for every incident

angle,

$$c = \left[\frac{1}{c_w^2} - \frac{2\Delta t cos\theta}{h c_w} + \frac{\Delta t^2}{h^2} \right]^{-\frac{1}{2}} \tag{8.11}$$

where θ is the incident angle. Following this calculation for all incident angles results in the phase velocity vs. incident angle plot shown in Figure 8.12. Note that the center portion corresponds to pressure velocity whereas the side portions correspond to shear velocity. These velocities are constant for all incident angles. The values of this two velocities result as numerical averages of the plots shown in Figure 8.12. If the laminate is transversely isotropic, the wave speed at zero degrees and at the first cutoff angle will be identical. Also, the wave speed will be represented as a straight line. The results in the figure are not perfectly transversely isotropic, but the deviation is small enough to assume that the material has this behavior.

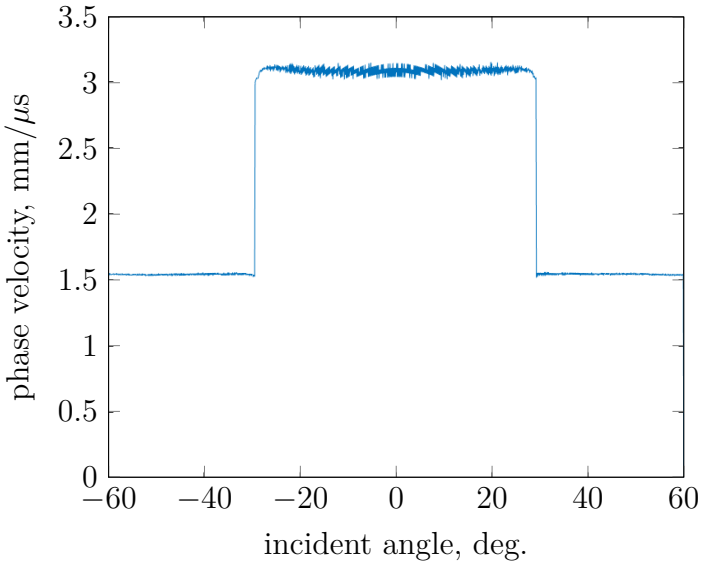

Figure 8.12: Phase velocity for all incident angles

8.3.5 Optimization

The optimization routine is similar to the guided wave optimization in chapter 7. An initial guess of the stiffness matrix must be provided, along with the experimental incident angles (Figure 8.13). These parameters, along with the remaining properties,

are read into an algorithm for determining the bulk phase velocitites. The results are compared to the experimental values and the process is interated until the least squares of the difference has been minimized.

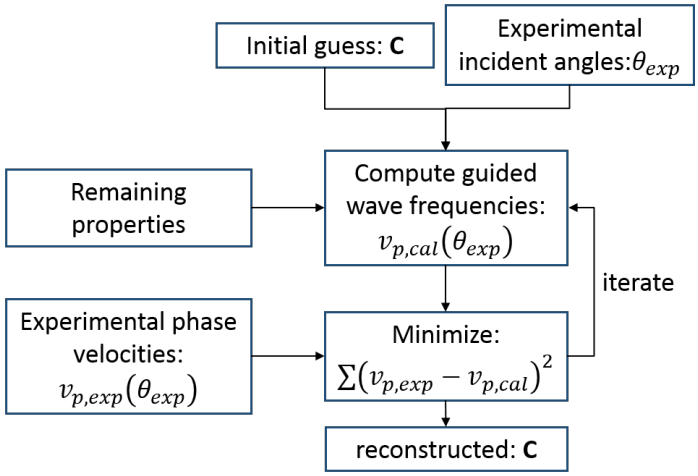

Figure 8.13: Optimization algorithm flow chart

8.4 Results

This section will present the results for the material characterization of a fiber reinforced laminate. Typically, these laminates are assumed to be transversely isotropic, or contain isotropic properties in the plane that is transverse to the fibers. This is easily verified with the presented experimental method. The scatter results in Figure 8.14 are for a 90 degree orientation, where the wave travels transverse to the fiber direction.

Now, the stiffness matrix components are optimized for these experimental results. The material is assumed to be transversely isotropic; therefore, five independent components must be determined. Two curves are shown in Figure 8.14 for both the estimated and optimized material properties. The improved match is clear from the figure. Also, the process is repeated for the 0 degree experimental data (Figure 8.15). Once again the optimized material properties provide a good match. These figures show why this method can generate more accurate results than a point-wise method.

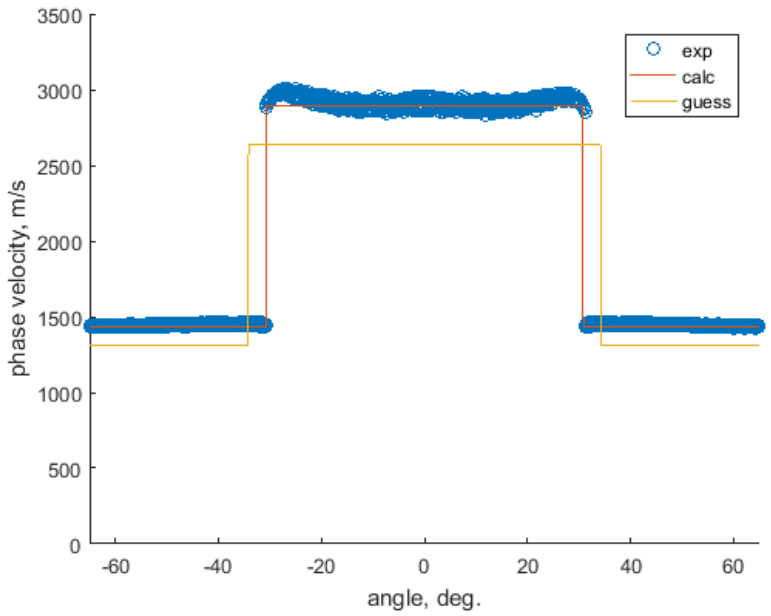

Figure 8.14: Optimization results for the 90 degree orientation test

The point-wise method uses the minimum number of data points in order to determine the material properties. By using the full symmetric array of data points, the critical angle is included in the data. Due to the nature of a least squares minimization, a deviation from the critical angle generates a large error, making the critical angle a sensitive feature in the optimization. This improves the accuracy because the critical angle is an accurate direct way of calculating several of the stiffness components.

Finally, the estimated and optimized material properties are shown in Table 8.1. There is discrepancy between several of the components when optimized at different orientations. This difference is largely attributed to differences in the sensitivity of each individual component to a change in the wave speed. In the algorithm, the sensitivities were initially normalized to reduce the effect of the behavior. The large discrepancy at E_1 is due to the large influence of the critical angle. A small difference in the critical angle can lead to large differences between the velocities. As a result, the optimization is very sensitive to this value. Since the critical angle for the zero degree experimental directly correlates to the value of C_11, and consequently E_11,

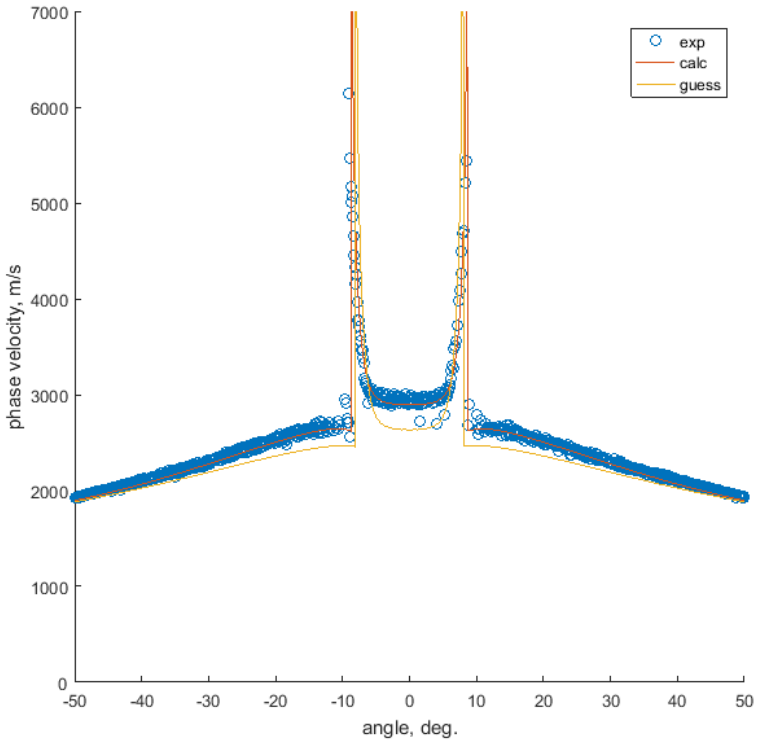

Figure 8.15: Optimization results for the 0 degree orientation test

Table 8.1: Optimized material properties for a carbon fiber reinforced polymer laminate

Elastic Property	Initial	90 deg.	0 deg.
E_1, GPa	171.4	170.8	144.3
E_2, GPa	8.0	9.6	9.6
ν_{12}	0.32	0.314	0.319
ν_{23}	0.5	0.5	0.49
G_{12}, GPa	5.29	5.29	5.35

the sensitivity is very large. The more accurate estimate of E_1 is generated from the 0 degree results due to the increased sensitivity.

Part III

Structural Health Monitoring

Chapter 9

Disbond Detection Through Local Vibration

9.1 State-of-the-Art

There are a variety of non-destructive inspection (NDT) techniques available for detecting disbonds. One option would be conventional or phased array ultrasonic inspection [100]. This method is capable of finding disbonds which have separated from the substrate, providing a void that can easily reflect the incident pressure wave. If the disbond has little to no void, then vibrational methods can be utilized. These methods take advantage of the shift in natural frequency of a structure due to the decrease in stiffness in the damaged zone. Adams et al. [101] used the one dimensional axial and torsional vibration of bars in order to detect damage. Cawley and Adams [102] extended this method to the study of aluminum and carbon fiber reinforced plastic plates. Additional techniques were developed, including the mechanical impedance method. This method was initially proposed to detect disbonds by Cawley [103], taking advantage of the change in out-of-plane mechanical impedance when a force is applied over the disbond. While both methods are capable of detecting disbonds, they require direct access to the inspected part, which is often difficult to provide in fixed wing aircraft, except during D checks. As well as the grounding of the aircraft while the procedure is performed. An improved approach would be a permanently installed NDT system, which would be capable of performing the inspection in-situ. This type of approach requires a permanently installed sensor, and this study considered the piezoelectric wafer active sensor (PWAS) [104].

The PWAS is composed a thin wafer of lead zirconate titanate (PZT) which, when polarized, possesses piezoelectric properties. The PWAS used in this study contained electrodes on the top and bottom surfaces of the wafer and was polarized across the electrodes in the out-of-plane direction. This type of sensor is thin and unobtrusive when bonded to a surface. The PWAS are capable of generating and detecting elastic waves within structures, and are primarily used for structural health monitoring (SHM) with guided waves or local vibration techniques. Building on the mechanical impedance method, which excites the structures surface with an out-of-plane force, PWAS excite structures with an in-plane force; however, there is no second sensor to measure the velocity. Instead, the electrical impedance of the sensor is measured with respect to the frequency of excitation. This method is referred to as electromechanical impedance spectroscopy (EMIS); initial work was performed by Liang, Sun and Rogers [105]. It has been shown that the real part of the electrical impedance of the PWAS attached to a structure matches the imaginary part of the frequency response function of the structure [106]. As a disbond or other damage is introduced into the structure, the frequency response changes and this change can be detected through the EMIS method. The EMIS method along with permanently bonded PWAS have been used to detect defects for various applications [106][107][108][109]. More recently the method has been used to detect adhesive disbonds and delaminations [110][111][112][113][114].

This paper expands on the previous work in three ways. First, this paper discusses a methodology for the proper selection of sensor location and frequency based on the fundamental mechanics of vibration. Second, this paper explores this methodology through a case study in detecting corner disbonds in an adhesively bonded aluminum doubler. Third, the numerical results are verified through laser Doppler velocimetry.

9.2 Test Coupon

In modern stressed skin aerospace structures, stiffeners and doublers are used to stiffen thin plate sections and reinforce cutouts. It has become common to use adhesives to join these thin sections: as such, this configuration has been chosen for the test article. The test article consisted of a host plate which was 500 mm long, 60 mm wide and 1.6 mm thick. A second doubler plate was bonded to the host plate with Ten Cate BF548 film adhesive. The doubler plate was the same width and thickness, but only 100 mm long. A disbond was artificially created in one of the test articles by securing Teflon film to the host plate under one corner of the doubler plate. The location and size of the disbond was chosen to simulate what might be seen in a real structure. A schematic of the described configuration is shown in Figure 9.1.

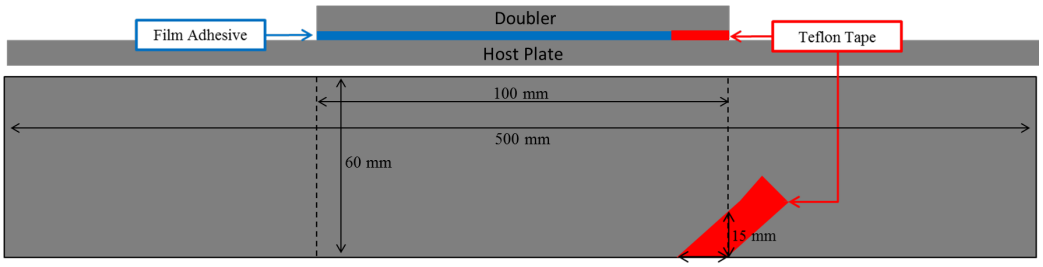

Figure 9.1: Test article assembly schematic

Once the plates were cut to the appropriate size, a thorough surface preparation was performed to the bonding region. The surface preparation consisted of the following steps; degreasing, dry sanding with 320 grit silicon carbide sand paper, wet sanding with 400 grit silicon carbide sand paper in a weak solution of phosphoric acid, wiping the surface clean, scrubbing the surface with a weak solution of ammonium hydroxide and sodium tetraborate pentahydrate until no visible residue remains. Next, the Teflon film was secured to the host plate. The film adhesive was removed from the freezer, cut to the appropriate size and placed onto the doubler plate. The doubler plate was carefully aligned onto the host plate. The assembly was then placed onto caul plates within a hot pressed and cured for 15 minutes at 121 ÂřC (250 ÂřF) and

4,448 N (1,000 lbf) of compression. Once the cure cycle was complete, the excess adhesive and Teflon film were removed from the test article. A razor plate was used to open the disbond at the corner of the doubler plate.

In order to verify that the triangular area was disbonded, the entire coupon was scanned with phased array pulse echo ultrasonic inspection equipment. The coupon was scanned from the bottom side of the host plate, and water was used as the couplant. A gate was set up in the time domain to measure the amplitude of the signal in the expected location of the reflection off of the back wall of the host plate. This A-scan is shown in the upper left window of Figure 9.2. The upper right window shows the amplitude of the signal for all 64 elements across the width of the host plate or B-scan. The cursor line in this window is located over the disbond. The strong reflection from the top surface of the plate, and another strong reflection in the region of the disbond can be seen in this window. This strong reflection is due to the large acoustic impedance mismatch between aluminum and air, which is stronger than the aluminum epoxy interface. The lower window in this figure shows the C-scan of the plate. The color corresponds to the amplitude within the gate set at the back wall of the host plate. There is a strong reflection over the disbond, which is similar in amplitude to the non-doubler sections of the plate. This is expected because this reflection is also from an aluminum air interface. This inspection has shown that the disbond is as expected.

The final step in the assembly of the test article is the installation of the PWAS. The determination of the appropriate PWAS configuration is discussed in the next section; however, the installation is shown here. A total of five PWAS were installed. All of the PWAS were purchased from STEM Inc., and they were seven millimeters in diameter and two hundred micrometers thick. They were bonded to the doubler plate with Vishay M-Bond 200, a cyanoacrylate commonly used to bond strain gages. The surface preparation consisted of the same procedure for bonding the plates. A

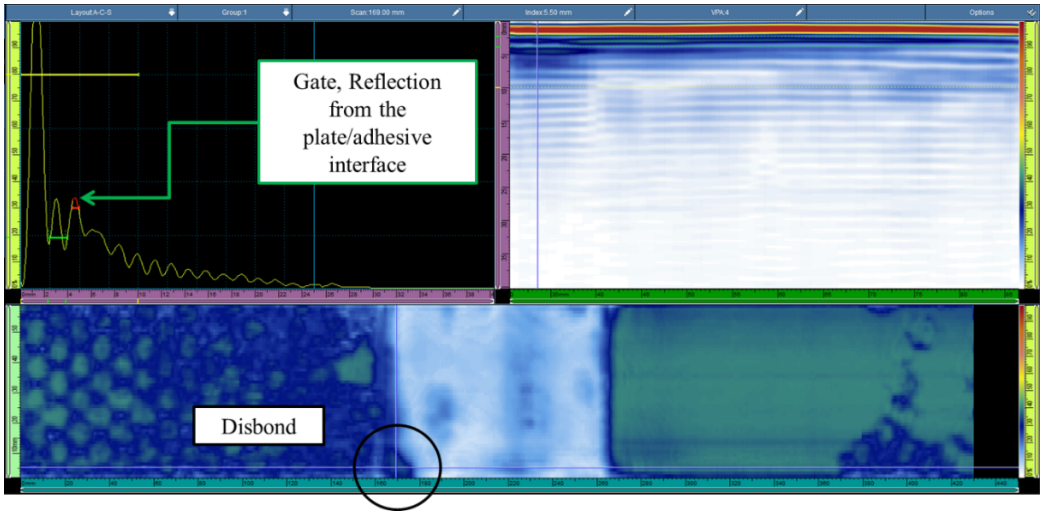

Figure 9.2: Ultrasonic inspection of the disbond region

thin electrical wire was soldered to the top electrode of each PWAS, and the wire was run across the plate to an attachment point. The grounding wire was bonded onto the doubler plate with conductive adhesive, while all of the PWAS are attached to this connection through the adhesive attachment to the doubler plate. The PWAS layout and a picture of the test articles are displayed in Figure 9.3.

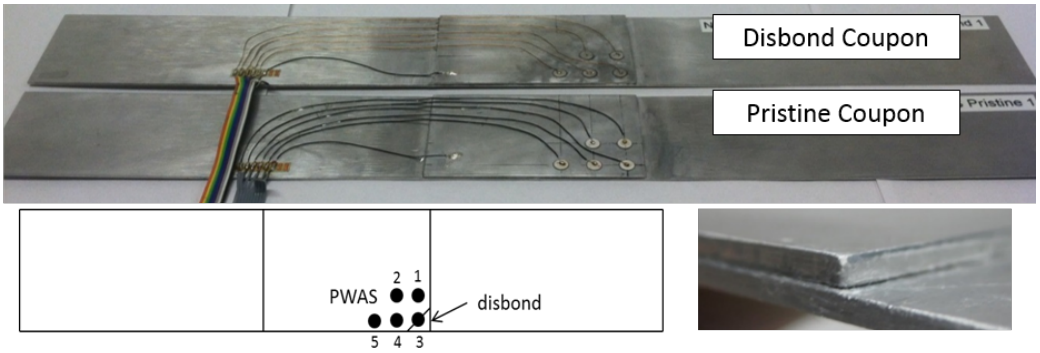

Figure 9.3: Final test coupons, PWAS layout and the artificial disbond

The pertinent material properties for the aluminum and adhesive were gathered from the suppliers and shown in Table 9.1.

Also, the material properties of the PWAS are shown in Table 9.2, Table 9.3 and Table 9.4.

Table 9.1: Material Properties for the Structure

Material Properties	**Aluminum**	**Adhesive**
Young's modulus	73 GPa	3 GPa
Poisson's ratio	0.33	0.30
Mass density	2780 $\frac{kg}{m^3}$	1200 $\frac{kg}{m^3}$

Table 9.2: Material Properties for the PWAS

Property	**Value**
Mass density	7800 $\frac{kg}{m^3}$
Dielectric permittivity, xx	1319 $10^{-8}\frac{F}{m}$
Dielectric permittivity, yy	1319 $10^{-8}\frac{F}{m}$
Dielectric permittivity, zz	1319 $10^{-8}\frac{F}{m}$

Table 9.3: Piezoelectric matrix for the PWAS, $10^{-12}\frac{C}{m^2}$

0	0	0	0	660	0
0	0	0	660	0	0
-190	-190	450	0	0	0

Table 9.4: Anisotropic stiffness matrix for the PWAS, GPa

96.8	39	28.2	0	0	0
39	96.8	28.2	0	0	0
28.2	28.2	67.9	0	0	0
0	0	0	27.7	0	0
0	0	0	0	27.7	0
0	0	0	0	0	28.8

9.3 Electromechanical Impedance Spectroscopy

Electromechanical impedance spectroscopy (EMIS) is a local vibration technique for detecting damage in a structure. It has its origins in the coin tap and hammer tests that were developed through the past century, and has similarities with the modern mechanical impedance methods. The primary advantages that this method has over the NDT methods is that it can be performed in situ and requires very little head-space for the sensor allowing it to be placed in very low clearance areas. The fundamental idea behind this method is that a measurement of the frequency dependent electrical impedance or admittance of a structurally bonded PWAS will reveal the resonance peaks of the structure. If damage has been introduced into the structure, then the resonances will shift and/or previously undetected resonances will appear. This method depends on the PWAS becoming a part of the system through permanent bonding to the structure, and this is a fundamental difference between this method and the NDT methods.

The one dimensional equation for the electrical impedance and admittance of a structurally constrained PWAS, Eq. (9.1), is determined through the use of the following diagram and the constitutive equations of a piezoelectric material, Figure 9.4.

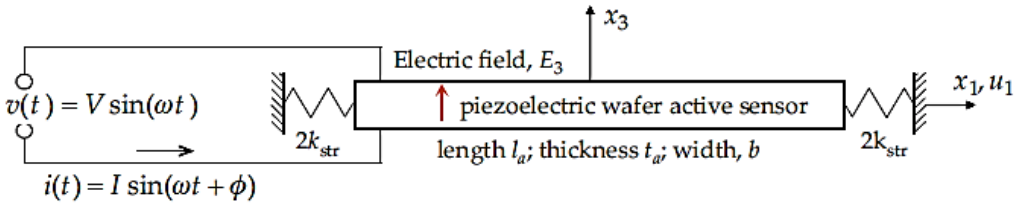

Figure 9.4: Diagram for a PWAS constrained by a structure [104]

This equation assumes that the frequencies remain below the first resonance frequency of the PWAS.

$$Z(\omega) = \frac{1}{i\omega C}\left[1 - k_{31}^2 \frac{Z_{str}(\omega)}{Z_{str}(\omega) + Z_{PWAS}(\omega)}\right]$$
$$Y(\omega) = Z^{-1}(\omega) \tag{9.1}$$

As can be seen in the equation the impedance of the PWAS is highly dependent on the impedance of the structure. This has been proven experimentally by Giurgiutiu [104] (Giurgiutiu V. , Structural health monitoring with piezoelectric wafer active sensors, 2014). This fundamental concept will now be applied in a case study of a specific adhesive joint and disbond.

9.4 Predictive Modeling

The first step in the predictive modeling process is to perform model analysis; resulting in the natural frequencies and mode shapes of the model. When a disbond is introduced into the domain, the natural frequencies will be shifted and the mode shape will change. For a model with a simple geometry and an analytical solution, i.e. bending of a beam, the shift in natural frequency could be easily identified and correlated back to a loss of stiffness due to the disbond. However, when realistic three dimensional geometries are used in collaboration with all possible modes of vibration, it becomes very difficult to solve analytically and conversely identify single modes and correlate the shift back to the disbond size. Often multiple modes shift up and down

in the frequency spectrum, making it difficult to follow trends. Instead, the mode shape or modal displacements provide more useful information for detecting disbonds. While the frequency may be slightly shifted in the presence of a disbond, especially when analyzing larger structures, the modal displacements, particularly those in the vicinity of the disbond, may be altered greatly. This statement highlights the main limitation in the EMIS method, the detection is often limited to the local vicinity of the disbond. This is due to the fact that the mode shape, a great distance from the disbond, will often be nearly unchanged by the presence of the flaw. This is also due to other factors, such as energy loss from damping and an excitation source which is incompatible with the displacements of the desired mode number.

The identification of appropriate mode shapes is only the first piece of the puzzle. If a desirable mode shape is identified, it will only be useful if it can be properly excited and detected. Proper excitation requires that the transducer excite the structure in such a way as to cause local displacements which partially match the desired mode shape. This idea is best explained through the modal expansion theorem [115]. As shown in Eq. (9.2), an arbitrary displacement vector can be described as the summation of the product of normal mode displacements and natural coordinates, where N is the number of degrees of freedom.

$$\{u(t)\} = \sum_{i=1}^{N} \{\phi\}^i \cdot q_i(t) \tag{9.2}$$

It is clear from this equation that the natural coordinates for a desired modal number must be at least greater than zero for a given displacement field to contain the desired mode shape.

Since most excitations are force controlled, as opposed to displacement controlled, it is more beneficial to have this expression in terms of applied force. Eq. (9.3)(a) is the equation of motion in the matrix form. If the applied force and resulting displacements are harmonic, and only Rayleigh damping is utilized, then the equation

of motion can be expressed as Eq. (9.3)(b).

$$\begin{aligned} [M]\{\ddot{u}\} + [C]\{\dot{u}\} + [K]\{u\} &= \{F\} \\ \Big((1+\beta)[F] - \omega^2(1+\alpha)[M]\Big)\{u\} &= F \end{aligned} \tag{9.3}$$

The damping contributions and applied force are removed from the equation, and the natural frequencies are determined by solving for the N frequencies which allow the determinant to equal zero, modal analysis. Then, as shown in Eq. (9.4), the mode shapes are calculated.

$$\begin{aligned} \Big|[K] - \omega_1^2[M]\Big| &= 0 \\ \Big([K] - \omega_i^2[M]\Big)\{\phi\}_i &= \{0\} \end{aligned} \tag{9.4}$$

Next, the frequency dependent compliance matrix can be expressed as Eq. (9.5) in order to simplify the equations.

$$[C(\omega)] = (1+\beta)[K] - \omega^2(1+\alpha)[M] \tag{9.5}$$

Combining Eq. (9.2), Eq. (9.3)(b) and Eq. (9.5), the equation of motion is expressed in terms of the compliance matrix, the mode shapes, the natural coordinates and the applied force.

$$[C(\omega)] \cdot \sum_{i=1}^{N} \{\phi\}^i q_i = \{F\} \tag{9.6}$$

In Eq. (9.7), the equation of motion is converted into index notation with Einstein summation, and it is transformed so that the natural coordinates can be determined from known mode shapes, applied force and compliance matrix. It is important to note that the solution to part (b) results in frequency dependent natural coordinates.

$$\begin{aligned} C(\omega)_{ij}\psi_{ik}q_k &= F_j \\ q(\omega)_k &= \phi_{ik}^{-1} C(\omega)_{ij}^{-1} F_j \end{aligned} \tag{9.7}$$

This equation can help to determine the ideal location for the transducer to excite a given mode. If a modal analysis is performed through finite element analysis (FEA),

then the results can be analyzed to determine the disbond dependent mode shapes. Next, multiple transducer location are selected and Eq. (9.7) is used to determine the best transducer location. If FEA is used to obtain the mode shapes, then the second step requires the extraction of the compliance matrix and subsequent inversion for each frequency. Another approach is to perform a harmonic analysis within the FEA software for each sensor location and in the desired frequency range; extracting the nodal displacements for each frequency step. Since a harmonic solution is assumed, Eq. (9.2) can be converted to the harmonic form.

$$\{u(\omega)\} = \sum_{i=1}^{N} \{\phi\}^i q_i(\omega) \tag{9.8}$$

The direct solution of this equation would require all mode shapes, not a possibility with a continuous system. There are some methods that may work, but this solution is not required in the case of EMIS. Since the PWAS acts as both the excitation source and the sensor, only displacements at the PWAS interface are necessary to determine the ideal location. This also limits the possible PWAS locations since we know from the modal analysis that the change in displacements will be greatest around the disbond. Therefore, we expect the best PWAS locations to be over or very close to the disbond locations. In this sense, a better method would be to separate the excitation source and sensor. So, the method used to find the ideal locations for EMIS is to perform a harmonic analysis over the desired frequency range and extract the displacements at the excitations points. Then the mechanical impedance can be determined for each location, as well as for both the pristine and disbonded cases. The best locations will be those that have the greatest change in mechanical impedance at the predetermined frequencies for the given disbond size.

Now the procedure can be performed on the test coupon. First, a modal analysis must be performed on the model. This is accomplished by assuming a harmonic displacements and solving Eq. (9.4). In this paper, FEA is used to determine the natural frequencies and mode shapes. Once a set of mode shapes has been determined

for both the pristine and disbond models, the mode shapes are compared to identify unique local displacements for detecting the disbond. One way to compare the mode shapes is through a manually process, comparing each mode shape by visually inspecting the graphical interpretation of the nodal displacements. This method is tedious and prone to human judgment. Instead, the nodal displacements of a given disbond mode can be compared to the nodal displacements of each pristine mode through a numerical algorithm, which will rank each comparison and decide on the most likely match between a disbond mode shape and pristine mode shape.

The mode matching is accomplished by first performing the dot product of the normalized nodal displacements for the pristine and disbond model. Then the mean value of the dot product at each node is calculated. The resulting equation, as shown in Eq. (9.9), produces a mode matching index for each disbond mode shape and pristine mode shape comparison.

$$x_{ij} = \frac{1}{N}\sum_{k=1}^{N} \frac{\underset{\sim}{u}_k^{d_i} \cdot \underset{\sim}{u}_k^{p_j}}{\sqrt{\underset{\sim}{u}_k^{d_i} \cdot \underset{\sim}{u}_k^{d_I}}\sqrt{\underset{\sim}{u}_k^{p_j} \cdot \underset{\sim}{u}_k^{p_j}}} \quad \text{(Mode matching index)} \tag{9.9}$$

At this time, must be noted that this calculation is only possible for coherent FEM models, i.e. same FEM mesh. One method for accomplishing this will be shown later.

The next step is to determine the best match. In other words, we want the pristine mode which best matches a given disbond mode. This is accomplished through equation9.10, where the value of y_i is the pristine mode number which is the best matched pristine mode with the disbond mode number i.

$$y_i = \underset{j}{\text{argmax}} x_{ij} \quad \text{(Matched mode)} \tag{9.10}$$

Now that each disbond mode has been matched with a pristine mode, the local disbond displacements are compared through root mean square deviation, as shown in Eq. (9.11).

$$z_i = \sqrt{\frac{\sum_{k=1}^{N}\left(\underset{\sim}{u}_k^{d_i} - \underset{\sim}{u}_k^{p_i}\right)\cdot\left(\underset{\sim}{u}_k^{d_i} - \underset{\sim}{u}_k^{p_i}\right)}{N}} \quad \text{(Mode ranking index)} \tag{9.11}$$

When using this equation, only nodes in a predetermined vicinity of the disbond are used. The values of z, mode ranking index, are then ranked in order of greatest magnitude, providing an easy method of determining the mode shapes of greatest value.

For the test article presented in this paper, the commercial FEM code ANSYS was used to perform a modal analysis on both the pristine and disbonded cases. The dimensions and material properties of the model are given in a previous section. The model was meshed with hexahedral elements having a general edge length of 2 mm, except for through the thickness, where 4 elements were used for the aluminum and 2 elements for the adhesive. The hexahedral elements were modeled as Solid186 within the ANSYS mechanical solver. This is a three dimensional 20 node element with quadratic displacement functions. The debonding of the adhesive from the host plate was modeled with contact overlay elements. Conta174 elements were placed on the surface of the host plate elements, and Targe170 elements were placed on the surface of the adhesive. Both elements use the preexisting nodes on the corresponding surfaces. During the pristine solution, the contact is considered rigid. For the disbonded case, the contact across the disbond is disabled, allowing the adhesive and host plate to pass through each other. This method is required, as mentioned previously, to ensure that the same number of nodes, as well as nodal coordinates, are used on each model.

The first six hundred mode shapes were calculated, and the nodal displacements for each mode shape was exported. The mode matching technique, as mentioned in the previous paragraphs, was formulated into a MATLAB script, and the mode shapes were compared to generate the best matches. Next, the mode ranking index calculation was performed on a fifteen millimeter square corner of the doubler plate where the disbond is located, as shown in Eq. (9.11). The resulting values were ranked in order of largest magnitude. The largest mode ranking index value occurred for the disbond mode number 121 at a frequency of 15.125 kHz. As shown in Figure 9.5, the

displacements in the vicinity of the disbond result in a“flapping” action, similar to the first mode shape of a cantilever beam, of the region of the doubler plate that is above the disbond. This mode of vibration is not present in the pristine model. This large motion clearly differs from the pristine motion, and provides a clear indication that this region is disbonded.

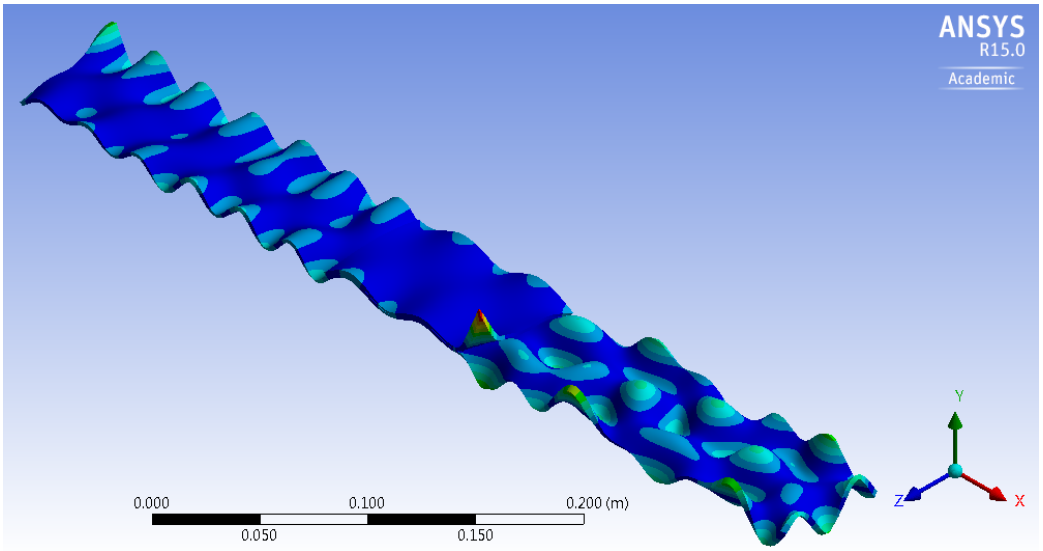

Figure 9.5: Disbond mode shape at 15.125 kHz, largest mode ranking index value

The second largest value occurs at a frequency of 14.529 kHz. This mode shape is shown in Figure 9.6, and has a similar“flapping” motion as the previous mode shape. Also, through observation of the displacements in the host structure, it appears that these two mode shapes may be twin modes.

Almost all of the largest RMSD values correspond with the “flapping” mode, and they occur at a wide range of frequencies from eleven to twenty-three kHz. Figure 9.7 to Figure 9.12 show more mode shapes with this unique disbond mode of vibration. While the flapping occurs in all of these mode shapes, the rest of the model is in a unique vibration pattern.

The mode ranking index values have been plotted against the corresponding disbond model frequency in Figure 9.13. It is clear from the table that the largest mode ranking index values occur in a grouping around fifteen kHz. This grouping, along

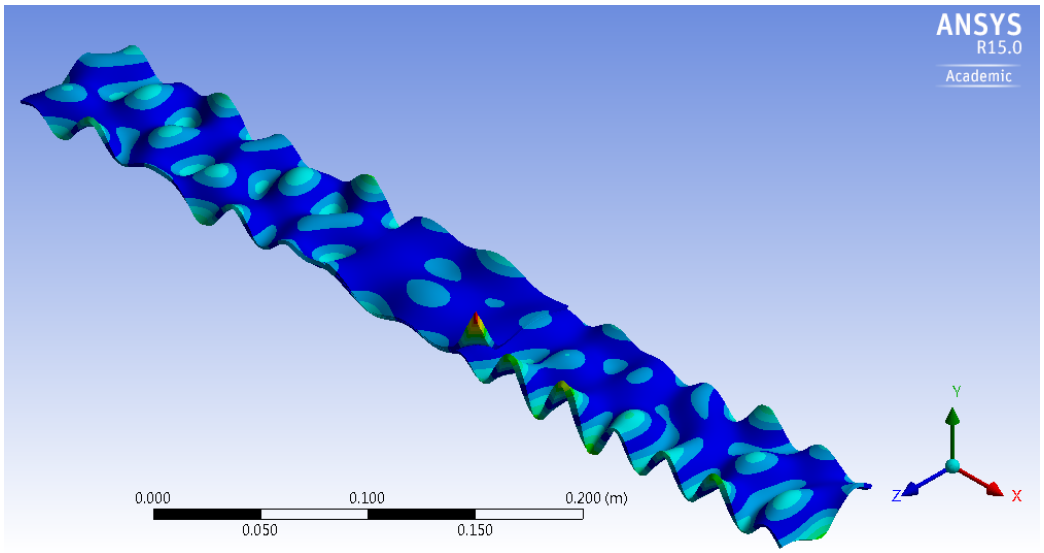

Figure 9.6: Disbond mode shape at 14.529 kHz, 2nd largest mode ranking index value

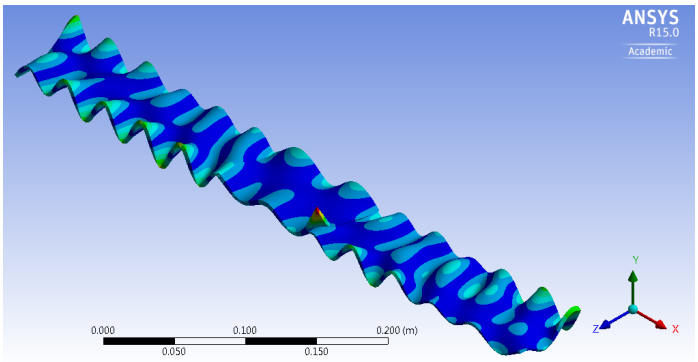

Figure 9.7: Disbond mode shape at 11.828 kHz, 3rd largest mode ranking index value

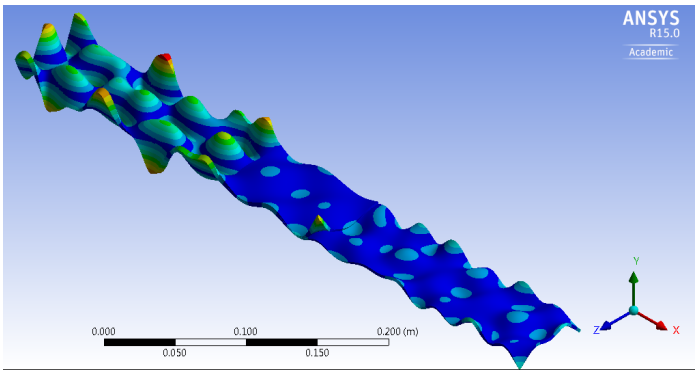

Figure 9.8: Disbond mode shape at 15.251 kHz, 4th largest mode ranking index value

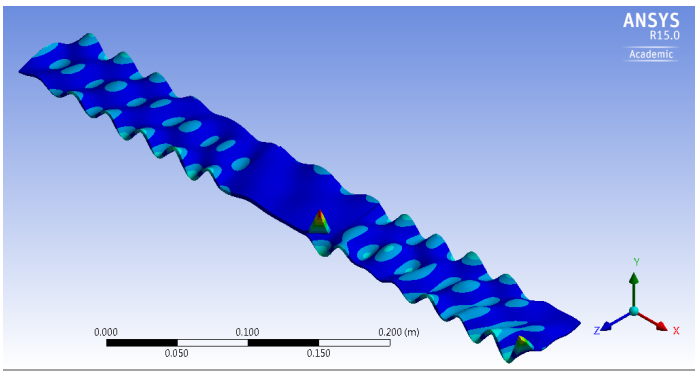

Figure 9.9: Disbond mode shape at 15.839 kHz, 5th largest mode ranking index value

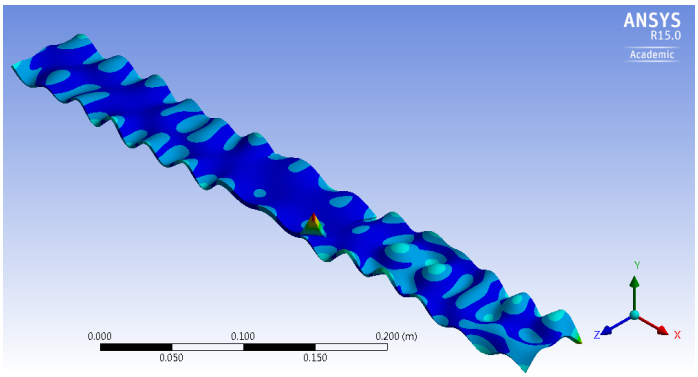

Figure 9.10: Disbond mode shape at 13.411 kHz, 6th largest mode ranking index value

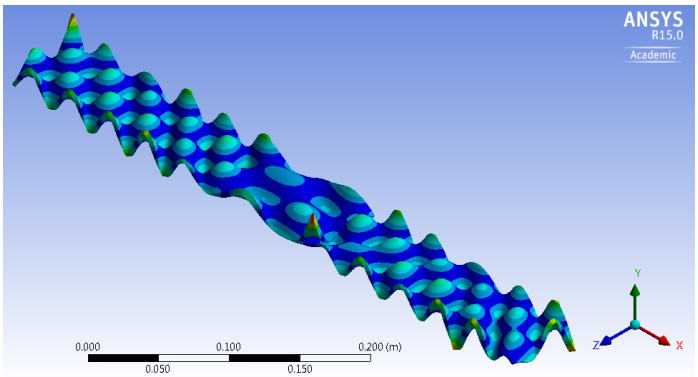

Figure 9.11: Disbond mode shape at 17.962 kHz

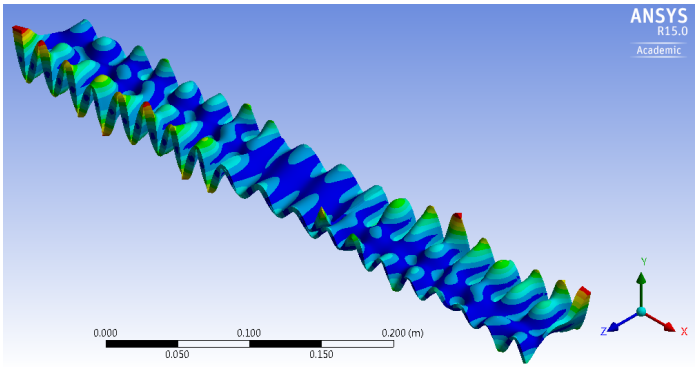

Figure 9.12: Disbond mode shape at 23.109 kHz

with some of the modes outside, correspond to the "flapping" mode demonstrated in the previous figures. The excitation frequencies in this range present the best chance of detecting the disbond.

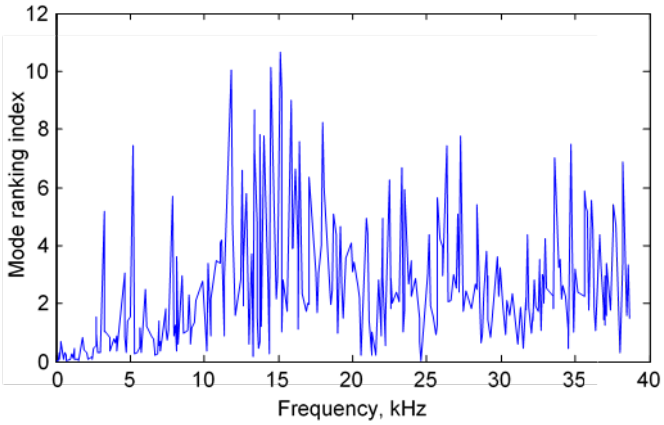

Figure 9.13: Plot of mode ranking index vs. Frequency

Now that several mode shapes have been identified, the sensor locations must be determined. This is accomplished through a finite element sensitivity study. A harmonic analysis is performed on bath the pristine and disbonded model. A total of 60 possible PWAS locations are simulated in the model, and all of the possible locations are shown in Figure 9.14. For each PWAS location, nodal forces are applied on the top surface of the doubler at the edge of the potential PWAS. Each of the nodal forces are applied normal to the edge of the PWAS.

An excitation frequency of 15.125 kHz was selected in order to find the ideal PWAS

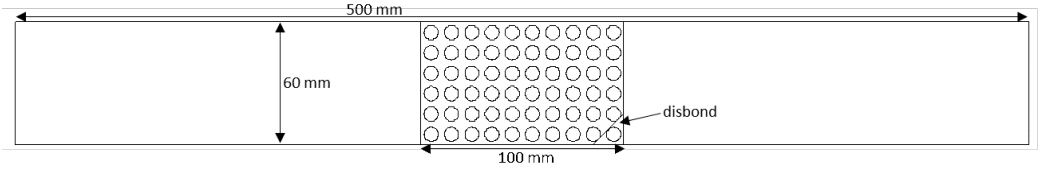

Figure 9.14: Possible PWAS locations used in the sensitivity study

location for detecting the primary mode shape of interest. The displacements of each excitation node was exported from ANSYS for analysis. One way to analyze the results would be to calculate the mechanical impedance at each node, since the force and velocities are know; however, this leads to the issue of what to do with 24 values for each PWAS location. Instead, the change in area of the theoretical PWAS location was used. This complex value should relate to the change in electrical impedance of a PWAS in the same location. For each PWAS location the difference between the real part of the change in area from the pristine and disbond model were divided by the real part of the change in area for the pristine model. These results were then used to generate a surface plot overlaid by the PWAS location, see Figure 9.15. As seen in this figure, the greatest differences come from the PWAS locations over and next to the disbond. This information was used to select the locations for the PWAS on the test coupon.

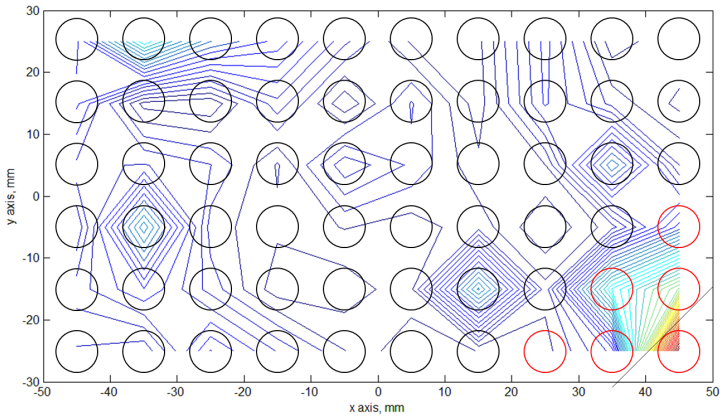

Figure 9.15: Results of the sensitivity study

9.5 Experimental Results

The first step in the experimental validation is to measure the impedance and admittance of the five PWAS on each test coupon. This measurement was performed using an HP 4194A impedance analyzer and the results were saved through a LabVIEW VI. Figure 9.16 shows the experimental setup.

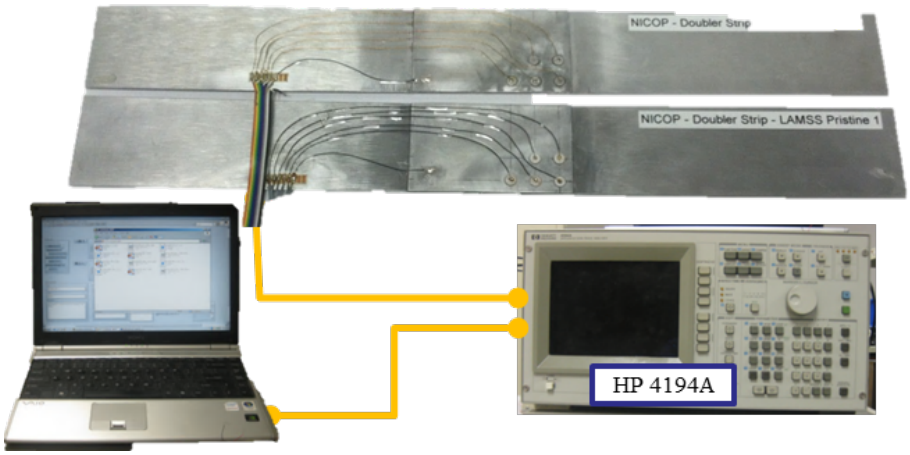

Figure 9.16: Experimental Setup for measuring the impedance and admittance of the PWAS

Once the results were gathered, they were compared between the pristine and disbond coupons for each PWAS location. The real admittance was used as the metric, and the peaks should correspond to resonance frequencies for the structure. Figure 9.17 shows the real admittance for PWAS 3. The results are compared for the disbond and pristine test coupon, and the disbonded case is shifted up in order to provide a clear view of both spectra. The circles indicate regions with large changes in admittance.

It is difficult to distinguish clear peaks with this frequency range; therefore, a new plot was created between 10 and 20 kHz. Figure9.18 shows this new plot. Again, the circles mark the new resonance peaks, which correspond to the FEA results that were discussed in the predictive modeling section. Also, the 15.5 kHz peak is labeled in the figure, and the FEA mode shape at this frequency is shown on the right side

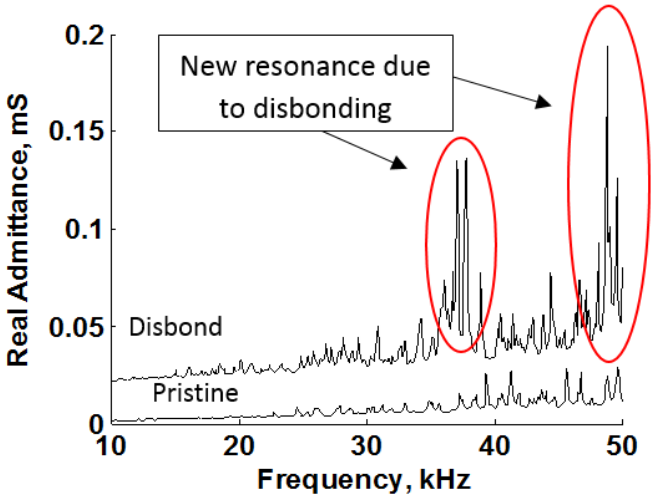

Figure 9.17: PWAS 3: Real admittance for the pristine and disbond test coupon (encircled peaks indicate newly detected resonances due to disbonding)

of the figure. This mode shape is highly localized around the disbond.

Another plot was created from 30 to 40 kHz. Figure 9.19 shows a higher frequency range, and additional resonance peaks are once again present. Again the circles show regions which contain additional peaks when compared to the pristine case.

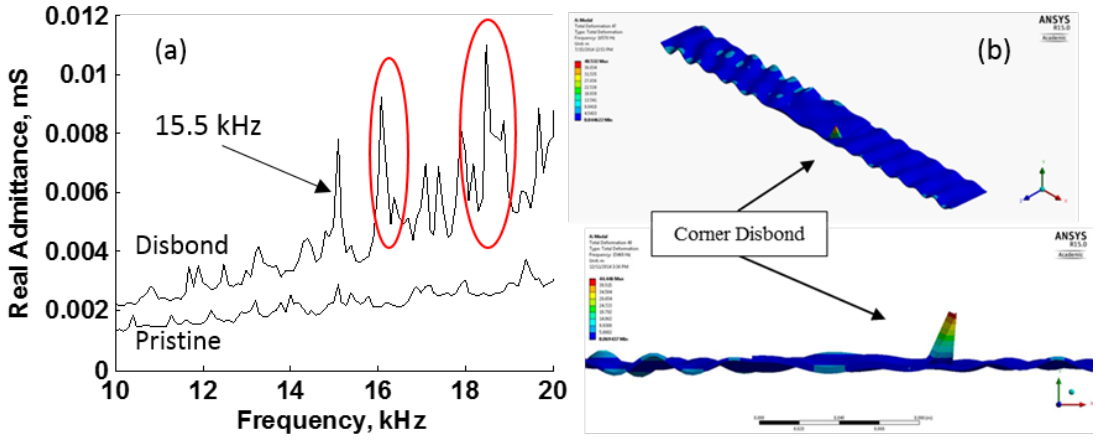

Figure 9.18: (a) Real admittance of PWAS 3 (encircled peaks indicate new resonances due to disbonding) (b) FEA mode shape at 15.5 kHz for disbond model indicating unique displacements over the disbond

In order to compare the five PWAS locations, the RMSD was calculated for each location, see Eq. (9.12). This metric is commonly used to determine the damage

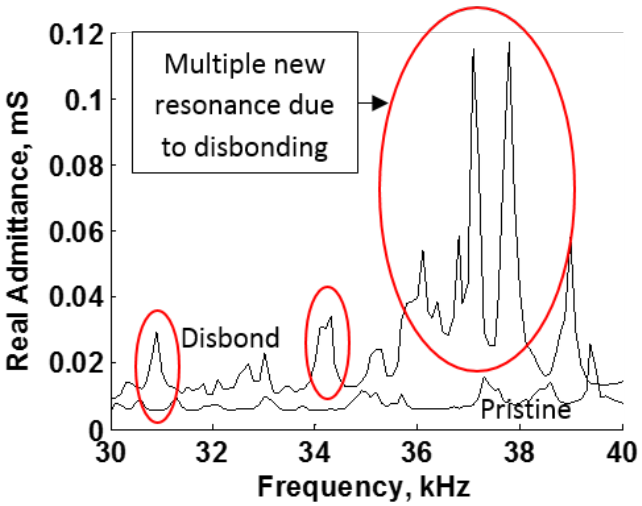

Figure 9.19: Real admittance of PWAS 3 (encircled peaks indicate new resonances due to disbonding)

Table 9.5: Experimental RMSD values for the five PWAS

PWAS #	1	2	3	4	5
RMSD	1.78	N/A	2.29	0.41	0.42

state.

$$RMSD = \sqrt{\frac{\sum_{i=1}^{N}\left[Re(Y_i) - Re(Y_i^0)\right]^2}{\sum_{i=1}^{N}\left[Re(Y_i^0)\right]^2}} \tag{9.12}$$

First, the RMSD was calculated for the entire frequency range. These results are shown in Table 9.5. The second PWAS on the pristine test coupon had an electrical fault; therefore, the results for this PWAS are not shown at this time. It is clear from the table that PWAS 3 has the largest RMSD value; therefore, it has the best chance at identifying the disbond. The other PWAS locations also provide good results, and can be used to differentiate between the pristine and disbonded structure.

Since the predictive modeling has shown that there are clear damage modes for the coupon, the RMSD can also be applied to a small frequency range near the expected damage modes. This was first calculated for a frequency range between 15 and 20 kHz, this is shown in Table 9.6. Now, the additional PWAS are producing higher

Table 9.6: Experimental RMSD values for 15 - 20 kHz

PWAS #	1	2	3	4	5
RMSD	1.08	N/A	1.36	1.27	0.70

Table 9.7: Experimental RMSD values for 35 - 40 kHz

PWAS #	1	2	3	4	5
RMSD	1.72	N/A	1.74	0.82	0.61

RMSD values than the broad frequency case. Therefore, identifying the appropriate frequency ranges for the expected disbond will allow the PWAS to detect this disbond from a greater distance than a blind frequency sweep.

Also, the RMSD was collected for frequencies between 35 and 40 kHz, corresponding to the second damage mode. These results are provided in Table 9.7. Again the potential detectability of the PWAS is improved through the identification of damage modes and the corresponding frequency range.

9.6 Laser Doppler Velocimetry

In order to verify that these changes in the admittance of the PWAS do correlate with the damage modes identified through FEA, a second experiment was set up to experimentally create these mode shapes. This can be accomplished with the use of scanning laser Doppler velocimetry. This technique measures the out of plane velocity of the structure by utilizing the Doppler Effect. The disbonded test coupon is placed on blocks to maintain the traction free boundaries. Each PWAS will individually be excited with a chirp signal from 10 to 80 kHz. The equipment then scans a section of the coupon and measures the velocity at a point for the entire chirp signal before moving to the next point. In this way a matrix of values for the velocity field is

generated for both the magnitude and phase. The experimental setup is shown in Figure 9.20.

Figure 9.20: Experimental setup for the scanning laser Doppler velocimetry

The mode shape is then created based on this data and a surface plot is created and superimposed over an image of the test coupon. The mode shape for 17.8 kHz is shown in Figure 9.21. This mode shape is comparable to the 17.7 kHz mode shape created in ANSYS, as seen in Figure 9.22. These two mode shapes show good agreement and prove that this change in vibration is the driving factor behind the change in admittance of the PWAS.

This has also been performed for the third damage mode. The mode shape from the LDV for 65.1 kHz is shown in Figure 9.23. This compares well to the mode shape generated in ANSYS for 65.4 kHz, shown in Figure 9.24. These results verify the predictive modeling methodology for detecting disbonds with the EMIS method.

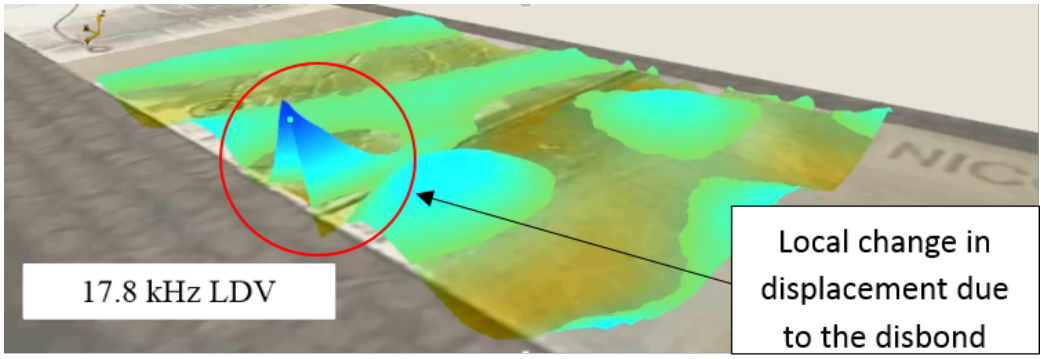

Figure 9.21: Experimental mode shape from the LDV for 17.8 kHz

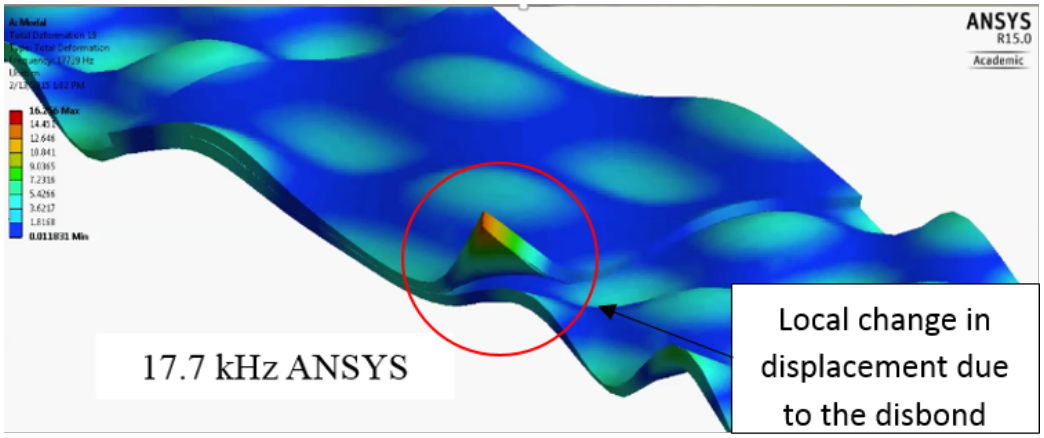

Figure 9.22: Numerical mode shape from ANSYS for 17.7 kHz

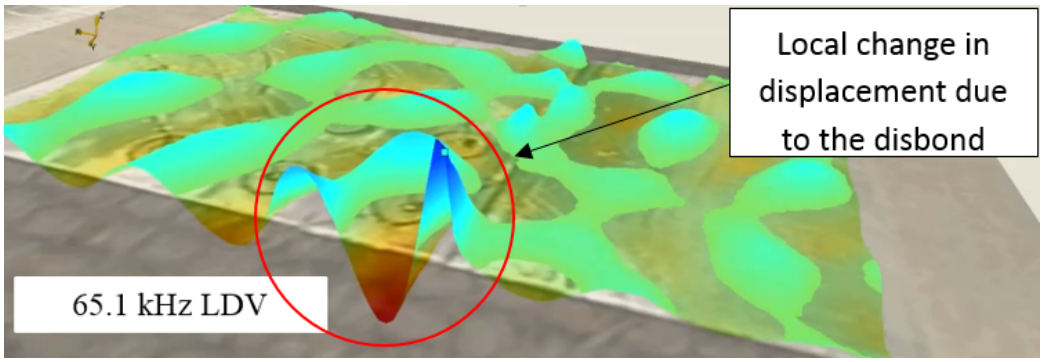

Figure 9.23: Experimental mode shape from the LDV for 65.1 kHz

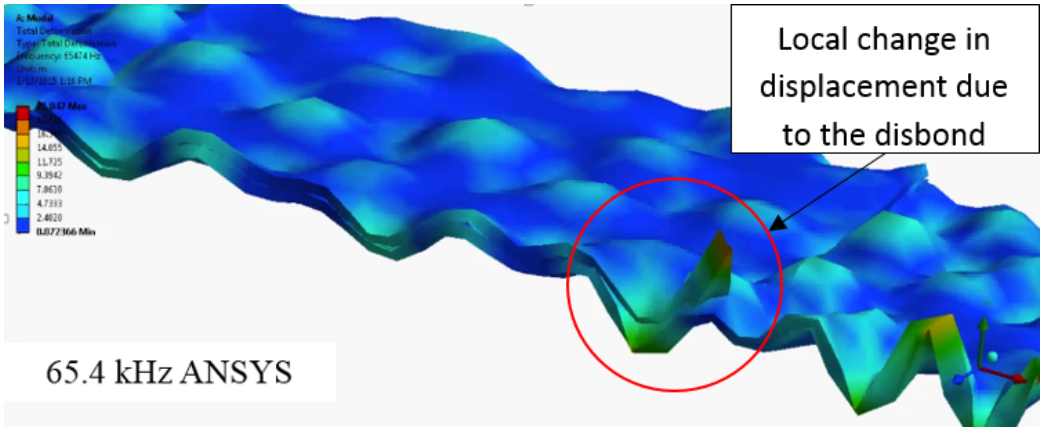

Figure 9.24: Numerical mode shape from ANSYS for 65.4 kHz

9.7 Conclusion

I have presented a process for determining the frequency range and sensor locations for the application of EMIS to PWAS attached to an adhesively bonded joint as part of an SHM program. The goal of the work is to contribute towards a method of continuously monitoring adhesive joints in-situ so that adhesive can be used in primary aerospace structures. The presented process was applied to a test article and the numerical results were validated through experimental measurements of EMIS and visualization of the vibration with laser Doppler velocimetry. The experimental results showed that the method can accurately predict the frequencies which cause local vibration of the disbond. Therefore, the proper frequency ranges can be identified quickly for geometries which are not easily modeled analytically through the use of FE modal analysis and the algorithm discussed in the paper.

Chapter 10

Disbond Detection through Guided Wave Inspection

10.1 Motivation

The previous chapter discussed the potential of detecting adhesive disbonding through a local vibration method. It was demonstrated that the technique is sensitive to damage within a sensing zone, but this may still require a great number of sensors to cover a large area. Guided wave inspection provides the possibility of detecting damage with a relatively sparse array of sensors. This chapter is concerned with the detection of adhesive disbonding, and in particular the sizing of the disbond. The following sections will demonstrate a technique for exciting local vibration modes with guided waves, and how the frequency of the scattered wave can be used to determine the length of the disbond.

10.2 Problem Setup

The goal is to detect the growth of an edge disbond within the adhesive of an aluminum doubler. This inspection schemes consists of a transmitter and receiver on either side of the doubler (Figure 10.1). In this chapter, only the two dimensional case is considered. A finite element analysis (FEA) is used to relate the frequency dependent scattered signal to the disbond length. In order to efficiently perform this analysis, a harmonic, instead of a transient, method is utilized. In order to remove the edge reflections, which would create full-specimen standing waves, non-reflecting

boundaries are implemented at the model boundary. Note that in ABAQUS, infinite elements can be used to prevent the scattering of waves; however, these elements are designed for bulk waves, not guided waves, and they will not work for this case. The model (Figure 10.1) uses infinite elements at plate ends along with linear dashpot elements within the non-reflecting region at the top and bottom surfaces of the plate. These surface elements absorb the energy of the waves reflected at the plate top and bottom surfaces adjacent to the plate ends; they are fashioned in wedge-like geometry diminishing as one departs from the plate ends. The infinite elements are left to absorb any bulk waves that are traveling along the length of the plate. The damping constant is ramped up along the plate from a very small value to the maximum value at the plate edge; as shown in Figure 10.1. The length of this non-reflecting zone is set to be four times the largest wavelength to ensure that no guided waves are reflected from the plate ends.

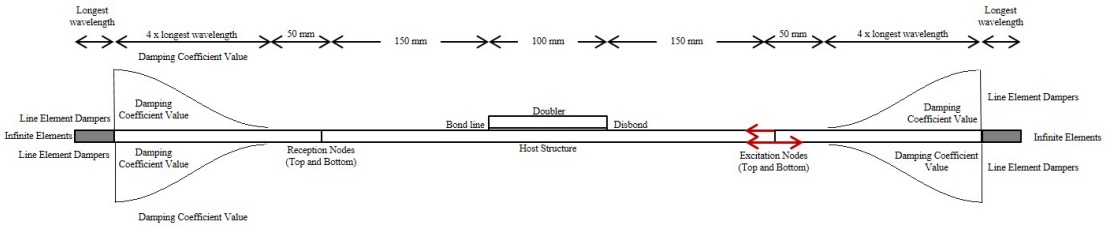

Figure 10.1: 2D FEM harmonic analysis problem setup with non-reflecting boundaries

The FEA mesh was implemented with quadratic elements with minimal distortion. The element length was set so that there were 30-40 elements per wave length, dependent on the smallest wavelength in the desired frequency range (Figure 10.2). The non-reflecting zone occupied around half of the model size. The guided waves were generated by unit forces applied to top-bottom excitation nodes placed at the right hand side of the model (Figure 10.1). The traveling guided waves were captured as strain measured at the receiving nodes placed a the left hand side of the model. Symmetric and antisymmetric guided wave modes were excited through symmetric and antisymmetric arrangement of the excitation forces. The top and bottom

measurements were resolved into symmetric and antisymmetric components.

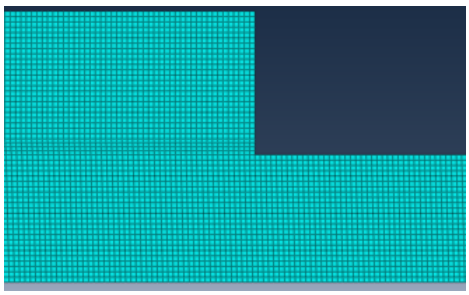

(a) Example mesh density

(b) Full view of model meshing with linear dashpot elements

Figure 10.2: Example mesh requirements for the 2D FEM harmonic analysis in ABAQUS

10.3 Results

10.3.1 No Doubler

The implementation of the non-reflecting boundaries was first verified through a model without a doubler (Figure 10.3). Both symmetric and anti-symmetric waves were excited separately. This is clear from the results in Figure 10.4, where only symmetric modes where detected at the receiver when a symmetric excitation was performed, and the same was observed for an anti-symmetric excitation.

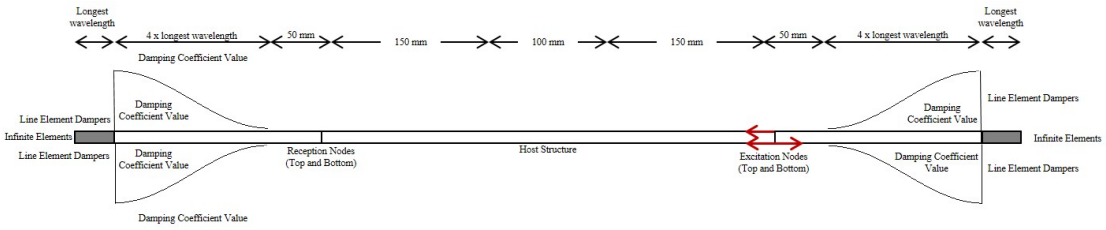

Figure 10.3: 2D FEM harmonic analysis problem setup with non-reflecting boundaries

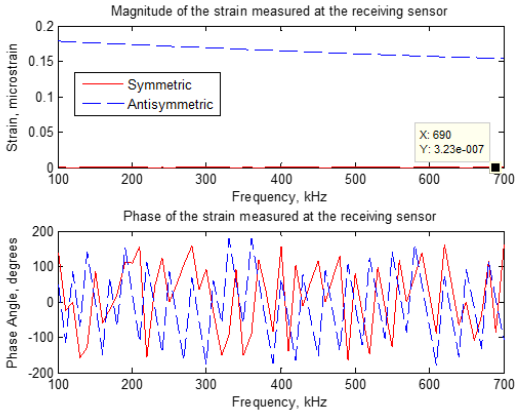

(a) Anti-symmetric excitation

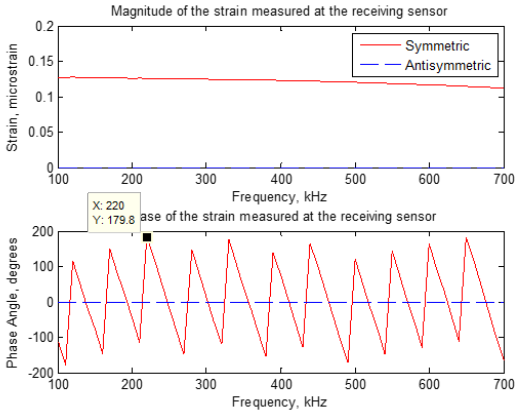

(b) Symmetric excitation

Figure 10.4: Strain at the reception nodes

10.3.2 Doubler, No Disbond

Next, the adhesively bonded doubler is added to the model. These results represent the pristine case. Now both symmetric and antisymmetric guided waves are present at the receiver when either symmetric or antisymmetric wave excitation is applied (Figure 10.5). This is due to mode conversion at the discontinuity at the doubler ends. The peaks and troughs in the data are due to resonances that are generated within the doubler, as well as shifting mode shapes with frequency.

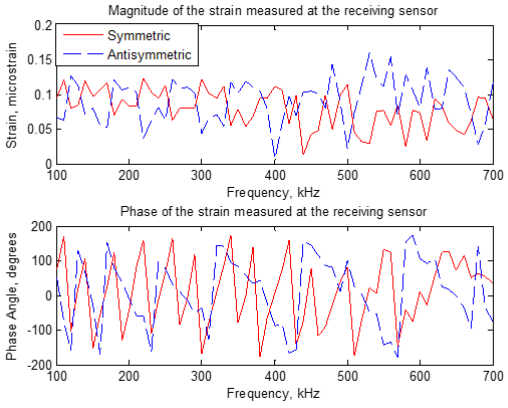

(a) Symmetric excitation

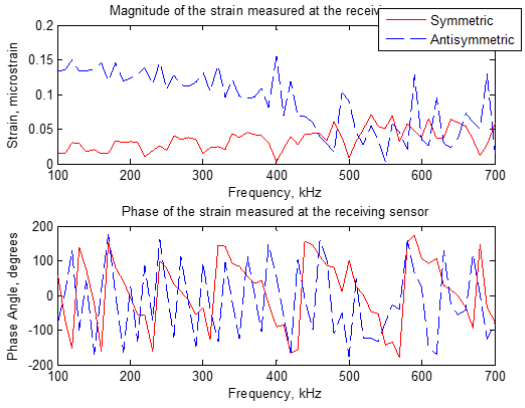

(b) Anti-symmetric excitation

Figure 10.5: Strain at the reception nodes

10.3.3 10 mm Disbond

A 10 mm disbond was inserted between the doubler and the substrate at the end adjacent to the excitation nodes. The disbond was created by removing the nodal connection at the host plate structure to the adhesive. Once again the frequency spectrum of the received signal has changed. The anti-symmetric transmitted waves from an anti-symmetric excitation are not showing a clear repetitious pattern of troughs in the received signal (Figure 10.6).

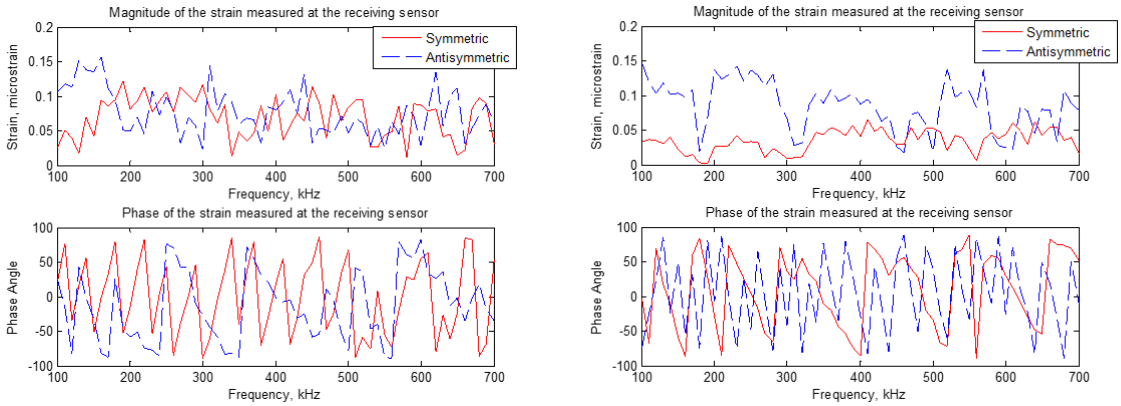

(a) Symmetric excitation

(b) Anti-symmetric excitation

Figure 10.6: Strain at the reception nodes

10.4 Damage Index

In order to evaluate the affect of the disbond on the received signal, a damage index is proposed. The damage index is the difference between the pristine and damaged signals. This could also be considered as a separate wave generated at the damage site. Four different damage indexes are generated: the comparison of a symmetric excitation with a symmetric transmitted wave (SS); symmetric excitation with anti-symmetric transmission (SA), anti-symmetric with anti-symmetric (AA); and anti-symmetric with symmetric (AS) (Figure 10.7). Investigation of the full damage index shows that the AA results contain peaks at 180 and 320 kHz. It was hypothesized

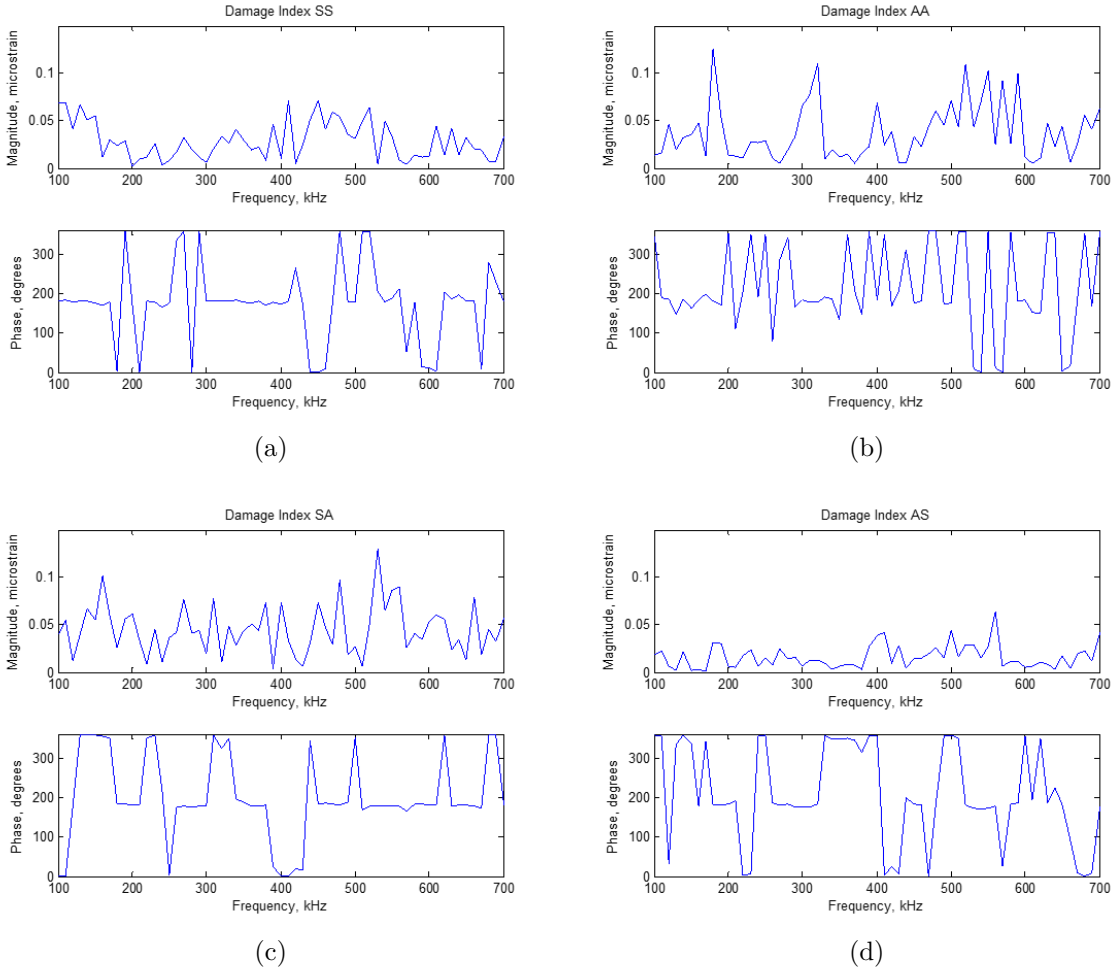

Figure 10.7: Damage index: 100 mm doubler with a 10 mm disbond

that these peaks correspond to local vibration of the disbond. In other words, the guided waves at these frequencies excite a local flexural mode, similar to the flexural vibration of a cantilever beam. As a result, less energy is transmitted across the doubler to the receiving nodes.

In order to verify this hypothesis, a second model was created with a 15 mm disbond (Figure 10.8). Now the peaks have shifted down to 170 and 270 kHz. This would be expected for the local vibration of a two dimensional disbond, where the flexural vibration frequencies will decrease when the length of the beam is increased.

To further verify the connection between these local vibration resonances and the

disbond, we tested the hypothesis that the peaks were not due to disbond but to the doubler length. In this case, the results should be similar to decreasing the doubler length by 10 mm. in order to simulate this case, the doubler length was reduced from 100 mm to 90 mm, and the results were treated like damage (Figure 10.9). As can be seen, the peaks have disappeared; therefore, they must be specific to the disbond.

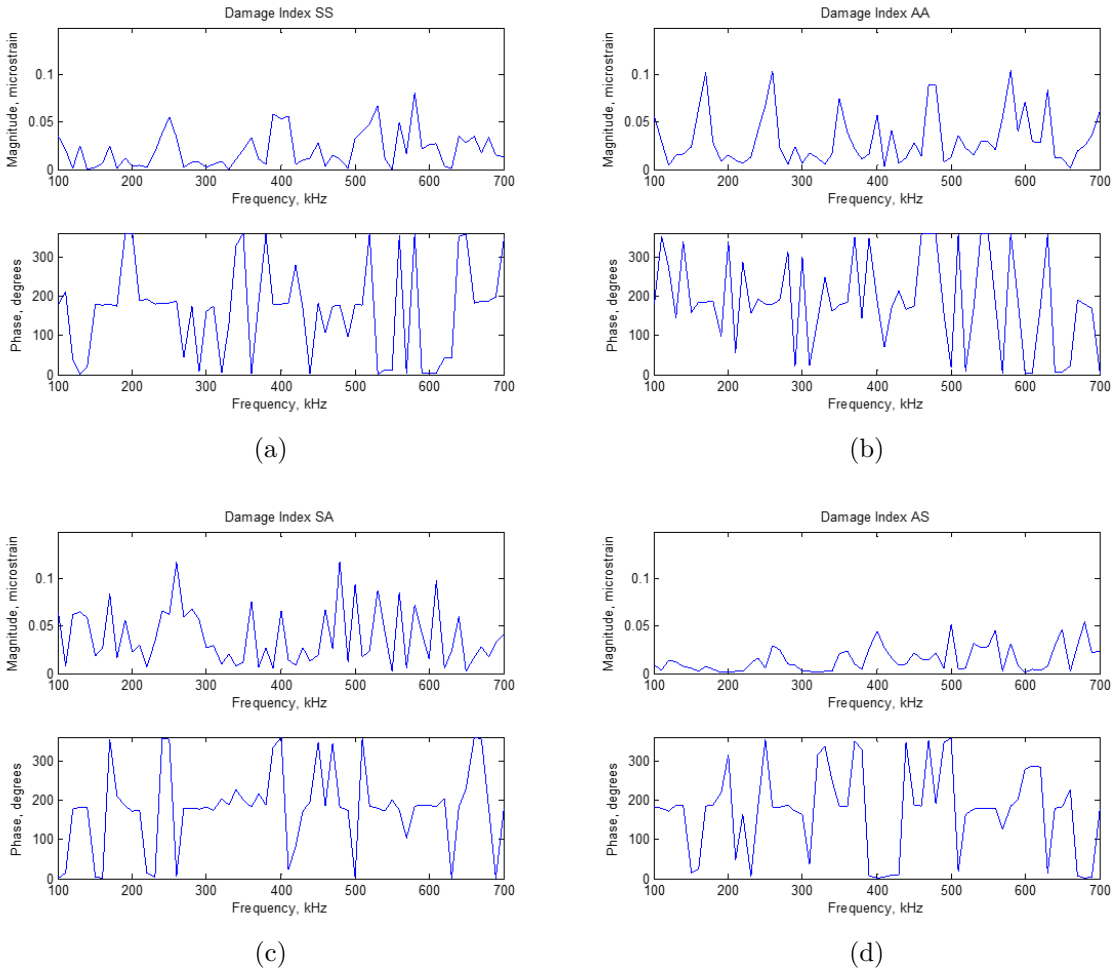

Figure 10.8: Damage index: 100 mm doubler with a 15 mm disbond

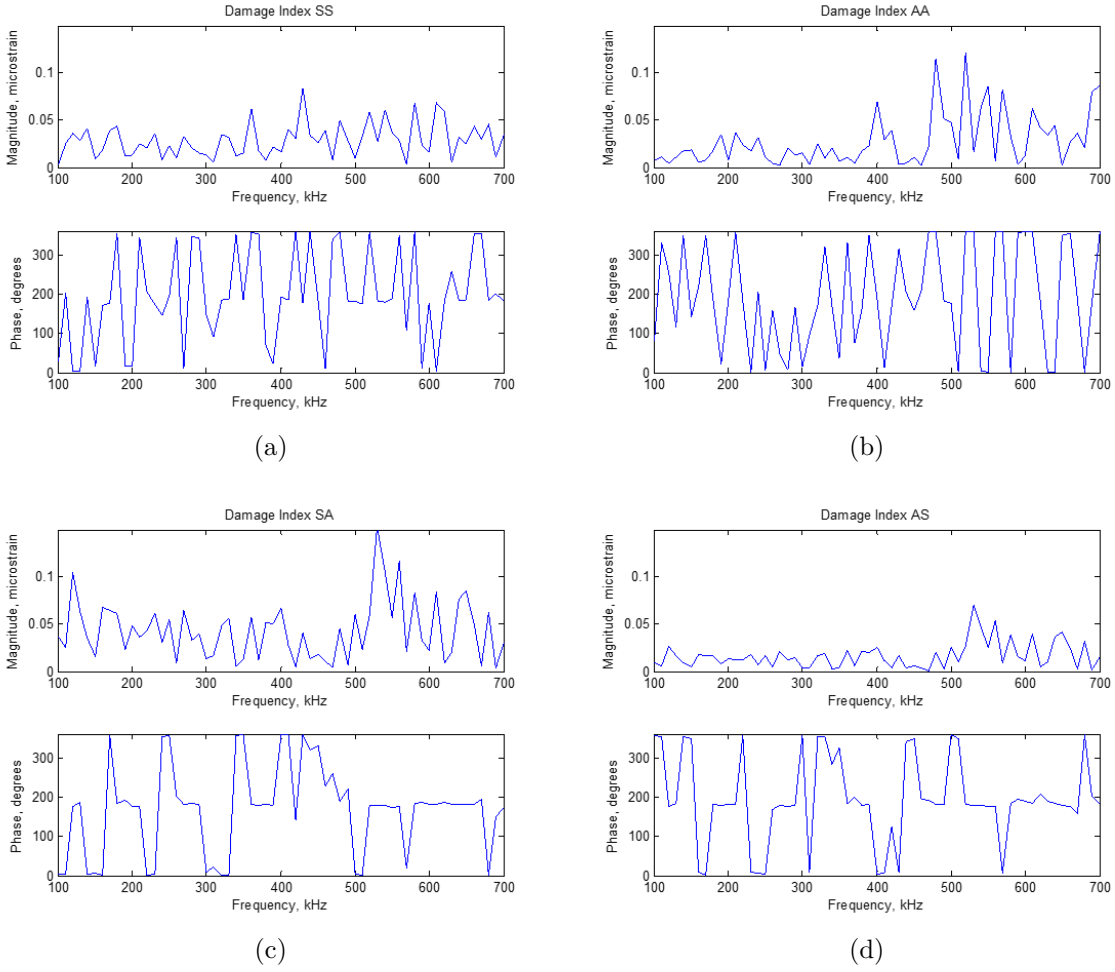

Figure 10.9: Damage index: 90 mm doubler vs. a 100 mm doubler

10.5 Local Vibration Modes

To further the proof that these peaks in the AA damage index are due to local vibration resonances, the mode shape of the model is shown for several frequencies (Figure 10.10). At 180 kHz, the disbonded model exhibits a local vibration similar to the flexural vibration of a beam. This behavior is not present in the pristine model, and there is very little excitation of the disbond at 220 kHz.

Similar behavior is observed for the 15 mm disbond (Figure 10.11). Now the local flexural vibration mode appears to be a higher order.

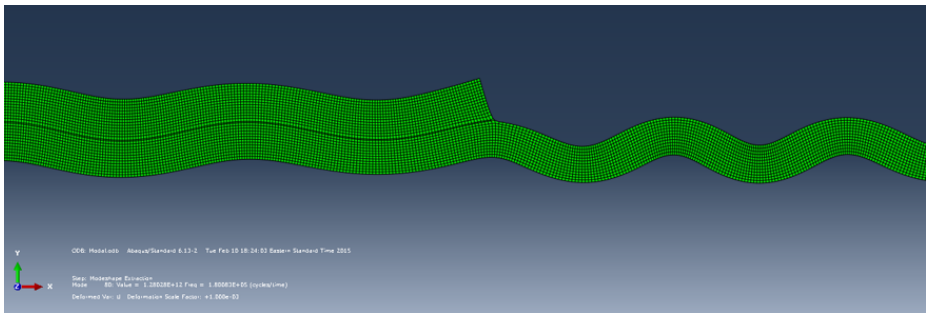

(a) 180 kHz Pristine

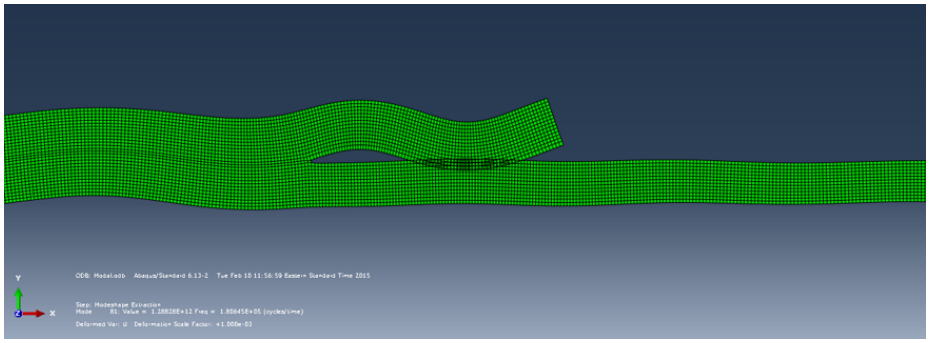

(b) 180 kHz; 10 mm disbond

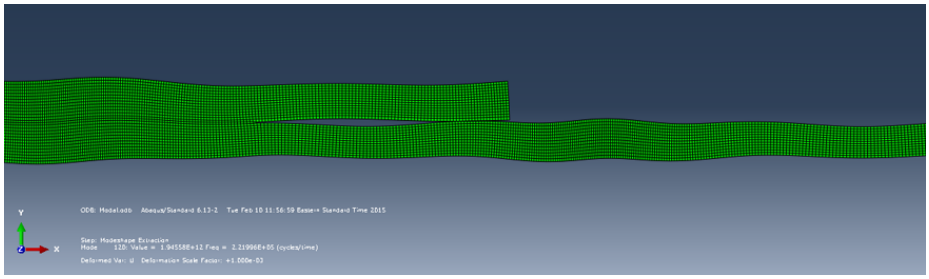

(c) 220 kHz; 10 mm disbond

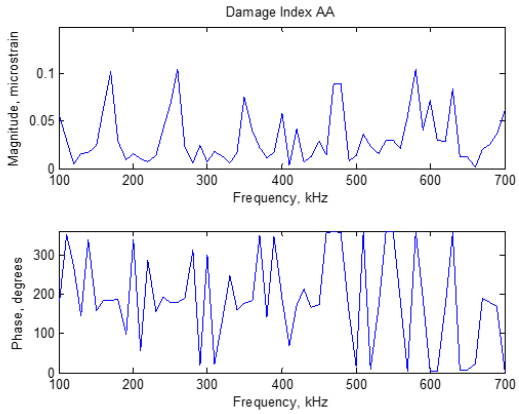

(d) 10 mm disbond; damage index AA

Figure 10.10: Peaks in the damage index correspond to the generation of local vibration resonances at the disbond site

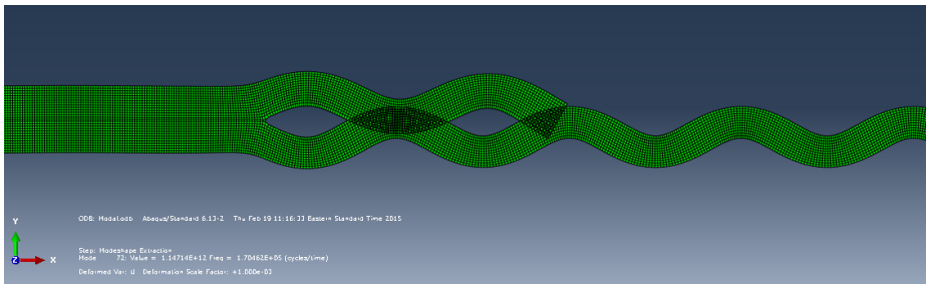

(a) 170 kHz; 15 mm disbond

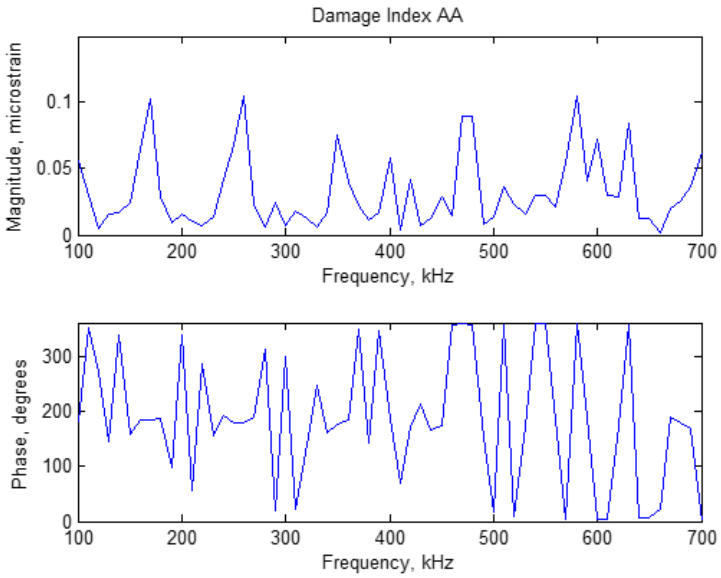

(b) 15 mm disbond; damage index AA

Figure 10.11: Peaks in the damage index correspond to the generation of local vibration resonances at the disbond site

10.6 Conclusion

This chapter has clearly demonstrated that local vibration modes exist within a disbond (this was also shown in the previous chapter for a mode complicated geometry). These local flexural modes can be exited by guided waves, and the frequency dependent change in the transmission coefficients of the guided waves through the doubler can be used to both detect and size a disbond. A relatively simple model may be used to relate the AA damage model peaks to the disbond length for the two dimensional case. This work can be extended to three dimensional models and disbonds, as

done in the previous chapter which discussed the electromechanical impedance spectroscopy method.. These more complicated disbond geometries will also have unique local vibration modes, and the mode comparison algorithm of the previous chapter could be used to relate these frequencies to the disbond size.

Chapter 11

Conclusions and Future Work

11.1 Research Conclusions

This dissertation has provided an overview of adhesively bonded structures; structure, analysis and NDE. As well as the presentation of the fundamentals of elastic wave propagation in anisotropic media and a thorough state-of-the-art for guided wave inspection of adhesively bonded structures.

The solution methods for guided waves was thoroughly explored and several techniques were proposed. Analytical, semi-analytical and numerical approaches to finding the eigenvalues of the system of equations were demonstrated, where the semi-analytical approach was a novel development. The typical brute force method of generating initial guess was analyzed, and a new, novel approach based on the observed behavior was proposed and demonstrated.

Several inspection methodologies for the detection of defects in adhesively bonded structures were proposed and demonstrated. The predictive modeling of guided wave inspection was discussed and methods based on both the mode shape and damage modeling were proposed. The existence of an intermediate zone between the plate and embedded waves was discovered. Modeling of a weak interface as a reduced stiffness model was demonstrated for adhesively bonded composite structures. A new method for determining the properties of adhesive and interphase was proposed through the optimization of guided wave behavior.

A new experimental technique for calculating the full phase velocity information

of a fiber reinforced polymer lamina is presented, along with an optimization process for determining the stiffness matrix components.

A novel finite element post-processing technique was proposed and demonstrated for investigating the frequency range and sensor locations for the application of EMIS for the detection of adhesive disbonding. The process was applied to a test article and the numerical results were validated through experimental measurements of EMIS and laser Doppler vibrometry.

A finite element harmonic analysis was used to show how local vibrations of a disbond can be excited and detected through guided wave inspection. The model was limited to two dimensions, where the disbond length can be correlated to the frequency spectrum. More complicated disbond geometry should have similar results.

11.2 Major Contributions

1. Novel approach for the calculation of the full complex dispersion of guided waves in multi-layered anisotropic plates.

2. Novel semi-analytical approach to determine the eigenvalue and eigenmodes for guided waves in multi-layered anisotropic plates.

3. Used a reduced stiffness approach to model the guided wave behavior of an adhesively bonded composite structure with weak bonding.

4. Measuring the experimental dispersion curves for adhesively bonded structures, including weak bonding and disbonding.

5. Novel approach of determining the adhesive and weak interface properties through the optimization of guided wave dispersion.

6. Novel experimental approach for the optimization of the stiffness matrix of a fiber reinforced composite laminate.

7. Novel approach to post-process finite element modal analysis results in order to track mode shapes through damage and determine the optimum inspection frequencies for detecting disbonding of an adhesively bonded structure.

8. Used finite element harmonic analysis with non-reflecting boundaries to prove that the guided waves can excite local vibration modes in adhesively bonded structures, and that the frequency spectrum of the scattered wave can be used to determine the length of the disbond.

11.3 Recommendation for Future Work

1. Experimental validation of complex dispersion results.

2. Use the complex dispersion algorithm to generate guided wave scattered fields for discrete damage.

3. Improve the optimization routine for guided waves.

4. Perform the optimization of adhesive properties with composite adherends.

5. Use the contact phased array experimental method to generate and detect embedded guided waves within an adhesive layer.

6. Extend the local vibration of a disbond through guided wave excitation to a full three dimensional model and validate through experiments.

Bibliography

[1] A. Higgins, "Adhesive bonding of aircraft structures," *International Journal of Adhesion and Adhesives*, vol. 20, pp. 367–376, 2000.

[2] A. Beevers, "Forensic studies of adhesive joints. part 2 âĂŞ bonded aircraft structures," *Project 3: Environmental Durability of Adhesive Bonds*, 1995.

[3] G. M. Light and H. Kwun, "Nondestructive evaluation of adhesive bond quality: State-of-the-art review," *Southwest Research Institute*, 1989.

[4] D. J. Hagemaier, "Adhesive-bonded joints," *ASM Handbook*, vol. 17, pp. 610–640, 1989.

[5] T. T. Wang, F. W. Ryan, and H. Schonhorn, "Effect of bonding defects on shear strength in tension of lap joints having brittle adhesives," *Journal of Applied Polymer Science*, vol. 16, no. 8, pp. 1901–1909, 1972.

[6] R. D. Adams and B. W. Drinkwater, "Nondestructive testing of adhesively-bonded joints," *NDT&E International*, vol. 30, no. 2, pp. 93–98, 1997.

[7] R. D. Adams and P. Cawley, "A review of defect types and nondestructive testing techniques for composites and bonded joints," *NDT International*, vol. 21, no. 4, pp. 208–222, 1988.

[8] M. D. Bode, M. J. Holle, and D. Westlund, "Literature review of weak adhesive bond fabrication and nondestructive inspection for strength measurement," *DOT/FAA/TC-14/39, US. Department of Transportation*, 2015.

[9] O. Volkerson, "Die niektraftverteilung in zugbeanspruchten mit konstanten laschenquerschritten," *Luftfahrtforschung*, vol. 15, pp. 41–47, 1938.

[10] M. Goland and E. Reissner, "The stresses in cemented joints," *Journal of Applied Mechanics*, 1944.

[11] L. F. da Silva, P. J. das Neves, R. Adams, and J. Spelt, "Analytical models of adhesively bonded joints - part 1: Literature survey," *International Journal of Adhesion & Adhesives*, vol. 29, pp. 319–330, 2009.

[12] D. Gleich, *Stress Analysis of Structural Bonded Joints*. PhD thesis, Delft University of Technology, Delft, Netherlands, 2002.

[13] F. J. Chaves, L. da Silva, M. de Moura, D. Dillard, and V. Esteves, "Fracture mechanics tests in adhesively bonded joints: A literature review," *The Journal of adhesion*, vol. 90, no. 12, pp. 955–992, 2014.

[14] D. Hunston, "Failure, fracture mechanics, and toughening in adhesive joints," in *Adhesion Science and Technology Short Course*, Adhesion Society, 2015.

[15] T. Kinloch, "Industrial applications of adhesive fracture mechanics," in *Adhesion Science and Technology Short Course*, Adhesion Society, 2015.

[16] L. F. da Silva, *Modeling of Adhesively Bonded Joints*. Berlin: Springer-Verlag, 2008.

[17] M. Alfano, F. Furgiuele, A. Leonardi, C. Maletta, and G. H. Paulino, "Mode I fracture of adhesive joints using tailored cohesive zone models," *International Journal of Fracture*, pp. 193–204, 2009.

[18] M. de Moura, J. Goncalves, and A. Magalhaes, "A straightforward method to obtain the cohesive laws of bonded joints under mode I loading," *International Journal of Adhesion & Adhesives*, vol. 39, pp. 54–59, 2012.

[19] R. Campilho, M. Banea, J. Neto, and L. da Silva, "Modelling adhesive joints with cohesive zone models: effect of the cohesive law shape of the adhesive layer," *," International Journal of Adhesion & Adhesives*, vol. 44, pp. 48–56, 2013.

[20] B. Blackman, H. Hadavinia, A. Kinlock, and T. Williams, "The use of a cohesive zone model to study the fracture of fibre composites and adhesively-bonded joints," *International Journal of Fracture*, vol. 119, pp. 45–46, 2003.

[21] M. Lee, E. Yeo, M. Blacklock, M. Janardhana, S. Feih, and C. H. Wang, "Predicting the strength of adhesively bonded joints of variable thickness using a cohesive element approach," *International Journal of Adhesion & Adhesives*, vol. 58, pp. 44–52, 2015.

[22] M. de Moura, J. Goncalves, J. Chousal, and R. Campilho, "Cohesive and continuum mixed-mode damage models applied to the simulation of the mechanical behavior of bonded joints," *International Journal of Adhesion & Adhesives*, vol. 28, pp. 419–426, 2008.

[23] D. M. Gleich, M. J. L. van Tooren, and A. Beukers, "A stress singularity approach to failure initiation in a bonded joint with varying bondline thickness," *Journal of Adhesion Science and Technology*, vol. 15, no. 10, pp. 1247–1259, 2001.

[24] D. M. Gleich, M. J. L. van Tooren, and A. Beukers, "Analysis and evaluation of bondline thickness effects on failure load in adhesively bonded structures," *Journal of Adhesion science and Technology*, vol. 15, no. 9, pp. 1091–1101, 2001.

[25] M. J. L. van Tooren, D. M. Gleich, and A. Beukers, "Experimental verification of a stress singularity model to predict the effect of bondline thickness on joint strength," *Journal of Adhesion Science and Technology*, vol. 18, no. 4, pp. 395–412, 2004.

[26] M. J. L. van Tooren and L. A. Krakers, "A generalized stress singularity approach for material failure prediction and its application to adhesive joint strength analysis," *Journal of Adhesion Science and Technology*, vol. 20, no. 9, pp. 981–995, 2006.

[27] E. Segal, G. Thomas, and J. L. Rose, "Hope for solving the adhesive bond nightmare," *Proceedings of the 12th Symposium on NDE*, pp. 269–281, 1979.

[28] R. D. Adams and P. Cawley, "The mechanics of the coin-tap method of nondestructive testing," *Journal of Sounds and Vibration*, vol. 122, no. 2, pp. 299–316, 1988.

[29] O. R. Gericke, "Determination of the geometry of hidden defects by ultrasonic pulse analysis testing," *Journal of the Acoustic Society of America*, vol. 35, no. 3, pp. 364–368, 1983.

[30] R. S. Williams and P. E. Zwicke, "Assessment of adhesive properties using pattern recognition analysis of ultrasonic NDE data," *Materials Evaluation*, vol. 40, pp. 312–317, 1982.

[31] H. G. Tattersall, "The ultrasonic pulse-echo technique applied to adhesive testing," *Journal of Physics D: Applied Physics*, vol. 6, pp. 819–832, 1973.

[32] J. L. Rose and P. A. Meyer, "Ultrasonic procedure for predicting adhesive bond strength," *Materials Evaluation*, pp. 109–114, 1973.

[33] P. A. Meyer and J. L. Rose, "Ultrasonic determination of bond strength due to surface preparation variations in aluminum to aluminum adhesive bond systems," *Journal of Adhesion*, vol. 8, pp. 145–153, 1976.

[34] T. Chernobelskaya, S. Kovnovich, and E. Harnik, "The testing of adhesive bonded joints by a very high resolution ultrasonic probe," *Journal of Physics D: Applied Physics*, vol. 12, 1979.

[35] L. Adler and H. L. Whaley, "Interference effect in a multi-frequency ultrasonic pulse echo and its application to flaw characterization," *Journal of the Acoustic Society of America*, vol. 51, pp. 881–887, 1972.

[36] G. Alers, P. L. Flynn, and J. L. Buckley, "Ultrasonic techniques for measuring the strength of adhesive bonds," *Materials Evaluation*, vol. 35, no. 4, pp. 77–84, 1977.

[37] F. H. Chang, J. C. Couchman, and B. G. W. Yee, "Transmission frequency spectra of ultrasonic waves through multi-layer media," in *Proceedings from the 1973 Ultrasonic Symposium*, pp. 209–215, IEEE, 1973.

[38] F. H. Chang, B. G. Yee, and J. C. Couchman, "Spectral analysis technique of ultrasonic NDT of advanced composite materials," *Nondestructive Testing*, pp. 194–198, August 1974.

[39] F. H. Chang, P. L. Flynn, D. E. Gordon, and J. R. Bell, "Principles and application of ultrasonic spectroscopy in NDE of adhesive bonds," *IEEE Transactions on Sonics and Ultrasonics*, vol. SU-23, no. 5, pp. 334–338, 1976.

[40] S. Rokhlin, D. E. Chimenti, and P. B. Nagy, *Physical Ultrasonics of Composites*. Oxford, UK: Oxford University Press, 2011.

[41] H. Lamb, "On waves in an elastic plate," *Proceedings of the Royal Society of London, Series A*, vol. 93, p. 114, 1917.

[42] J. W. S. Rayleigh, "On waves propagated along the plane surface of an elastic solid," *Proceedings of the London Mathematical Society*, vol. 17, pp. 4–11, 1887.

[43] R. Stoneley, "Elastic waves at the surface of separation of two solids," *Proceedings of the Royal Society of London*, vol. 106, no. 738, pp. 416–428, 1924.

[44] J. P. Jones and J. S. Whittier, "Waves at a flexibly bonded interface," *Journal of Applied Mechanics*, pp. 905–909, December 1967.

[45] P. B. Nagy and L. Adler, "Nondestructive evaluation of adhesive joints by guided waves," *Journal of Applied Physics*, vol. 66, no. 10, pp. 4658–4663, 1989.

[46] D. W. schindel, "Air-coupled ultrasonic measurements of adhesively bonded multi-layered structures," *Ultrasonics*, vol. 37, pp. 185–200, 1999.

[47] Y. Bar-Cohen, "Ultrasonic nde of composites âĂŞ a review," *Solid Mechanics Research for Quantitative Non-Destructive Evaluation*, vol. 6, pp. 187–201, 1987.

[48] T. Kundu, A. Maji, T. Ghosh, and K. Maslov, "Detection of kissing bonds by lamb waves," *Ultrasonics*, vol. 35, no. 8, pp. 573–580, 1998.

[49] Y. Bar-Cohen and D. E. Chimenti, "Nondestructive evaluation of composites by leaky lamb waves," *Review of Progress in Quantitative Nondestructive Evaluation*, 1985.

[50] C. M. Teller, K. J. Diercks, Y. Bar-Cohen, and N. N. Shah, "Nondestructive evaluation of adhesive bonds using leaky lamb waves," *Review of Progress in Quantitative Nondestructive Evaluation*, vol. 7, pp. 935–942, 1988.

[51] P. B. Nagy and L. Adler, "Adhesive joint characterization by leaky guided interface waves," *Review of Progress in Quantitative Nondestructive Evaluation*, vol. 7, pp. 1417–1424, 1988.

[52] M. J. S. Lowe and P. Cawley, "The applicability of plate wave techniques for the inspection of adhesive and diffusion bonded joints," *Journal of Nondestructive Evaluation*, vol. 13, no. 4, pp. 185–200, 1994.

[53] S. I. Rokhlin, W. Wang, and Y. J. Wang, "Ultrasonic evaluation of interphasial properties in adhesive joints," *Review of Progress in Quantitative Nondestructive Evaluation*, vol. 9, pp. 1231–1238, 1990.

[54] A. K. Mal, P.-c. Xu, and Y. Bar-Cohen, "Leaky lamb waves for the ultrasonic nondestructive evaluation of adhesive bonds," *Journal of Engineering Materials and Technology*, vol. 112, no. 3, pp. 255–259, 1990.

[55] Y. Bar-Cohen, A. K. Mal, and S.-S. Lih, "NDE of composite materials using ultrasonic oblique insonification," *Materials Evaluation*, pp. 1285–1296, 1993.

[56] A. K. Mal, S.-S. Lih, and Y. Bar-Cohen, "Nondestructive characterization of adhesive bonds from guided wave data," in *17th Annual Adhesion Society Meeting*, (Orlando, Florida), February 1994.

[57] T. Kundu and K. Maslov, "Material interface inspection by lamb waves," *International Journal of Solids and Structures*, vol. 34, no. 29, pp. 3885–3901, 1997.

[58] P. Karpur, T. Kundu, and J. J. Ditri, "Adhesive joint evaluation using lamb wave modes with appropriate displacement, stress, and energy distribution profiles," *Review of Progress in Quantitative Nondestructive Evaluation*, vol. 18, pp. 1533–1542, 1999.

[59] Z. Fan, W. Jiang, M. Cai, and W. M. D. Wright, "The effects of air gap reflections during air-coupled leaky lamb wave inspection of thin plates," *Ultrasonics*, vol. 65, pp. 282–295, 2016.

[60] S. Mezil, F. Bruno, S. Raetz, J. Laurent, and D. Royer, "Investigation of interfacial stiffnesses of a tri-layer using zero-group velocity lamb modes," *Journal of the Acoustical Society of America*, vol. 138, no. 5, pp. 3202–3209, 2015.

[61] P. B. Nagy, "Ultrasonic detection of kissing bonds at adhesive interfaces," *Journal of Adhesion Science Technology*, vol. 5, no. 8, pp. 619–630, 1991.

[62] R. O. Claus and R. A. Kline, "Adhesive bondline interrogation using stoneley wave methods," *Journal of Applied Physics*, vol. 50, no. 12, pp. 8066–8069, 1979.

[63] S. I. Rokhlin, M. Hefets, and M. Rosen, "An elastic interface wave guided by a thin film between solids," *Journal of Applied Physics*, vol. 51, no. 7, pp. 3579–3582, 1980.

[64] S. I. Rokhlin, M. Hefets, and M. Rosen, "An ultrasonic interface-wave method for predicting the strength of adhesive bonds," *Journal of Applied Physics*, vol. 52, no. 4, pp. 2847–2851, 1981.

[65] H. Lourme, B. Hosten, and P. Brassier, "Sensitivity of the guided waves to the adhesion of lap joints: finite element modeling and experimental investigations," *Review of Quantitative Nondestructive Evaluation*, vol. 28, pp. 1134–1141, 2009.

[66] B. Ren and C. J. Lissenden, "Ultrasonic guided wave transmission through a geometry transition and NDE of composite-to-adhesive bond," *AIP Conference Proceedings*, vol. 1581, pp. 1165–1172, 2014.

[67] G. A. Alers and R. B. Thompson, "Application of trapped modes in layered media to the testing of adhesive bonds," *IEEE Ultrasonics Symposium Proceedings*, pp. 138–142, 1976.

[68] F. Lanza di Scalea, R. Piervincenzo, and A. Marzani, "Propagation of ultrasonic guided waves in lap-shear adhesive joints," *2004 SEM X International Congress & Exposition on Experimental & Applied Mechanics*, 2004.

[69] P. B. Nagy and L. Adler, "Interface characterization by true guided modes," *Review of Progress in Quantitative Nondestructive Evaluation*, vol. 10B, pp. 1295–1302, 1991.

[70] M. S. Harb and F. G. Yuan, "A rapid, fully non-contact, hybrid system for generating lamb wave dispersion curves," *Ultrasonics*, vol. 61, pp. 62–70, 2015.

[71] M. S. Harb and F. G. Yuan, "Non-contact ultrasonic technique for lamb wave characterization in composite plates," *Ultrasonics*, vol. 64, pp. 162–169, 2016.

[72] K. Heller, L. J. Jacobs, and J. Qu, "Characterization of adhesive bond properties using lamb waves," *NDT&E International*, vol. 33, no. 8, pp. 555–563, 2000.

[73] R. Seifried, L. J. Jacobs, and J. Qu, "Characterization of adhesive bond properties with lamb waves," *AIP Conference Proceedings*, vol. 557, pp. 1074–1081, 2001.

[74] P. D. Juarez and C. A. C. Leckey, "Multi-frequency local wavenumber analysis and ply correlation of delamination damage," *Ultrasonics*, vol. 62, pp. 56–65, 2015.

[75] M. Castaings and B. Le Crun, "Sh guided waves to infer the shear stiffness of adhesive bonds," *Review of Progress in Quantitative Nondestructive Evaluation*, vol. 30, pp. 1071–1078, 2011.

[76] J. G. Scholte, "The range of existence of rayleigh and stoneley waves," *Geophys. Suppl. MNRAS*, vol. 5, no. 5, pp. 120–126, 1947.

[77] W. L. Pilant, "Complex roots of the stoneley-wave equation," *Bulletin of the Seismological Society of America*, vol. 62, no. 1, pp. 285–299, 1972.

[78] F. I. Solyanik, "Transmission of plane waves through a layered medium of anisotropic materials," *Sov. Phys. Acoust*, vol. 23, pp. 533–536, 1977.

[79] W. Huang and S. I. Rokhlin, "Interface waves along an anisotropic imperfect interface between anisotropic solids," *Journal of Nondestructive Evaluation*, vol. 11, no. 3, pp. 185–198, 1992.

[80] S. I. Rokhlin and W. Huang, "Generalized boundary conditions for imperfect interface between two solid anisotropic media," *Review of Progress in Quantitative Nondestructive Evaluation*, vol. 11, pp. 169–176, 1992.

[81] H. Cho and S. I. Rokhlin, "Interface wave propagation and edge conversion at a low stiffness interphase layer between two solids: A numerical study," *Ultrasonics*, vol. 62, pp. 213–222, September 2015.

[82] S. Delrue and K. V. D. Abeele, "Detection of defect parameters using nonlinear air-coupled emission by ultrasonic guided waves at contact acoustic nonlinearities," *Ultrasonics*, vol. 63, pp. 147–154, 2015.

[83] J. Koreck, C. Valle, J. Qu, and L. J. Jacobs, "Computational characterization of adhesive bond properties using guided waves in bonded plates," *AIP Conference Proceedings*, vol. 894, pp. 1111–1118, 2007.

[84] E. T. Hauck, J. L. Rose, and C. A. Moose, "Bondline inspection of complex structures using guided waves," *Review of Quantitative Nondestructive Evaluation*, vol. 27, pp. 207–214, 2008.

[85] H. Kannajosyula, C. J. Lissenden, and J. L. Rose, "Inhomogeneous interface waves in a thin layer between half spaces and their relationship to lamb waves," *Review of Quantitative Nondestructive Evaluation*, vol. 29, pp. 104–110, 2010.

[86] P. Puthillath, J. M. Galan, B. Ren, C. J. Lissenden, and J. L. Rose, "Ultrasonic guided wave propagation across waveguide transitions: Energy transfer and mode conversion," *Journal of the Acoustical Society of America*, vol. 133, no. 5, pp. 2624–2633, 2013.

[87] P. Puthillath, B. Ren, C. J. Lissenden, and J. L. Rose, "Guided wave mode pairs for transmissibility in adhesively bonded metal plates," *Review of Progress in Quantitative Nondestructive Evaluation*, vol. 39, pp. 199–206, 2013.

[88] B. Poddar, *Physics based modeling of guided waves for detection and characterization of structural damage in NDE and SHM*. PhD thesis, University of South Carolina, 2016.

[89] *NDT of kissing bond in aeronautical structures*, August 2013.

[90] R. L. V. Kumar, M. R. Bhat, and C. R. L. Murthy, "Non-destructive evaluation of degradation in bond line of glass fiber reinforced polymer composite adhesive lap joints," *International Journal of Aerospace Innovations*, vol. 5, no. 3, pp. 61–72, 2013.

[91] C. J. Brotherhood, B. W. Drinkwater, and F. J. Guild, "A comparison of the detectability of dry contact kissing bonds in adhesive joints using longitudinal, shear and high power ultrasonic techniques," *Review of Quantitative Nondestructive Evaluation*, vol. 22, pp. 1033–1040, 2003.

[92] S. Ebnesajjad, "Introduction to adhesion theories," in *Adhesives Technology Handbook 2nd Edition*, Norwich, NY: William Andrew Inc.„ 2008.

[93] J. C. Seferis, M. S. Tillman, and B. S. Hayes, "Scaled analysis of composite interphase properties," *Journal of Macromolecular Science, Part B: Physics*, vol. 40, no. 5, pp. 923–934, 2001.

[94] J. F. Maguire, P. L. Talley, and M. Lupkowski, "The interphase in adhesion: Bridging the gap," *Journal of Adhesion*, vol. 45, pp. 269–290, 1994.

[95] J. J. Bikerman, *The Science of Adhesive Joints*. New York: Academic Press, 1961.

[96] J. Schiltz and M. Nardin, "Theories and mechanisms of adhesion," in *Handbook of Adhesive Technology 2nd Edition*, New York: Marcel Dekker Inc., 2003.

[97] J. D. Delong, K. J. Hook, and M. J. Rich, "Spectroscopic characterization of fiber-polymer interphases," *Controlled Interphases in Composite Materials: Part I*, pp. 87–95, 1990.

[98] S. I. Rokhlin and Y. J. Wang, "Analysis of ultrasonic wave interaction with imperfect interface between solids," *Review of Progress in Quantitative Nondestructive Evaluation*, vol. 10A, pp. 185–192, 1991.

[99] J. L. Rose, J. Dale, and T. D. Ngoc, "Evaluation of various interface layer models for ultrasonic inspection of weak bonds," *Review of Progress in Quantitative Nondestructive Evaluation*, vol. 9, pp. 1309–1316, 1990.

[100] J. Krautkramer and H. Krautkramer, *Ultrasonic Testing of Materials*. Berlin: Springer-Verlag, 4 ed., 1990.

[101] R. D. Adams, P. Cawley, C. J. Pye, and B. J. Stone, "A vibration technique for non-destructively assessing the integrity of structures," *Journal of Mechanical Engineering Science*, vol. 20, no. 2, pp. 93–100, 1978.

[102] P. Cawley and R. D. Adams, "The location of defects in structures from measurement of natural frequencies," *The Journal of Strain Analysis for Engineering Design*, vol. 14, no. 2, pp. 49–57, 1979.

[103] P. Cawley, "The impedance method for nondestructive inspection," *NDT International*, vol. 17, no. 2, pp. 59–65, 1984.

[104] V. Giurgiutiu, *Structural health monitoring with piezoelectric wafer active sensors*. Oxford, UK: Elsevier Inc., 2 ed., 2014.

[105] C. Liang, F. P. Sun, and C. A. Rogers, "Coupled electro-mechanical analysis of adaptive material system-determination of the actuator power consumption and system energy transfer," *Journal of Intelligent Material Systems and Structures*, no. 5, pp. 12–20, 1994.

[106] V. Giurgiutiu and A. N. Zagrai, "Characterization of piezoelectric wafer active sensors," *Journal of Intelligent Material Systems and Structures*, vol. 11, pp. 959–976, 2000.

[107] F. P. Sun, C. Liang, and C. A. Rogers, "Experimental modal testing using piezoceramic patches as collocated sensors-actuators," in *SEM Spring Conference & Exhibits*, (Baltimore, MD), 1994.

[108] S. Bhalla and C. K. Soh, "Structural impedance based damage diagnosis by piezo-transducer," *Earthquake engineering and structural dynamics*, pp. 1897–1916, 2003.

[109] W. Yan and W. Q. Chen, "Review article: structural health monitoring using high-frequency electromechanical impedance signatures," *Advances in Civil Engineering*, 2010.

[110] V. Giurgiutiu, K. Harries, M. Petrou, J. Bost, and J. B. Quattlebaum, "Disbond detection with peizoelectric wafer active sensors in rc structures strengthened with frp composite overlays," *Earthquake Engineering and Engineering Vibration*, vol. 2, no. 2, 2003.

[111] M. Gresil, L. Yu, V. Giurgiutiu, and M. Sutton, "Predictive modeling of electromechanical impedance spectroscopy for composite materials," *Structural Health Monitoring*, vol. 11, no. 6, pp. 671–683, 2012.

[112] W. Yan, J. B. Cai, and W. Q. Chen, "Monitoring interfacial defects in a composite beam using impedance signatures," *Journal of Sound and Vibration*, vol. 326, pp. 340–352, 2009.

[113] C. Bois and C. Hochard, "Monitoring of laminated composites delamination based on electro-mechanical impedance measurement," *Journal of Intelligent Material Systems and Structures*, pp. 59–67, 2004.

[114] A. A. Khalil and A. N. Kagho, "Non-destructive testing of adhesively bonded joints using vibrational analysis," *International Journal of Adhesion and Adhesives*, vol. 11, no. 2, pp. 121–127, 1991.

[115] W. T. Thomson and M. D. Dahleh, *Theory of vibration with applications*. Upper Saddle River, NJ: Prentice-Hall, 1998.

Appendix A: Material Symmetries

Monoclinic Symmetry

Single plane of symmetry on the x_1x_2 plane. Thirteen independent variables.

$$\mathbf{C} = \begin{bmatrix} C_{11} & C_{12} & C_{13} & 0 & 0 & C_{16} \\ C_{12} & C_{22} & C_{23} & 0 & 0 & C_{26} \\ C_{13} & C_{23} & C_{33} & 0 & 0 & C_{36} \\ 0 & 0 & 0 & C_{44} & C_{45} & 0 \\ 0 & 0 & 0 & C_{45} & C_{55} & 0 \\ C_{16} & C_{26} & C_{36} & 0 & 0 & C_{66} \end{bmatrix}$$

Orthotropic Symmetry

Three orthogonal planes of mirror symmetry on the x_1x_2, x_2x_3 and x_1x_3 planes. Nine independent variables.

$$\mathbf{C} = \begin{bmatrix} C_{11} & C_{12} & C_{13} & 0 & 0 & 0 \\ C_{12} & C_{22} & C_{23} & 0 & 0 & 0 \\ C_{13} & C_{23} & C_{33} & 0 & 0 & 0 \\ 0 & 0 & 0 & C_{44} & 0 & 0 \\ 0 & 0 & 0 & 0 & C_{55} & 0 \\ 0 & 0 & 0 & 0 & 0 & C_{66} \end{bmatrix}$$

Transversely Isotropic Symmetry

This class has an axis of symmetry (x_1) normal to a plane of isotropy (x_2x_3). Five independent variables.

$$\mathbf{C} = \begin{bmatrix} C_{11} & C_{12} & C_{12} & 0 & 0 & 0 \\ C_{12} & C_{22} & C_{23} & 0 & 0 & 0 \\ C_{12} & C_{23} & C_{22} & 0 & 0 & 0 \\ 0 & 0 & 0 & C^*_{44} & 0 & 0 \\ 0 & 0 & 0 & 0 & C_{55} & 0 \\ 0 & 0 & 0 & 0 & 0 & C_{55} \end{bmatrix}$$

Where,

$$C_{44} = \frac{C_{22} - C_{23}}{2}$$

Cubic Symmetry

Three orthogonal planes of mirror symmetry and three orthogonal four-fold symmetry axes. Many single-crystal metals have cubic symmetry; such as aluminum, steel, copper, nickel and diamond. Possible some fiber-placed composites. Three independent variables.

$$\mathbf{C} = \begin{bmatrix} C_{11} & C_{12} & C_{12} & 0 & 0 & 0 \\ C_{12} & C_{11} & C_{12} & 0 & 0 & 0 \\ C_{12} & C_{12} & C_{11} & 0 & 0 & 0 \\ 0 & 0 & 0 & C_{44} & 0 & 0 \\ 0 & 0 & 0 & 0 & C_{44} & 0 \\ 0 & 0 & 0 & 0 & 0 & C_{44} \end{bmatrix}$$

Isotropic Material

Same properties in every direction. Two independent variables.

$$\mathbf{C} = \begin{bmatrix} \lambda + 2\mu & \lambda & \lambda & 0 & 0 & 0 \\ \lambda & \lambda + 2\mu & \lambda & 0 & 0 & 0 \\ \lambda & \lambda & \lambda + 2\mu & 0 & 0 & 0 \\ 0 & 0 & 0 & \mu & 0 & 0 \\ 0 & 0 & 0 & 0 & \mu & 0 \\ 0 & 0 & 0 & 0 & 0 & \mu \end{bmatrix}$$

Where,

$$G = \mu = \frac{E}{2(1+\nu)}$$

$$\nu = \frac{\lambda}{2\lambda + 2\mu}$$

$$E = \frac{\mu(3\lambda + 2\mu)}{\lambda + \mu}$$

$$\lambda = \frac{E\nu}{(1+\nu)(1-2\nu)}$$

$$K = \frac{E}{3(1-2\nu)}$$

Appendix B: Bulk Wave Speeds

Table B.1: Monoclininc Symmetry

Wave Normal	Particle Direction	Type of Wave	Equation Relating Elastic Moduli and Phase Velocity
$\begin{Bmatrix}1\\0\\0\end{Bmatrix}$	x_3	T	$\rho V_p^2 = C_{55}$
	x_1x_2	QT	$\rho V_P^2 = \frac{C_{11}+C_{66}}{2} - \frac{\sqrt{C_{11}^2-2C_{11}C_{66}+4C_{16}^2+C_{66}^2}}{2}$
	x_1x_2	QL	$\rho V_P^2 = \frac{C_{11}+C_{66}}{2} + \frac{\sqrt{C_{11}^2-2C_{11}C_{66}+4C_{16}^2+C_{66}^2}}{2}$
$\begin{Bmatrix}0\\1\\0\end{Bmatrix}$	x_3	T	$\rho V_p^2 = C_{44}$
	x_1x_2	QT	$\rho V_P^2 = \frac{C_{22}+C_{66}}{2} - \frac{\sqrt{C_{22}^2-2C_{22}C_{66}+4C_{26}^2+C_{66}^2}}{2}$
	x_1x_2	QL	$\rho V_P^2 = \frac{C_{22}+C_{66}}{2} + \frac{\sqrt{C_{22}^2-2C_{22}C_{66}+4C_{26}^2+C_{66}^2}}{2}$
$\begin{Bmatrix}0\\0\\1\end{Bmatrix}$	x_3	L	$\rho V_p^2 = C_{33}$
	x_1x_2	QT	$\rho V_P^2 = \frac{C_{44}+C_{55}}{2} - \frac{\sqrt{C_{44}^2-2C_{44}C_{55}+4C_{45}^2+C_{55}^2}}{2}$
	x_1x_2	QT	$\rho V_P^2 = \frac{C_{44}+C_{55}}{2} + \frac{\sqrt{C_{44}^2-2C_{44}C_{55}+4C_{45}^2+C_{55}^2}}{2}$
$\begin{Bmatrix}\frac{1}{\sqrt{2}}\\\frac{1}{\sqrt{2}}\\0\end{Bmatrix}$	x_3	T	$\rho V_p^2 = C_{45} + \frac{C_{44}+C_{55}}{2}$
	x_1x_2	QT	Too long to include here
	x_1x_2	QL	Too long to include here

Table B.2: Orthotropic Symmetry

Wave Normal	Particle Direction	Type of Wave	Equation Relating Elastic Moduli and Phase Velocity
$\begin{Bmatrix}1\\0\\0\end{Bmatrix}$	x_1	L	$\rho V_p^2 = C_{11}$
	x_2	T	$\rho V_P^2 = C_{66}$
	x_3	T	$\rho V_P^2 = C_{55}$
$\begin{Bmatrix}0\\1\\0\end{Bmatrix}$	x_2	L	$\rho V_p^2 = C_{22}$
	x_1	T	$\rho V_P^2 = C_{66}$
	x_3	T	$\rho V_P^2 = C_{44}$
$\begin{Bmatrix}0\\0\\1\end{Bmatrix}$	x_3	L	$\rho V_p^2 = C_{33}$
	x_1	T	$\rho V_P^2 = C_{55}$
	x_2	T	$\rho V_P^2 = C_{44}$
$\begin{Bmatrix}\frac{1}{\sqrt{2}}\\\frac{1}{\sqrt{2}}\\0\end{Bmatrix}$	x_3	T	$\rho V_p^2 = \frac{C_{44}+C_{55}}{2}$
	x_1x_2	QT	$\rho V_p^2 = \frac{C_{11}+C_{22}+C_{66}}{2}$ $\mp\frac{\sqrt{C_{11}^2-2C_{11}C_{22}+4C_{12}^2+8C_{12}C_{66}+C_{22}^2+4C_{66}^2}}{4}$
	x_1x_2	QL	
$\begin{Bmatrix}0\\\frac{1}{\sqrt{2}}\\\frac{1}{\sqrt{2}}\end{Bmatrix}$	x_1	T	$\rho V_p^2 = \frac{C_{66}+C_{55}}{2}$
	x_2x_3	QT	$\rho V_p^2 = \frac{C_{22}+C_{33}+C_{44}}{2}$ $\mp\frac{\sqrt{C_{22}^2-2C_{22}C_{33}+4C_{23}^2+8C_{23}C_{44}+C_{33}^2+4C_{44}^2}}{4}$
	x_2x_3	QL	
$\begin{Bmatrix}\frac{1}{\sqrt{2}}\\0\\\frac{1}{\sqrt{2}}\end{Bmatrix}$	x_2	T	$\rho V_p^2 = \frac{C_{66}+C_{44}}{2}$
	x_1x_3	QT	$\rho V_p^2 = \frac{C_{11}+C_{33}+C_{55}}{2}$ $\mp\frac{\sqrt{C_{11}^2-2C_{11}C_{33}+4C_{13}^2+8C_{13}C_{55}+C_{33}^2+4C_{55}^2}}{4}$
	x_1x_3	QL	

Table B.3: Transversely Isotropic Symmetry

Wave Normal	Particle Direction	Type of Wave	Equation Relating Elastic Moduli and Phase Velocity
$\begin{Bmatrix}1\\0\\0\end{Bmatrix}$	x_1	L	$\rho V_p^2 = C_{11}$
	x_2	T	$\rho V_P^2 = C_{55}$
	x_3	T	$\rho V_P^2 = C_{55}$
$\begin{Bmatrix}0\\1\\0\end{Bmatrix}$	x_2	L	$\rho V_p^2 = C_{22}$
	x_1	T	$\rho V_P^2 = C_{55}$
	x_3	T	$\rho V_P^2 = C_{44}$
$\begin{Bmatrix}0\\0\\1\end{Bmatrix}$	x_3	L	$\rho V_p^2 = C_{22}$
	x_1	T	$\rho V_P^2 = C_{55}$
	x_2	T	$\rho V_P^2 = C_{44}$
$\begin{Bmatrix}\frac{1}{\sqrt{2}}\\\frac{1}{\sqrt{2}}\\0\end{Bmatrix}$	x_3	T	$\rho V_p^2 = \frac{C_{44}+C_{55}}{2}$
	x_1x_2	QT	$\rho V_p^2 = \frac{C_{11}+C_{22}+C_{55}}{2}$ $\mp\frac{\sqrt{C_{11}^2-2C_{11}C_{22}+4C_{12}^2+8C_{12}C_{55}+C_{22}^2+4C_{55}^2}}{4}$
	x_1x_2	QL	
$\begin{Bmatrix}0\\\frac{1}{\sqrt{2}}\\\frac{1}{\sqrt{2}}\end{Bmatrix}$	x_1	T	$\rho V_p^2 = C_{55}$
	x_2x_3	QT	$\rho V_p^2 = C_{22} + \frac{C_{44}}{2} - \frac{\sqrt{4C_{13}^2+8C_{13}C_{44}+4C_{44}^2}}{4}$
	x_2x_3	QL	$\rho V_p^2 = C_{22} + \frac{C_{44}}{2} + \frac{\sqrt{4C_{13}^2+8C_{13}C_{44}+4C_{44}^2}}{4}$
$\begin{Bmatrix}\frac{1}{\sqrt{2}}\\0\\\frac{1}{\sqrt{2}}\end{Bmatrix}$	x_2	T	$\rho V_p^2 = \frac{C_{55}+C_{44}}{2}$
	x_1x_3	QT	$\rho V_p^2 = \frac{C_{11}+C_{22}+C_{55}}{2}$ $\mp\frac{\sqrt{C_{11}^2-2C_{11}C_{22}+4C_{13}^2+8C_{13}C_{55}+C_{22}^2+4C_{55}^2}}{4}$
	x_1x_3	QL	

Table B.4: Cubic

Wave Normal	Particle Direction	Type of Wave	Equation Relating Elastic Moduli and Phase Velocity
$\begin{Bmatrix} 1 \\ 0 \\ 0 \end{Bmatrix}$	x_1	L	$\rho V_p^2 = C_{11}$
	x_2	T	$\rho V_P^2 = C_{44}$
	x_3	T	$\rho V_P^2 = C_{44}$
$\begin{Bmatrix} 0 \\ 1 \\ 0 \end{Bmatrix}$	x_2	L	$\rho V_p^2 = C_{11}$
	x_1	T	$\rho V_P^2 = C_{44}$
	x_3	T	$\rho V_P^2 = C_{44}$
$\begin{Bmatrix} 0 \\ 0 \\ 1 \end{Bmatrix}$	x_3	L	$\rho V_p^2 = C_{11}$
	x_1	T	$\rho V_P^2 = C_{44}$
	x_2	T	$\rho V_P^2 = C_{44}$
$\begin{Bmatrix} \frac{1}{\sqrt{2}} \\ \frac{1}{\sqrt{2}} \\ 0 \end{Bmatrix}$	x_3	T	$\rho V_p^2 = C_{44}$
	x_1x_2	T	$\rho V_p^2 = \frac{C_{11}-C_{12}}{2}$
	x_1x_2	L	$\rho V_p^2 = \frac{C_{11}+C_{12}}{2} + C_{44}$
$\begin{Bmatrix} 0 \\ \frac{1}{\sqrt{2}} \\ \frac{1}{\sqrt{2}} \end{Bmatrix}$	x_1	T	$\rho V_p^2 = C_{44}$
	x_2x_3	T	$\rho V_p^2 = \frac{C_{11}-C_{12}}{2}$
	x_2x_3	L	$\rho V_p^2 = \frac{C_{11}+C_{12}}{2} + C_{44}$
$\begin{Bmatrix} \frac{1}{\sqrt{2}} \\ 0 \\ \frac{1}{\sqrt{2}} \end{Bmatrix}$	x_2	T	$\rho V_p^2 = C_{44}$
	x_1x_3	T	$\rho V_p^2 = \frac{C_{11}-C_{12}}{2}$
	x_1x_3	L	$\rho V_p^2 = \frac{C_{11}+C_{12}}{2} + C_{44}$

Appendix C: Normal Incidence Ultrasonic Inspection

List of Equipment

- Water tank gantry
- Ultrasonic immersion transducer
- Glass plate reflector
- Spacers for specimen placement
- JSR DPR300 Pulser/Reciever
- Lenovo S20 ThinkStation

Starting Settings

The settings files for normal UT inspection have been saved to the Lenovo S20 ThinkStation in the following folder.

`C:Users/LAMSS/Documents/William/normalinspectionsettings`

The MATLAB files can be found within the Roth share drive under the following folder.

`Dissertation/Files/AppendixC-Normalincidenceultrasonicinspection`

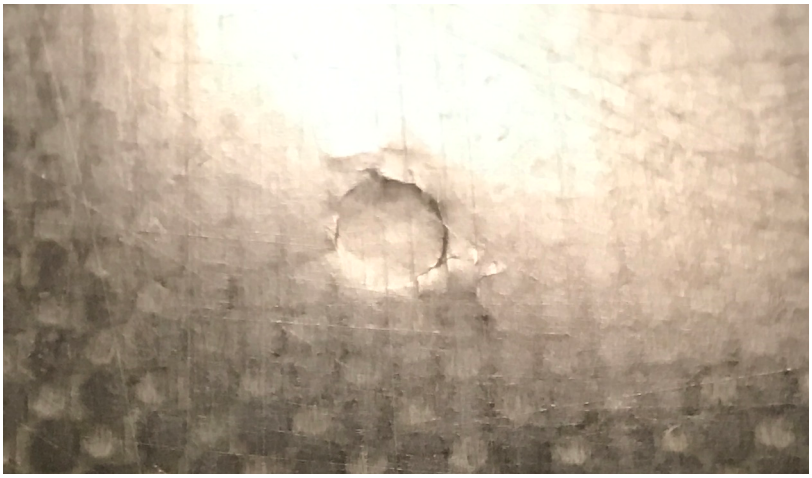

Figure C.1: Impact damage on the interior surface

Case Study: Inspection of a CFRP window cutout

Inspection Part

The inspected part was a window cutout from a carbon fiber reinforced polymer fuselage section. The thickness was approximately 6 mm (no measurement), and the part had a radius of curvature of approximately 2-3 m. From visual inspection, there were two damaged regions. The first was the entry path for the tool used to cut out the window on the exterior surface, and the second appears to be impact damage on the interior surface, see Figure C.1.

Inspection Technique

The part was inspected with a 4-axis ultrasonic immersion gantry. The part was immersed in water and placed on top of a Plexiglas plate. The plate is used to reflect the transmitted signal. The inspection was performed with a 2.25 MHz, 0.50 in. diameter unfocused centrascan composite immersion transducer, see Figure C.2. The low frequency was chosen to minimize the signal attenuation through the composite part and maximize the transmission in order to utilize the double transmission technique. Due to the curvature of the part, only the central region, where the angle is

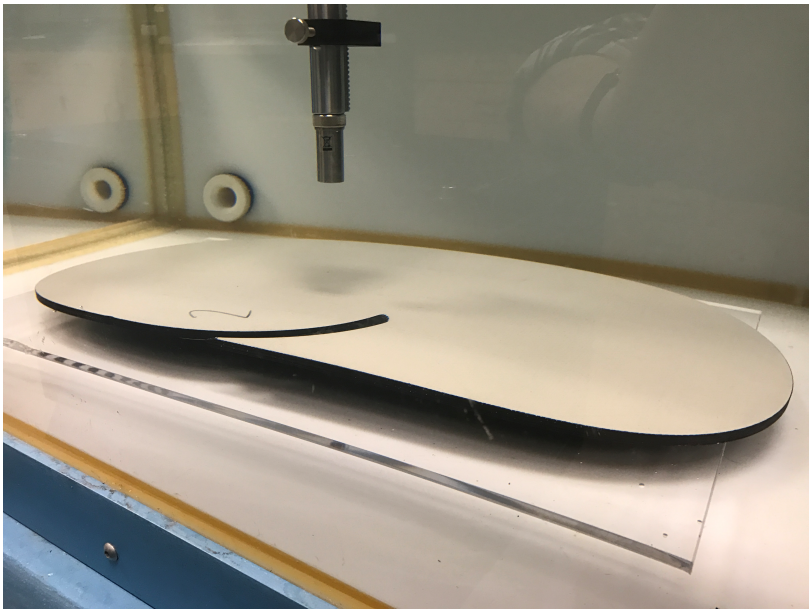

Figure C.2: Ultrasonic immersion inspection of the part

minimized, was scanned, where the scan area was 2 in. by 6 in.

Four gates were used in the inspection. The first gate detected the reflection from the top surface of the part, all remaining gates were based on the location of this gate. The second gate was set to detect the reflection from the back surface of the part. The third gate picked up the double transmission of the signal; the wave was transmitted through the part, reflected off the glass plate and transmitted back to the transducer. The final gate was set-up to detect reflections within the part. Damaged regions will be detected as a decrease in the amplitude of the signal at the backwall and transmission. Additionally the damage should be observed as the triggering of the interior gate due to a strong reflection within the part.

Results

Front Surface

The time-of-flight (TOF) of the singal reflection from the front gate is shown in Figure C.3. The curvature of the part is clear from the change in the TOF, as well

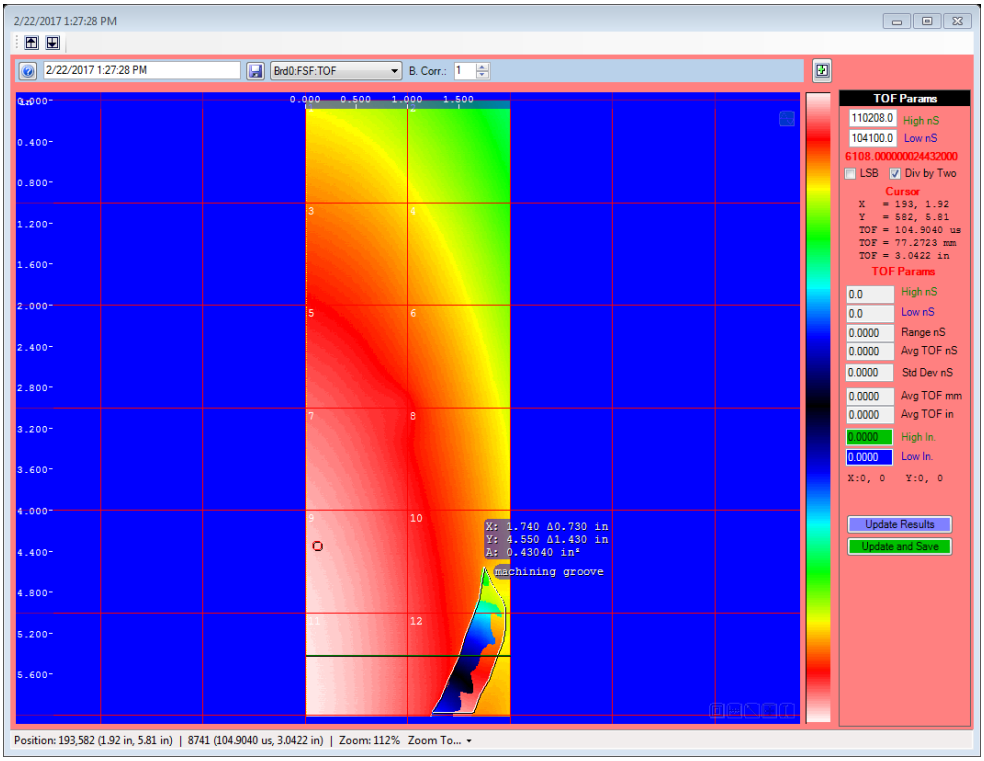

Figure C.3: C-Scan - Time-Of-Flight (TOF) - Front Surface Gate

as the machining groove.

Back Surface

The back surface gate is used to detect the presence of damage. Figure C.4 shows the absolute peak amplitude (APA) of the signal within the backwall gate. This method clearly picks up the impact damage, as well as the machining groove. It should be noted that the amplitude changes that extend beyond the dimensions of the groove are due to the diameter of the transducer beam. In these regions, part of the wave is within the undamaged plate and part is within the groove.

The large change in amplitude is best demonstrated in Figure C.5, which shows the A-Scans at two locations, the locations are marked in Figure C.4.

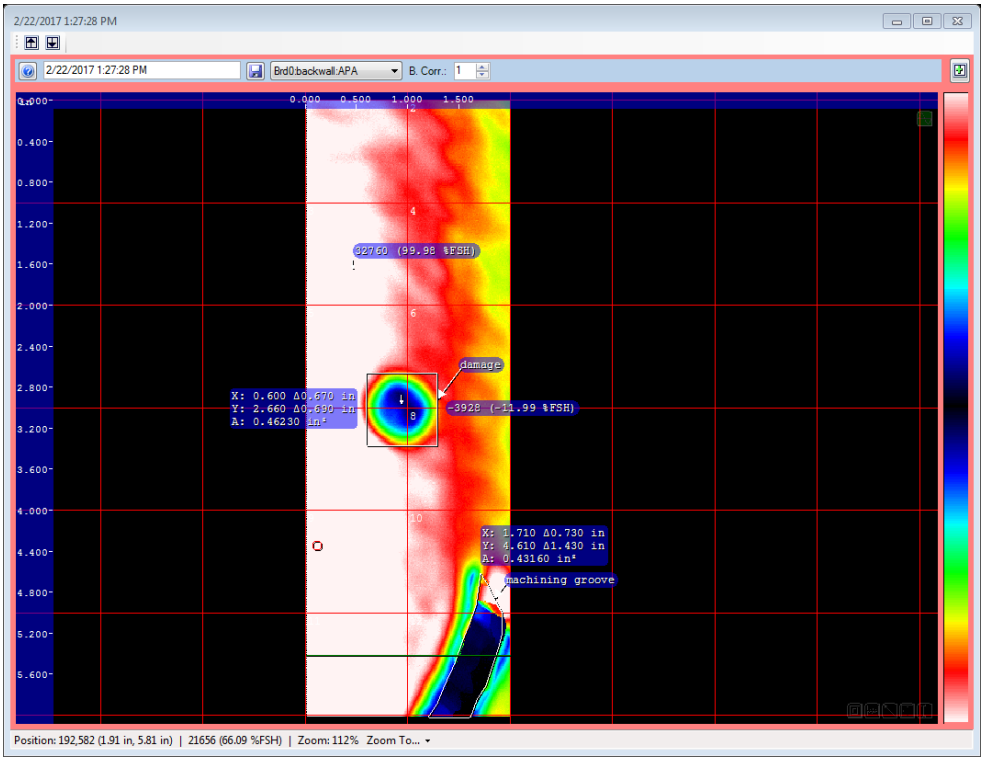

Figure C.4: C-Scan - Absolute Peak Amplitude (APA) - Backwall Gate

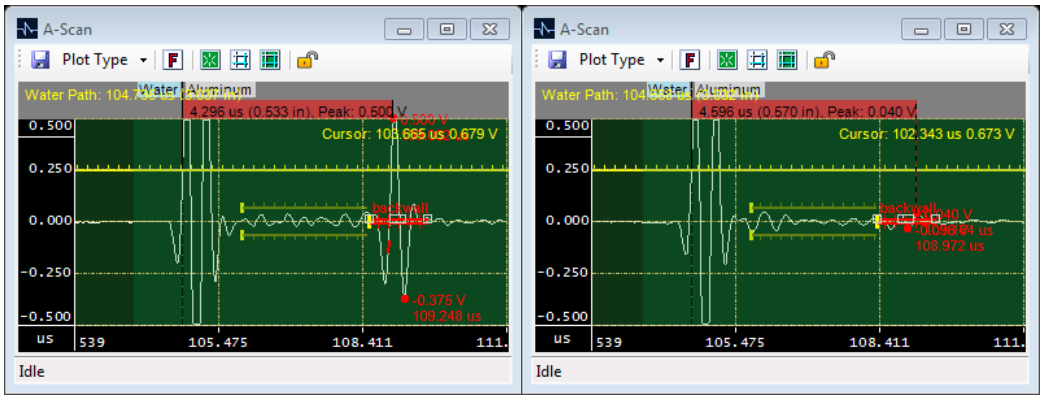

(a) undamaged (b) damaged

Figure C.5: A-Scan - Demonstration of the change in the backwall signal amplitude for (a) undamaged and (b) damaged regions

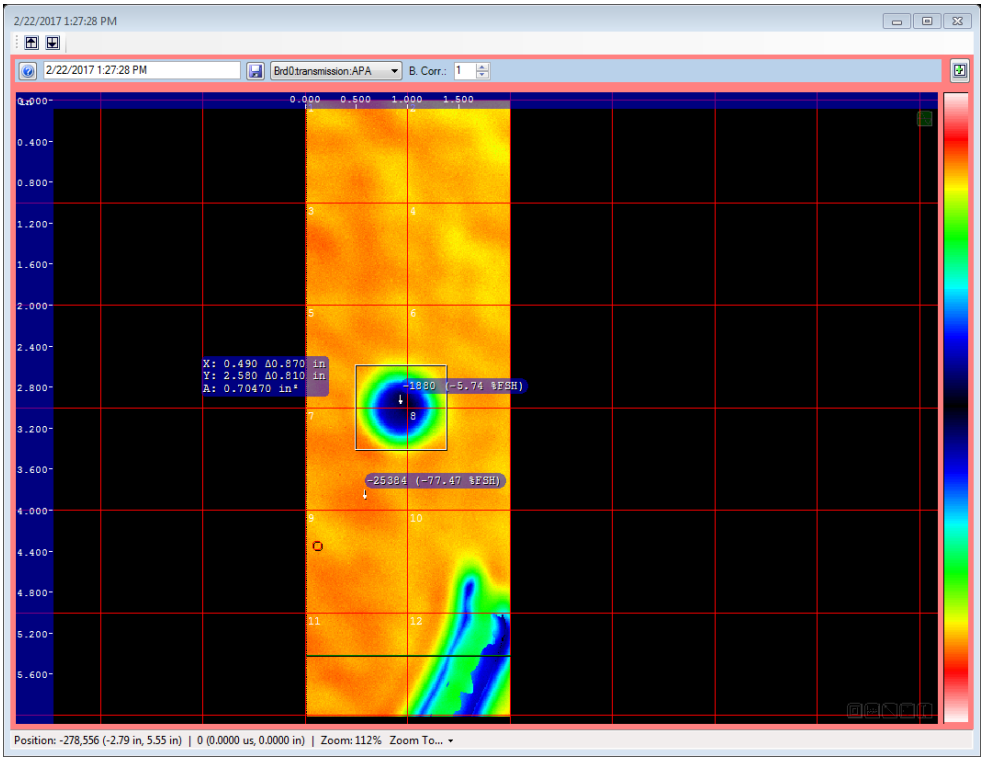

Figure C.6: C-Scan - Absolute Peak Amplitude (APA) - Transmission Gate

Double Transmission

The through transmission of the wave is a good method to detect a variety of potential defects. Any strong attenuators or reflectors will greatly diminish the amplitude of the transmitted wave. The resulting C-Scan is shown in Figure C.6, with clear indication of the impact damage.

The change in strength of the transmitted wave is demonstrated in Figure C.7. The wave amplitude has completely diminished over the impact region.

Interior Gate

The interior gate is used to detect delaminations and inclusions within the composite part. The C-Scan of the APA from the interior gate is shown in Figure C.8. A series of flower pedal like delaminations are observed surrounding the impact location. Additionally, several regions within the scan triggered the delamination gate. A com-

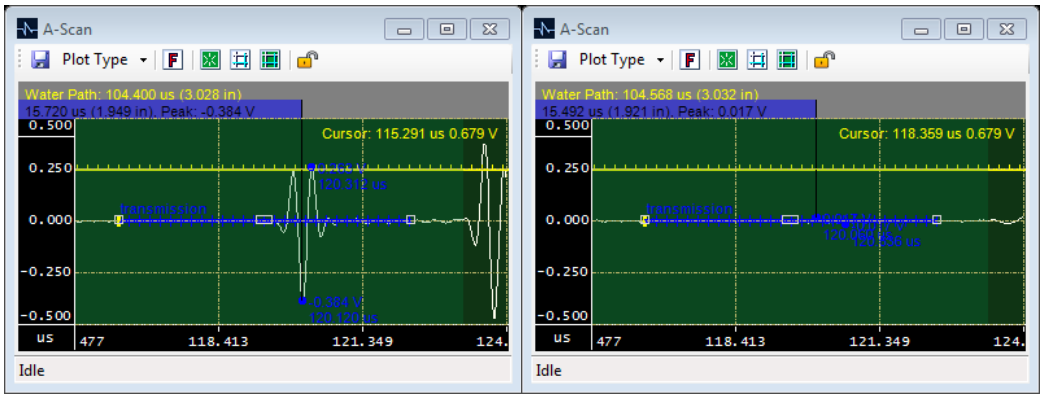

(a) undamaged (b) damaged

Figure C.7: A-Scan - Demonstration of the change in the double transmission signal amplitude for (a) undamaged and (b) damaged regions

parison of the A-Scan for the impact delaminations, one of the unexpected potential damaged regions and an undamaged region is shown in Figure C.10. Additionally, a C-Scan for the TOF is shown in Figure C.9. This figure shows that the delaminations surrounding tee impact damage are stacked at several different depths, and it shows the depth of the potential damage regions.

Conclusions

The inspection has revealed clear damage to the impact area. The impact dent is surrounded by a series of stacked delaminations in a flower pedal arrangement. The area of the delamination region is shown in several of the C-Scan images. Additionally, the inspection revealed potential flaws within the inspected region. Additional inspections are required to provide details on these regions. The inspection region was limited for this simple scan. A contact method or custom scan path will be necessary to provide a complete C-scan of the part.

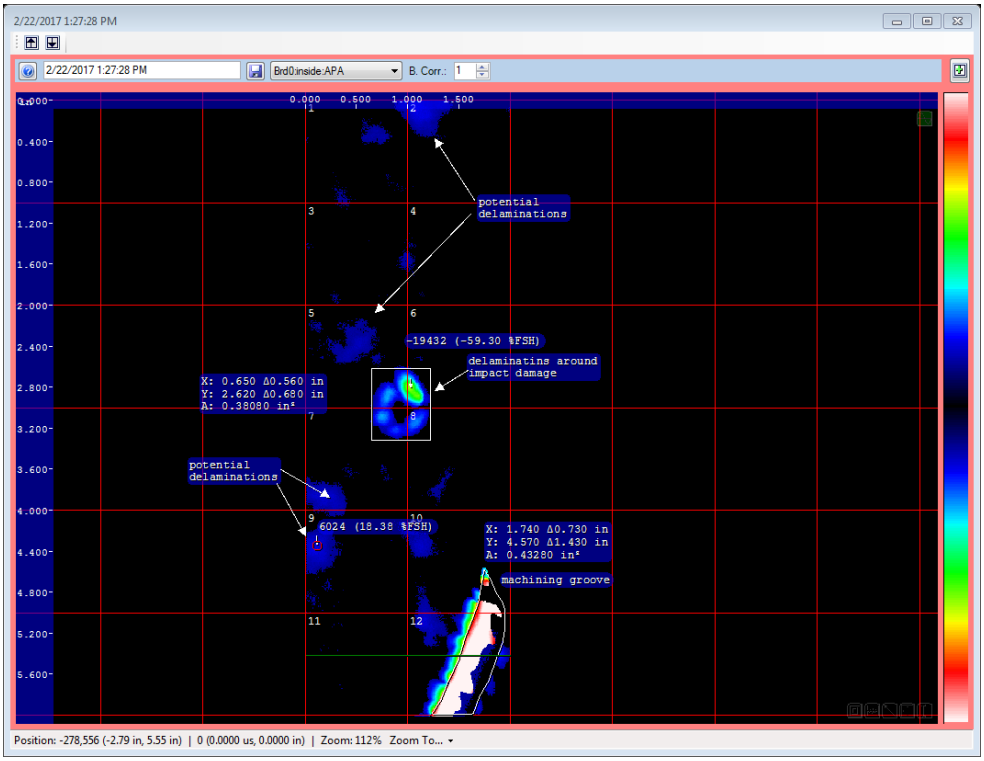

Figure C.8: C-Scan - Absolute Peak Amplitude (APA) - Inside Gate

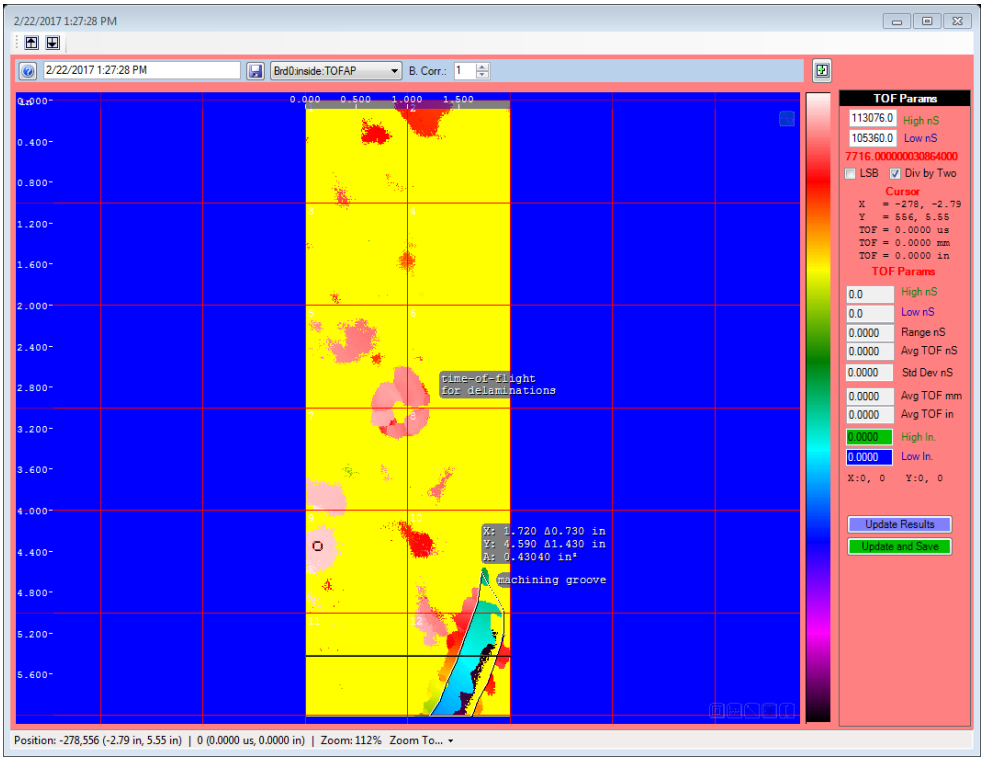

Figure C.9: C-Scan - Time-Of-Flight (TOF) - Inside Gate

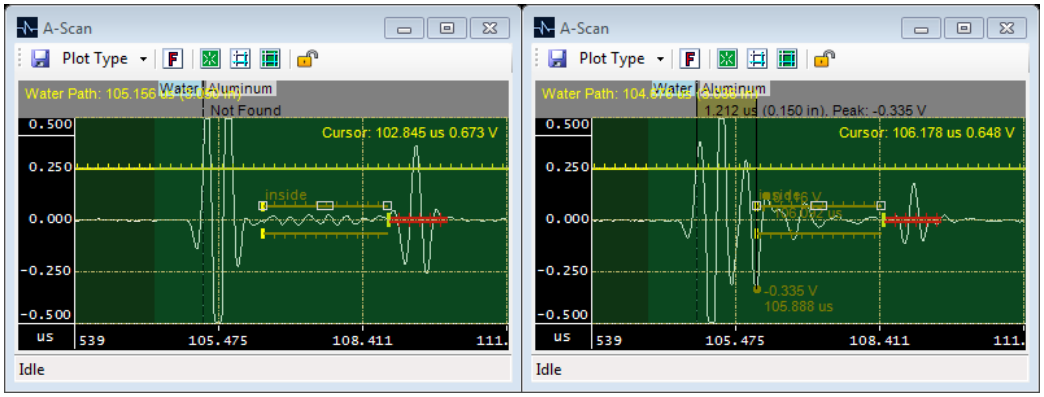

(a) undamaged

(b) large reflection from a near surface delamination

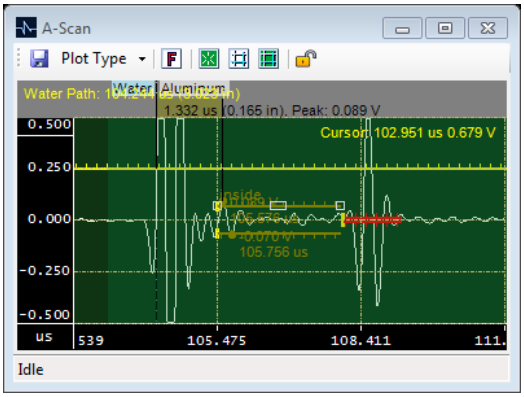

(c) small reflection from a near surface defect

Figure C.10: A-Scan - Demonstration of the signal amplitude between the front and back surfaces for (a) undamaged, (b) delaminated and (c) potential delamination

Appendix D: Contact Phased Array Method

List of Equipment

- AOS OEMPA 64/64
- Olympus phased array transducer 5L64 A12
- Olympus fixed angle wedge SA12-N55S
- Variable angle wedge Panametrics ABWX-2001
- Olympus conventional transducer C403
- VGA 3+9 adapter
- JSR DPR300 Pulser/Reciever
- Computer with MATLAb and AOS software
- Ultrasonic couplant

Starting Settings

All settings files, AOS information and MATLAB files can be found within the Roth share drive under the following folder.
`Dissertation/Files/AppendixD-Contactphasedarraymethod`

Case Study: Dispersion curve for a single aluminum plate

Specimen description

The specimen was a 12 in. by 12 in. plate of aluminum 2024 with a thickness of 1.6 mm.

Data collection and data processing

First, all equipment and instruments must be properly connected. The computer is connected to the AOS box through an Ethernet cable. The AOS box is connected to the PA transducer through the large connection on the front of the box. The variable angle transducer is connected to the pulser/receiver through a coaxial cable. The VGA adapter is used to output the trigger signal to the pulser/receiver. Also, ultrasonic couplant must be placed at all interfaces from each transducer along the wave path into the inspected plate. For the PA set this includes the interface between transducer and wedge. For the variable angle transducer this includes the interfaces between the transducer and sliding plate, sliding plate and wedge, and wedge and inspecting plate.

Once all equipment is on and the communication between the AOS box and computer is set up, the MATLAB program can be run in order to determine the dispersion curve. The MATLAB code will upload the correct focal law to the AOS box, gather the data and convert the data into the dispersion curve. Once the program is running, the only job of the operator is to ensure that the wedges remain in contact and aligned on the part (Figure D.1) and to smoothly adjust the variable wedge angle. The program will collect many data sets, and it is the job of the operator to adjust the variable wedge angle to ensure a range of phase velocities are generated. The program will display two plots in real time (Figure D.2). The left plot is the incident angle versus time; this shows the bulk wave within the phased array wedge. The right

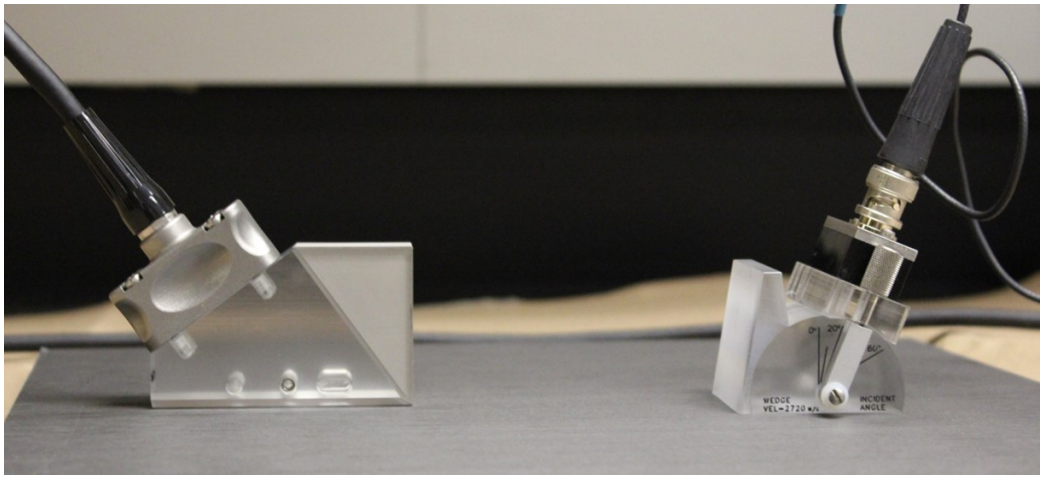

Figure D.1: Orientation of the transducers; the transmitter is the variable angle wedge on the right side of the figure and the reciever is the phased array probe and wedge on the left side of the figure.

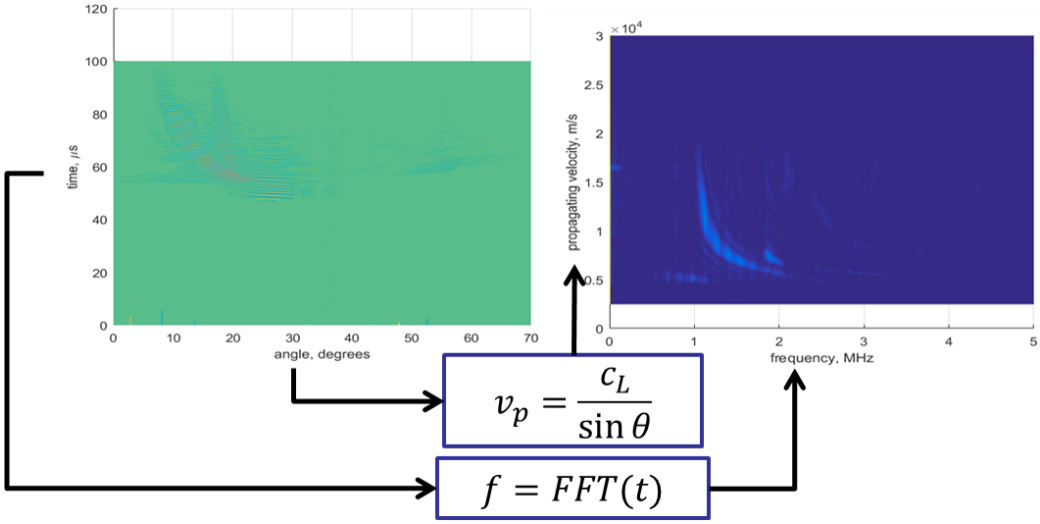

Figure D.2: Converting the time domain signal into frequency - phase velocity

plot is the dispersion data; Figure D.2 shows how the focal law data is converted into the dispersion data. Watch these two plots and adjust the wedge angle to ensure that the full range of phase velocities, or incident angles, is covered.

As mentioned previously, Figure D.2 demonstrates how the time domain data is converted into a dispersion curve. The time domain is transformed into frequency domain through a fast Fourier transform, and the incident angle is converted into guided wave phase velocity through Snell's law. These actions are performed within

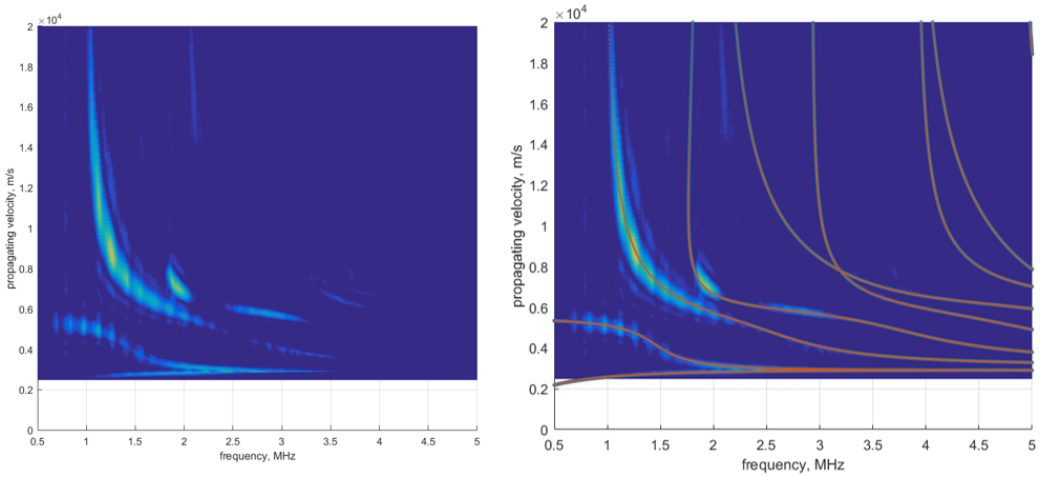

Figure D.3: Dispersion results for a 1.6 mm thick 2024 plate

the MATLAB code. After the program finishes running, all of the data sets are combined into a single dispersion curve (Figure D.3). The left side of the figure shows the combined results, and the right side of the figure shows an overlay of the computed dispersion curve for comparison. Obviously there is a good match, and this shows that both the analytical and experimental methods match well.

Appendix E: Immersion Leaky Guided Wave Method

List of Equipment

- Water tank gantry
- 2 ultrasonic transducers (one for transmission and one for reception)
- Immersion fixture
- Cross bar
- search bar
- search tube
- sled
- JSR DPR300 Pulser/Reciever
- Lenovo S20 ThinkStation

Starting Settings

The settings files have been saved to the Lenovo S20 ThinkStation in teh following folder.

`C:/Users/LAMSS/Documents/William/dispersion`

The MATLAB files can be found within the Roth share drive under the following folder.

`Dissertation/Files/AppendixE-Immersionleakyguidedwavemethod`

Case Study: Dispersion curve for a bonded aluminum plate

Specimen description

See Section 7.4.1.

Data collection procedure

The experimental procedure requires measuring the transmitted wave over a range of incident angles, see Figure E.1. The receiving transducer is translated in order to detect the wave pulse as the angle changes. The angle ϕ is varied between 0 and 90

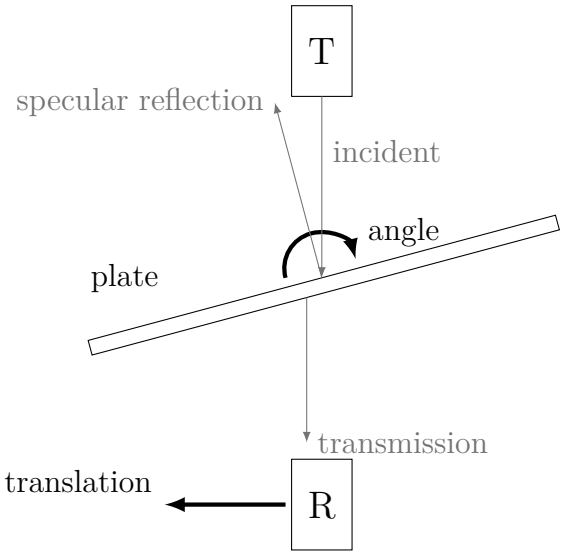

Figure E.1: Through transmission technique

degrees through the use of a specialty built fixture. Figure E.2 shows an experimental fixture immersed in the water tank. The coupon is within the fixture, which is bolted to the turntable. The transmitter and receiver are shown on opposite sides of the fixture. The rotation of ϕ and θ_i is controlled by the fixture and turntable, which is illustrated in Figure E.3. The translation of the receiving transducer is controlled by the y-axis motor of the immersion scanner, see Figure E.4. The receiver distance from the coupon is controlled by the x-axis motor; while the transmitter distance is controlled by the position of the crossbar, which travels on the x-axis rails. The

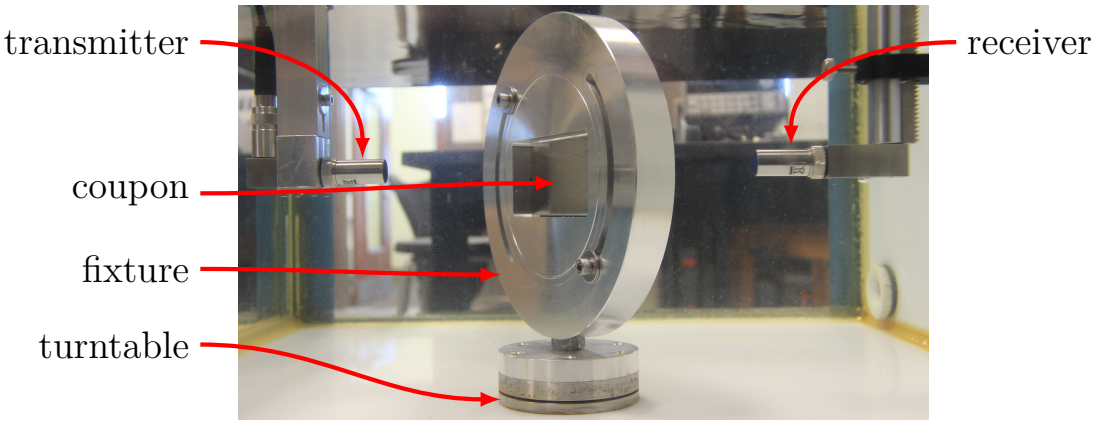

Figure E.2: Experimental setup

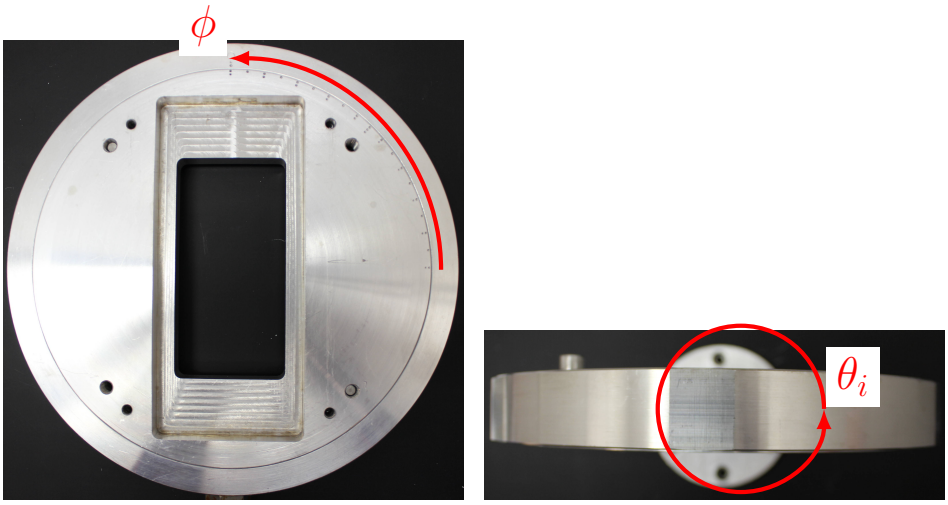

(a) Rotating ϕ from 0 to 90 degrees (b) Rotating θ_i from 0 to 360 degrees

Figure E.3: The fixture is used to vary the angles for (a) ϕ and (b) θ_i

position of the transmitter along the z-axis is set, but the z-axis position of the receiver is controlled by varying the height of the search tube.

Once the coupon, fixture and all supporting equipment have been loaded into the water tank, the following steps must be taken to ensure the collection of relevant and correct data.

Find θ_0

The first step is to orient the turntable so that the incident angle, herein referred to as θ, is at zero degrees. This is accomplished by using a pulse echo technique. The

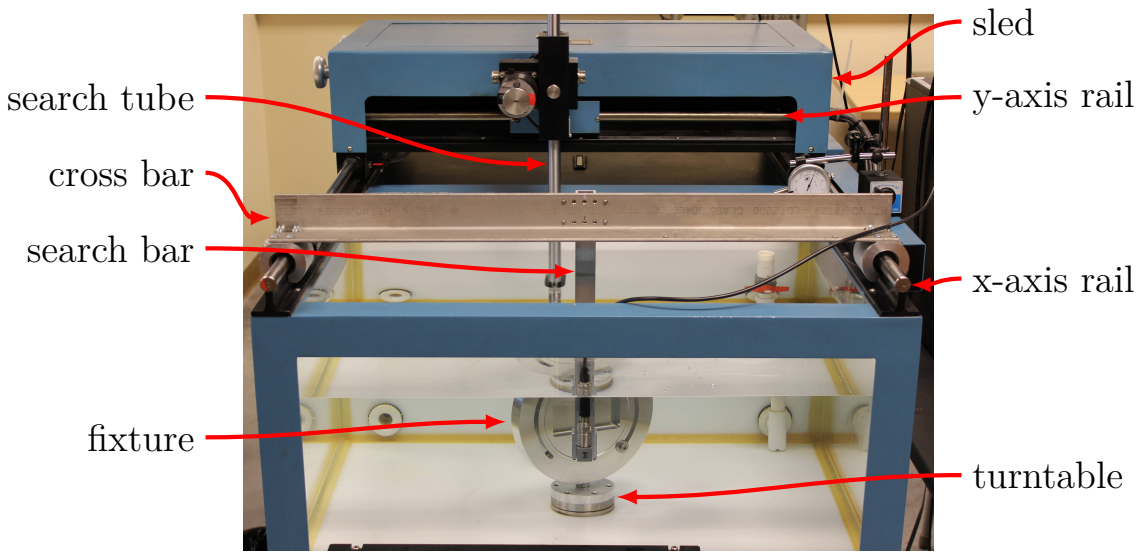

Figure E.4: Immersion tank with 4 DOF

transmitter transducer both emits and receives the acoustic wave pulse. A gate is set up around the first incoming pulse so that the absolute peak amplitude (APA) of the pulse is measured. A scan is preformed where the angle of the turntable is varied through several degrees from the estimated θ_0. The angle at which the peak amplitude occurs is the θ_0.

Find y_0 and z_0

Next, the origin of the receiver position is determined. This is accomplished with a two dimensional through transmission scan. Again, a gate is set up to find the APA of the first wave pulse. The receiver is scanned in the y and z directions. The resulting C-scan is shown in Figure E.5. The datum is located at the center of the circle.

Collect data

The data for each ϕ angle is collected as a two dimensional scan. A new gate is set up to collect all of the time data within the gate boundaries. This is called a waveform gate. This gate is set to the absolute scale, instead of using a follower gate. This is

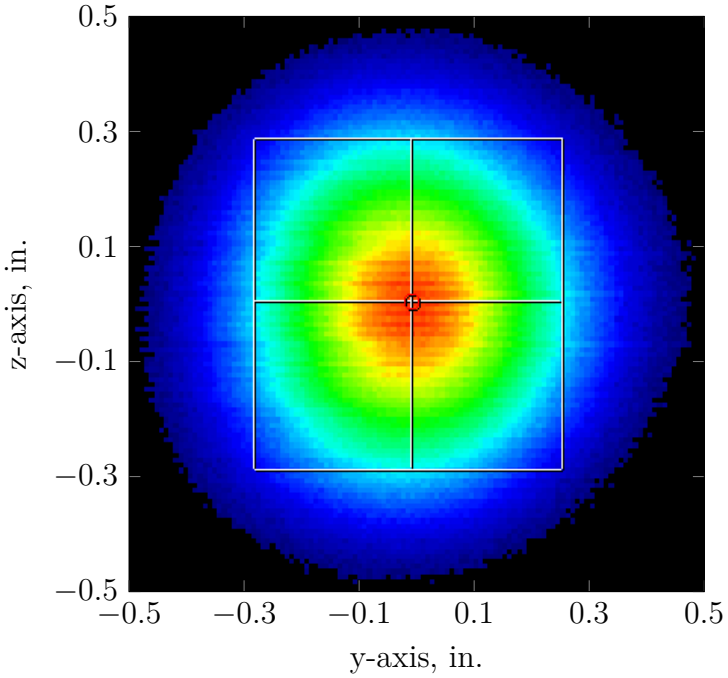

Figure E.5: APA of the through transmission

required because the absolute time is needed for the correct calculation of the phase velocity. The scan is performed with the turntable and y-axis. A total distance of 2-2.4 inches is selected for the y-axis. The turntable is swept through a total range of 120-140 degrees. The resulting data is extracted for post-processing.

Data Processing

The data processing is necessary to convert the raw waveforms into a dispersion plot. The first step is to further refine the datum location.

Find Datum

The accuracy of the datum location, when using the machine setup, is limited to the step size of the rotary encoder, and it is vulnerable to operator interpretation. The first step in data processing is to refine this measurement through calculations. Figure E.6 is a visual guide to the required process. The process begins with a two

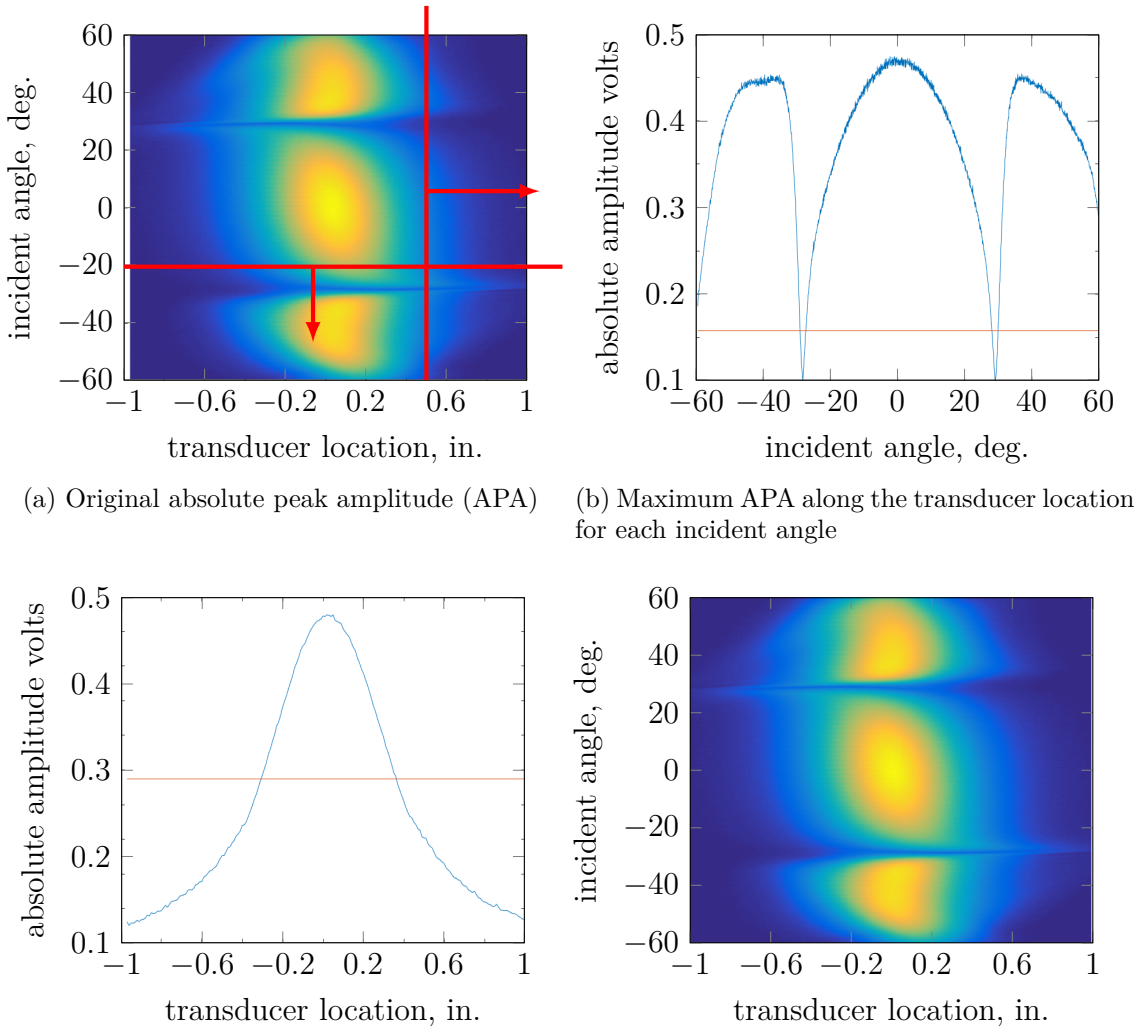

(a) Original absolute peak amplitude (APA)

(b) Maximum APA along the transducer location for each incident angle

(c) Maximum APA along the incident angle for each transducer location

(d) APA with the correct datum

Figure E.6: Determining the datum

dimensional array of absolute peak amplitude, as shown in Figure E.6a as a surface plot. In order to find θ_0, the maximum amplitude along the y-axis for every incident angle is collected. The resulting data is plotted inFigure E.6b. Instead of finding the peak of the plot, the x-axis is shifted up and the roots, or zero crossing, are determined. It is the averaged half-way point between these roots that is used as the θ_0. The same process is followed to determine the y_0, see Figure E.6c. The corrected APA data is shown in Figure E.6d.

Find frequency content

The frequency content at every angle must be determined. The first step is to select a single transducer location for each incident angle. This is accomplished by finding the location of the APA for each incident angle, see Figure E.7. Next the time domain signal undergoes a fast Fourier transform (FFT) to convert the signal into the time domain. The incident angle is then converted into the propagating phase velocity through Snell's law and the pressure velocity of water. This is the same procedure as performed for the contact phased array method (Figure D.2).

$$c = \frac{V_p^{water}}{sin(\theta)}$$

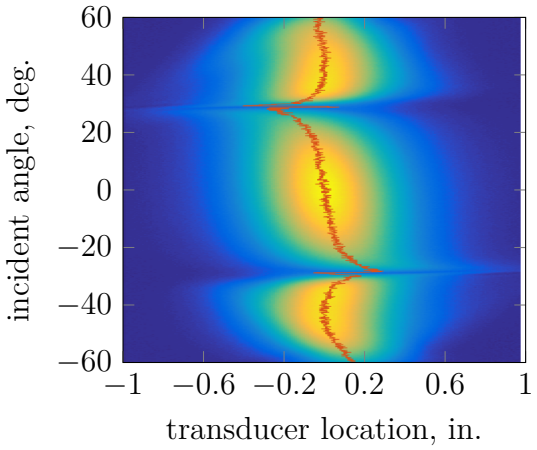

Figure E.7: The location of maximum APA for each incident angle

Results

Finally, the dispersion curve is generated through a surface plot of the frequency content for every incident angle, which is converted to phase velocity through Snell's law (Figure E.8). Figure (a) is the dispersion curve for a 2.25 MHz center frequency transducer (unfocused), and Figure (b) shows the dispersion curve when a 5 MHz transducer is used for the transmitter and receiver, again unfocused.

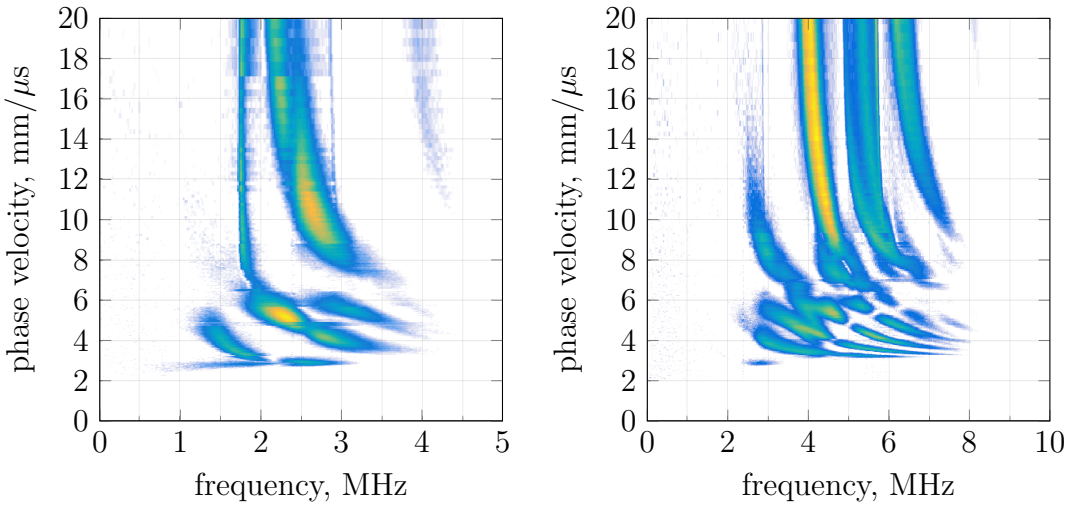

(a) 2.25 MHz transducer, both unfocused

(b) 5 MHz transducer, both unfocused

Figure E.8: Experimental dispersion curves from the immersion technique, coupon I